ABSTRACT

IR-Improved DGLAP-CS Parton Shower Effects in

W + Jets at $\sqrt{s} = 7$, 8, and 13 TeV

Bahram Shakerin, Ph.D.

Advisor: B. F. L. Ward, Ph.D.

The invention and development of collider physics in the twentieth century provides us with opportunities to determine which particles exist in nature, their properties, and the ways they interact with each other. The discovery of the Higgs boson, the last undetected particle predicted in the Standard Model (SM) of Particle Physics, brought a lot of excitement to the international physics community. The SM is based on the gauge group $SU(3)_{QCD} \times SU(2)_{weak} \times U(1)_{hypercharge}$. Through a process called Spontaneous Symmetry Breaking (SSB), it is broken down to $SU(3)_{QCD} \times U(1)_{EM}$ at a scale around 247 GeV [1]. Since the SM is a renormalizable theory with 27 parameters, we can test it by performing enough experiments with enough precision. It is possible to improve the infrared aspects of the standard treatment of the DGLAP-CS evolution theory to take into account a large class of higher-order corrections that significantly improve the precision of the theory for any given level of fixed-order calculation of its respective kernels [2]. We use recently introduced MC realizations of IR-improved DGLAP-CS parton showers to study the attendant improvement effects in W + jets at the LHC in the MG5_aMC@NLO framework for exact $O(\alpha_s)$ corrections. Implementation of the new IR-improved kernels in the framework

of HERWIG6.5 yields the new IR-improved parton shower MC HERWIRI1.031 [3]. Events are showered by HERWIG6.5 and HERWIRI1.031 with PTRMS = 2.2 GeV and PTRMS = 0 GeV, respectively. We compare our results with the available LHC data and discuss the corresponding phenomenological implications. In Chapter Four we have used the latest results provided by CMS and ATLAS for 7 TeV. In Chapter Five we have used the CMS results published in 2017 for 8 TeV.

IR-Improved DGLAP-CS Parton Shower Effects in

W + Jets at $\sqrt{s}$ = 7, 8, and 13 TeV

by

Bahram Shakerin, B.Sc., M.Sc.

A Dissertation

Approved by the Department of Physics

Dwight P. Russell, Ph.D., Interim Chairperson

Submitted to the Graduate Faculty of
Baylor University in Partial Fulfillment of the
Requirements for the Degree
of
Doctor of Philosophy

Approved by the Thesis Committee

B. F. L. Ward, Ph.D., Chairperson

Lorin S. Matthews, Ph.D.

Jay R. Dittmann, Ph.D.

Gerald B. Cleaver, Ph.D.

Keith E. Schubert, Ph.D.

Accepted by the Graduate School
December 2017

J. Larry Lyon, Ph.D., Dean

Page bearing signatures is kept on file in the Graduate School.

TABLE OF CONTENTS

LIST OF FIGURES

LIST OF TABLES

ACKNOWLEDGMENTS

I would like to thank Dr. B.F.L. Ward for his support and encouragement during years I have been working under his supervision. During these years, he has been not only an extraordinary teacher and mentor, but a good friend as well. I also would like to thank our Physics Department at Baylor University and our staff members Mrs. Chava Baker and Mrs. Marian Nunn-Graves for their responsibility and dedication to duty.

To

Ludwig Wittgenstein,

to my wife

Paniz,

to my parents

Dr. Bijan Shakerin and Ladan Khodayar,

to

N. C, C. W, C. H, K. C.

CHAPTER ONE

The Standard Model of Particle Physics

1.1 Introduction

The main aim of particle physics is to search for increasingly accurate theories to describe the fundamental laws of nature. The most fundamental theory of elementary particles according to our current understanding is the Standard Model (SM). The SM merges two separate theories: Quantum ChromoDynamics (QCD), a theory describing the strong force, which is responsible for the attraction between the protons and the neutrons in the nuclei of atoms, and the ElectroWeak (EW) theory, which is responsible for some types of radioactive decays such as beta radiation. In other words, the Standard Model unifies electromagnetism and the two nuclear forces into one model based on Yang-Mills gauge theories.

The electroweak theory as introduced by Glashow [5], Salam [6], and Weinberg [7] describes the electromagnetic and weak interactions between quarks and leptons. In 1961, Glashow constructed a model for weak and electromagnetic interactions of leptons based on gauge $SU(2) \times U(1)$ invariance. He assumed that, together with photons, there also exist charged W and neutral Z intermediate bosons. The masses of the W and Z bosons were inserted by hand. The model introduced by Glashow was unrenormalizable, so he threw it away. In 1967–68, Weinberg and Salam constructed the $SU(2) \times U(1)$ model of electroweak interactions of leptons using the spontaneous breakdown of the gauge symmetry [8–12]. In 1971–72, it was proved by t'Hooft and Veltman [13–17] that models of this type are renomalizable. Weinberg [18] then generalized the model to quarks using the mechanism proposed by Glashow, Iliopoulos and Maiani [19]. The GWS (Glashow-Weinberg-Salam) theory is based on the notion that there exist charged and neutral intermediate vector bosons and it is constructed in such a way that massless fundamental fermions have $SU(2) \times U(1)$ gauge invariance. Then, the interaction of Higgs [8, 20] scalar fields, with both gauge vectors and fermions, is introduced. As a consequence of the breakdown of the underlying symmetry, leptons, quarks and intermediate bosons acquire masses. In 1973, Politzer [21], Gross and Wilczek [22, 23] discovered a remarkable property of Yang-Mills theories [24], "asymptotic freedom," which means that the running coupling constant solution of the renormalization group equation goes to zero when the energy goes to infinity. That could explain the experimental fact that the nucleon behaves in high energy deep inelastic lepton scattering as if it is composed of free quarks [25]. The strong interactions are mediated by eight massless vector bosons called gluons, which are in the adjoint representation of $SU(3)$. QCD has the beautiful property of asymptotic freedom, which provides the means of confining quarks and gluons.

1.1.1 Predictions

The Glashow-Weinberg-Salam (GWS) theory predicts the existence of neutral currents. The neutral current of GWS theory is a linear combination of the third component of the $V - A$ isovector current and the electromagnetic current. The only free parameter, which enters the definition of the neutral current in the standard theory, is $\sin^2(\theta_W)$ where θ_W is called the Weinberg angle. Neutral currents were discovered at CERN in 1973 using a large bubble chamber named Gargamelle [26–29]. In the Gargamelle experiment, the $\nu_\mu(\bar{\nu}_\mu) + N \rightarrow \nu_\mu(\bar{\nu}_\mu) + X$ processes and the $\bar{\nu}_\mu + e \rightarrow \bar{\nu}_\mu + e$ process were observed.

After the discovery of the weak interactions between electrons and nucleons by Stanford [30, 31] and Novosibirsk [32, 33], it became possible to perform a complete phenomenological analysis of all the neutral current data. In 1980–81, experiments on the e^+e^- beams [34] provided new data that also agree with the standard electroweak theory. For more than five decades, different experiments were performed to increase the precision of the parameters proposed and used in the standard model of particle physics. The Higgs boson was still undetected, although in some experiments people could find some constraints on its mass [35]. Finally, the ATLAS and CMS experiments at CERN's Large Hadron Collider (LHC) announced they had each observed a new particle in the mass region around 126 GeV [36]. The discovery of the Higgs boson showed that the standard model of particle physics is a consistent mathematical framework with the ability to have observational predictions. It seems that a new era of higher precision has begun.

1.1.2 The Precision Theory

The perturbative nature of quantum field theory provides the possibility of organizing any calculation regarding Feynman diagrams. The computation of higher-order Feynman diagrams involves the inclusion of real and virtual corrections and is characterized by different kinds of singularities. Ultraviolet (UV) singularities appear only in virtual diagrams and are removed by renormalization. Infrared (IR) soft and collinear divergences, appearing in theories with massless particles, like QED and QCD, cancel out when summing over all the degenerate physical states. The Bloch-Nordsieck theorem [37] states that IR divergences cancel out in transition probabilities for inclusive processes. Order by order in perturbative QED, the sum of the virtual and real corrections is IR finite.

In this dissertation, we start with the method developed by Yennie, Frautschi and Suura (YSF) [38, 39] for resumming the infrared terms in QED and extend it to the non-abelian gauge theories, e.g. QCD, EW, QCD $\otimes$ QED, and Monte Carlo event generators [2, 40–48]. At the end, we give a comparison of the exact amplitude-based resummation theory with the LHC data for W + jets at $\sqrt{s} = 7$ and 8 TeV.

1.2 The SM of the Strong and Electroweak Interactions

In this section, we attempt to formulate a gauge theory of electroweak interactions and strong interactions. We first study the SM before electroweak symmetry breaking. Then, by introducing spontaneous symmetry breaking, we write the Lagrangian density of the SM along with the Higgs field and show how the Higgs mechanism generates masses for the three gauge bosons and fermions.

1.2.1 The SM Before Electroweak Symmetry Breaking

Before introducing the SM Lagrangian density, we focus on two different kinds of fields in the SM, i.e., matter fields and gauge fields. There are three different generations of left-handed and right-handed chiral quarks and leptons. The left-handed fermions are in weak isodoublets, while the right-handed fermions are in weak isosinglets. We write these three different generations as follows:

$$\begin{aligned}
&L_1 = \begin{pmatrix} \nu_e \\ e^- \end{pmatrix}_L, \quad e_{R_1} = e_R^-, \quad Q_1 = \begin{pmatrix} u \\ d \end{pmatrix}_L, \quad u_{R_1} = u_R, \quad d_{R_1} = d_R \\
&L_2 = \begin{pmatrix} \nu_\mu \\ \mu^- \end{pmatrix}_L, \quad e_{R_2} = \mu_R^-, \quad Q_2 = \begin{pmatrix} s \\ c \end{pmatrix}_L, \quad u_{R_2} = c_R, \quad d_{R_2} = s_R \\
&L_3 = \begin{pmatrix} \nu_\tau \\ \tau^- \end{pmatrix}_L, \quad e_{R_3} = \tau_R^-, \quad Q_3 = \begin{pmatrix} t \\ b \end{pmatrix}_L, \quad u_{R_3} = t_R, \quad d_{R_3} = b_R,
\end{aligned} \tag{1.1}$$

where left-handed and right-handed fermions are defined

$$\begin{cases} \psi_L = \dfrac{(1-\gamma_5)}{2}\psi \\[2ex] \psi_R = \dfrac{(1+\gamma_5)}{2}\psi. \end{cases} \tag{1.2}$$

We note that the left-handed fermions all transform as left-handed Weyl spinors, i.e., in the $(\frac{1}{2}, 0)$ representation of the Lorentz group, the right-handed fermions all happen to be $SU(2)$ singlets so they are uncharged under the weak interactions and they transform as right-handed Weyl spinors under the Lorentz group. It is worth to noting that the right-handed neutrinos are pure gauge singlets that are beyond the observables addressed by the GWS theory.

The fermion hypercharge, defined in terms of the third component of the weak isospin I_f^3 and the electric charge Q_f in units of the proton charge $+e$, is given by

$$Y_f = 2Q_f - 2I_f^3. \tag{1.3}$$

We easily find the fermions hypercharge as follows:

$$\begin{aligned}
Y_{\{e^-,\mu^-,\tau^-\}} &= 2(-1) - 2(-\frac{1}{2}) = -1 \Rightarrow Y_{L_i} = -1 \\
Y_{\{e_R^-,\mu_R^-,\tau_R^-\}} &= 2(-1) - 2(0) = -2 \Rightarrow Y_{e_{R_i}} = -2 \\
Y_{\{u,\,c,\,t\}} &= 2(\frac{2}{3}) - 2(\frac{1}{2}) = \frac{1}{3} \Rightarrow Y_{Q_i} = \frac{1}{3} \\
Y_{\{d,\,s,\,b\}} &= 2(-\frac{1}{3}) - 2(-\frac{1}{2}) = \frac{1}{3} \Rightarrow Y_{Q_i} = \frac{1}{3} \\
Y_{u_{R_i}} &= 2(\frac{2}{3}) - 2(0) = \frac{4}{3} \\
Y_{d_{R_i}} &= 2(-\frac{1}{3}) - 2(0) = -\frac{2}{3}.
\end{aligned} \tag{1.4}$$

We note that the quarks are triplets under the $SU(3)_c$ group, while leptons are color singlets. This leads to the important relation

$$\sum_f Y_f = \sum_f Q_f = 0, \tag{1.5}$$

which ensures the cancellation of chiral anomalies within each generation and preserves the renormalizability of the electroweak theory. Besides fermions, there are the gauge fields corresponding to the spin-one bosons that meditate the interactions. In the electroweak sector we have the field $B_\mu(x)$, which corresponds to the generator Y of the $U(1)_Y$ group, and the three fields $W_\mu^1(x)$, $W_\mu^2(x)$, and $W_\mu^3(x)$, which correspond to the generators of the $SU(2)_L$ group; these generators for $SU(2)_L$ are the famous Pauli matrices (apart from an additional factor of $\frac{1}{2}$) with the commutation relations between these generators given by

$$[Y, Y] = 0 \quad \text{and} \quad [T^a, T^b] = i\epsilon_{abc}T^c \quad \text{with} \quad a, b, c = 1, 2, 3, \tag{1.6}$$

where ϵ_{abc} is the famous antisymmetric tensor. In the strong interaction sector, there is an octet of gluon fields $G^1_\mu(x), \ldots, G^8_\mu(x)$, which correspond to the eight generators of the $SU(3)_c$ group. These correspond to the anti-commuting Gell-Mann matrices, which obey the relations

$$[T^a, T^b] = if_{abc}T^c \quad \text{with} \quad a, b, c = 1, \ldots, 8, \tag{1.7}$$

and

$$\mathrm{Tr}[T^a T^b] = \frac{1}{2}\delta_{ab}, \tag{1.8}$$

where the tensor f_{abc} is for the structure constants of the $SU(3)_c$ group.

The gauge fields are given by

$$\begin{aligned} G^a_{\mu\nu}(x) &= \partial_\mu G^a_\nu(x) - \partial_\nu G^a_\mu(x) + g_s f_{abc} G^b_\mu(x) G^c_\nu(x) \\ W^a_{\mu\nu}(x) &= \partial_\mu W^a_\nu(x) - \partial_\nu W^a_\mu(x) + g_2 \epsilon_{abc} W^b_\mu(x) W^c_\nu(x) \\ B_{\mu\nu}(x) &= \partial_\mu B_\nu(x) - \partial_\nu B_\mu(x), \end{aligned} \tag{1.9}$$

where g_s, g_2, and g_1 are, respectively, the coupling constants of $SU(3)_c$, $SU(2)_L$, and $U(1)_Y$. The non-Abelian nature of the $SU(3)_c$ and $SU(2)_L$ groups causes self-interactions between gauge fields $W^a_\mu(x)$ and $W^a_\mu(x)$ such as

$$\text{quadratic gauge boson coupling:} \; -\frac{1}{4}g_s^2 f_{abc} f_{dec} G^a_\mu G^b_\nu G^{d\mu} G^{e\nu}, \tag{1.10}$$

and

$$\text{triple gauge boson couplings:} \quad g_s f_{abc} G^a_\mu G^b_\nu \partial^\mu G^{c\nu}. \tag{1.11}$$

The matter fields ψ are minimally coupled to the gauge fields through the covariant derivative D_μ which for the case of quarks is defined as

$$D_\mu \psi = \left(\partial_\mu - ig_s T^a G_{a\mu} - ig_2 T^a W_{a\mu} - ig_1 \frac{Y_q}{2} B_\mu\right)\psi, \tag{1.12}$$

which leads to the coupling between the fermion and gauge fields, for example

$$-g_s \bar{\psi} G^a_\mu \gamma^\mu \psi. \tag{1.13}$$

The SM Lagrangian without mass terms for fermions and gauge bosons is given by

$$\begin{aligned}\mathcal{L}_{SM} = &-\frac{1}{4}G^a_{\mu\nu}G^{\mu\nu}_a - \frac{1}{4}W^a_{\mu\nu}W^{\mu\nu}_a - \frac{1}{4}B_{\mu\nu}B^{\mu\nu} \\ &+ i\bar{L}_i \not{D}_\mu L_i + i\bar{e}_{R_i}\not{D}_\mu e_{R_i} + i\bar{Q}_i \not{D}_\mu Q_i + i\bar{u}_{R_i}\not{D}_\mu u_{R_i} i\bar{d}_{R_i}\not{D}_\mu d_{R_i}.\end{aligned} \tag{1.14}$$

This Lagrangian is clearly invariant under any local $SU(3)_c \times SU(2)_L \times U(1)_Y$ gauge transformations for fermions and gauge fields. In the case of the electroweak sector, for instance, we have

$$\begin{cases} L(x) \to L^{'}(x) = e^{i\sum_{a=1}^{3}\alpha_a(x)T^a + i\beta(x)Y}L(x) \\ R(x) \to R^{'}(x) = e^{i\beta(x)Y}R(x) \\ \vec{W}_\mu(x) \to \vec{W}^{'}_\mu(x) = \vec{W}_\mu(x) - \frac{1}{g_2}\partial_\mu\vec{\alpha}(x) - \vec{\alpha}(x) \times \vec{W}_\mu(x) \\ B_\mu(x) \to B^{'}_\mu(x) = B_\mu(x) - \frac{1}{g_1}\partial_\mu\beta(x). \end{cases} \tag{1.15}$$

The gauge bosons and the fermions have been kept massless in this Lagrangian. We show how by implementing the Higgs mechanism, which is based on spontaneous symmetry breaking, the fermions and gauge bosons gain masses.

1.3 The Higgs Mechanism

We start with a simple scalar real field ϕ with the usual Lagrangian

$$\mathcal{L} = \frac{1}{2}\partial_\mu\phi\partial^\mu\phi - \frac{1}{2}\mu^2\phi^2 - \frac{1}{4}\phi^4. \tag{1.16}$$

This Lagrangian is clearly invariant under the transformation $\phi \to -\phi$ since it does not include cubic terms. If the mass term μ^2 is positive, the potential $V(\phi)$ is also positive if the self-coupling λ is positive and the minimum of the potential is obtained for $\phi_0 \equiv \langle 0|\phi|0\rangle = 0$ shown in the left-hand side of Figure (1.1). If $\mu^2 < 0$, the potential $V(\phi)$ has a minimum, which can be found as follows

$$\frac{d}{d\phi}V(\phi) = \mu^2\phi + \lambda\phi^3 = 0 \Rightarrow \phi = 0, \pm\sqrt{-\frac{\mu^2}{\lambda}}. \tag{1.17}$$

Since $\frac{d^2}{d\phi^2}V(\pm\sqrt{-\frac{\mu^2}{\lambda}}) > 0$, we conclude that $\phi_0^2 \equiv \left\langle 0|\phi^2|0\right\rangle = -\frac{\mu^2}{\lambda} \equiv v^2$, and it is obvious that $\phi = 0$ is not a minimum as shown in the right-hand side of Figure 1.1.

We must expand ϕ around one of the minima v by defining the field σ as $\phi = v + \sigma$. We rewrite the Lagrangian in terms of new field σ, and the Lagrangian becomes

$$\mathcal{L} = \frac{1}{2}\partial_\mu\sigma\partial^\mu\sigma - (-\mu^2)\sigma^2 - \sqrt{-\mu^2\lambda}\sigma^3 - \frac{\lambda}{4}\sigma^4 - \frac{\lambda}{4}(\frac{\mu^2}{\lambda^2})^2. \quad (1.18)$$

The Lagrangian in Eq. (1.18) is related to a theory of scalar field of mass $m^2 = -2\mu^2$,

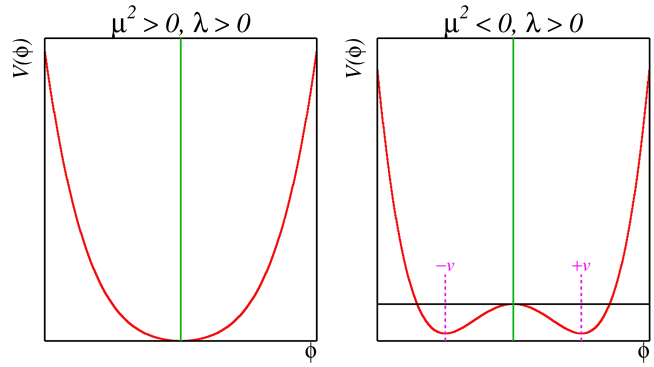

Figure 1.1: The potential V of the scalar field ϕ in the case $\mu^2 > 0$ (left) and $\mu^2 < 0$ (right).

with σ^3 and σ^4 self-interactions. Since the new Lagrangian now contains cubic terms, the $\sigma \to -\sigma$ symmetry is broken: it is not anymore apparent in $\mathcal{L}$. It can be shown that for every spontaneously broken continuous symmetry, besides massive particles, the theory also contains massless scalar spin-0 particles called Goldstone bosons. This brings us to the Goldstone theorem: For every spontaneously broken continuous symmetry, the theory contains massless scalar (spin-0) particles called Goldstone bosons.

1.3.1 The Higgs Mechanism in an Abelian Theory

We can apply the same argument to the case of a local $U(1)$ symmetry. A complex scalar field coupled to itself and to an electromagnetic field $A_\mu(x)$

$$\mathcal{L} = -\frac{1}{4}F_{\mu\nu}F^{\mu\nu} + D_\mu\phi^* D^\mu\phi - \mu^2\phi^*\phi - \lambda(\phi^*\phi)^2, \quad (1.19)$$

with $D_\mu = \partial_\mu - ieA_\mu$. The Lagrangian is invariant under the usual local symmetry $U(1)$ transformation

$$\phi(x) \to e^{i\alpha(x)}\phi(x) \quad \text{and} \quad A_\mu(x) \to A_\mu(x) - \frac{1}{e}A_\mu(x). \tag{1.20}$$

For $\mu^2 < 0$, the field $\phi(x)$ will acquire a vacuum expectation value and the minimum of the potential V will be at

$$\langle \phi_0 \rangle \equiv \langle 0|\phi|0\rangle = \sqrt{(-\frac{\mu^2}{2\lambda})} \equiv \frac{v}{\sqrt{2}}. \tag{1.21}$$

We thus expand the scalar field $\phi(x)$ around the vacuum state $\langle \phi_0 \rangle$

$$\phi(x) = \frac{1}{\sqrt{2}}\left[v + \phi_1(x) + i\phi_2(x)\right] \tag{1.22}$$

and rewrite the Lagrangian in the form

$$\mathcal{L} = -\frac{1}{4}F_{\mu\nu}F^{\mu\nu} + \frac{1}{2}(\partial_\mu\phi_1)^2 + \frac{1}{2}(\partial_\mu\phi_2)^2 - v^2\lambda\phi_1^2 + \frac{1}{2}e^2v^2A_\mu(x)A^\mu(x) - evA_\mu(x)\partial^\mu\phi_2. \tag{1.23}$$

We can conclude:

- There is photon mass term in the Lagrangian with $M_A = ev = -\frac{e\mu^2}{\lambda}$.
- We still have a scalar particle ϕ_1 with mass $M_{\phi_1} = -2\mu^2$.
- We have a Goldstone boson ϕ_2.

1.4 The Higgs Mechanism in the SM

Applying the Higgs mechanism to the case of SM is more complicated than our example for Abelian gauge theory. We have different gauge bosons in the standard model. Only three gauge bosons $W^\pm$ and Z should acquire mass and the photon and gluons should still remain massless. Therefore, we need at least three degrees of freedom for the scalar fields. The simplest choice is a complex $SU(2)$ doublet of scalar field ϕ

$$\Phi_H(x) = \begin{pmatrix} \phi^+ \\ \phi^0 \end{pmatrix}, \tag{1.24}$$

with $Y_\phi = +1$ and $I^3_\phi = -\frac{1}{2}$. We now add the invariant terms of the scalar field part

$$\mathcal{L}_H = (D_\mu \Phi_H(X))(D^\mu \Phi_H(X)) - \mu^2 \Phi^\dagger_H(x)\Phi_H(x) - \lambda(\Phi^\dagger_H(x)\Phi_H(x)), \tag{1.25}$$

with

$$D_\mu \Phi_H(x) = \left(\partial_\mu - ig_2 \frac{\tau^a}{2} W^a_\mu - ig_1 \frac{1}{2} B_\mu\right)\Phi_H(x). \tag{1.26}$$

For $\mu^2 < 0$, the neutral component of the doublet field Φ_H will develop a non-zero vacuum expectation value

$$\langle \Phi_H \rangle_0 \equiv \langle 0|\Phi_H|0\rangle = \begin{pmatrix} 0 \\ \frac{v}{\sqrt{2}} \end{pmatrix} \quad \text{with} \quad v = \sqrt{-\frac{\mu^2}{\lambda}} \tag{1.27}$$

We now write the field $\Phi_H(x)$ in terms of four fields $\theta_{1,2,3}(x)$ and $H(x)$ at first order as follows

$$\Phi_H(x) = \begin{pmatrix} \theta_2 + i\theta_1 \\ \frac{1}{\sqrt{2}}(v + H(x)) - i\theta_3 \end{pmatrix} = e^{i\theta_a(x)\frac{\tau^a}{v}} \begin{pmatrix} 0 \\ \frac{1}{\sqrt{2}}(v + H(x)) \end{pmatrix}. \tag{1.28}$$

We then define the gauge transformation for $\Phi_H(x)$ in the form

$$\Phi_H(x) \to \Phi'_H(x) = e^{-i\theta_a(x)\tau^a}\Phi_H(x) = \begin{pmatrix} 0 \\ \frac{1}{\sqrt{2}}(v + H(x)) \end{pmatrix}. \tag{1.29}$$

One can prove that $|D_\mu \Phi_H(x)|^2$ can be written in the form

$$\begin{aligned} |D_\mu \Phi_H(x)|^2 &= \left|\left(\partial_\mu - ig_2 \frac{\tau_a}{2} W^a_\mu - i\frac{1}{2} g_1 B_\mu(x)\right)\Phi_H(x)\right|^2 \\ &= \frac{1}{2}\left| \begin{pmatrix} \partial_\mu - \frac{i}{2}(g_2 W^3_\mu + g_1 B_\mu) & -\frac{ig_2}{2}(W^1_\mu - iW^2_\mu) \\ g - \frac{ig_2}{2}(W^1_\mu + iW^2_\mu) & \partial_\mu + \frac{i}{2}(g_2 W^3_\mu - g_1 B_\mu) \end{pmatrix} \begin{pmatrix} 0 \\ v + H(x) \end{pmatrix} \right|^2 \\ &= \frac{1}{2}(\partial_\mu H)^2 + \frac{1}{8} g_2^2 (v+H)^2 |W^1_\mu + iW^2_\mu|^2 + \frac{1}{8}(v+H)^2 |g_2 W^3_\mu - g_1 B_\mu|^2. \end{aligned} \tag{1.30}$$

Now we define the new fields $W^\pm$ and Z_μ:

$$W^\pm = \frac{1}{\sqrt{2}}(W^1_\mu + iW^2_\mu), \; Z_\mu = \frac{g_2 W^3_\mu - g_1 B_\mu}{\sqrt{g_1^2 + g_2^2}}, \; A_\mu = \frac{g_2 W^3_\mu + g_1 B_\mu}{\sqrt{g_1^2 + g_2^2}}. \tag{1.31}$$

By picking up the terms that are bilinear in the fields W$^{\pm}$, Z$_\mu$, A_μ, we obtain

$$M_W^2 W_\mu^+ W^{-\mu} + \frac{1}{2} M_Z^2 Z_\mu Z^\mu + \frac{1}{2} M_A^2 A_\mu A^\mu. \tag{1.32}$$

During the spontaneous breaking of symmetry, the gauge bosons W$^{\pm}$ and Z$_\mu$ gain masses. A_μ still remains massless:

$$M_W = \frac{v}{g_2},\ M_Z = \frac{v}{2}\sqrt{g_1^2 + g_2^2},\ M_A = 0. \tag{1.33}$$

So far, we have shown how gauge fields acquire masses through the Higgs mechanism. The question is how fermions gain masses under the spontaneous breaking of symmetry. We can generate the fermion masses using the same scalar field Φ_H with hypercharge $Y = 1$ by using the isodoublet $\tilde{\Phi}_H(x) = i\tau_2 \Phi_H^*(x)$, which has hypercharge $Y = -1$. We introduce the $SU(2)_L \times U(1)_Y$ invariant Yukawa Lagrangian

$$\mathcal{L}_{fermion} = -\lambda_e \bar{L} \Phi_H e_R - \lambda_d \bar{Q} \Phi_H d_R - \lambda_u \bar{Q} \tilde{\Phi}_H u_R + h.c. \tag{1.34}$$

For the case of the electron, we obtain

$$\begin{aligned} \mathcal{L}_e &= -\frac{1}{\sqrt{2}} (\bar{\nu}_e, \bar{e}_L) \begin{pmatrix} 0 \\ (v + H(x)) \end{pmatrix} e_R \\ &= -\frac{1}{\sqrt{2}} \lambda_e (v + H) \bar{e}_L e_R, \end{aligned} \tag{1.35}$$

which leads to $m_e = \dfrac{\lambda_e v}{\sqrt{2}}$. Similarly, we find $m_u = \dfrac{\lambda_u v}{\sqrt{2}}$ and $m_d = \dfrac{\lambda_d v}{\sqrt{2}}$.

1.4.1 The Higgs Particle in the SM

We find the Higgs Lagrangian in terms of the vacuum expectation value (VEV) and $H(x)$. We start with the Higgs potential term $V(\Phi_H) = \mu^2 \Phi_H^\dagger \Phi_H + \lambda(\Phi_H^\dagger \Phi_H)^2$

$$\begin{aligned} V &= \frac{\mu^2}{2}(0, v + H) \begin{pmatrix} 0 \\ (v + H(x)) \end{pmatrix} + \frac{\lambda}{4} \left| (0, v + H) \begin{pmatrix} 0 \\ (v + H(x)) \end{pmatrix} \right|^2 \\ &= -\frac{1}{2} \lambda v^2 (v + H)^2 + \frac{1}{4}(v + H)^4. \end{aligned} \tag{1.36}$$

We rewrite the Higgs Lagrangian in the form

$$\begin{aligned}\mathcal{L}_H &= \frac{1}{2}(\partial_\mu H)(\partial^\mu H) - V \\ &= \frac{1}{2}(\partial_\mu H)^2 - \lambda v^2 H^2 - \lambda v H^3 - \frac{\lambda}{4}H^4.\end{aligned} \tag{1.37}$$

From the Higgs Lagrangian, one can find that the Higgs particle mass reads

$$M_H^2 = 2\lambda v^2 = -2\mu^2. \tag{1.38}$$

The VEV, v, is fixed in terms of W bosons mass M_{W} or the Fermi constant G as follows

$$M_W = \frac{1}{2}g_2 v = \left(\frac{\sqrt{2}g^2}{8G}\right)^{\frac{1}{2}} \Rightarrow v = \frac{1}{(\sqrt{2}G)^{\frac{1}{2}}} \simeq 246 \text{ GeV}. \tag{1.39}$$

Finally, we summarize the interactions of the fermions and gauge bosons in the electroweak standard model. The equations for the field rotation that lead to the physical gauge bosons in Eq. (1.31) define the Weinberg angle θ_W[1] as follows

$$\begin{cases} A_\mu = \cos\theta_W B_\mu + \sin\theta_W W_\mu^3 \\ Z_\mu = -\sin\theta_W B_\mu + \cos\theta_W W_\mu^3 \end{cases} \tag{1.40}$$

where

$$\sin\theta_W = \frac{g_1}{\sqrt{g_1^2 + g_2^2}} = \frac{e}{g_2} = \sqrt{1 - \frac{M_W^2}{M_Z^2}}. \tag{1.41}$$

Using the results in Eq. (1.40), we can rewrite the fermionic part of the SM Lagrangian in the form

$$\begin{aligned}\mathcal{L}_{N.C.} &= eJ_\mu^A A^\mu + \frac{g_2}{\cos\theta_W}J_\mu^Z Z^\mu, \\ \mathcal{L}_{C.C.} &= \frac{g_2}{\sqrt{2}}(J_\mu^+ W^{+\mu} + J_\mu^- W^{-\mu}),\end{aligned} \tag{1.42}$$

[1] Angle by which spontaneous symmetry breaking rotates the original vector boson plane and producing as a result the Z boson and the photon.

for the neutral and charged current parts, respectively. The corresponding currents are given by

$$\begin{aligned}
J_\mu^A &= Q_f \bar{f} \gamma_\mu f, \\
J_\mu^Z &= \frac{1}{4} \bar{f} \gamma_\mu [(2I_f^3 - 4Q_f \sin^2\theta_W) - 2\gamma_5 I_f^3)] f, \\
J_\mu^+ &= \frac{1}{2} \bar{f}_u \gamma_\mu (1-\gamma_5) f_d.
\end{aligned} \tag{1.43}$$

1.5 Summary

We can summarize our discussion of the SM in a compact Figure 1.2. The electroweak theory with QCD forms the Standard Model of particle physics. In the SM there is some interplay between the electroweak sector and the QCD sector due to the fact that particles feel both forces. The SM summarizes the present knowledge of particle physics.

- There are twelve force carriers: the eight gluons, the $W^\pm$, Z^0 and the photon.
- The matter particles are divided into two types: leptons and quarks. We also must include their antiparticles.
- We have a grand total of 61 particles in the SM: 6×2 leptons, $6 \times 3 \times 2$ quarks, 12 gauge bosons and the Higgs boson.

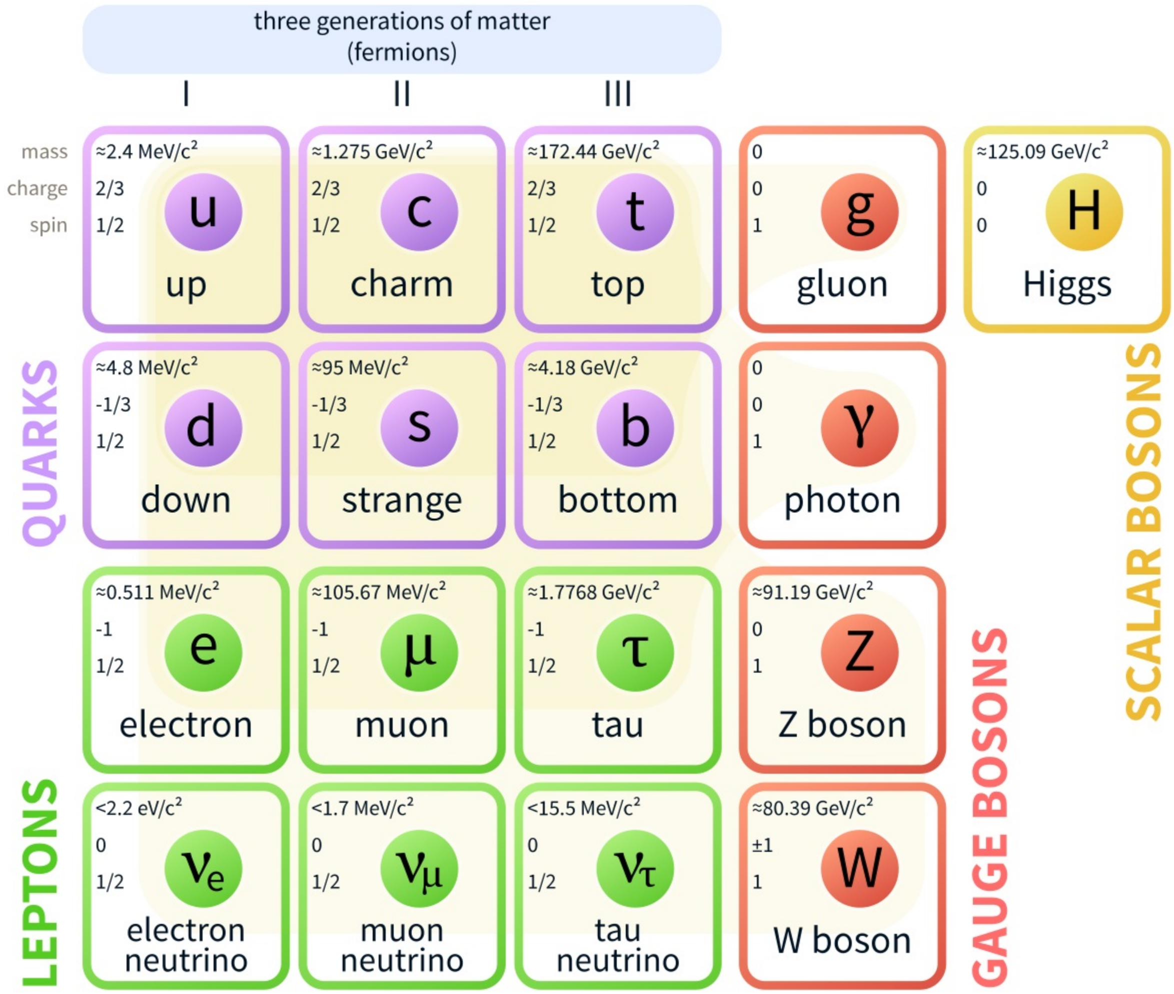

Figure 1.2: Elementary particles in the SM[2]

[2]Picture taken from `https://en.wikipedia.org/wiki/Standard_Model/`

CHAPTER TWO

DGLAP-CS Theory

2.1 Introduction

The quark parton model introduced by Feynman [49, 50] provides us with a simple description of the physics of deep inelastic scattering. Later on, Gross and Wilczek [22, 23] and Politzer [21] independently introduced a theoretical framework, which is given by the asymptotically free gauge theory of strong interactions based on the color algebra. In the leading logarithmic approximation, the results can be phrased in the parton language by assigning a well determined Q^2 dependence to the parton densities.

In this chapter we prove that an alternative derivation of all results for the Q^2 behaviour of deep inelastic scattering is possible. This approach, although less general, is simpler than the usual approach, which can be derived in a direct way from the basic vertices of QCD.

2.2 The Master Equations

We start with the unpolarized case when only the densities

$$q^i(x) = q^i_+(x) + q^i_-(x) \tag{2.1}$$

are relevant. We start by considering the simplest case of only one flavour of quark. We denote it by $q^{NS}(x)$ in which we mean the net number of quarks in the proton, that is, the algebraic summation of quarks and anti-quarks in the proton as follows:

$$q^{NS}(x,t) = q(x,t) - \bar{q}(x,t), \tag{2.2}$$

where the variable t is defined as $t = \ln(\frac{Q^2}{Q_0^2})$ with Q_0^2 a suitable renormalization point. The label NS stands for non singlet. The Q^2 dependence can be expressed in terms of moments of parton densities. We define

$$M_n^{NS}(t) = \int_0^1 dx\ x^{n-1} q^{NS}(x,t). \tag{2.3}$$

One can prove [22, 23] that the t dependence of the moments is of the form

$$M_n^{NS}(t) = M_n^{NS}(0) \left[\frac{\alpha(0)}{\alpha(t)}\right]^{\frac{A_n^{NS}}{2\pi b}}. \tag{2.4}$$

Here $\alpha(t)$ is the running coupling constant of QCD, where $\alpha(t) = \frac{g^2(t)}{4\pi}$. In the leading logarithmic approximation $\alpha(t)$ is of the form [51, 52]

$$\frac{\alpha}{\alpha(t)} = 1 + b\alpha t, \tag{2.5}$$

with $\alpha = \alpha(0)$ and $b = \frac{11C_2(G) - 4T(R)}{12\pi}$, where $C_2(G)$ and $T(R)$ are Casimir operators for the adjoint representation G of the color group and for the representation R of the fermion, respectively (see Appendix A).

Now we differentiate both sides of Eq. (2.4) with respect to t to find the differential equation for $M_n^{NS}(t)$ by using the result in Eq. (2.5). One can show:

$$\frac{d}{dt} M_n^{NS}(t) = M_n^{NS}(0) \frac{d}{dt} \left[\frac{\alpha(0)}{\alpha(t)}\right]^{\frac{A_n^{NS}}{2\pi b}} \tag{2.6}$$

$$= M_n^{NS}(0) \frac{d}{dt} \left[1 + \alpha b t\right]^{\frac{A_n^{NS}}{2\pi b}} \tag{2.7}$$

$$= \frac{A_n^{NS}}{2\pi} \alpha(0) \left[1 + \alpha b t\right]^{\frac{A_n^{NS} - 1}{2\pi b}}. \tag{2.8}$$

A little simplification yields:

$$\frac{d}{dt} M_n^{NS}(t) = \frac{\alpha(t)}{2\pi} M_n^{NS}(t) A_n^{NS}, \tag{2.9}$$

with assigned initial value $M_n^{NS} = M_n^{NS}(0)$. It is easy to show that Eq. (2.9) can be written of the form:

$$\frac{dq^{NS}(x,t)}{dt} = \frac{\alpha(t)}{2\pi} \int_x^1 \frac{dy}{y} q^{NS}(y,t) P\left(\frac{x}{y}\right), \tag{2.10}$$

provided that

$$\int_0^1 dz\ z^{n-1}P(z) = A_n^{NS}. \tag{2.11}$$

We multiply both sides of Eq. (2.11) by x^{n-1} and integrate from 0 to 1. We then find:

$$\int_0^1 dx \frac{dq^{NS}(x,t)}{dt} x^{n-1} = \frac{\alpha(t)}{2\pi} \int_0^1 dx\ x^{n-1} \int_x^1 \frac{dy}{y} q^{NS}(y,t) P\left(\frac{x}{y}\right). \tag{2.12}$$

By using Eq. (2.3) we rewrite the left hand side of Eq. (2.12) as follows:

$$\frac{dM_n^{NS}}{dt} = \frac{\alpha(t)}{2\pi} \int_0^1 dx\ x^{n-1} \int_x^1 \frac{dy}{y} q^{NS}(y,t) P\left(\frac{x}{y}\right). \tag{2.13}$$

It is easy to show the integration order can be interchanged by using $\int_0^1 dx \int_x^1 dy\ (...) = \int_0^1 dy \int_0^y dx\ (...)$. We can rewrite Eq. (2.13) as follows:

$$\frac{dM_n^{NS}}{dt} = \frac{\alpha(t)}{2\pi} \int_0^1 dy\ x^{n-1} \int_0^y \frac{dx}{y} q^{NS}(y,t) P(\frac{x}{y}). \tag{2.14}$$

Introducing a new variable $z = \frac{x}{y}$ yields:

$$\frac{dM_n^{NS}}{dt} = \frac{\alpha(t)}{2\pi} \int_0^1 dy\ y^{n-1} q^{NS}(y,t) \int_0^1 dz\ z^{n-1} P(z). \tag{2.15}$$

We compare Eq. (2.15) with Eq. (2.9) and find that

$$M_n^{NS}(t) = \int_0^1 dy\ y^{n-1} q^{NS}(y,t) \tag{2.16}$$

is valid if and only if $A_n^{NS} = \int_0^1 dz\ z^{n-1}P(z)$. It is convenient to rewrite Eq. (2.10) in the form

$$q^{NS}(x,t) + dq^{NS}(y,t) = \int_0^1 dy \int_0^1 dz\ \delta(zy-x) q^{NS}(y,t) \left[\delta(z-1) + \frac{\alpha}{2\pi} P(z) dt\right]. \tag{2.17}$$

The interpretation of this equation is very easy. Given a quark with momentum y there is a chance that it radiates a gluon by reducing its energy from y to x. we can easily conclude that the quantity

$$\mathcal{P}_{qq} + d\mathcal{P}_{qq} = \delta(z-1) + \frac{\alpha}{2\pi} P(z) dt, \tag{2.18}$$

is the probability density of finding, inside a quark, another quark with fraction z of the parent momentum. The $\frac{\alpha}{2\pi}P(z)dt$ term is the variation per unit t at order α of the probability density of finding inside a quark another quark with fraction z of the parent momentum.

In parton language, singlet density is a combination of the sum of all quark and anti-quark densities and gluon densities inside the proton in the P_∞ frame. We write down differential equations similar to Eq. (2.10) that describe the Q^2 dependence in the general case we demonstrated above. They are

$$\frac{dq^i(x,t)}{dt} = \frac{\alpha(t)}{2\pi} \int_x^1 \frac{dy}{y} \left[\sum_{j=1}^{2f} q^j(y,t) P_{q^i q^j}\left(\frac{x}{y}\right) + G(y,t) P_{q^i G}\left(\frac{x}{y}\right) \right], \tag{2.19}$$

$$\frac{dG(x,t)}{dt} = \frac{\alpha(t)}{2\pi} \int_x^1 \frac{dy}{y} \left[\sum_{j=1}^{2f} q^j(y,t) P_{Gq^j}\left(\frac{x}{y}\right) + G(y,t) P_{GG}\left(\frac{x}{y}\right) \right]. \tag{2.20}$$

The indices i and j run over quarks and anti-quarks of all flavours. Quarks at higher energy can lose energy by gluon radiation. Similarly, a gluon inside the proton may annihilate into a quark and anti-quark or a gluon-gluon pair. This is why the number of gluons changes.

One can simplify Eqs. (2.19) and (2.20) by using the fact that color and flavour commute. We immediately derive the following properties for splitting functions as follows:

- A gluon is emitted without flavour exchange $\rightarrow P_{q^i q^j}$ is diagonal.
- The probability of a emitting a gluon is the same for all flavours if we neglect the mass of all particles $\rightarrow P_{Gq^j} = P_{Gq}$.

- Gluon annihilation creates a quark and anti-quark pair with equal probability for all flavours $\rightarrow P_{q^iG} = P_{qG}$.

By imposing the above conditions on Eqs. (2.19) and (2.20), one can rewrite them in the simpler form

$$\frac{dq^i(x,t)}{dt} = \frac{\alpha(t)}{2\pi}\int\limits_x^1 \frac{dy}{y}\left[q^i(y,t)P_{qq}\left(\frac{x}{y}\right) + G(y,t)P_{qG}\left(\frac{x}{y}\right)\right], \tag{2.21}$$

$$\frac{dG(x,t)}{dt} = \frac{\alpha(t)}{2\pi}\int\limits_x^1 \frac{dy}{y}\left[\sum_{j=1}^{2f} q^j(y,t)P_{Gq}\left(\frac{x}{y}\right) + G(y,t)P_{GG}\left(\frac{x}{y}\right)\right]. \tag{2.22}$$

By summing Eq. (2.22) over $i = 1, \ldots, 2f$, we find

$$\frac{d\sum_{i=1}^{2f} q^i(x,t)}{dt} = \frac{\alpha(t)}{2\pi}\int\limits_x^1 \frac{dy}{y}\left[\sum_{j=1}^{2f} q^j(y,t)P_{q^iq^j}\left(\frac{x}{y}\right) + 2fG(y,t)P_{q^iG}\left(\frac{x}{y}\right)\right]. \tag{2.23}$$

It is the matrix

$$\int\limits_0^1 dz\, z^{n-1}\begin{pmatrix} P_{qq}(z) & 2fP_{qG}(z) \\ P_{Gq}(z) & P_{GG}(z) \end{pmatrix} \equiv \begin{pmatrix} A_n^{NS} & 4T(R)A_n^{qG} \\ A_n^{Gq} & A_n^{GG}) \end{pmatrix} \tag{2.24}$$

that gives the logarithmic exponents for each n as given in [22, 23, 53]. It is clear that for each value of n the matrix in Eq. (2.24) must be diagonalized to find the eigenvalues and eigenvectors of the Q^2 evolution equations.

We can also find the derivatives for two quarks (or a quark and an anti-quark) for the non-singlet case by subtracting Eq. (2.21) twice. We obtain

$$\frac{dq^i(x,t)}{dt} = \frac{\alpha(t)}{2\pi}\int\limits_x^1 \frac{dy}{y}\left[q^i(y,t)P_{qq}\left(\frac{x}{y}\right) + G(y,t)P_{qG}\left(\frac{x}{y}\right)\right], \tag{2.25}$$

$$\frac{dq^j(x,t)}{dt} = \frac{\alpha(t)}{2\pi}\int\limits_x^1 \frac{dy}{y}\left[q^j(y,t)P_{qq}\left(\frac{x}{y}\right) + G(y,t)P_{qG}\left(\frac{x}{y}\right)\right]. \tag{2.26}$$

By subtracting Eq. (2.25) from Eq. (2.26) one can find

$$\frac{d\big[q^i(x,t) - q^j(x,t)\big]}{dt} = \frac{\alpha(t)}{2\pi}\int\limits_x^1 \frac{dy}{y}\big[q^i(x,t) - q^j(x,t)\big]P_{qq}\left(\frac{x}{y}\right). \tag{2.27}$$

This shows that P_{qq} is the same function for singlet quarks and for all types of non-singlet anti-quarks.

The functions $\frac{\alpha(t)}{2\pi}P_{Gq}(z)$ and $\frac{\alpha(t)}{2\pi}P_{qG}(z)$ can be interpreted as probability densities. The first, $\frac{\alpha(t)}{2\pi}P_{Gq}(z)$, is the probability density per unit t at order α of finding a gluon inside a quark (or an anti-quark) with fraction z of the momentum of the parent quark. Similarly, $\frac{\alpha(t)}{2\pi}P_{qG}(z)$ can be interpreted as the probability density per unit t at order α of finding a quark (or an anti-quark) inside a gluon with with fraction z of the momentum of the parent gluon. Needless to say, either $\frac{\alpha(t)}{2\pi}P_{Gq}(z)$ or $\frac{\alpha(t)}{2\pi}P_{qG}(z)$ is non-diagonal. For the diagonal functions $\frac{\alpha(t)}{2\pi}P_{qq}(z)$ and $\frac{\alpha(t)}{2\pi}P_{GG}(z)$ the probability involves delta function singularities at $z = 1$. For example, for cases including gluons one can write

$$\mathcal{P}_{GG} + d\mathcal{P}_{GG} = \delta(z-1) + \frac{\alpha}{2\pi}P_{GG}(z)dt. \tag{2.28}$$

Therefore only for $z < 1$, $\frac{\alpha(t)}{2\pi}P_{Gq}(z)$ and $\frac{\alpha(t)}{2\pi}P_{qG}(z)$ are probability densities.

2.3 Properties of DGLAP-CS Splitting Functions

Based on conservation of momentum and the number of particles, we can immediately find some interesting properties of these splitting functions as explained below.

1. The total number of quarks minus anti-quarks is conserved. This means that the probability of finding a quark in a quark over all values of z must add up to one. It follows that the integrated correction of order α must be zero

$$\int_0^1 dz\ P_{qq}(z) = 0, \tag{2.29}$$

which means

$$A_n^{NS} = 0 \text{ for } n = 1. \tag{2.30}$$

This is another indication that charges are protected against Q^2 corrections. We shall see that the values of A_n^{NS} are all negative for $n > 1$ due to the presence of δ function singularities that destroy the positive definiteness of the integrals P_{qq} and P_{GG}.

2. Momentum conservation puts further restrictions on the P functions at $z < 1$. We obtain

$$P_{qq}(z) = P_{Gq}(1-z), \tag{2.31}$$

$$P_{qG}(z) = P_{qG}(1-z), \qquad (z < 1) \tag{2.32}$$

$$P_{GG}(z) = P_{GG}(1-z). \tag{2.33}$$

To interpret Eq. (2.31), one can say when a quark splits into a gluon with fraction $(1-z)$ of its momentum and another quark with fraction z of its momentum, conservation of momentum requires that $P_{qq}(z) = P_{Gq}(1-z)$. Otherwise, momentum conservation is violated.

3. At $z = 1$, due to the presence of the δ function, Eqs. (2.31), (2.32), and (2.33) are violated. But it must remain true that the total momentum of the proton remains unchanged. We obtain

$$\int_0^1 dz\; z\big[P_{qq}(z) + P_{Gq}(z)\big] = 0, \tag{2.34}$$

$$\int_0^1 dz\; z\big[P_{qG}(z) + P_{GG}(z)\big] = 0, \tag{2.35}$$

which guarantee the conservation of the total momentum of the proton, as expected.

We return to the master equation, Eq. (2.24). Based on the properties of the DGLAP-CS splitting functions derived above, we find some useful relationships between matrix elements A_n^{NS}, A_n^{qG}, A_n^{Gq}, and A_n^{GG}. For example, using Eqs. (2.24) and (2.31) results in

$$A_n^{NS} = \int_0^1 dz\; z^{n-1} P_{qq}(z) = \int_0^1 dz\; z^{n-1} P_{Gq}(1-z). \tag{2.36}$$

Making a change of variable $z \to 1 - z$ and replacing z by $1 - z$ results in

$$A_n^{NS} = \int_0^1 dz\ (1-z)^{n-1} P_{Gq}(z) = \int_0^1 dz \sum_{k=0}^{n-1} (-1)^k z^k \binom{n-1}{k} P_{Gq}(z) \tag{2.37}$$

$$= \sum_{k=0}^{n-1} (-1)^k \binom{n-1}{k} \int_0^1 dz\ z^k P_{Gq}(z) = \sum_{k=0}^{n-1} (-1)^k \binom{n-1}{k} A_{k+1}^{Gq}. \tag{2.38}$$

Eq. (2.29) implies for $n = 1$ that $A_1^{Gq} = 0$. We can eliminate A_1^{Gq} from Eq. (2.38) and write a sum rule for the logarithmic exponents with $n > 1$, which reads

$$A_n^{NS} = \sum_{k=1}^{n-1} (-1)^k \binom{n-1}{k} A_{k+1}^{Gq}. \tag{2.39}$$

Another similar sum rule is obtained for the combination A_n^{qG} and A_n^{GG} by using Eqs. (2.31), (2.32), (2.33), (2.34), and (2.35). We start with

$$\int_0^1 dz\ z^{n-1} \big[2f P_{qG}(1-z) + P_{GG}(1-z)\big] = \int_0^1 dz (1-z)^n \big[2f P_{qG}(z) + P_{GG}(z)\big] \tag{2.40}$$

$$= \sum_{k=0}^{n-1} (-1)^k \binom{n-1}{k} \int_0^1 dz\ (z)^n \big[2f P_{qG}(z) + P_{GG}(z)\big]. \tag{2.41}$$

We find B_n:

$$B_n = 2f A_n^{qG} + A_n^{GG} = \sum_{k=2}^{n-1} (-1)^k \binom{n-1}{k} \big[2f A_{K+1}^{qG} + A_{K+1}^{GG}\big] \tag{2.42}$$

$$= \sum_{k=2}^{n-1} (-1)^k \binom{n-1}{k} B_{k+1}. \tag{2.43}$$

Or equivalently,

$$\big[1 + (-1)^n\big] B_n = \sum_{j=3}^{n-1} (-1)^{j-1} \binom{n-1}{j-1} B_j. \tag{2.44}$$

This relation implies that the B_n's for even n are determined by the B_n's for odd n.

2.4 *Calculation of Logarithmic Exponents*

2.4.1 *Spin Average Case*

In this section we compute the splitting functions P_{qq}, P_{qG}, P_{Gq}, and P_{GG} based on the basic vertices of QCD. The method we deal with here is the extension of the results of von Weizsacker-Williams [54] in quantum electrodynamics (QED). In this case, the equivalent number of photons inside an electron with fraction z of the electron momentum is evaluated to order α and contains a factor of $\ln(\frac{E}{m_e})$, which plays the same role as $t = \ln(\frac{Q^2}{Q_0^2})$ in our case.

We first calculate $P(z)$ at $z < 1$ in the absence of the δ function in $P(z)$, and then we shall deal with with δ function singularities at $z = 1$. We want to evaluate the probability of finding a particle B inside a particle A with fraction z of the momentum of A in the p_∞ frame to lowest order α. We derived the probability formula in the previous section

$$d\mathcal{P}_{BA} = \frac{\alpha}{2\pi} P_{BA}(z) dz\ dt. \tag{2.45}$$

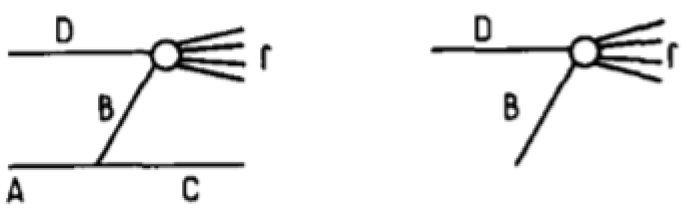

Figure 2.1: (Left) The intermediate state B added to the process $A + D \to C + f$. (Right) $B + D \to f$[1].

We suppose that C is the third particle in the vertex where B and A appear. By comparing the cross section for the two processes in Figure 2.1, where D is a given particle and f is an arbitrary final state, we can easily identify the probability. We

[1]Taken from Ref. [52].

first define the matrix element

$$S_{ij} - \delta_{ij} = 2\pi i \delta(E_j - E_i) M_{ij} \prod_k \frac{1}{\sqrt{2E_k}}, \tag{2.46}$$

where k runs over all external particles. We use the old perturbation theory results to find the contribution to M_{ij} in Eq. (2.46) of a given intermediate state B for the left diagram in Figure 2.1. $M_{A+D\to C+f}$ can be written

$$M_{A+D\to C+f} = g^2 \frac{V_{A\to B+C} V_{B+D\to f}}{2E_B(E_B + E_C - E_A)}, \tag{2.47}$$

where V_{ij} is the invariant matrix element of the interaction. Similarly, for the right diagram in Figure 2.1 we obtain

$$M_{B+D\to f} = g V_{B+D\to f}. \tag{2.48}$$

We can easily find the cross section associated with the left and right diagrams in Figure 2.1 as follows

$$\begin{aligned} d\sigma_{Left} = & \frac{g^4}{8E_A E_D} \frac{|V_{A\to B+C}|^2 |V_{B+D\to f}|^2}{4E_B^2(E_B + E_C - E_A)^2} \\ & \times (2\pi)^2 \delta^4(k_A + k_D - k_C - k_f) \frac{d^3 k_C}{(2\pi)^3 2E_C} \prod_f \frac{d^3 P_f}{(2\pi)^3 2E_k} \end{aligned} \tag{2.49}$$

$$d\sigma_{Right} = \frac{g^2}{8E_A E_D} |V_{B+D\to f}|^2 (2\pi)^4 \delta^4(K_B + k_D - k_f) \prod_f \frac{d^3 P_f}{(2\pi)^3 2E_k}. \tag{2.50}$$

By using Eq. (2.45),

$$d\sigma_{Left} = d\mathcal{P}_{BA}\ dz\ d\sigma_{Right}, \tag{2.51}$$

and one can relate Eqs. (2.49) and (2.50) to obtain $d\mathcal{P}_{BA}$:

$$d\mathcal{P}_{BA}\ dz = \frac{E_B}{E_A} \frac{|V_{A\to B+C}|^2}{4E_B^2(E_B + E_C - E_A)^2} \frac{d^3 k_C}{(2\pi)^3 (2E_C)}. \tag{2.52}$$

We use our results in Appendix C to simplify the above equation:

$$k_A^\mu = (p, \vec{0}, p) \tag{2.53}$$

$$k_B^\mu = (zp + \frac{P_T^2}{2zp}, \vec{P_T}, zp) \tag{2.54}$$

$$k_C^\mu = ((1-z)p + \frac{P_T^2}{2(1-z)p}, -\vec{P_T}, (1-z)p). \tag{2.55}$$

We thus have

$$\begin{aligned} 4E_B^2(E_B + E_C - E_A)^2 &= \frac{P_T^4}{(1-z)^2p^2}(p + \frac{P_T^2}{2z^2p})^2 \\ &= \frac{P_T^4}{(1-z)^2} + O(P_T^8), \end{aligned} \tag{2.56}$$

$$\begin{aligned} \frac{d^3k_C}{(2\pi)^3(2E_C)} &= \frac{dk_C^1 d^2k_C}{16\pi^3(1-z)} \\ &= \frac{dz dP_T^2}{16\pi^2(1-z)}, \end{aligned} \tag{2.57}$$

while $dk_C^1 d^2k_C = \pi d((1-z)p)(-dP_T^2) = \pi p dz\ dP_T^2$.

Thus, the result is

$$d\mathcal{P}_{BA}(z) = \frac{\alpha}{2\pi}\frac{z(1-z)}{2}\overline{\sum_{spins}}\frac{|V_{A\to B+C}|^2}{P_T^2}\ d\ln(P_T^2), \tag{2.58}$$

where the sum is over the spins of B and C and an average over the spin of A is indicated (if it is necessary). In the case of interest, $|V_{A\to B+C}|^2$ vanishes linearly in P_T^2. This indicates that the ratio $\frac{|V_{A\to B+C}|^2}{P_T^2}$ in Eq. (2.58) is finite at $P_T^2 = 0$. Also, for a virtual mass $-Q^2$ for particle D, the integral in P_T^2 has an upper limit of order Q^2, so at the leading logarithmic approximation, $d\ln(P_T^2)$ can be directly interpreted as dt. By comparing Eq. (2.58) and (2.45) we obtain

$$P_{BA}(z) = \frac{1}{2}z(1-z)\overline{\sum_{spins}}\frac{|V_{A\to B+C}|^2}{P_T^2} \quad (z < 1), \tag{2.59}$$

which only depends on the vertex ABC as expected.

2.4.2 The Quark-Gluon Vertex

Let us now focus on the quark gluon vertex in Figure 2.2 in order to evaluate $P_{Gq}(z)$. In this case $V_{A\to B+C} = V_{q\to Gq}$. We must find

$$\overline{\sum_{spins}}|V_{q\to Gq}|^2 = \overline{\sum_{spins}} V_{q\to Gq} \times V^{\dagger}_{q\to Gq}.$$

It is easy to show

$$V_{q\to Gq} = i\bar{u}^j_s(k_C)\gamma^\mu t^a_{ij} u^i_s(k_A)\epsilon_\mu, \tag{2.60}$$

where ϵ_μ is the gluon's polarization. We obtain

$$\begin{aligned}
\overline{\sum_{spins}}|V_{q\to Gq}|^2 &= \frac{1}{2\times 3}\sum_{spins,pol,color} |i\bar{u}_s(k_C)\gamma^\mu t^a_{ij} u_s(k_A)\epsilon_\mu|^2 \\
&= \frac{1}{2}\frac{\sum_a \mathrm{Tr}(t^a t^a)}{3}\mathrm{Tr}(\not{k}_C\gamma^\mu \not{k}_A\gamma^\nu)\sum_{pol}\epsilon_\mu\epsilon^*_\nu \\
&= \frac{1}{2}C_2(R)\mathrm{Tr}(\not{k}_C\gamma^\mu \not{k}_A\gamma^\nu)\sum_{pol}\epsilon_\mu\epsilon^*_\nu \\
&= \frac{1}{2}C_2(R)(4)(k^\mu_C k^\nu_A + k^\nu_C k^\mu_A - k_C\cdot k_A g^{\mu\nu})\sum_{pol}\epsilon_\mu\epsilon^*_\nu.
\end{aligned} \tag{2.61}$$

Care must be taken so that only physical transverse gluon states are included in the sum, and we therefore write

$$\sum_{pol}\epsilon_\mu\epsilon^*_\nu \to \delta^{ij} - \frac{k^i_B k^j_B}{k^2_B}. \tag{2.62}$$

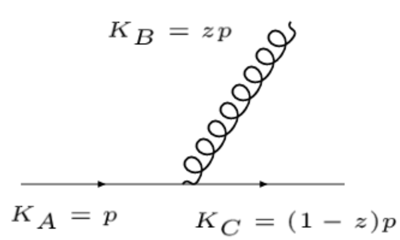

Figure 2.2: The quark gluon vertex which determines P_{Gq} and P_{qq}.

We use Eq. (2.62) to simplify Eq. (2.61). One can show

$$
\begin{aligned}
\overline{\sum_{spins}}|V_{q\to Gq}|^2 &= \frac{1}{2}C_2(R)(4)(k_C^j k_A^i + k_C^i k_A^j - (k_C\cdot k_A)g^{ij}) \times (\delta_{ij} - \frac{k_{Bi}k_{Bj}}{k_B^2}) \\
&= \frac{1}{2}C_2(R)(4)(2\vec{k}_A\cdot\vec{k}_C - 2\frac{(\vec{k}_A\cdot\vec{k}_B)(\vec{k}_C\cdot\vec{k}_B)}{\vec{k^2}_B} + 2(k_A\cdot k_C)) \\
&= 4C_2(R)\left[(1-z)p^2 - \frac{(zp^2)(z(1-z)p^2 - P_T^2)}{z^2p^2} + \frac{P_T^2}{1-z}\right] \\
&\simeq \frac{2C_2(R)}{z^2(1-z)}(1+(1-z)^2)P_T^2 + O(P_T^4).
\end{aligned}
\tag{2.63}
$$

We can thus state the result

$$
\begin{aligned}
P_{Gq}(z) &= \frac{1}{2}z(1-z)\overline{\sum_{spins}}|V_{q\to Gq}|^2 \times \frac{1}{P_T^2} \\
&= C_2(R)\frac{1+(1-z)^2}{z} \to P_{Gq}(z) = C_2(R)\frac{1+(1-z)^2}{z},
\end{aligned}
\tag{2.64}
$$

which holds for all z, since we are dealing with a non-diagonal density. From the last equation, by using the symmetry relation $P_{Gq}(z) = P_{qq}(1-z)$, we also obtain

$$
p_{qq}(z) = C_2(R)\frac{1+z^2}{1-z} \quad (z<1). \tag{2.65}
$$

The $\frac{1}{1-z}$ singularity in $P_{qq}(z)$ arises from the soft gluon Bremsstrahlung spectrum and are typical of vector theories. We will regularize it by interpreting it as a distribution function.

2.4.3 The Gluon Annihilation Vertex

We now calculate P_{qG} from the vertex in Figure 2.3. Since P_{qG} is proportional to the probability density of finding inside a gluon (averaged over colors) a quark (or an anti-quark) of given flavour and of any color, in this case the sum and average in color space simply bring in a factor of $\frac{1}{2}$. We have

$$
V_{G\to q\bar{q}} = iv_s^j(k_C)\gamma^\mu t_{ij}^a \bar{u}_s^i(k_B)\epsilon_\mu, \tag{2.66}
$$

$$
\begin{aligned}
\overline{\sum_{spins}}|V_{G\to q\bar{q}}|^2 &= \frac{1}{8}\sum_{spins,pol,color}|iv_s(k_C)\gamma^\mu t^a_{ij}\bar{u}_s(k_B)\epsilon_\mu|^2 \\
&= \frac{\sum_a \mathrm{Tr}(t^a t^a)}{8}\mathrm{Tr}(\not{k}_C\gamma^\mu\not{k}_B\gamma^\nu)\frac{1}{2}\sum_{pol}\epsilon_\mu\epsilon^*_\nu \\
&= \frac{1}{4}\mathrm{Tr}(\not{k}_C\gamma^\mu\not{k}_B\gamma^\nu)\sum_{pol}\epsilon_\mu\epsilon^*_\nu \\
&= \frac{1}{4}(4)(k^\mu_C k^\nu_B + k^\nu_C k^\mu_B - (k_C\cdot k_B)g^{\mu\nu})\sum_{pol}\epsilon_\mu\epsilon^*_\nu \qquad (2.67) \\
&= (k^i_C k^j_B + k^j_C k^i_B - (k_C\cdot k_B)g^{ij}) \times (\delta^{ij} - \frac{k^i_A k^j_A}{k^2_A}) \\
&= 2(\vec{k}_B\cdot\vec{k}_C - \frac{(\vec{k}_A\cdot\vec{k}_C)(\vec{k}_B\cdot\vec{k}_A)}{\vec{k^2}_A} + (k_A\cdot k_C)) \\
&= P^2_T\frac{z^2+(1-z)^2}{z(1-z)}.
\end{aligned}
$$

We finally derive

$$
P_{qG}(z) = \frac{z^2+(1-z)^2}{2}. \qquad (2.68)
$$

The symmetry under the change of z into $(1-z)$ in expected because $P_{qG}(z) = P_{\bar{q}G}(1-z) = P_{qG}(1-z)$ as we mentioned before.

2.4.4 The Three-Gluon Vertex

One can show

$$
V_{G\to GG} = -2iC_{abc}\Big[(\epsilon^a_A\cdot\epsilon^b_B)(k_B\cdot\epsilon^c_C) - (\epsilon^a_A\cdot\epsilon^c_C)(k_C\cdot\epsilon^b_B) - (\epsilon^c_C\cdot\epsilon^b_B)(k_B\cdot\epsilon^a_A)\Big], \quad (2.69)
$$

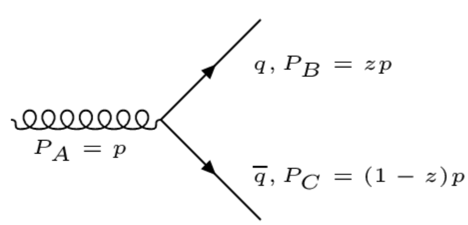

Figure 2.3: The annihilation vertex of a gluon into quark and anti-quark pair, which fixes P_{qG}.

where $k_A \cdot \epsilon_A^a = k_B \cdot \epsilon_B^b = k_C \cdot \epsilon_C^c = 0$ and $\frac{1}{N^2-1}\sum_{bc} C_{abc}C_{abc} = C_2(G)$. It is only a matter of algebra to derive the result for the three-gluon vertex in Figure 2.4 as follows:

$$\overline{\sum_{spins}} |V_{G\to GG}|^2 = 4C_2(G)\frac{P_T^2}{z(1-z)}\left[\frac{1-z}{z} + \frac{z}{1-z} + z(1-z)\right], \tag{2.70}$$

and

$$P_{GG}(z) = 2C_2(G)\left[\frac{1-z}{z} + \frac{z}{1-z} + z(1-z)\right] \quad (z < 1), \tag{2.71}$$

which is completely consistent with $P_{GG}(z) = P_{GG}(1-z)$. We now complete the determination of $P_{qq}(z)$ and $P_{GG}(z)$ by fixing their behaviour at $z = 1$. Note that all moments of these two functions would be divergent at $z = 1$. We therefore start by regularizing the factor $\frac{1}{1-z}$ by reinterpreting it as a distribution $\frac{1}{(1-z)_+}$ that has the following properties:

$$\int_0^1 \frac{dz\ f(z)}{(1-z)_+} \equiv \int_0^1 \frac{f(z)-f(1)}{1-z}dz = \int_0^1 dz \ln(1-z)\frac{d}{dz}f(z) \tag{2.72}$$

$$\int_0^1 dz\frac{1}{(1-z)_+} = 0, \tag{2.73}$$

with $f(z)$ being an arbitrary test function that is sufficiently regular at the end point. We then add to $P_{qq}(z)$and $P_{GG}(z)$ a $\delta(1-z)$ with the coefficient determined by the

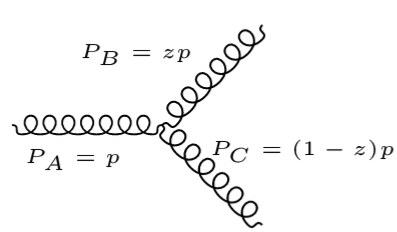

Figure 2.4: The three-gluon vertex relevant to P_{GG}.

constraints in the equations above. We thus rewrite $P_{qq}(z)$ and $P_{GG}(z)$ as follows:

$$P_{qq}(z) = C_2(R)\left[\frac{1+z^2}{(1-z)_+} + \frac{3}{2}\delta(1-z)\right], \tag{2.74}$$

and

$$P_{GG}(z) = 2C_2(G)\left[\frac{z}{(1-z)_+} + \frac{1-z}{z} + z(1-z) + \left(\frac{11}{12} - \frac{1}{3}\frac{T(R)}{C_2(G)}\right)\delta(1-z)\right]. \tag{2.75}$$

2.4.5 The Logarithmic Exponents

By having $P_{qq}(z)$, $P_{qG}(z)$, $P_{Gq}(z)$, and $P_{GG}(z)$, one can evaluate the moments of the $P(z)$ functions, which give the set of constants A_n according to Eq. (2.24). We first calculate the moments of $\frac{1}{(1-z)_+}$, which is useful for future calculations. A straightforward integration yields

$$\int_0^1 \frac{dz\ z^{n-1}}{(1-z)_+} \equiv \int_0^1 \frac{z^{n-1}-1}{1-z}dz = -\sum_{j=1}^{n-1}\frac{1}{j}. \tag{2.76}$$

We finally obtain

$$A_n^{NS} \equiv \int_0^1 dz\ z^{n-1}P_{qq}(z) = C_2(R)\left[-\frac{1}{2} + \frac{1}{n(n+1)} - 2\sum_{j=2}^{n}\frac{1}{j}\right], \tag{2.77}$$

$$A_n^{Gq} \equiv \int_0^1 dz\ z^{n-1}P_{Gq}(z) = C_2(R)\frac{n^2+n+2}{n(n^2-1)}, \tag{2.78}$$

$$4T(R)A_n^{qG} \equiv 2f\int_0^1 dz\ z^{n-1}P_{qG}(z) = 2T(R)\frac{n^2+n+2}{n(n+1)(n+2)}, \tag{2.79}$$

and

$$A_n^{GG} \equiv \int_0^1 dz\ z^{n-1}P_{GG}(z) = C_2(G) \left[-\frac{1}{6} + \frac{2}{n(n-1)} + \frac{2}{(n+1)(n+2)} - 2\sum_{j=2}^{n}\frac{1}{j} - \frac{2}{3}\frac{T(R)}{C_2(G)}\right]. \tag{2.80}$$

This set of logarithmic exponents coincide with the results of Refs. [22, 23, 53].

2.5 Spin-dependent Case

2.5.1 The Master Equations

We consider the Q^2 dependence of quark densities with given helicity, which are relevant for scaling breaking effects in deep inelastic scattering on polarized targets. Based on a similar approach in the previous section, one can write the master equations as follows:

$$\begin{aligned}\frac{dq^i_\pm(x,t)}{dt} = \frac{\alpha(t)}{2\pi}\int_x^1 \frac{dy}{y}\Bigg[& q^i_+(y,t)P_{q_\pm q_+}\left(\frac{x}{y}\right) + q^i_-(y,t)P_{q_\pm q_-}\left(\frac{x}{y}\right) \\ &+ G_+(y,t)P_{q_\pm G_+}\left(\frac{x}{y}\right) + G_-(y,t)P_{q_\pm G_-}\left(\frac{x}{y}\right)\Bigg],\end{aligned} \tag{2.81}$$

$$\begin{aligned}\frac{dG_\pm(x,t)}{dt} = \frac{\alpha(t)}{2\pi}\int_x^1 \frac{dy}{y}\Bigg[& \sum_{i=1}^{2f} q^i_+(y,t)P_{G_\pm q_+}\left(\frac{x}{y}\right) + \sum_{i=1}^{2f} q^i_-(y,t)P_{G_\pm q_-}\left(\frac{x}{y}\right) \\ &+ G_+(y,t)P_{G_\pm G_+}\left(\frac{x}{y}\right) + G_-(y,t)P_{G_\pm G_-}\left(\frac{x}{y}\right)\Bigg].\end{aligned} \tag{2.82}$$

The previous set of equations can be simplified by considering that parity conservation in QCD implies the relation $P_{A_+B_\pm}(z) = P_{A_-B_\mp}(z)$ for any A and B. We define the sums $q^i_+ + q^i_- = q^i$, $G_+ + G_- = G$ and differences $\Delta q^i = q^i_+ - q^i_-$, $\Delta G = G_+ - G_-$. For the sums we have

$$P_{AB} = P_{A_+B_+} + P_{A_-B_+}. \tag{2.83}$$

It is also convenient to define

$$\Delta P_{AB} = P_{A_+B_+} - P_{A_-B_+}. \tag{2.84}$$

We then derive the master equations in the form

$$\frac{d}{dt}\Delta q^i(x,t) = \frac{\alpha(t)}{2\pi}\int_x^1 \frac{dy}{y}\left[\Delta q^i(y,t)\Delta P_{qq}\left(\frac{x}{y}\right) + \Delta G(y,t)\Delta P_{qG}\left(\frac{x}{y}\right)\right], \tag{2.85}$$

$$\frac{d}{dt}\Delta G(x,t) = \frac{\alpha(t)}{2\pi}\int_x^1 \frac{dy}{y}\left[\sum_{i=1}^{2f}\Delta q^i(y,t)\Delta P_{Gq}\left(\frac{x}{y}\right) + \Delta G(y,t)\Delta P_{GG}\left(\frac{x}{y}\right)\right]. \tag{2.86}$$

In the simplest case of non-singlet quark densities, one can show

$$\frac{d}{dt}\Delta q^{NS}(x,t) = \frac{\alpha(t)}{2\pi}\int_x^1 \frac{dy}{y}\Delta q^{NS}(y,t)\Delta P_{qq}\left(\frac{x}{y}\right). \tag{2.87}$$

When masses are neglected, the vector quark-gluon coupling in Figure 2.2 is helicity conserving. We directly conclude that

$$P_{q_-q_+}(z) = 0, \tag{2.88}$$

$$P_{q_+q_+}(z) = P_{qq} = \Delta P_{qq}(z) = C_2(R)\left[\frac{1+z^2}{(1-z)_+} + \frac{3}{2}\delta(1-z)\right]. \tag{2.89}$$

The same quark-gluon vertex of Figure 2.2 also determines $P_{G_+q_+}(z)$ and $P_{G_+q_+}(z)$. Similar calculations reveal

$$V_{q\to G_\pm q} = i\bar{u}_s^j(k_C)(\frac{1+\gamma_5}{2})t^a_{ij}u^i_s(k_A)\epsilon^{*\mu}_\pm, \tag{2.90}$$

and

$$\begin{aligned}
|V_{q\to G_\pm q}|^2 &= \frac{1}{2\times 3}\sum_a \mathrm{Tr}(t^a t^a)\ \mathrm{Tr}\left(\not{k}_C\gamma^\mu\not{k}_A\gamma^\nu(\frac{1+\gamma_5}{2})^2\right)\ \epsilon^*_{\pm\mu}\epsilon_{\pm\nu} \\
&= C_2(R)\ \mathrm{Tr}\left(\not{k}_C\gamma^\mu\not{k}_A\gamma^\nu(\frac{1+\gamma_5}{2})\right)\ \epsilon^*_{\pm\mu}\epsilon_{\pm\nu} \\
&= \frac{P_T^2}{2z(1-z)}\frac{1}{z}\Big[(2-2z+z^2) \pm z(2-z)\Big].
\end{aligned} \tag{2.91}$$

We note that we have defined the gluon momentum in the form

$$k_B^\mu = \left(zp + \frac{P_T^2}{2zp}, p_x, p_y, zp)\right), \tag{2.92}$$

and for the corresponding polarization 4-vector for positive and negative helicity we can approximately set

$$\epsilon_\pm \simeq \left(0, \sqrt{\frac{1}{2}}, \pm i\sqrt{\frac{1}{2}}, -\frac{p_x \pm ip_y}{\sqrt{2}zp}\right), \tag{2.93}$$

where $k_B^\mu.\epsilon_\pm = 0$. We thus obtain

$$P_{G_+q_+}(z) = C_2(R)\frac{1}{z}, \tag{2.94}$$

$$P_{G_-q_+}(z) = C_2(R)\frac{(1-z)^2}{z}, \tag{2.95}$$

$$\Delta P_{Gq}(z) = P_{G_+q_+}(z) - P_{G_-q_+}(z) = C_2(R)\frac{1-(1-z)^2}{z}. \tag{2.96}$$

We now evaluate $P_{q_+G_+}(z)$ and $P_{q_-G_+}(z)$ from the annihilation vertex in Figure 2.3. The invariant vertex gives

$$V_{G_+\to q_\pm\bar{q}} = iv_s^j(k_C)\gamma^\mu t_{ij}^a \bar{u}_s^i(k_B)\epsilon_{\pm\mu}. \tag{2.97}$$

A sum over the final anti-quark spin yields

$$\begin{aligned}
|V_{G_+\to q_\pm\bar{q}}|^2 &= \frac{1}{8}\sum_{a,b}\mathrm{Tr}(t^a t^b)\mathrm{Tr}\left(\not{k}_C\gamma^\mu\frac{(1\pm\gamma_5)}{2}\not{k}_B\frac{(1\pm\gamma_5)}{2}\gamma^\nu\right)\ \epsilon^*_{+\mu}\epsilon_{+\nu} \\
&= \frac{1}{2}\mathrm{Tr}\left(\not{k}_C\gamma^\mu\frac{(1\pm\gamma_5)}{2}\not{k}_B\frac{(1\pm\gamma_5)}{2}\gamma^\nu\right)\ \epsilon^*_{+\mu}\epsilon_{+\nu} \\
&= \frac{1}{2}\mathrm{Tr}\left(\not{k}_C\gamma^\mu\not{k}_B\gamma^\nu\frac{(1\pm\gamma_5)}{2}\right)\ \epsilon^*_{+\mu}\epsilon_{+\nu} \\
&= \frac{P_T^2}{z(1-z)}\left[(z^2+(1-z)^2)\pm(z^2-(1-z)^2)\right].
\end{aligned} \tag{2.98}$$

We find

$$P_{q_+G_+}(z) = \frac{1}{2}\ z^2, \tag{2.99}$$

$$P_{q_-G_+}(z) = \frac{1}{2}\ (1-z)^2, \tag{2.100}$$

$$\Delta P_{qG}(z) = P_{q_+G_+}(z) - P_{q_-G_+}(z) = \frac{1}{2}\left[z^2-(1-z)^2\right]. \tag{2.101}$$

We must now evaluate $P_{G_+G_+}$ and $P_{G_-G_+}$ from the three-gluon vertex in Figure 2.4. The polarization vectors are

$$\epsilon_{+A} = \sqrt{\frac{1}{2}}\ (0,1,i,0), \tag{2.102}$$

$$\epsilon_{\pm B} = \sqrt{\frac{1}{2}}\ (0,1,\pm i,-\frac{p_x\pm ip_y}{zp}), \tag{2.103}$$

$$\epsilon_{\pm C} = \sqrt{\frac{1}{2}}\ (0,1,\pm i,\frac{p_x\pm ip_y}{zp}), \tag{2.104}$$

where $(k_A \cdot \epsilon_{+A}) = (k_B \cdot \epsilon_{\pm B}) = (k_C \cdot \epsilon_{\pm C}) = 0$.

We finally find

$$V_{G_+ \to G_\pm G_\pm} = -2iC_{abc}\Big((\epsilon_{+A} \cdot \epsilon^*_{\pm B})(k_B \cdot \epsilon^*_{\pm C}) - (\epsilon_{+A} \cdot \epsilon^*_{\pm C})(k_C \cdot \epsilon^*_{\pm B}) \\ - (\epsilon_{+A} \cdot k_B)(\epsilon^*_{\pm C} \cdot \epsilon_{\pm B})\Big). \tag{2.105}$$

Simple algebra leads to

$$P_{G_+G_+} = C_2(G)(1+z^4)\left(\frac{1}{z} + \frac{1}{1-z}\right), \quad (z < 1) \tag{2.106}$$

$$P_{G_-G_+} = C_2(G)\frac{(1-z)^3}{z}. \tag{2.107}$$

The behaviour at $z = 1$ of the diagonal density $P_{G_+G_+}$ is immediately obtained by similar analogy to previous section as follows:

$$P_{G_+G_+} = C_2(G)\left[(1+z^4)\left(\frac{1}{z} + \frac{1}{(1-z)_+}\right) + \left(\frac{11}{6} - \frac{2}{3}\frac{T(R)}{C_2(G)}\right)\delta(1-z)\right], \tag{2.108}$$

and

$$\Delta P_{GG}(z) = C_2(G)\left[(1+z^4)\left(\frac{1}{z} + \frac{1}{(1-z)_+}\right) - \frac{(1-z)^3}{z} - \left(\frac{11}{6} - \frac{2}{3}\frac{T(R)}{C_2(G)}\right)\delta(1-z)\right]. \tag{2.109}$$

2.5.2 *The Logarithmic Exponents*

The logarithmic exponents are defined as follows

$$\int_0^1 dz\ z^{n-1}\begin{pmatrix} \Delta P_{qq}(z) & 2f\Delta P_{qG}(z) \\ \Delta P_{Gq}(z) & \Delta P_{GG}(z) \end{pmatrix} \equiv \begin{pmatrix} \widetilde{A}_n^{NS} & 4T(R)\widetilde{A}_n^{qG} \\ \widetilde{A}_n^{Gq} & \widetilde{A}_n^{GG} \end{pmatrix}, \tag{2.110}$$

which are

$$\widetilde{A}_n^{NS} = A_n^{NS}, \tag{2.111}$$

$$\widetilde{A}_n^{Gq} = C_2(R)\ \frac{n+2}{n(n+1)}, \tag{2.112}$$

$$\widetilde{A}_n^{qG} = \frac{1}{2}\frac{n-1}{n(n+1)}, \tag{2.113}$$

$$\widetilde{A}_n^{GG} = C_2(G)\ \left[\frac{11}{6} - \frac{2}{3}\frac{T(R)}{C_2(G)} + \frac{2}{n} - \frac{4}{n+1} - 2\sum_{j=1}^{n-1}\frac{1}{j}\right]. \tag{2.114}$$

All the results we have found in this chapter are in complete agreement with the results of [55–57], obtained by the operator formalism.

2.6 Parton Shower with HERWIG

HERWIG [58] provides a full simulation of hard lepton-lepton, lepton-hadron, and hadron-hadron scattering and soft hadron-hadron collisions in a single package with the following special features:

- Initial- and final-state QCD jet evolution with soft gluon interference taken into account via angular ordering;
- Color coherence of both initial and final partons in all hard processes;
- Azimuthal correlation within and between jets due to gluon interference and polarization;
- A cluster model for jet hadronization based on non-perturbative gluon splitting, and similar clustering for soft and underlying hadronic events;
- A space-time picture of event development, from parton shower to hadronic decays.

HERWIG is written in FORTRAN with the ability for the user to modify and develop the main program HWIGPR to generate the type and number of events required [58]. Final-state parton showering is generated by a so-called coherent algorithm with the following properties in Ref. [58]:

- The energy fractions are distributed according to the leading-order DGLAP-CS splitting functions derived in this chapter;
- The full available phase space is restricted to an angular-ordered region;
- The emission angles are distributed according to the famous Sudakov form factors, with the virtual corrections and unresolved real emissions;
- For soft emitted gluons, the azimuth is distributed according to the eikonal dipole distribution [59];
- For non-soft emitted gluons, the azimuth is distributed according to spin effects [60, 61];
- In each branching the scale of α_s is the relative transverse momentum of the two daughters;
- In the heavy flavour production case the mass of the quark modifies the angular-ordered phase space.

The HERWIG parton shower evolution is done in terms of variables z and ξ, where z is the parton energy fraction and ξ is an angular variable defined as follows:

$$P_i \to P_j + P_k \Rightarrow \quad z_j = \frac{E_j}{E_i} \tag{2.115}$$

$$P_i \to P_j + P_k \Rightarrow \quad \xi_{jk} = \frac{(p_j.p_k)}{E_j E_k}. \tag{2.116}$$

For massless partons at small angles $\xi_{jk} \simeq \frac{1}{2}\theta^2_{jk}$. The values of z are chosen according to DGLAP-CS splitting functions and the distribution of ξ_{jk} is determined by the Sudakov form factors.

CHAPTER THREE

IR-Improved DGLAP-CS Theory

3.1 Introduction

In this chapter, it is shown that the exact, amplitude-based resummation allows IR-improvement of the usual DGLAP-CS theory [2, 40]. The resummation of large infrared effects in the kernels of the usual DGLAP-CS theory improves their infrared behavior and gives better control of the accuracy of a given fixed-order calculation throughout the entire phase space of the respective physical process, especially when the prediction is given by Monte Carlo methods.

3.1.1 Resummation

In perturbative quantum field theory, one can write the observable O as follows:

$$O = \sum_n (c_n \alpha_s^n + R_n), \tag{3.1}$$

where c_n is computed from the Feynman diagram and R_n is the remainder of order n. The observable O must be infrared safe, R_n has to be very small, c_n must be well behaved for large n, and α_s is a small coupling constant. If all of those conditions are satisfied, the resummation can be written as

$$\begin{aligned} O &= 1 + \alpha_s(L^2 + L + 1) + \alpha_s^2(L^4 + L^3 + L^2 + L + 1) + \dots \\ &= \exp\left(Lg_1(\alpha_s L) + g_2(\alpha_s L) + \alpha_s g_3(\alpha_s L) + \dots \right) \times C(\alpha_s) + \dots \end{aligned} \tag{3.2}$$

where L is large logarithm, e.g. $\ln(\frac{Q}{Q_0})$ or $\ln(\frac{s}{m_e^2})$. Writing down any observable in the form of Eqs. (3.1) and (3.2) enables us to restore the predictive power, increases theoretical accuracy, and has better physical description of the problem.

3.1.2 Resummation and Exponentiation in QED

In 1961, Yennie, Frautschi, and Suura (YFS) [38] developed a general treatment of the infrared divergence problem in QED. The main feature of this treatment is based on the separation of the infrared divergences as multiplicative factors, which are treated to all orders of perturbation theory, and the conversion of the residual perturbation into one which has no infrared divergence, and hence no need for an infrared cutoff. Following the YSF approach, for a typical process of the Abelian gauge theory, e.g. $e^+(p_e)\ e^-(p_{\bar{e}}) \to \bar{f}(p_{\bar{f}})\ f(p_f) + n(\gamma)(k_1, k_2, \ldots, k_n)$, one can prove that the total cross section for the process can be represented by

$$\begin{aligned} d\sigma_{exp} = \exp(2\alpha\ ReB + 2\alpha\tilde{B}) \sum_{n=0}^{\infty} \int \prod_{j=1}^{n} \frac{d^3k_j}{k_j^0} \int \frac{d^4y}{(2\pi)^4}\ e^{iy\cdot(p_1+q_1-p_2-q_2-\sum_j k_j)+D} \\ \times \bar{\beta}_n(k_1, k_2, \ldots, k_n) \frac{d^3p_2}{p_2^0} \frac{d^3q_2}{q_2^0} \end{aligned} \tag{3.3}$$

where B and $\tilde{B}$ are the virtual infrared function and real infrared function respectively, $\bar{\beta}_n(k_1, k_2, \ldots, k_n)$ are hard photon residuals and

$$2\alpha\tilde{B} = \int^{k\leq K_{max}} \frac{d^3k}{k_0}\ \tilde{S}(k), \tag{3.4}$$

$$D = \int d^3k \frac{\tilde{S}(k)}{k_0} (e^{-iy\cdot k} - \theta(K_{max} - k), \tag{3.5}$$

$$B = \frac{-i}{8\pi^3} \int \frac{d^4k}{k^2 - \lambda^2} \sum_{i<j} Z_i\theta_i Z_j\theta_j \left(\frac{(2p_i\theta_i - k)_\mu}{k^2 - 2k.p_i\theta_i} + \frac{(2p_j\theta_j + k)_\mu}{k^2 + 2k.p_j\theta_j} \right)^2, \tag{3.6}$$

where Z_i has the sign of the ith charge and $\theta_i = -(+)$ if is outgoing (incoming) and

$$\tilde{S}(k) = \frac{\alpha}{4\pi^2} \sum_{i<j} Z_i\theta_i Z_j\theta_j \left(\frac{p_{i\mu}}{k.p_i} - \frac{p_{j\mu}}{k.p_j} \right)^2. \tag{3.7}$$

Eqs. (3.6) and (3.7) can be expressed in the form

$$\begin{aligned} \tilde{S}(k) = \frac{\alpha}{4\pi^2} \Bigg[-\left(\frac{p_{\bar{e}\mu}}{p_{\bar{e}}.k} - \frac{p_{e\mu}}{p_e.k} \right)^2 + e_f \left(\frac{p_{f\mu}}{p_f.k} - \frac{p_{e\mu}}{p_e.k} \right)^2 - e_f \left(\frac{p_{\bar{f}\mu}}{p_{\bar{f}}.k} - \frac{p_{e\mu}}{p_e.k} \right)^2 \\ - e_f \left(\frac{p_{f\mu}}{p_f.k} - \frac{p_{\bar{e}\mu}}{p_{\bar{e}}.k} \right)^2 + e_f \left(\frac{p_{\bar{f}\mu}}{p_{\bar{f}}.k} - \frac{p_{\bar{e}\mu}}{p_{\bar{e}}.k} \right)^2 - e_f^2 \left(\frac{p_{\bar{f}\mu}}{p_{\bar{f}}.k} - \frac{p_{f\mu}}{p_f.k} \right)^2 \Bigg], \end{aligned} \tag{3.8}$$

and

$$B = \frac{-i}{8\pi^3}\int \frac{d^4k}{k^2-\lambda^2+i\epsilon}\Bigg[-\left(\frac{-2p_{e\mu}-k_\mu}{k^2+2k.p_e+i\epsilon}+\frac{-2p_{\bar{e}\mu}+k_\mu}{k^2-2k.p_{\bar{e}}+i\epsilon}\right)^2$$
$$+e_f\left(\frac{-2p_{e\mu}-k_\mu}{k^2+2k.p_e+i\epsilon}+\frac{2p_{f\mu}+k_\mu}{k^2+2k.p_f+i\epsilon}\right)^2-e_f\left(\frac{-2p_{e\mu}-k_\mu}{k^2+2k.p_e+i\epsilon}+\frac{2p_{\bar{f}\mu}+k_\mu}{k^2+2k.p_{\bar{f}}+i\epsilon}\right)^2$$
$$-e_f\left(\frac{-2p_{\bar{e}\mu}-k_\mu}{k^2+2k.p_{\bar{e}}+i\epsilon}+\frac{2p_{\bar{f}\mu}+k_\mu}{k^2+2k.p_{\bar{f}}+i\epsilon}\right)^2+e_f\left(\frac{-2p_{\bar{e}\mu}-k_\mu}{k^2+2k.p_{\bar{e}}+i\epsilon}+\frac{2p_{f\mu}+k_\mu}{k^2+2k.p_f+i\epsilon}\right)^2$$
$$+e_f^2\left(\frac{2p_{f\mu}-k_\mu}{k^2-2k.p_f+i\epsilon}+\frac{2p_{f\mu}+k_\mu}{k^2+2k.p_f+i\epsilon}\right)^2\Bigg]. \tag{3.9}$$

3.1.3 QCD Exponentiation

We assume that the amplitude for the emission of n real gluons in our typical subprocess, $Q^\alpha + \bar{Q}'^{\bar{\alpha}} \to Q''^{\gamma}\bar{Q}'''^{\bar{\gamma}} + n(G)$, where α, $\bar{\alpha}$, γ, and $\bar{\gamma}$ are color indices, is represented by

$$\mathcal{M}^{(n)\alpha\bar{\alpha}}_{\gamma\bar{\gamma}l} = \sum_l M^{(n)\alpha\bar{\alpha}}_{\gamma\bar{\gamma}l}, \tag{3.10}$$

where $M_l^{(n)}$ is the contribution to $\mathcal{M}^{(n)}$ from Feynman diagrams with l virtual loops. Symmetrization yields

$$M_l^{(n)} = \frac{1}{l!}\int \prod_{j=1}^{l} \frac{d^4k_j}{(2\pi)^4(k_j^2-\lambda^2+i\epsilon)}\rho_l^{(n)}(k_1,k_2,\ldots,k_l), \tag{3.11}$$

where $\rho_l^{(n)}$ is a symmetric function of its arguments $k_1, k_2, \ldots, k_l$ and will be our infrared gluon regulator mass for IR singularities. We now define the virtual IR emission factor $S_{QCD}(k)$ for a gluon with four-momentum k, for the $k \to 0$ regime such that

$$\lim_{k\to 0} k^2\left(\rho^{(n)\alpha\bar{\alpha}}_{\gamma\bar{\gamma}1}|_{leading\ Casimir\ contribution} - S_{QCD}(k)\rho^{(n)\alpha\bar{\alpha}}_{\gamma\bar{\gamma}0}\right) = 0. \tag{3.12}$$

One can write $\rho_l^{(n)}$ as follows

$$\rho_l^{(n)} = S_{QCD}(k_l)\ \rho_{l-1}^{(n)}(k_1,\ldots,k_{l-1},k_l) + \beta_l^1(k_1,\ldots,k_{l-1};k_l), \tag{3.13}$$

where the residual amplitude $\beta_l^1(k_1,\ldots,k_{l-1},k_l)$ will now be taken as defined by Eq. (3.13). $\beta_l^1(k_1,\ldots,k_{l-1},k_l)$ has two properties:

- it is symmetric in its first $l-1$ arguments;
- has no infrared singularity since the IR singularities for gluon l are contained in $S_{QCD}(k_l)$.

Iteration of Eq. (3.13) yields

$$\begin{aligned}\rho_l^{(n)} &= S_{QCD}(k_l)S_{QCD}(k_{l-1})\rho_{l-2}^{(n)}(k_1,\ldots,k_{l-2}) + S_{QCD}(k_l)\beta_{l-1}^1(k_1,\ldots,k_{l-2};k_{l-1})\\ &\quad + S_{QCD}(k_{l-1})\beta_{l-1}^1(k_1,\ldots,k_{l-2};k_l) + \beta_l^2(k_1,\ldots,k_{l-2};k_{l-1},k_l).\end{aligned} \tag{3.14}$$

Again, the residual amplitude $\beta_l^2(k_1,\ldots,k_{l-2};k_{l-1},k_l)$ in Eq. (3.14) has the following properties:

- it is symmetric in its first $l-2$ arguments and in its two arguments k_{l-1} and k_l;
- it has no infrared singularity since the IR singularities for gluons l and $l-1$ are contained in $S_{QCD}(k_l)$ and $S_{QCD}(k_{l-1})$.

Repeated iterations of Eq. (3.13) and exploitation of the symmetry of ρ^n now leads to the relation

$$\begin{aligned}\rho_l^{(n)} &= S_{QCD}(k_l)S_{QCD}(k_{l-1})\ldots S_{QCD}(k_1)\beta_0^0\\ &\quad + \sum_{i=1}^{l} S_{QCD}(k_l)\ldots S_{QCD}(k_{i+1})S_{QCD}(k_{i-1})\ldots S_{QCD}(k_1)\beta_1^1\\ &\quad + \ldots + \sum_{i=1}^{l} S_{QCD}(k_i)\beta_{l-1}^{l-1}(k_1,\ldots,k_{i-1},k_{i+1},\ldots,k_l) + \beta_l^l(k_1,\ldots,k_l),\end{aligned} \tag{3.15}$$

where the virtual gluon residuals have the following properties:

- they are symmetric functions of their arguments;
- they do not have any infrared singularities since the IR singularities are contained in the product $S_{QCD}(k_1,\ldots,S_{QCD}(k_i)$.

Eq. (3.15) can be expressed in a compact equation

$$\begin{aligned}\rho_l^{(n)} &= S_{QCD}(k_l)S_{QCD}(k_{l-1})\ldots S_{QCD}(k_1)\beta_0^0 \\ &+ \sum_{i=1}^{l}\prod_{j\neq i} S_{QCD}(k_j)\beta^1(k_j) + \ldots + \beta_l^l(k_1,\ldots,k_l).\end{aligned} \tag{3.16}$$

By following the YFS approach, one can prove that the Eqs. (3.10) and (3.11) can be expressed as

$$\mathcal{M}^{(n)} = e^{(\alpha_s B_{QCD})}\sum_{j=0}^{\infty} m_j^{(n)}, \tag{3.17}$$

where we have defined

$$\alpha_s B_{QCD} = \int \frac{d^4k}{k^2-\lambda^2+i\epsilon}S_{QCD}(k), \tag{3.18}$$

$$m_j^{(n)} = \frac{1}{j!}\int\prod_{i=1}^{j}\frac{d^4k_i}{k_i^2-\lambda^2+i\epsilon}\beta_j(k_1,\ldots,k_j). \tag{3.19}$$

We note that the cross section can be written as

$$\begin{aligned}d\tilde{\sigma}^n = \frac{e^{(2\alpha_s \mathrm{Re}B_{QCD})}}{n!}\int\prod_{m=1}^{n}\frac{d^3k_m}{\sqrt{k_m^2+\lambda^2}}\delta(p_1+q_1-p_2-q_2-\sum_{i=1}^{n}k_i) \\ \times\, \bar{\rho}^{(n)}(p_1,p_2,q_1,q_2,k_1,\ldots,K_n)\frac{d^3p_2}{p_2^0}\frac{d^3q_2}{q_2^0},\end{aligned} \tag{3.20}$$

where we have defined

$$\bar{\rho}^{(n)}(p_1,p_2,q_1,q_2,k_1,\ldots,K_n) = \sum_{spin,color}\left\|\sum_{j=0}^{\infty}m_j^{(n)}\right\|^2 \tag{3.21}$$

in the incoming $Q\bar{Q}'$ center of mass system and the remaining kinematical factors have been absorbed into the normalization of the amplitudes for simplicity.

The exponentiated cross section can be easily derived by summing over all $d\tilde{\sigma}^n$, analogous to YFS arguments [38] of quantum elecrodynamics. The YFS-like cross section is in the form

$$\begin{aligned}d\hat{\sigma}_{exp} = \sum_{n=0}^{\infty} d\tilde{\sigma}^n = e^{SUM_{IR}(QCD)}\sum_{n=0}^{\infty}\left(\frac{1}{n!}\right)\int\prod_{j=1}^{n}\int\frac{d^3k_j}{k_j^0} \\ \times\int\frac{d^4y}{2(\pi)^4}e^{iy\cdot((p_1+q_1-p_2-q_2-\sum k_i)+D_{QCD}}\ \beta_n(k_1,\ldots,k_n)\frac{d^3p_2}{p_2^0}\frac{d^3q_2}{q_2^0}\end{aligned} \tag{3.22}$$

with

$$SUM_{IR}(QCD) = 2\alpha_s ReB_{QCD} + 2\alpha_s \tilde{B}_{QCD}(K_{max}), \tag{3.23}$$

$$2\alpha_s \tilde{B}_{QCD}(K_{max}) = \int \frac{d^3k}{k^0} \tilde{S}_{QCD}(k)\theta(K_{max} - k), \tag{3.24}$$

$$D_{QCD} = \int \frac{d^3k}{k} \tilde{S}_{QCD}(k)\left[e^{-iy.\cdot k} - \theta(K_{max} - k)\right], \tag{3.25}$$

$$\frac{1}{2}\bar{\beta}_0 = d\sigma^{(1-loop)} - 2\alpha_s ReB_{QCD} d\sigma_B, \tag{3.26}$$

$$\frac{1}{2}\bar{\beta}_1 = d\sigma^{B_1} - \bar{S}_{QCD}(k) d\sigma_B, \tag{3.27}$$

where the $\bar{\beta}_n$ are the QCD hard gluon residuals, and $d\sigma^{(1-loop)}$ and $d\sigma^{B_1}$ are the exact one-loop and single Bremsstrahlung cross sections, respectively. It is worth mentioning that the right-hand side of Eq. (3.22) does not depend on the dummy parameter K_{max}, which has been introduced for cancellation of the infrared divergences in $SUM_{IR}(QCD)$ to all order in α_s.

So far, we have found the exponentiated cross section for QCD based on the extension of the YFS approach. In the YFS method we are dealing with the emission of soft photons, and due to the Abelian nature of quantum electrodynamics, it is very easy to show that the soft photon residuals, $\beta(k_1, \ldots, k_n)$, are IR finite. In QCD, because of the non-Abelian gauge theory origins, it is generally expected that there are infrared divergences in the $\bar{\beta}_n$ that are not removed into the $S_{QCD}(k)$ and $S^{'}_{QCD}(k)$ when these infrared functions are isolated in our calculation of the exponentiated cross section. Here we demonstrate that these infrared singularities, if they still exist in β_n, give a vanishing contribution to the cross section in Eq. (3.22).

We start with the left-hand side of Eq. (3.22). Renormalizability of quantum chromodynamics along with the Bloch-Nordsieck cancellation theorem [37] guarantees the infrared finiteness of the left-hand side of Eq. (3.22). From the infrared finiteness of $d\sigma_{exp}$ and $SUM_{IR}(QCD)$ it follows that the quantity

$$d\bar{\hat{\sigma}}_{exp} \equiv e^{-SUM_{IR}(QCD)} d\sigma_{exp} \tag{3.28}$$

must be infrared finite to all orders in α_s. Let us now define the residual non-Abelian infrared divergence part of each contribution $\bar{\beta}_n^{(l)}$ via

$$\bar{\beta}_n^{(l)} = \tilde{\bar{\beta}}_n^{(l)} + D\bar{\beta}_n^{(l)}, \tag{3.29}$$

where the new function $\tilde{\bar{\beta}}_n^{(l)}$ is free of any infrared divergences and $D\bar{\beta}_n^{(l)}$ contains all leftover infrared divergences in $\bar{\beta}_n^{(l)}$. It is clear that in the limit $f_{abc} \to 0$, where f_{abc} are the group structure constants, the function $D\bar{\beta}_n^{(l)}$ vanishes. We define $D\bar{\beta}_n^{(l)}$ by a minimal subtraction of the IR divergences in it so that it only contains the actual pole and transcendental constants, $\frac{1}{\epsilon} - C_E$ for $\epsilon = 2 - \frac{d}{2}$, in dimensional regularization or $\ln \lambda^2$ in the gluon mass regularization. We can write this as

$$\int dPh \; D\bar{\beta}_n^{(l)} \equiv \sum_{i=1}^{n+l} d_i^{n,l} \ln^i(\lambda^2), \tag{3.30}$$

where coefficients $d_i^{n,l}$ are independent of λ when $\lambda \to 0$.

At order $\mathcal{O}(\alpha_s^n)$, the infrared finiteness of the contribution to $d\bar{\hat{\sigma}}_{exp}$ requires the contribution

$$\begin{aligned} d\bar{\hat{\sigma}}_{exp}^n \equiv & \int \sum_{l=0}^{n} \frac{1}{l!} \prod_{j=1}^{l} \int_{k_j \geq K_{max}} \frac{d^3K_j}{k_j} \tilde{S}_{QCD}(k_j) \sum_{i=0}^{n-l} \frac{1}{i!} \prod_{j=l+1}^{l+i} \int \\ & \times \frac{d^3k_j}{k_j^0} \bar{\beta}_i^{(n-l-i)}(k_{l+1}, \ldots, k_{l+i}) \frac{d^3p_2}{p_2^0} \frac{d^3q_2}{q_2^0} \end{aligned} \tag{3.31}$$

to be finite. We conclude that

$$\begin{aligned} Dd\bar{\hat{\sigma}}_{exp}^n \equiv & \int \sum_{l=0}^{n} \frac{1}{l!} \prod_{j=1}^{l} \int_{k_j \geq K_{max}} \frac{d^3K_j}{k_j} \tilde{S}_{QCD}(k_j) \sum_{i=0}^{n-l} \frac{1}{i!} \prod_{j=l+1}^{l+i} \int \\ & \times \frac{d^3k_j}{k_j^0} D\bar{\beta}_i^{(n-l-i)}(k_{l+1}, \ldots, k_{l+i}) \frac{d^3p_2}{p_2^0} \frac{d^3q_2}{q_2^0} \end{aligned} \tag{3.32}$$

is finite. Since the integration for the final states is completely arbitrary, the independent power of the infrared regulator $\ln(\lambda^2)$ in Eq. (3.32) must give vanishing contributions, which means we can drop the $D\bar{\beta}_n^{(l)}$ from our calculation for the cross section in Eq. (3.22), since they do not make a net contribution to the final parton cross section. We can rewrite Eq. (3.22) as follows:

$$d\hat{\sigma}_{exp} = \sum_{n=0}^{\infty} d\tilde{\sigma}^n = e^{SUM_{IR}(QCD)} \sum_{n=0}^{\infty} \left(\frac{1}{n!}\right) \int \prod_{j=1}^{n} \int \frac{d^3k_j}{k_j^0} \\ \times \int \frac{d^4y}{(2\pi)^4} e^{iy\cdot((p_1+q_1-p_2-q_2-\sum k_i)+D_{QCD}} \;\tilde{\bar{\beta}}_n(k_1,\ldots,k_n)\frac{d^3p_2}{p_2^0}\frac{d^3q_2}{q_2^0} \tag{3.33}$$

where the hard gluon residuals $\tilde{\bar{\beta}}_n(k_1,\ldots,k_n)$ are defined as

$$\tilde{\bar{\beta}}_n(k_1,\ldots,k_n) = \sum_{l=0}^{\infty} \tilde{\bar{\beta}}_n^{(l)}(k_1,\ldots,k_n) \tag{3.34}$$

and are all infrared finite to all orders in $\mathcal{O}(\alpha_s)$ [62].

3.1.4 QCED Resummation

The new QCED [63, 64], $QED \otimes QCD$, theory is obtained by simultaneously resumming the large IR terms in QCD and the exact IR-divergent terms in QED for a prototypical process

$$pp \to \bar{l}l + m(\gamma) + n(g) + X \tag{3.35}$$

where n and $m(g)$ here refers to the number of real photons and real gluons respectively. We can easily extend our results in the two previous sections to arrive at the new results as follows:

$$d\hat{\sigma}_{exp} = \sum_{n=0}^{\infty} d\tilde{\sigma}^n = e^{SUM_{IR}(QCED)} \sum_{n,m=0}^{\infty} \int \prod_{j_1=1}^{n} \frac{d^3k_{j1}}{k_{j1}} \prod_{j_2=1}^{m} \frac{d^3k'_{j2}}{k'_{j2}} \\ \times \int \frac{d^4y}{(2\pi)^4} e^{iy\cdot(p_1+q_1-p_2-q_2-\sum k_{j1}-\sum k'_{j2})+D_{QCED}} \\ \times \tilde{\bar{\beta}}_{n,m}(k_1,\ldots,k_n;k'_1,\ldots,k'_m)\frac{d^3p_2}{p_2^0}\frac{d^3q_2}{q_2^0} \tag{3.36}$$

where the new YFS residuals are $\tilde{\bar{\beta}}_{n,m}(k_1,\ldots,k_n;k'_1,\ldots,k'_m)$ with n hard gluons and m hard photons. The infrared functions are now given by

$$SUM_{IR}(QCED) = 2\alpha_s Re B^{nls}_{QCED} + 2\alpha_s \tilde{B}^{nls}_{QCED}(K_{max}), \tag{3.37}$$

$$2\alpha_s \tilde{B}_{QCED}(K_{max}) = \int \frac{d^3k}{k^0} \tilde{S}^{nls}_{QCED}(k)\theta(K_{max} - k), \tag{3.38}$$

$$D_{QCED} = \int \frac{d^3k}{k} \tilde{S}^{nls}_{QCD}(k)\left[e^{-iy\cdot k} - \theta(K_{max} - k)\right], \tag{3.39}$$

and the functions $SUM_{IR}(QCED)$, D_{QCED} are determined from their QCD analogues $SUM_{IR}(QCD)$, D_{QCD} via the following substitutions

$$\begin{cases} B^{nls}_{QCD} \to B^{nls}_{QCD} + B^{nls}_{QED} \equiv B^{nls}_{QCED}, \\ \tilde{B}^{nls}_{QCD} \to \tilde{B}^{nls}_{QCD} + \tilde{B}^{nls}_{QED} \equiv \tilde{B}^{nls}_{QCED}, \\ \tilde{S}^{nls}_{QCD} \to \tilde{S}^{nls}_{QCD} + \tilde{S}^{nls}_{QED} \equiv \tilde{S}^{nls}_{QCED}. \end{cases} \tag{3.40}$$

The residuals $\bar{\tilde{\tilde{\beta}}}_{n,m}(k_1, \ldots, k_n; k_1', \ldots, k_m')$ are free of infrared singularities, so Eq. (3.36) is a representation that is exact and IR finite and can therefore be used to make contact with parton shower MC's without double counting or unnecessary averaging of effects such as the gluon azimuthal angular distribution relative to its parent's momentum direction.

3.2 DGLAP-CS Splitting Functions

In this section, we apply the QCD master formula in Eq. (3.22), following the analogous argument for QED in Ref. [52], to find $P^{exp}_{qq}(z)$. The basic starting point of

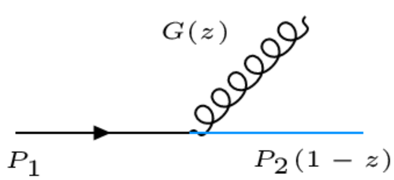

Figure 3.1: The usual process $q \to q(1-z) + G(z)$.

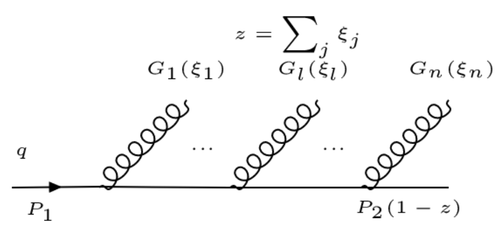

Figure 3.2: Multiple gluon improvement $q \to q(1-z) + G(\xi_1) + \ldots + G(\xi_x)$ where $z = \sum_j \xi_j$.

our analysis is the infrared divergences in the kernel that determines this evolution:

$$\frac{d}{dt}q^{NS}(x,t) = \frac{\alpha_s(t)}{2\pi}\int_x^1 \frac{dy}{y}q^{NS}(y,t)P_{qq}\left(\frac{x}{y}\right) \tag{3.41}$$

where the result for the kernel $P_{qq}(z)$ is

$$P_{qq}(z) = C_F\frac{1+z^2}{1-z} \quad \text{for} \quad z < 1. \tag{3.42}$$

It is obvious that this kernel has a non-integrable IR singularity at $z = 1$, which is the point of zero energy gluon emission, and this is as it should be. The standard treatment of this problem is to regularize it by the following replacement

$$\frac{1}{(1-z)} \to \frac{1}{(1-z)_+} \tag{3.43}$$

where the distribution $\frac{1}{(1-z)_+}$ is the +-function distribution with the possible representation

$$\frac{1}{(1-z)_+} = \frac{1}{(1-z)}\theta(1-\epsilon-z) + \ln\epsilon\delta(1-z) \quad \text{for} \quad \epsilon \to 0 \tag{3.44}$$

The final result for $P_{qq}(z)$ is then

$$P_{qq}(z) = C_F\left(\frac{1+z^2}{(1-z)_+} + \frac{3}{2}\delta(1-z)\right), \tag{3.45}$$

which satisfies the physical condition

$$\int_0^1 dz\ P_{qq}(z) = 0. \tag{3.46}$$

The behaviour of the differential spectrum of the process for $z \to 0$ in $\mathcal{Q}(\alpha_s)$ is non-integrable and has to be cut off, and thus this spectrum is only poorly represented by the $\mathcal{Q}(\alpha_s)$ calculation. We intend to show that the resummation of the large, soft higher-order effects changes the $z \to 0$ behaviour non-trivially and we will find that the $\frac{1}{1-z}$ behaviour is modified to $(1-z)^{\gamma-1}$.

For Figure (3.1), we write our exact amplitude-based exponentiated cross section as follows:

$$\begin{aligned} d\hat{\sigma}_{exp} = e^{SUM_{IR}(QCD)} \int \Bigg\{ \frac{1}{0!}\, \tilde{\bar{\beta}}_0 \int \frac{d^4y}{(2\pi)^4}\; e^{iy\cdot(P_1-P_2)+D_{QCD}} \\ + \frac{1}{1!} \int \frac{d^3k_1}{k_1^0} \tilde{\bar{\beta}}_1(k_1) \int \frac{d^4y}{(2\pi)^4}\; e^{iy\cdot(P_1-P_2-k_1)+D_{QCD}} + ... \Bigg\} \frac{d^3P_2}{P_2^0}\frac{d^3q_2}{q_2^0} \end{aligned} \tag{3.47}$$

We simplify Eq. (3.47) by using the following calculations:

$$\begin{aligned} \int \frac{d^4y}{(2\pi)^4}\; e^{iy\cdot(P_1-P_2)+D_{QCD}} \frac{d^3P_2}{P_2^0}\frac{d^3q_2}{q_2^0} &= \int \frac{dy^0}{2\pi} e^{iy^0(E_1-E_2)+D_{QCD}} \\ &\times \int \frac{d^3y}{(2\pi)^3} e^{i\vec{y}\cdot(\vec{P}_1-\vec{P}_2)} \frac{d^3P_2}{P_2^0}\frac{d^3q_2}{q_2^0} \\ &= \int \frac{dy^0}{2\pi} e^{iy^0(E_1-E_2)+D_{QCD}} \delta^3(\vec{P}_1-\vec{P}_2) \frac{d^3P_2}{P_2^0}\frac{d^3q_2}{q_2^0}, \end{aligned} \tag{3.48}$$

and similar calculation yields

$$\begin{aligned} \int \frac{d^4y}{(2\pi)^4}\; e^{iy\cdot(P_1-P_2-k_1)+D_{QCD}} \frac{d^3P_2}{P_2^0}\frac{d^3q_2}{q_2^0} &= \int \frac{dy^0}{2\pi} e^{iy^0(E_1-E_2-k_1^0)+D_{QCD}} \\ &\times \int \frac{d^3y}{(2\pi)^3} e^{i\vec{y}\cdot(\vec{P}_1-\vec{P}_2-\vec{k}_1)} \frac{d^3P_2}{P_2^0}\frac{d^3q_2}{q_2^0} \\ &= \int \frac{dy^0}{2\pi} e^{iy^0(E_1-E_2-k_1^0)+D_{QCD}} \delta^3(\vec{P}_1-\vec{P}_2-\vec{k}_1) \frac{d^3P_2}{P_2^0}\frac{d^3q_2}{q_2^0}, \end{aligned} \tag{3.49}$$

where we have used the definition of Dirac's delta function

$$\delta^3(x) = \int \frac{d^3k}{(2\pi)^3} e^{-i\vec{k}.\vec{x}}. \tag{3.50}$$

Substituting Eqs. (3.48) and (3.49) into Eq. (3.47) results in

$$\begin{aligned} d\hat{\sigma}_{exp} = e^{SUM_{IR}(QCD)} \int \Bigg\{ \tilde{\bar{\beta}}_0 \int_{-\infty}^{\infty} \frac{dy}{(2\pi)} e^{\left\{ iy(E_1-E_2)+\int^{k<K_{max}} \frac{d^3k}{k} \tilde{S}_{QCD}(k)[e^{iy.k}-1] \right\}} \\ \int \frac{d^3k_1}{k_1} \tilde{\bar{\beta}}_1(k_1) \int_{-\infty}^{\infty} \frac{dy}{(2\pi)} e^{\left\{ iy(E_1-E_2-k_1^0)+\int^{k<K_{max}} \frac{d^3k}{k} \tilde{S}_{QCD}(k)[e^{iy.k}-1] \right\}} \\ + ... \Bigg\} \frac{1}{q_2^0}\frac{d^3P_2}{P_2^0}, \end{aligned} \tag{3.51}$$

where we used the following identities to simplify Eq. (3.51):

$$\int_{-\infty}^{\infty}\int_{-\infty}^{\infty}\int_{-\infty}^{\infty} d^3q_2\; \delta^3(\vec{q}_1-\vec{q}_2) = 1, \tag{3.52}$$

and

$$\int_{-\infty}^{\infty}\int_{-\infty}^{\infty}\int_{-\infty}^{\infty} d^3q_2\ \delta^3(\vec{q}_1 - \vec{q}_2 - \vec{k}_1) = 1, \tag{3.53}$$

where

$$\begin{cases} for \quad n = 0 \Rightarrow P_1^\mu - P_2^\mu = q_1^\mu - q_2^\mu \\ for \quad n = 1 \Rightarrow P_1^\mu - P_2^\mu - k_1^\mu = q_1^\mu - q_2^\mu. \end{cases} \tag{3.54}$$

Now we use the decomposition of P_1^μ, P_2^μ, and k_1^μ to simplify Eq. (3.51) as follows:

$$\begin{cases} P_1^\mu = (E, E, 0, 0) \\ k_1^\mu = (zE + \frac{P_T^2}{2zE}, P_x, P_y, zE) \\ P_2^\mu = ((1-z)E + \frac{P_T^2}{2(1-z)E}, -P_x, -P_y, (1-z)E). \end{cases} \tag{3.55}$$

One can find

$$E_1 - E_2 = P_1^0 - P_2^0 = E - (1-z)E = zE \quad \text{if} \quad \mathcal{O}(P_T^2) = 0. \tag{3.56}$$

Thus we write Eq. (3.51) in the form of

$$\begin{aligned} d\hat{\sigma}_{exp} = e^{SUM_{IR}(QCD)} \int \Big\{ \tilde{\bar{\beta}}_0 \int_{-\infty}^{\infty} \frac{dy}{(2\pi)} e^{\left\{ iy(zE)) + \int^{k<K_{max}} \frac{d^3k}{k} \tilde{S}_{QCD}(k)[e^{iy\cdot k} - 1] \right\}} \\ \int \frac{d^3k_1}{k_1} \tilde{\bar{\beta}}_1(k_1) \int_{-\infty}^{\infty} \frac{dy}{(2\pi)} e^{\left\{ iy(zE - k_1^0) + \int^{k<K_{max}} \frac{d^3k}{k} \tilde{S}_{QCD}(k)[e^{iy\cdot k} - 1] \right\}} \\ + ... \Big\} \frac{1}{q_2^0} \frac{d^3P_2}{P_2^0}. \end{aligned} \tag{3.57}$$

Using the results in Ref. [38], one can derive

$$I_{YFS}(zE, 0) = \int_{-\infty}^{\infty} \frac{dy}{(2\pi)} e^{\left\{ iy(zE)) + \int^{k<K_{max}} \frac{d^3k}{k} \tilde{S}_{QCD}(k)[e^{iy.k} - 1] \right\}} = F_{YFS}(\gamma_q) \frac{\gamma_q}{zE} \tag{3.58}$$

and

$$\begin{aligned} I_{YFS}(zE, k_1) &= \int_{-\infty}^{\infty} \frac{dy}{(2\pi)} e^{\left\{ iy(zE - k_1^0) + \int^{k<K_{max}} \frac{d^3k}{k} \tilde{S}_{QCD}(k)[e^{iy.k} - 1] \right\}} \\ &= \left(\frac{zE}{zE - k_1} \right)^{1-\gamma_q} I_{YFS}(zE, 0) = \left(\frac{zE}{zE - k_1} \right)^{1-\gamma_q} F_{YFS}(\gamma_q) \frac{\gamma_q}{zE}, \end{aligned} \tag{3.59}$$

where

$$\tilde{S}_{QCD}(k) = -\frac{\alpha_s C_F}{8\pi^2}\left(\frac{P_1^\mu}{k.P_1} - \frac{P_2^\mu}{k.P_2}\right)^2_{\text{DGLAP}-\text{CS synthesized}}, \tag{3.60}$$

and

$$\begin{aligned} F_{YFS}(\gamma_q) &= \frac{e^{-C_E\gamma_q}}{\Gamma(1+\gamma_q)} \\ \gamma_q &= C_F\frac{\alpha_s}{\pi}t = \frac{4C_F}{\beta_0} \quad \text{where} \quad \beta_0 = 11 - \frac{2}{3}n_f. \end{aligned} \tag{3.61}$$

Using the well-known results for the respective real and virtual infrared function from Refs. [43–45] we obtain

$$\begin{aligned} SUM_{IR}(QCD) &= 2\alpha_s ReB_{QCD} + 2\alpha_s\tilde{B}_{QCD}(K_{max}) \\ &= \frac{1}{2}\left(2C_F\frac{\alpha_s}{\pi}t\ln\frac{K_{max}}{E} + C_F\frac{\alpha_s}{2\pi}t + \frac{\alpha_s C_F}{\pi}(\frac{\pi^2}{3} - \frac{1}{2})\right), \end{aligned} \tag{3.62}$$

where on the right-hand side of the last result we have applied the DGLAP-CS synthesized procedure in Ref. [65] to remove the collinear singularities in accordance with the standard QCD factorization theorem [66–68].

We now define $z \equiv \frac{K_{max}}{E}$ and use it to simplify Eq. (3.62) as follows:

$$\begin{aligned} SUM_{IR}(QCD) &= 2\alpha_s ReB_{QCD} + 2\alpha_s\tilde{B}_{QCD}(K_{max}) \\ &= \frac{1}{2}\left(2C_F\frac{\alpha_s}{\pi}t\ln z + \frac{\alpha_s}{2\pi}t + \frac{\alpha_s C_F}{\pi}(\frac{\pi^2}{3} - \frac{1}{2})\right). \end{aligned} \tag{3.63}$$

And subsequently we find

$$\begin{aligned} \Rightarrow e^{SUM_{IR}(QCD)} &= \exp(C_F\frac{\alpha_s}{\pi}t\ln z)\exp(\frac{1}{2}\frac{\alpha_s}{2\pi}t)\exp\left(\frac{\alpha_s C_F}{\pi}(\frac{\pi^2}{3} - \frac{1}{2})\right) \\ &= z^{\gamma_q}\exp(\frac{1}{2}\frac{\alpha_s}{2\pi}t)\exp\left(\frac{\alpha_s C_F}{\pi}(\frac{\pi^2}{3} - \frac{1}{2})\right) \\ &= z^{\gamma_q}\ e^{\frac{1}{2}\delta_q}, \end{aligned} \tag{3.64}$$

where we have used

$$\exp(C_F\frac{\alpha_s}{\pi}t\ln z) = \left(\exp(\ln z)\right)^{C_F\frac{\alpha_s t}{\pi}} = z^{C_F\frac{\alpha_s t}{\pi}}, \tag{3.65}$$

since $\exp(\ln z) = z$. We can rewrite Eq. (3.57) in the following form:

$$\begin{aligned}\int \frac{\alpha_s}{2\pi} P_{BA}\ dt\ dz &= z^{\gamma_q}\ e^{\frac{1}{2}\delta_q} F_{YFS}(\gamma_q) \left\{ \left[\frac{\bar{\tilde{\beta}}_0 \gamma_q}{zE} + \int dk_1\ k_1\ d\Omega_1 \left(\frac{zE}{zE - k_1} \right)^{1-\gamma_q} \frac{\gamma_q}{zE} \right] \frac{d^3 P_2}{E_2 q_2^0} \right\} \\ &= z^{\gamma_q}\ e^{\frac{1}{2}\delta_q} F_{YFS}(\gamma_q) \int \frac{\alpha_s}{2\pi} P^0_{BA}\ dt\ dz + \mathcal{O}(\alpha_s^2).\end{aligned} \tag{3.66}$$

Now, using the definition from the previous chapter, we can find

$$P_{BA} = z^{\gamma_q}\ e^{\frac{1}{2}\delta_q} F_{YFS}(\gamma_q) P^0_{BA}, \tag{3.67}$$

where $P^0_{BA} = \frac{1}{2} z(1-z) \bar{\sum}_{spin} \frac{|V_{A \to B+C}|^2}{P_T^2} z^{\gamma_q}\ e^{\frac{1}{2}\delta_q} F_{YFS}(\gamma_q)$. If we choose $A = q$, $B = G$, and $C = q$ one can find

$$P^{exp}_{Gq}(z) = \frac{1}{2} z(1-z) \bar{\sum}_{spin} \frac{|V_{q \to G+q}|^2}{P_T^2} z^{\gamma_q}\ e^{\frac{1}{2}\delta_q} F_{YFS}(\gamma_q), \tag{3.68}$$

and

$$P^{exp}_{qq}(z) = \frac{1}{2} z(1-z) \bar{\sum}_{spin} \frac{|V_{q \to G+q}|^2}{P_T^2} (1-z)^{\gamma_q}\ e^{\frac{1}{2}\delta_q} F_{YFS}(\gamma_q). \tag{3.69}$$

Or equivalently, we write the final expressions for $P^{exp}_{Gq}(z)$ and $P^{exp}_{qq}(z)$ as follows:

$$\begin{aligned} P^{exp}_{qq}(z) &= C_F\ e^{\frac{1}{2}\delta_q} F_{YFS}(\gamma_q) \frac{1+z^2}{1-z} (1-z)^{\gamma_q}, \\ P^{exp}_{Gq}(z) &= C_F\ e^{\frac{1}{2}\delta_q} F_{YFS}(\gamma_q) \frac{1+(1-z)^2}{z}\ z^{\gamma_q} \quad \text{for} \quad z < 1, \end{aligned} \tag{3.70}$$

which is consistent with $P^{exp}_{Gq}(z) = P^{exp}_{Gq}(1-z)$.

The normalization condition in Eq. (3.46) gives us the final expression for $P^{exp}_{qq}(z)$:

$$P^{exp}_{qq}(z) = C_F\ e^{\frac{1}{2}\delta_q} F_{YFS}(\gamma_q) \left[\frac{1+z^2}{1-z} (1-z)^{\gamma_q} - f_q(\gamma_q) \delta(1-z) \right], \tag{3.71}$$

where

$$f_q(\gamma_q) = \frac{2}{\gamma_q} - \frac{2}{\gamma_q + 1} + \frac{1}{\gamma_q + 2}. \tag{3.72}$$

The result in Eq. (3.71) is then our IR-improved kernel for non-singlet DGLAP-CS evolution in QCD. We emphasize that the appearance of the integrable function $(1-$

$z)^{\gamma_q - 1}$ in the place of $\frac{1}{(1-z)_+}$ was anticipated by Gribov and Lipatov [69]. Conservation of momentum tells us that

$$\int_0^1 dz\ z\ (P_{Gq}^{exp}(z) + P_{qq}^{exp}(z)) \stackrel{?}{=} 0. \tag{3.73}$$

Using the results in Eqs. (3.70), (3.71), and (3.72) we have to check that the following integral vanishes:

$$\begin{aligned}
I &= \int_0^1 dz\ z\Big(\frac{1+(1-z)^2}{z} z^{\gamma_q} + \frac{1+z^2}{1-z}(1-z)^{\gamma_q} - f_q(\gamma_q)\delta(1-z)\Big) \\
&= \int_0^1 dz\ \Big((1+(1-z)^2) z^{\gamma_q} - (1+z^2)(1-z)^{\gamma_q} + \frac{1+z^2}{1-z}(1-z)^{\gamma_q} - f_q(\gamma_q)\delta(1-z)\Big) \\
&= 0
\end{aligned} \tag{3.74}$$

The first two terms on the right-hand side of Eq. (3.74) cancel out as one can see by using the change of variable $z \to 1-z$ in one of them, and integration over the last two terms on the right-hand side of Eq. (3.74) also vanishes due to the normalization condition in Eq. (3.46).

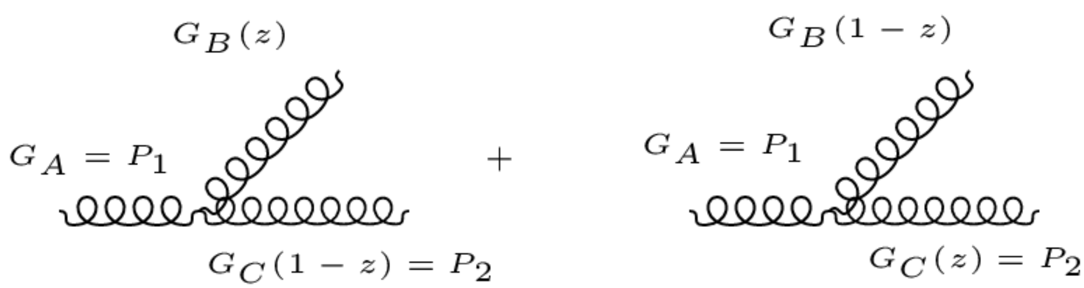

Figure 3.3: Three gluon vertex associated with the calculation of $P_{GG}(z)$.

We now find $P_{GG}^{exp}(z)$ using the two Feynman diagrams in Figure (3.3). We write the exact amplitude-based resummation cross section for Feynman diagrams in

Figure (3.3) as follows:

$$\int \frac{\alpha_s}{2\pi} P^{exp}_{GG}(z)\ dt\ dz = \frac{1}{2}\bigg(\int \frac{\alpha_s}{2\pi} P_{BA}\ dt\ dz + \int \frac{\alpha_s}{2\pi} P_{CA}\ dt\ dz \bigg), \tag{3.75}$$

where $B = G$ and $A = G$. In analogy with the previous results, one can show that

$$\begin{aligned}\int \frac{\alpha_s}{2\pi} P_{BA}\ dt\ dz &= e^{SUM_{IR}(QCD)} \bigg\{ \bigg[\frac{\tilde{\bar{\beta}}_0 \gamma_G}{zE} + \int dk_1\ k_1\ d\Omega_1 \bigg(\frac{zE}{zE - k_1} \bigg)^{1-\gamma_G} \frac{\gamma_G}{zE} \bigg] \frac{d^3 P_2}{E_2 q_2^0} \bigg\}, \\ &= e^{SUM_{IR}(QCD)} \int \frac{\alpha_s}{2\pi} P^0_{BA}(z)\ dt\ dz + \mathcal{O}(\alpha_s^2), \\ \Rightarrow P_{BA} &= 2C_G F_{YFS}(\gamma_G) e^{\frac{1}{2}\delta_G} \bigg[\frac{z(1-z)^{\gamma_G}}{1-z} + \bigg(\frac{1-z}{z} + z(1-z) \bigg) z^{\gamma_G} \bigg].\end{aligned} \tag{3.76}$$

and

$$\begin{aligned}\int \frac{\alpha_s}{2\pi} P_{CA}\ dt\ dz &= e^{SUM_{IR}(QCD)} \bigg\{ \bigg[\frac{\tilde{\bar{\beta}}_0 \gamma_G}{(1-z)E} + \int dk_1\ k_1\ d\Omega_1 \\ &\quad \times \bigg(\frac{(1-z)E}{(1-z)E - k_1} \bigg)^{1-\gamma_G} \frac{\gamma_G}{(1-z)E} \bigg] \frac{d^3 P_2}{E_2 q_2^0} \bigg\} \\ &= e^{SUM_{IR}(QCD)} \int \frac{\alpha_s}{2\pi} P^0_{CA}(1-z)\ dt\ dz + \mathcal{O}(\alpha_s^2), \\ \Rightarrow P_{CA} &= 2C_G F_{YFS}(\gamma_G) e^{\frac{1}{2}\delta_G} \bigg[\frac{(1-z)z^{\gamma_G}}{z} + \bigg(\frac{z}{1-z} + z(1-z) \bigg) (1-z)^{\gamma_G} \bigg].\end{aligned} \tag{3.77}$$

In these equations we have used

$$\gamma_G = C_G \frac{\alpha_s}{\pi} t = \frac{4C_G}{\beta_0} \tag{3.78}$$

$$\delta_G = \frac{\gamma_G}{2} + \frac{\alpha_s C_G}{\pi} \bigg(\frac{\pi^2}{3} - \frac{1}{2} \bigg). \tag{3.79}$$

We can find the final result for $P^{exp}_{GG}(z)$ by using the results in Eqs. (3.76) and (3.77) and plugging into Eq. (3.75):

$$\begin{aligned}P^{exp}_{GG}(z) &= \frac{1}{2}(P_{BA} + P_{CA}) \\ &= 2C_G F_{YFS}(\gamma_G) e^{\frac{1}{2}\delta_G} \bigg[\frac{z(1-z)^{\gamma_G}}{1-z} + \frac{(1-z)z^{\gamma_G}}{z} \\ &+ \frac{1}{2} \bigg((1-z) z^{\gamma_G+1} + z(1-z)^{\gamma_G+1} \bigg) \bigg]\end{aligned} \tag{3.80}$$

We see again that exponentiation has made the singularities at $z = 0$ and $z = 1$ integrable. Finally, the standard formula for $P_{qG}(z)$ is well-behaved integrable in the IR regime, we do not need to improve it here to make it integrable and we note that the singular contributions in the other kernels are expected to dominate the evolution effects in any case. $P_{qG}(z)$ is

$$p_{qG}(z) = \frac{1}{2}(z^2 + (1-z)^2). \tag{3.81}$$

To normalize $P_{GG}^{exp}(z)$, we take into account the virtual corrections such that the gluon momentum sum rule

$$\int_0^1 dz\ z(2n_f P_{qG}(z) + P_{GG}^{exp}(z)) = 0 \tag{3.82}$$

is satisfied. This gives us the IR-improved result as follows

$$\begin{aligned} P_{GG}^{exp}(z) = 2C_G F_{YFS}(\gamma_G) e^{\frac{1}{2}\delta_G} \Bigg\{ \frac{1-z}{z} z^{\gamma_G} + \frac{z}{1-z}(1-z)^{\gamma_G} \\ + \frac{1}{2}\Big((1-z) z^{\gamma_G+1} + z(1-z)^{\gamma_G+1} \Big) - f_G(\gamma_G)\delta(1-z) \Bigg\}, \end{aligned} \tag{3.83}$$

where for $f_G(\gamma_G)$ we find

$$\begin{aligned} f_G(\gamma_G) = \frac{n_f}{6C_G F_{YFS}(\gamma_G)} e^{-\frac{1}{2}\delta_G} + \frac{2}{\gamma_G(1+\gamma_G)(2+\gamma_G)} + \frac{1}{(1+\gamma_G)(2+\gamma_G)} \\ + \frac{1}{2(3+\gamma_G)(4+\gamma_G)} + \frac{1}{(2+\gamma_G)(3+\gamma_G)(4+\gamma_G)}. \end{aligned} \tag{3.84}$$

We summarize at this point the new IR-improved kernels set as follows

$$\begin{cases} P_{qq}^{exp}(z) = C_F\ e^{\frac{1}{2}\delta_q} F_{YFS}(\gamma_q) \left[\frac{1+z^2}{1-z}(1-z)^{\gamma_q} - f_q(\gamma_q)\delta(1-z) \right], \\ P_{Gq}^{exp}(z) = C_F\ e^{\frac{1}{2}\delta_q} F_{YFS}(\gamma_q) \frac{1+(1-z)^2}{z}\ z^{\gamma_q}, \\ p_{qG}(z) = \frac{1}{2}(z^2 + (1-z)^2), \\ P_{GG}^{exp}(z) = 2C_G F_{YFS}(\gamma_G) e^{\frac{1}{2}\delta_G} \Big\{ \frac{1-z}{z} z^{\gamma_G} + \frac{z}{1-z}(1-z)^{\gamma_G} \\ \qquad + \frac{1}{2}\Big((1-z) z^{\gamma_G+1} + z(1-z)^{\gamma_G+1} \Big) - f_G(\gamma_G)\delta(1-z) \Big\}. \end{cases} \tag{3.85}$$

Returning now to the improvement of $P_{qG}^{exp}(z)$ for the sake of completeness and for providing better precision, we apply the same arguments to the process $G \to q + \bar{q}$ to get the exponentiated result

$$P_{qG}^{exp}(z) = e^{\frac{1}{2}\delta_q} F_{YFS}(\gamma_q) \frac{1}{2} \left\{ z^2(1-z)^{\gamma_G} + (1-z)^2 z^{\gamma_G} \right\}, \tag{3.86}$$

where the gluon momentum sum rule gives the new normalization constant for $P_{GG}^{exp}(z)$

$$\begin{aligned} \bar{f}_G(\gamma_G) = & \frac{n_f}{C_G} \frac{1}{(1+\gamma_G)(2+\gamma_G)(3+\gamma_G)} + \frac{2}{\gamma_G(1+\gamma_G)(2+\gamma_G)} \\ & + \frac{1}{(1+\gamma_G)(2+\gamma_G)} + \frac{1}{2(3+\gamma_G)(4+\gamma_G)} + \frac{1}{(2+\gamma_G)(3+\gamma_G)(4+\gamma_G)}. \end{aligned} \tag{3.87}$$

The constant $\bar{f}_G(\gamma_G)$ should be substituted for $f_G(\gamma_G)$ in $P_{GG}^{exp}(z)$ whenever the exponentiated result is used.

3.3 The Logarithmic Exponents

We now look into the phenomenological effects of IR-improved on the moment of the structure functions by discussing the corresponding effects on the moments of the parton distributions.

We know that moments of the kernels determine the exponents in the logarithmic variation of the moments of the quark distributions and for the non-singlet case we have

$$\frac{d}{dt} M_n^{NS}(t) = \frac{\alpha_s(t)}{2\pi} A_n^{NS} M_n^{NS}(t), \tag{3.88}$$

where

$$M_n^{NS}(t) = \int_0^1 dz\ z^{n-1} q^{NS}(z,t) \tag{3.89}$$

and the quantity A_n^{NS} is given by

$$\begin{aligned} A_n^{NS} &= \int_0^1 dz\ z^{n-1}\ P_{qq}^{exp}(z) \\ &= C_F F_{YFS}(\gamma_q) e^{\frac{1}{2}\delta_q} [B(n,\gamma_q) + B(n+2,\gamma_q) - f_q(\gamma_q)], \end{aligned} \tag{3.90}$$

where the beta function, $B(x,y)$ is defined

$$B(x,y) = \frac{\Gamma(x)\Gamma(y)}{\Gamma(x+y)}. \tag{3.91}$$

One can find the remaining elements of the leading logarithmic exponents for the other IR-improved splitting functions as follows

$$A_n^{Gq} = \int_0^1 dz\; z^{n-1} P_{Gq}^{exp}(z) = C_F F_{YFS}(\gamma_q) e^{\frac{1}{2}\delta_q}\left[\frac{1}{n+\gamma_q-1} + B(3, n+\gamma_q-1)\right], \tag{3.92}$$

$$A_n^{GG} = \int_0^1 dz\; z^{n-1} P_{GG}^{exp}(z) = 2C_G F_{YFS}(\gamma_q) e^{\frac{1}{2}\delta_q}\Bigg[B(n+1,\gamma_G) + B(n+\gamma_G-1,2) + \frac{1}{2}\Big(B(n+1,\gamma_G+2) + B(n+\gamma_G+1,2)\Big) - \bar{f}(\gamma_G)\Bigg], \tag{3.93}$$

$$2n_f A_n^{qG} = 2n_f \int_0^1 dz\; z^{n-1} P_{qG}^{exp}(z) = n_f F_{YFS}(\gamma_G) e^{\frac{1}{2}\delta_G}\Big(B(n+2,1+\gamma_G) + B(n+\gamma_G,3)\Big). \tag{3.94}$$

We now compare the asymptotic behavior of A_n^{NS} and the IR-improved A_n^{NS} for large n. One can easily investigate that when $n \to \infty$,

$$\begin{cases} \lim_{n\to\infty} A_n^{NS} = -2C_F \lim_{n\to\infty} \ln(n) \to -\infty, \\ \lim_{n\to\infty} (A_n^{NS})_{\mathrm{IR-improved}} \to -f_q(\gamma_q) \;\text{ for }\; 0 \le z < 1. \end{cases} \tag{3.95}$$

The two results are also different at finite n, e.g. $n = 2$. We get, for example, for $\alpha_s \simeq 0.118$:

$$A_n^{NS} = \begin{cases} C_F(-1.33), & \mathrm{un-IR-improved} \\ C_F(-0.996), & \mathrm{IR-improved} \end{cases} \tag{3.96}$$

which shows that the effects we have calculated are important for all values of n in general. We also can solve the differential equation introduced in Eq. (3.88) by the standard method as

$$
\begin{aligned}
\ln M_n^{NS}(t)\Big|_{t_0}^{t} &= \int_{t_0}^{t} \frac{\alpha_s(t)}{2\pi} A_n^{NS}\, dt \\
\Rightarrow M_n^{NS}(t) &= M_n^{NS}(t_0) e^{\int_{t_0}^{t} \frac{\alpha_s(t)}{2\pi} A_n^{NS}\, dt}.
\end{aligned}
\tag{3.97}
$$

We then use the IR-improved A_n^{NS} result in Eq. (3.90) and substitute it into the final result we found in the previous equation:

$$
\begin{aligned}
M_n^{NS}(t) &= M_n^{NS}(t_0) e^{C_F F_{YFS}(\gamma_q)[B(n,\gamma_q)+B(n+2,\gamma_q)-f_q(\gamma_q)]} e^{\frac{\gamma_q}{4}} \\
&\times \int_{t_0}^{t} \frac{\alpha_s(t)}{2\pi} e^{\frac{\alpha(t) C_F}{\pi}\left(\frac{\pi^2}{3}-\frac{1}{2}\right)} dt \\
&= M_n^{NS}(t_0) e^{\frac{2C_F}{\beta_0} F_{YFS}(\gamma_q)[B(n,\gamma_q)+B(n+2,\gamma_q)-f_q(\gamma_q)]} e^{\frac{\gamma_q}{4}} \\
&\times e^{Ei(\frac{1}{2}\delta_1 \alpha_s(t_0)) - Ei(\frac{1}{2}\delta_1 \alpha_s(t))} \\
&= M_n^{NS}(t_0) e^{\bar{a}_n \left[Ei(\frac{1}{2}\delta_1 \alpha_s(t_0)) - Ei(\frac{1}{2}\delta_1 \alpha_s(t)) \right]},
\end{aligned}
\tag{3.98}
$$

where we have used

$$
\bar{a}_n = \frac{2C_F}{\beta_0} F_{YFS}(\gamma_q)[B(n,\gamma_q) + B(n+2,\gamma_q) - f_q(\gamma_q)] e^{\frac{\gamma_q}{4}}, \tag{3.99}
$$

$$
\delta_1 = \frac{C_F}{\pi}\left(\frac{\pi^2}{3} - \frac{1}{2}\right). \tag{3.100}
$$

The mathematical special function $Ei(x)$ is defined as follows

$$
Ei(x) = \int_{-\infty}^{x} \frac{dy}{y}\, e^y. \tag{3.101}
$$

We study the behavior of $M_n^{NS}(t)$ for large t and t_0 with $t \gg t_0$ by using the following expansion

$$
Ei(x) = \gamma + \ln|x| + \sum_{k=1}^{\infty} \frac{x^k}{k k!}, \tag{3.102}
$$

which leads to

$$Ei(\frac{1}{2}\delta_1\alpha_s(t_0)) - Ei(\frac{1}{2}\delta_1\alpha_s(t)) = \ln\frac{\alpha(t_0)}{\alpha(t)} + \sum_{k=1}^{\infty}\frac{1}{kk!}\Big((\frac{\alpha_s(t_0)\delta_1}{2})^k - (\frac{\alpha_s(t)\delta_1}{2})^k\Big)$$
$$\simeq \ln\frac{\alpha(t_0)}{\alpha_s(t)} + \frac{\delta_1}{2}(\alpha_s(t_0) - \alpha_s(t)) + \mathcal{O}(\alpha_s^2), \tag{3.103}$$

for $t \gg t_0 \Rightarrow \alpha_s(t_0) \gg \alpha_s(t)$. One can rewrite Eq. (3.98) in the form of

$$M_n^{NS}(t) = M_n^{NS}(t_0)\left(\frac{\alpha_s(t_0)}{\alpha_s(t)}\right)^{\bar{a}_n'}, \tag{3.104}$$

where

$$\bar{a}_n' = \bar{a}_n\left(1 + \frac{\delta_1}{2}\frac{(\alpha_s(t_0) - \alpha_s(t))}{\ln(\frac{\alpha(t_0)}{\alpha_s(t)})}\right). \tag{3.105}$$

We can compare these results with the un-IR-improved result in which Eq. (3.104) holds exactly with $\bar{a}_n' = 2A_n^{NS}\Big|_{\text{un}-\text{IR}-\text{improved}}$. Phenomenologically, for $n = 2$, taking $Q_0 = 2$ GeV and evolving to $Q = 100$ GeV, if we set $\Lambda_{QCD} = 0.2$ GeV and use $n_f = 5$ for definiteness of illusion, we see that we get a shift of the respective evolved NS moment by $\sim$5%.

We also note that the size of the exponent γ_q is what one would expect from analogy with QED [70–74], where with $Q = 100$ GeV we have the analogous result $\gamma_e = \frac{\alpha_{EM}}{\pi}(\ln\frac{Q^2}{m_e^2} - 1) \simeq 0.054$ whereas here, with $\alpha_s \simeq 0.118$, which is about 10 times α_{EM}, we get a value for γ_q that is about 10 times γ_e.

In sum, we have used exact rearrangment of the QCD Feynman series to isolate and resum the leading IR contributions to the physical processes that generate the evolution kernels in DGLAP-CS theory. Finally, we have a new scheme for precision LHC theory.

In obvious notation,

$$\begin{aligned}\sigma &= \sum_{i,j} \int dx_1 dx_2 F_i(x_1) F_j(x_2) \hat{\sigma}(x_1 x_2 s) \\ &= \sum_{i,j} \int dx_1 dx_2 F_i^{'}(x_1) F_j^{'}(x_2) \hat{\sigma}^{'}(x_1 x_2 s)\end{aligned} \tag{3.106}$$

where the primed quantities are associated with the IR-improved kernels in the standard QCD factorization calculus.

3.4 Parton Shower with HERWIRI1.031

The implementation of the new IR-improved kernels in the HERWIG6.5 environment results in a new MC, HERWIRI1.0(31), which stands for high energy radiation with IR improvement. This means

$$\mathrm{DGLAP} - \mathrm{CS}\ P_{AB} \Rightarrow \mathrm{IR} - \mathrm{improved\ DGLAP} - \mathrm{CS}\ P_{AB}^{exp}. \tag{3.107}$$

For the transition from HERWIG6.5 to HERWIRI1.0(31), we modify the kernels in the HERWIG6.5 module HWBRAN and in the attendant related modules as mentioned in Eq. (3.107). For the definiteness, we illustrate the implementation by an example. In this example [75], the probability that no branching occurs above the virtuality cutoff Q_0^2 is $\Delta_a(Q^2, Q_0^2)$, so that

$$d\Delta_a(t, Q_0^2) = -\frac{dt}{t} \Delta(t, Q_0^2) \sum_b \int dz\ \frac{\alpha_s}{2\pi} P_{ba}(z), \tag{3.108}$$

which can be solved and written in the following form

$$\Delta_a(Q^2, Q_0^2) = \exp\left(- \int_{Q_0^2}^{Q^2} \frac{dt}{t} \sum_b \int dz\ \frac{\alpha_s}{2\pi} P_{ba}(z) \right). \tag{3.109}$$

The attendant nonbranching probability appearing in the evolution is

$$\Delta(Q^2, t) = \frac{\Delta_a(Q^2, Q_0^2)}{\Delta_a(t, Q_0^2)}, \tag{3.110}$$

where $t = k_a^2$ is the virtuality of gluon a. The respective virtuality of parton a is then generated by

$$R = \Delta_a(Q^2, t), \tag{3.111}$$

where R is a random number uniformly distributed in [0,1]. Also, $\alpha_s(Q)$ is

$$\alpha_s(Q) = \frac{2\pi}{b_0 \ln(\frac{Q}{\Lambda})}, \tag{3.112}$$

where $\beta = b_0\big|_{n_c}$ and n_c is the number of colors. We now find all these parameters for $P_{qG}(z)$ and $P_{qG}^{exp}(z)$ as follows

$$\begin{aligned}
\Delta_a(Q^2, Q_0^2) &= \exp\left(- \int_{Q_0^2}^{Q^2} \frac{dt}{t} \int dz \; \frac{\alpha_s}{2\pi} P_{ba}(z) \right) \\
&= \exp\left(- \int_{Q_0^2}^{Q^2} \frac{1}{3} \frac{dt}{t} \frac{2}{b_0 \ln(\frac{t}{\Lambda^2})} \right) \\
&= \exp\left(- \frac{2}{3b_0 \ln(\frac{t}{\Lambda^2})} \Bigg|_{Q_0^2}^{Q^2} \right) \\
&= \exp\left(- \frac{2}{3b_0} \ln\left(\frac{\ln(\frac{Q^2}{\Lambda^2})}{\ln(\frac{Q_0^2}{\Lambda^2})} \right) \right) \\
&= \left[\frac{\ln(\frac{Q^2}{\Lambda^2})}{\ln(\frac{Q_0^2}{\Lambda^2})} \right]^{-\frac{2}{3b_0}},
\end{aligned} \tag{3.113}$$

where we have used

$$\begin{aligned}
\int_0 1 \; dz \frac{\alpha_s(Q^2)}{2\pi} P_{qG}(z) &= \frac{2}{b_0 \ln(\frac{Q^2}{\Lambda^2})} \int_0^1 \; dz \frac{1}{2}[z^2 + (1-z)^2] \\
&= \frac{2}{3} \frac{1}{b_0 \ln(\frac{Q^2}{\Lambda^2})}.
\end{aligned} \tag{3.114}$$

If we now use $\Delta_a(Q^2, t) = R$, then

$$\left[\frac{\ln(\frac{t}{\Lambda^2})}{\ln(\frac{Q_0^2}{\Lambda^2})} \right]^{\frac{2}{3b_0}} = R, \tag{3.115}$$

which implies that

$$t = \Lambda^2 \left(\frac{Q^2}{\Lambda^2} \right)^{R^{\frac{3b_0}{2}}}. \tag{3.116}$$

We recall in HERWIG6.5 [58] we have

$$\begin{aligned} b_0 &= \left(\frac{11}{3}n_c - \frac{2}{3}n_f\right) \\ n_f &= 5, \equiv \frac{2}{3}\ \texttt{BETAF}, \end{aligned} \tag{3.117}$$

where in the last line we used the notation in HERWIG6.5. The momentum available after a $q\bar{q}$ split in HERWIG6.5 is given by

$$\texttt{QQBAR} = \texttt{QCDL3}\left(\frac{\texttt{QLST}}{\texttt{QCDL3}}\right)^{R^{\texttt{BETAF}}} \tag{3.118}$$

which is in complete agreement with Eq. (3.116) when we note the identifications $t = \texttt{QQBQR}^2$, $\Lambda \equiv \texttt{QCDL3}$, and $Q \equiv \texttt{QLST}$.

We now repeat the above calculation for $P^{exp}_{qG}(z)$

$$\begin{aligned} \int_0^1 dz\ \frac{\alpha_s(Q^2)}{2\pi}P^{exp}_{qG}(z) &= \frac{2F_{YFS(\gamma_G)}e^{\frac{1}{2}\delta_G}}{b_0\ln(\frac{Q^2}{\Lambda^2})}\frac{1}{2}\int_0^1[z^2(1-z)^{\gamma_G}+(1-z)^2z^{\gamma_G}] \\ &= \frac{4F_{YFS(\gamma_G)}e^{\frac{1}{2}\delta_G}}{b_0\ln(\frac{Q^2}{\Lambda^2})(1+\gamma_G)(2+\gamma_G)(3+\gamma_G)}. \end{aligned} \tag{3.119}$$

This leads to

$$\begin{aligned} \Delta_a(Q^2,Q_0^2) &= \int_{Q^2}^{Q_0^2}\frac{dt}{t}\frac{4F_{YFS(\gamma_G)}e^{\frac{1}{2}\delta_G}}{b_0\ln(\frac{t}{\Lambda^2})(1+\gamma_G)(2+\gamma_G)(3+\gamma_G)} \\ &= \frac{4F_{YFS(\gamma_G)}e^{\frac{1}{2}\delta_G}}{b_0(1+\gamma_G)(2+\gamma_G)(3+\gamma_G)}Ei\left(1,\frac{8.369604402}{b_0\ln(\frac{t}{\Lambda^2})}\right)\Bigg|_{Q_0^2}^{Q^2}. \end{aligned} \tag{3.120}$$

And the IR-improved formula for $\Delta_a(Q^2,t)$ can be written in the form

$$\Delta_a(Q^2,t) = \exp[-F(Q^2)-F(t)], \tag{3.121}$$

where

$$F(Q^2) = \frac{4F_{YFS(\gamma_G)}e^{\frac{1}{2}\delta_G}}{b_0(1+\gamma_G)(2+\gamma_G)(3+\gamma_G)}Ei\left(1,\frac{8.369604402}{b_0\ln(\frac{Q^2}{\Lambda^2})}\right), \tag{3.122}$$

and the Ei is the integral function.

In HERWIG6.5 for the $q \to qG$ branching process, we have the implementation of the usual DGLAP-CS kernels, e.g.

```
      WMIN=MIN(ZMIN*(1.-ZMIN),ZMAX*(1.-ZMAX))
      ETEST=(1.+ZMAX**2)*HWUALF(5-SUDORD*2,QNOW*WMIN)
      ZRAT = ZMAX/ZMIN
30    Z1=ZMIN*ZRAT**HWRGEN(0)
      Z2 = 1.- Z1
      PGQW=(1.+Z2*Z2)
      ZTEST=PGQW*HWUALF(5-SUDORD*2,QNOW*Z1*Z2)
      IF(ZTEST.LT.ETEST*HWRGEN(1))GOTO30
```

...

where the branching of q to G at $z=$ `z1` occures in the interval from `zmin` to `zmax` set by the inputs to the program and the current value of the virtuality `QNOW`,`HWUALF` is the respective function for α_s in the program and `HWRGEN(J)` are uniformly distributed random numbers on the interval $[0,1]$.

We now make the replacement for the IR-improved kernels in the HERWIG6.5 to find the HERWIRI1.031 code

```
        NUMFLAV=5
        B0=11.-2./3.*NUMFLAV
        L=16./(3.*B0)
        DELTAQ=L/2+HWUALF(5.-SUDORD*2,QNOW*WMIN)*1.184056810
        ETEST=(1.+ZMAX**2)*HWUALF(5.-SUDORD*2,QNOW*WMIN)
       & *EXP(0.5*DELTAQ)*FYFSQ(NUMFLAV-1)*ZMAX**L
        ZRAT = ZMAX/ZMIN
30      Z1=ZMIN*ZRAT**HWRGEN(0)
        Z2 = 1.- Z1
        DELTAQ=L/2+HWUALF(5.-SUDORD*2,QNOW*WMIN)*1.184056810
```

```
PGQW=(1.Z2*Z2)*EXP(0.5*DELTAQ)*FYFSQ(NUMFLAV-1)*Z1**L
ZTEST=PGQW*HWUALF(5-SUDORD*2,QNOW*Z1*Z2)
IF(ZTEST.LT.ETEST*HWRGEN(1))GOTO30
...
```

so that with the identification $\gamma_q \equiv \texttt{L}$, $\delta_q \equiv \texttt{DELTAQ}$, $F_{YFS}(\gamma_q) \equiv \texttt{FYFSQ}(\texttt{NUMFLAV} - 1)$.

Final-state parton showering is generated by a so-called coherent algorithm with the following properties:

- The energy fractions are distributed according to the leading-order IR-improved DGLAP-CS splitting functions derived in this chapter;
- The full available phase space is restricted to an angular-ordered region;
- The emission angles are distributed according to the famous Sudakov form factors, with the virtual corrections and unresolved real emissions;
- For soft emitted gluons, the azimuth is distributed according to the eikonal dipole distribution [59];
- For non-soft emitted gluons, the azimuth is distributed according to spin effects [60, 61];
- In each branching the scale of α_s is the relative transverse momentum of the two daughters;
- In the heavy flavour production case, the mass of the quark modifies the angular-ordered phase space.

The HERWIRI1.031 parton shower evolution is done in terms of two variables z and ξ, where z is the parton energy fraction and ξ is an angular variable defined as follows:

$$P_i \to P_j + P_k \Rightarrow \quad z_j = \frac{E_j}{E_i} \tag{3.123}$$

$$P_i \to P_j + P_k \Rightarrow \quad \xi_{jk} = \frac{(p_j.p_k)}{E_j E_k}. \tag{3.124}$$

For massless partons at small angles, $\xi_{jk} \simeq \frac{1}{2}\theta_{jk}^2$. The values of z are chosen according to IR-improved DGLAP-CS splitting functions and the distribution of ξ_{jk} is determined by the Sudakov form factors.

We realize the IR-improved DGLAP-CS theory in the MADGRAPH5_aMC@NLO framework and specifically we recall the connection between our constructs in the master formula in Eq. (3.36) and the constructs in the MC@NLO methodology. We may represent the MC@NLO differential cross section via [76]:

$$d\sigma_{MC@NLO} = \left[B + V + \int (R_{MC} - C) d\Phi_R\right] d\Phi_B [\Delta_{MC}(0) + \int (R_{MC}/B)\Delta_{MC}(k_T) d\Phi_R] \\ + (R - R_{MC})\Delta_{MC}(k_T) d\Phi_B d\Phi_R \tag{3.125}$$

where B is Born distribution, V is the regularized virtual contribution, C is the corresponding counter-term required at exact NLO, R is the respective exact real emission distribution for exact NLO, $R_{MC} = R_{MC}(P_{AB})$ is the parton shower real emission distribution so that the Sudakov form factor is

$$\Delta_{MC}(p_T) = e^{[-\int d\Phi_R \frac{R_{MC}(\Phi_B,\Phi_R)}{B}\theta(k_T(\Phi_B,\Phi_R)-p_T)]},$$

where as usual it describes the respective no-emission probability. The respective Born and real emission differential phase spaces are denoted by $d\Phi_A,\ A = B,\ R$. We find it very important *still* to emphasize that the representation of the differential distribution for MC@NLO illustrates the compensation between real and virtual divergent soft effects discussed in the Appendices of Ref. [2, 42] in establishing the validity of Eq. (3.33) for QCD. More specifically, from comparison with Eq. (3.33) restricted to its QCD aspect we get the identifications, accurate to $\mathcal{O}(\alpha_s)$,

$$\begin{aligned} \frac{1}{2}\hat{\hat{\bar{\beta}}}_{0,0} &= \bar{B} + (\bar{B}/\Delta_{MC}(0)) \int (R_{MC}/B)\Delta_{MC}(k_T) d\Phi_R \\ \frac{1}{2}\hat{\hat{\bar{\beta}}}_{1,0} &= R - R_{MC} - B\tilde{S}_{QCD} \end{aligned} \tag{3.126}$$

where we defined [77]

$$\bar{B} = B(1 - 2\alpha_s \Re B_{QCD}) + V + \int (R_{MC} - C) d\Phi_R$$

and we understand that the DGLAP-CS kernels in R_{MC} are to be taken as the IR-improved ones as we derived in Refs. [2,42]. Although we have suppressed the superscript nls for simplicity of notation, to avoid double counting of effects the QCD virtual and real infrared functions B_{QCD} and $\tilde{S}_{QCD}$ are understood to be DGLAP-CS synthesized as explained in Refs. [2,42,63,64]. Most importantly, in view of Eq. (3.126), we observe that the way to the extension of frameworks such as MC@NLO to exact higher orders in $\{\alpha_s,\ \alpha\}$ is open via our $\hat{\bar{\bar{\beta}}}_{n,m}$ and will be taken up elsewhere [78].

We use the MC@NLO methodology in the automated MADGRAPH5_aMC@NLO framework to investigate IR-improvement effects in the processes $pp \to W + n$ jets + X in what follows.

CHAPTER FOUR

IR-improved DGLAP-CS Parton Shower Effects for Associated Production of a W Boson and Jets in pp Collisions at $\sqrt{s} = 7$ TeV

4.1 Event Generation, Analysis and Cuts (ATLAS Collaboration)

The generators for W + jet events are MADGRAPH5_aMC@NLO [79] interfaced with HERWIG6.521 and HERWIRI1.031, which use next-to-leading-order (NLO) matrix element calculations. The number of events generated for the W, W + 1 jet, W + 2 jets, and W + 3 jets processes are 10^7, 10^6, 10^5, and 10^5, respectively. These events are showered by MADGRAPH5_aMC@NLO/HERWIRI1.031 (PTRMS = 0) and MADGRAPH5_aMC@NLO/HERWIG6.521 (PTRMS = 2.2 GeV).[1] During the analysis, jets were reconstructed using the anti-k_t algorithm with $R = 0.4$ with FastJet [80] and the cuts in Table 4.1 were imposed.

Table 4.1: Kinematic criteria defining the fiducial phase space for the $W \to l + \nu_l$ channel.

Combined channel	$W \to l + \nu_l$ where $l = \{e, \mu\}$
Lepton P_T^l	$P_T^l > 25$ GeV
Lepton rapidity η_l	$\lvert\eta_l\rvert < 2.5$
Missing transverse energy	$E_T^{miss} > 25$ GeV
Transverse mass	$m_T > 40$ GeV
Jet algorithm	Anti-k_T
Radius parameter R	$R = 0.4$
Jet P_T^{jet}	$P_T^{jet} > 30$ GeV
Jet rapidity Y_{jet}	$\lvert Y_{jet}\rvert < 4.4$
Jet isolation	$\Delta R(l, \text{jet}) > 0.5$ (jet is removed)

[1]We will see later that HERWIRI gives either a better fit to the data or an acceptable fit without this extra Gaussian kick.

The transverse mass, m_T, is defined as $m_T = \sqrt{2P_T^l P_T^{\nu_l}(1-\cos\Delta\phi)}$ where $\Delta\phi$ is the difference in the azimuthal angle between the direction of the lepton momentum and the associated neutrino, ν_l, which can be written as

$$\Delta\phi = \phi^l - \phi^{\nu_l}. \tag{4.1}$$

Rapidity is defined as $\frac{1}{2}\ln\left[\frac{E+p_z}{E-p_z}\right]$, where E denotes the energy of the particle and p_z is the longitudinal component of the momentum. Finally, the jet isolation, ΔR, which is a Lorentz invariant quantity, is defined as

$$\Delta R(l,\text{jet}) = \sqrt{\Delta\phi^2(l,\text{jet}) + \Delta\eta^2(l,\text{jet})}, \tag{4.2}$$

where

$$\begin{cases} \Delta\phi(l,\text{jet}) = \phi_l - \phi_{\text{jet}}, \\ \Delta\eta(l,\text{jet}) = \eta_l - \eta_{\text{jet}}, \\ \eta = -\ln\tan\left(\frac{\theta}{2}\right). \end{cases} \tag{4.3}$$

4.2 Results (ATLAS Collaboration)

The measured W($\to l{+}\nu_l$) + jets fiducial cross sections [81] are shown and compared to the predictions of MADGRAPH5_aMC@NLO/HERWIRI1.031 and MADGRAPH5_aMC@NLO/HERWIG6.521. Each distribution is combined separately by minimizing a χ^2 function. The factors applied to the theory predictions are summarized in Appendix F.

We have used the following notation throughout this dissertation:

- herwiri $\equiv$ MADGRAPH5_aMC@NLO/HERWIRI1.031 (PTRMS = 0);
- herwig $\equiv$ MADGRAPH5_aMC@NLO/HERWIG6.521 (PTRMS = 2.2 GeV).

4.2.1 Transverse Momentum Distributions

The differential cross sections as a function of the leading jet transverse momentum are shown in Figure 4.1 and Figure 4.2 for the W + ≥1 jet and W + 1 jet cases, respectively. In both cases, there is agreement between the data and predictions provided by HERWIRI and HERWIG for $P_T \leq 200$ GeV. In Figure 4.1, $\left(\frac{\chi^2}{d.o.f}\right)_{\texttt{HERWIRI}} = 5.98$ and $\left(\frac{\chi^2}{d.o.f}\right)_{\texttt{HERWIG}} = 10.62$. In Figure 4.2, $\left(\frac{\chi^2}{d.o.f}\right)_{\texttt{HERWIRI}} = 5.18$ and $\left(\frac{\chi^2}{d.o.f}\right)_{\texttt{HERWIG}} = 4.91$. We note that the $\left(\frac{\chi^2}{d.o.f}\right)$ functions have been calculated for the first 9 bins. For $P_T \geq 200$ GeV, in most cases, the predictions underestimate the data. HERWIRI predictions in both figures, in three cases overlap with the data for $P_T \geq 200$ GeV.

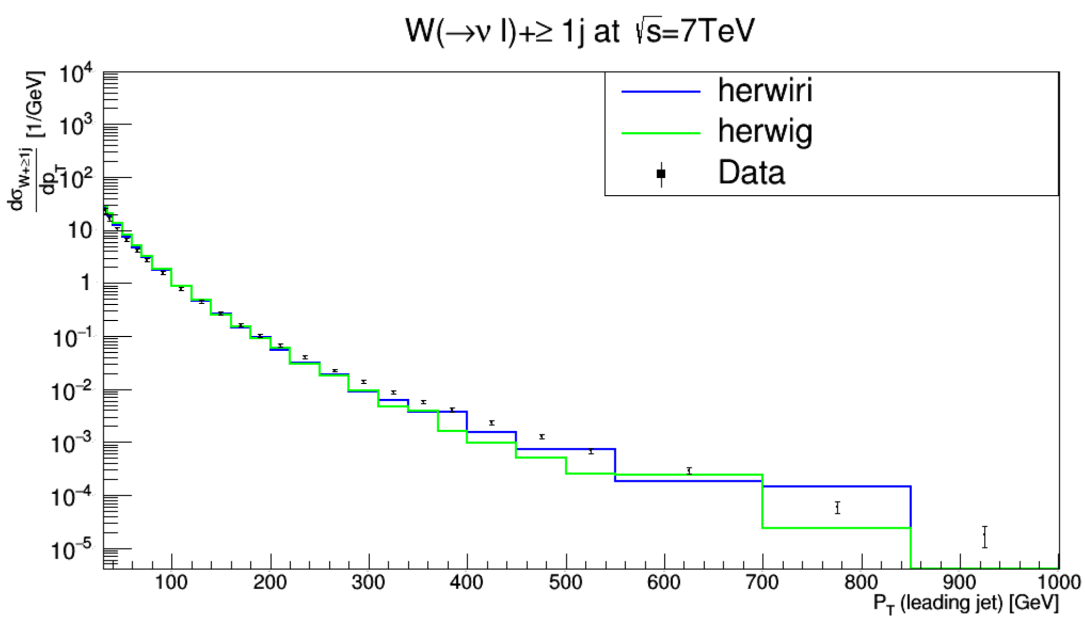

Figure 4.1: Cross section for the production of W + jets as a function of the leading jet P_T for $N_{jet} \geq 1$. The data are compared to predictions from MADGRAPH5_aMC@NLO/HERWIRI1.031 and MADGRAPH5_aMC@NLO/HERWIG6.521.

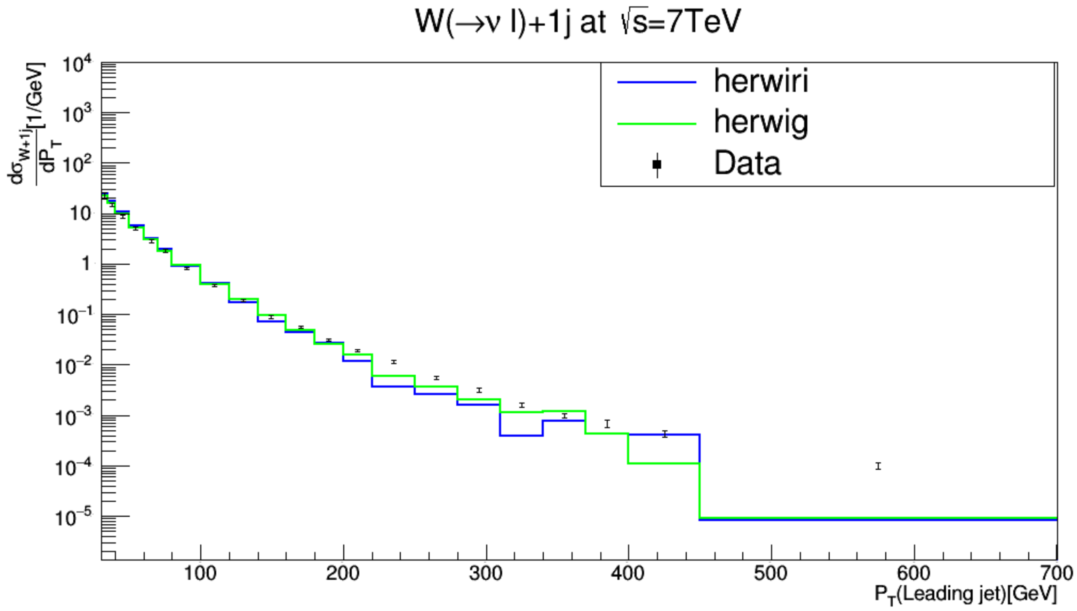

Figure 4.2: Cross section for the production of W + jets as a function of the leading jet P_T for $N_{jet} = 1$. The data are compared to predictions from MADGRAPH5_aMC@NLO/HERWIRI1.031 and MADGRAPH5_aMC@NLO/HERWIG6.521.

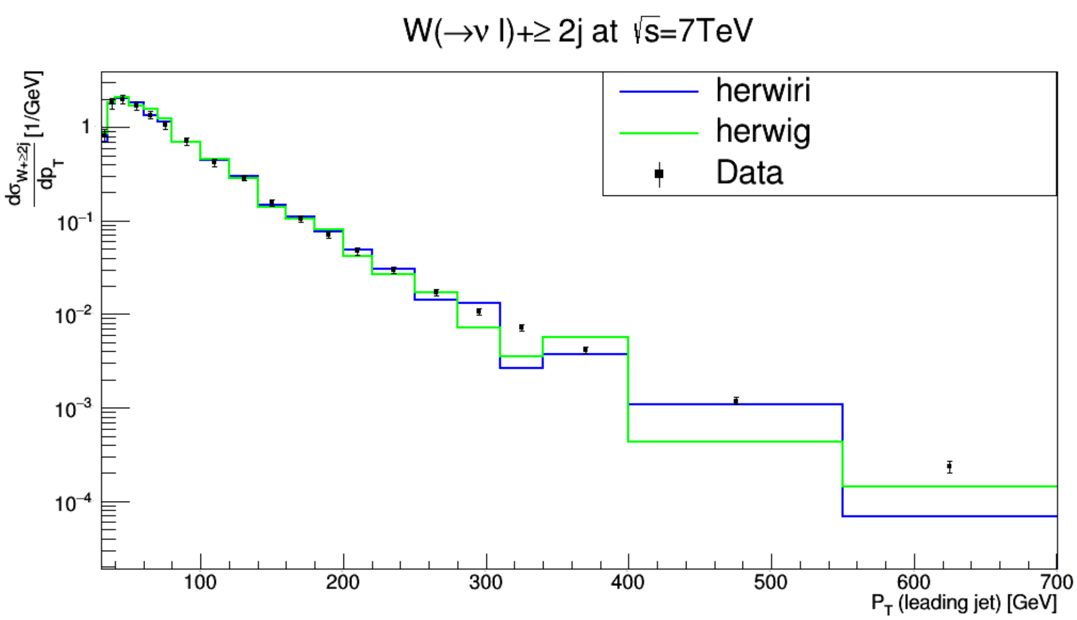

Figure 4.3: Cross section for the production of W + jets as a function of the leading jet P_T for $N_{jet} \geq 2$. The data are compared to predictions from MADGRAPH5_aMC@NLO/HERWIRI1.031 and MADGRAPH5_aMC@NLO/HERWIG6.521.

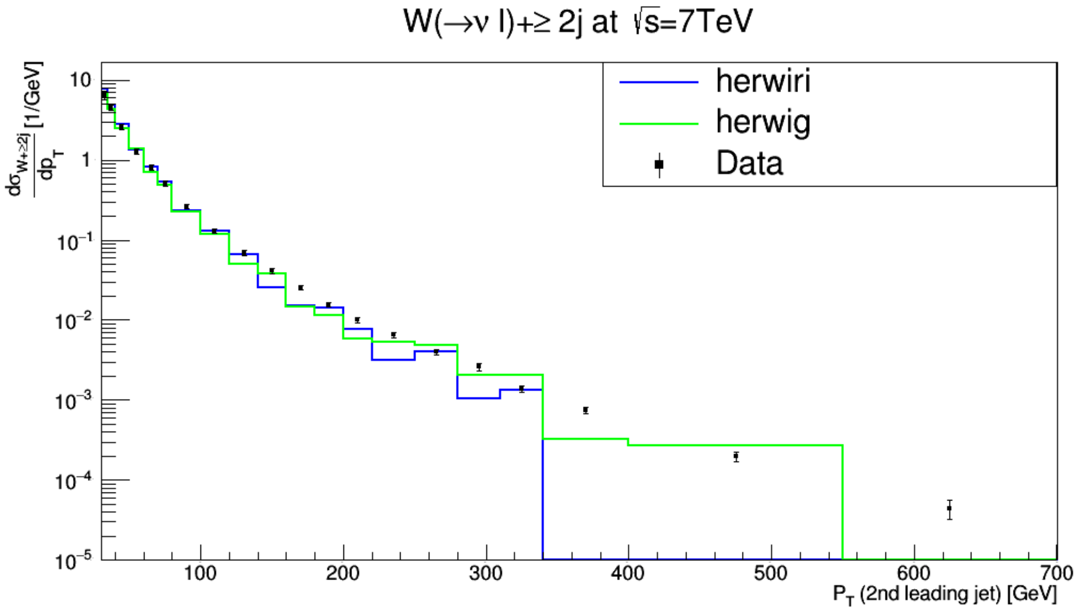

Figure 4.4: Cross section for the production of W + jets as a function of the second leading jet P_T for $N_{jet} \geq 2$. The data are compared to predictions from MADGRAPH5_aMC@NLO/HERWIRI1.031 and MADGRAPH5_aMC@NLO/HERWIG6.521.

The differential cross sections for the production of W + ≥2 jets as a function of the leading jet P_T and the second leading jet P_T are shown in Figure 4.3 and Figure 4.4, respectively. HERWIRI and HERWIG generally describe the data well for $P_T < 200$ GeV. In Figure 4.3, $\left(\frac{\chi^2}{d.o.f}\right)_{\texttt{HERWIRI}} = 1.19$ and $\left(\frac{\chi^2}{d.o.f}\right)_{\texttt{HERWIG}} = 1.49$, while for $200 < P_T < 350$ GeV it seems that they both fail to describe the data. For $250 < P_T < 550$ GeV, HERWIRI predictions overlap with the data while HERWIG either underestimates or overestimates the data. Finally, for energies higher than 550 GeV, they both underestimate the data.

Figure 4.4 shows that HERWIRI, in general, gives a better fit to the data for $P_T < 150$ GeV, where $\left(\frac{\chi^2}{d.o.f}\right)_{\texttt{HERWIRI}} = 1.06$ and $\left(\frac{\chi^2}{d.o.f}\right)_{\texttt{HERWIG}} = 1.69$. For higher P_T, in some cases HERWIRI predictions overlap with the data while HERWIG either underestimates or overestimates the data. We conclude that HERWIRI gives a better fit to the data as expected.

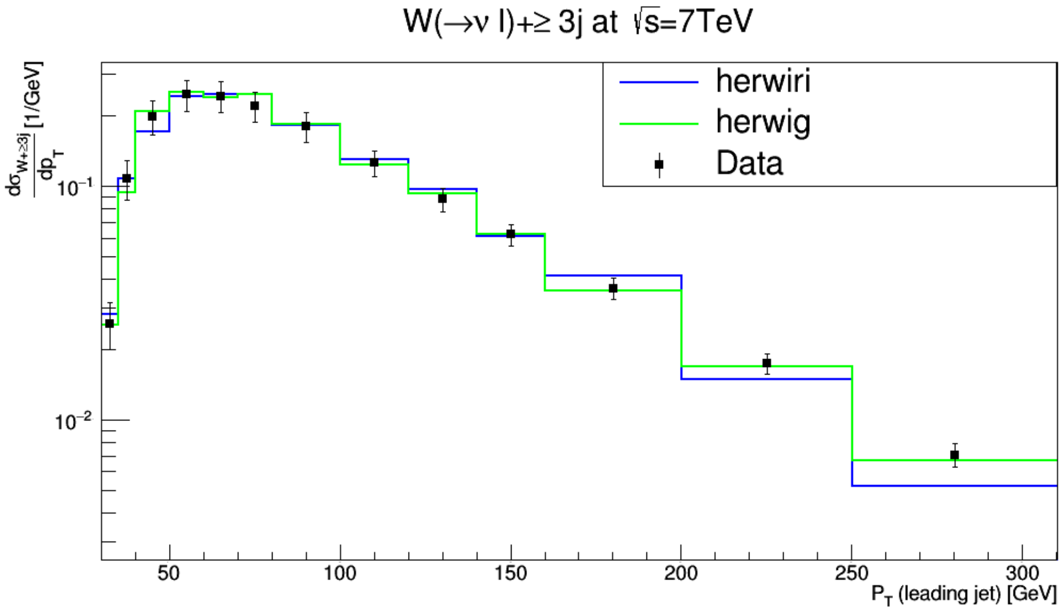

Figure 4.5: Cross section for the production of W + jets as a function of the leading jet P_T for $N_{jet} \geq 3$. The data are compared to predictions from MADGRAPH5_aMC@NLO/HERWIRI1.031 and MADGRAPH5_aMC@NLO/HERWIG6.521.

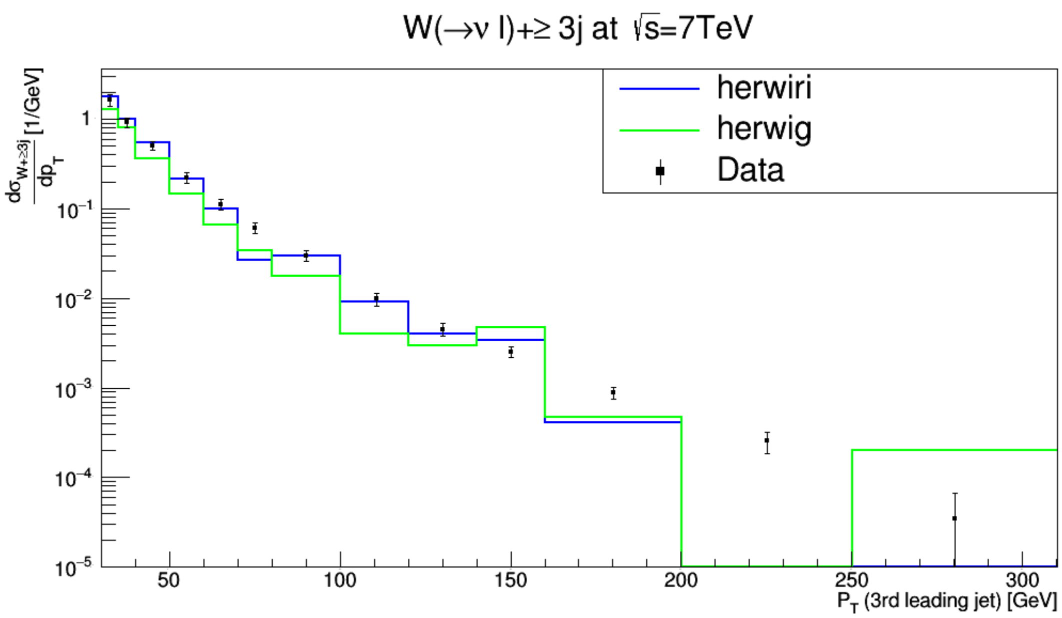

Figure 4.6: Cross section for the production of W + jets as a function of the third leading jet P_T for $N_{jet} \geq 3$. The data are compared to predictions from MADGRAPH5_aMC@NLO/HERWIRI1.031 and MADGRAPH5_aMC@NLO/HERWIG6.521.

The differential cross sections for the production of W + $\geq$3 jets as a function of the leading jet P_T and the third leading jet P_T are shown in Figure 4.5 and Figure 4.6, respectively. In Figure 4.5, for $P_T < 150$ GeV, the predictions provided by HERWIRI and HERWIG are in complete agreement with the data, where $\left(\frac{\chi^2}{d.o.f}\right)_{\texttt{HERWIRI}} = 0.27$ and $\left(\frac{\chi^2}{d.o.f}\right)_{\texttt{HERWIG}} = 0.20$. For $P_T > 150$ GeV, HERWIG gives a better fit to the data while HERWIRI underestimates the data. In Figure 4.6, HERWIRI clearly gives a better fit to the data for low P_T, where $\left(\frac{\chi^2}{d.o.f}\right)_{\texttt{HERWIRI}} = 3.32$ and $\left(\frac{\chi^2}{d.o.f}\right)_{\texttt{HERWIG}} = 9.44$. For large P_T, in almost all cases HERWIRI and HERWIG predictions underestimate the data.

In general, one could conclude that the predictions provided by HERWIRI give a better fit to the data for soft P_T.

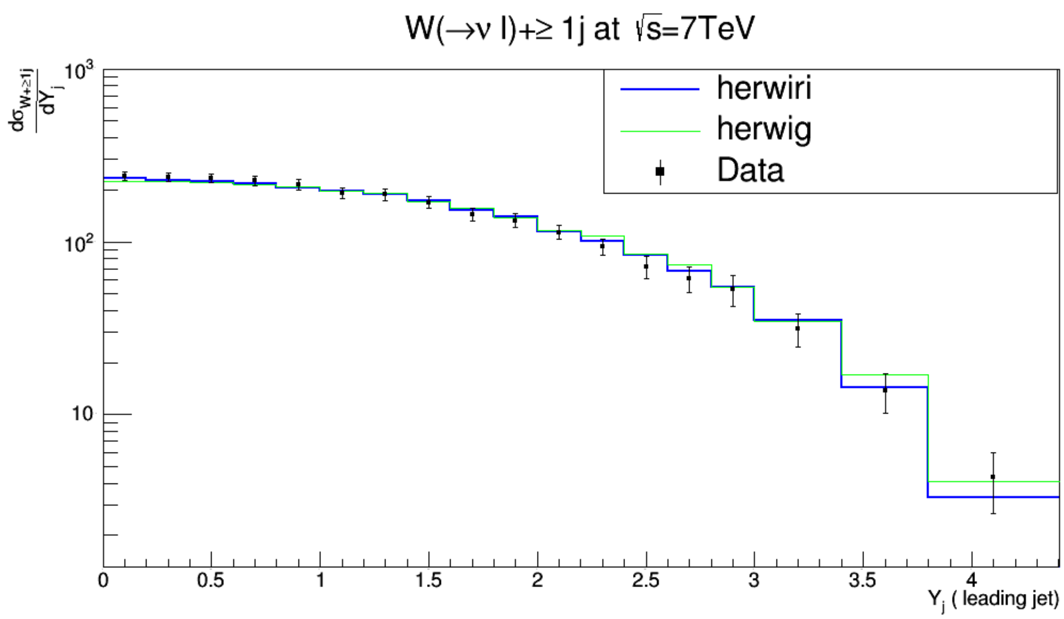

Figure 4.7: Cross section for the production of W + jets as a function of the leading jet Y_j for $N_{jet} \geq 1$. The data are compared to predictions from MADGRAPH5_aMC@NLO/HERWIRI1.031 and MADGRAPH5_aMC@NLO/HERWIG6.521.

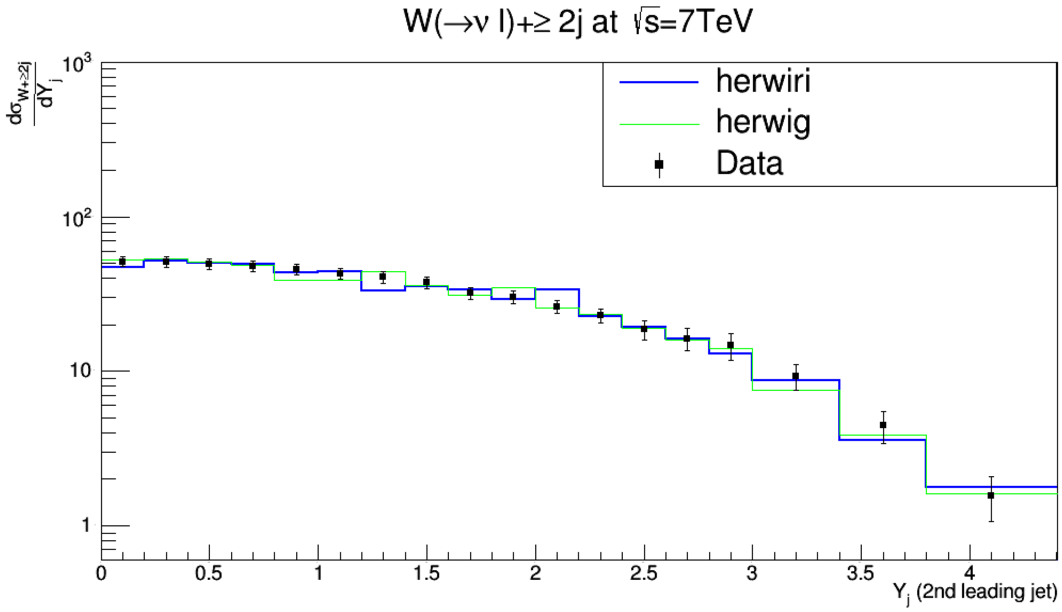

Figure 4.8: Cross section for the production of W + jets as a function of the second leading jet Y_j for $N_{jet} \geq 2$. The data are compared to predictions from MADGRAPH5_aMC@NLO/HERWIRI1.031 and MADGRAPH5_aMC@NLO/HERWIG6.521.

4.2.2 Rapidity Distributions

The differential cross sections for the production of W + ≥1 jet as a function of the leading jet Y_j are shown in Figure 4.7. The predictions provided by HERWIRI and HERWIG are generally in agreement with the data, although in three cases HERWIRI predictions overlap with the data while the HERWIG predictions either underestimate or overestimate the data. We clearly conclude that HERWIRI gives a better fit to the data with $\left(\frac{\chi^2}{d.o.f}\right)_{\texttt{HERWIRI}} = 0.35$ and $\left(\frac{\chi^2}{d.o.f}\right)_{\texttt{HERWIG}} = 0.70$.

The differential cross sections for the production of W + ≥2 jets as a function of the second leading jet Y_j are shown in Figure 4.8. The results provided by HERWIRI and HERWIG overlap with the data in almost all cases. In two cases, the HERWIRI predictions overlap with the data and in two cases the HERWIG results overlap with the data while HERWIRI predictions either underestimate or overestimate the data: $\left(\frac{\chi^2}{d.o.f}\right)_{\texttt{HERWIRI}} = 1.01$ and $\left(\frac{\chi^2}{d.o.f}\right)_{\texttt{HERWIG}} = 0.63$.

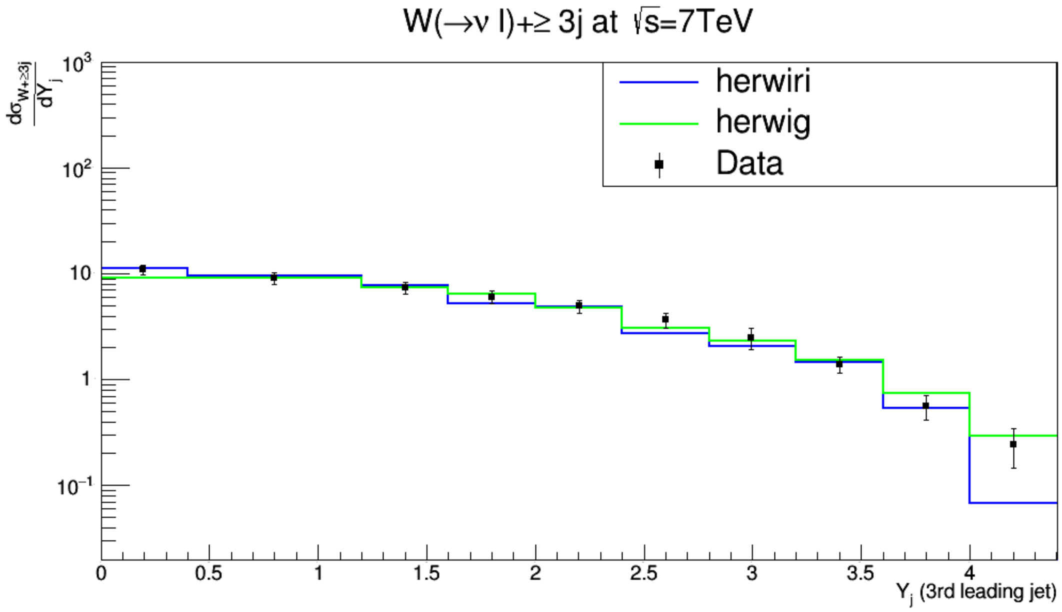

Figure 4.9: Cross section for the production of W + jets as a function of the third leading jet Y_j for $N_{jet} \geq 3$. The data are compared to predictions from MADGRAPH5_aMC@NLO/HERWIRI1.031 and MADGRAPH5_aMC@NLO/HERWIG6.521.

The differential cross sections for the production of W + $\geq$ 3 jets as a function of the third leading jet Y_j are shown in Figure 4.9. For $Y_j < 3.6$, with the exception of one case in which only the HERWIG prediction overlaps with the data, HERWIRI and HERWIG predictions are in agreement with the data. For $Y_j > 3.6$, in one case HERWIRI overlaps with the data while HERWIG overestimates the data, and in the other case HERWIG overlaps with the data while HERWIRI underestimates the data: $\left(\frac{\chi^2}{d.o.f}\right)_{\texttt{HERWIRI}} = 1.05$ and $\left(\frac{\chi^2}{d.o.f}\right)_{\texttt{HERWIG}} = 0.43$.

4.2.3 Dijet Angular Variables, Invariant Mass, Separation

In this subsection the differential cross sections are shown as functions of the difference in azimuthal angle ($\Delta\phi_{j_1,j_2}$), the difference in the rapidty ($\Delta Y_{j_1,j_2}$), the angular separation ($\Delta R_{j_1,j_2}$) and the dijet invariant mass (m_{j_1,j_2}), compared to the data. We define the above variables as follows

$$\Delta Y_{j_1,j_2} = |Y_{j_1} - Y_{j_2}|, \tag{4.4}$$

$$\Delta\phi_{j_1,j_2} = |\phi_{j_1} - \phi_{j_2}|, \tag{4.5}$$

$$\Delta R_{j_1,j_2} = \sqrt{(\Delta\phi_{j_1,j_2})^2 + \Delta\eta_{j_1,j_2})^2}, \tag{4.6}$$

$$m_{j_1,j_2} = \sqrt{(E_{j_1} + E_{j_2})^2 - (\vec{P}_{j_1} + \vec{P}_{j_2})^2} = \sqrt{m_{j_1}^2 + m_{j_2}^2 + 2(E_{j_1}E_{j_2} - \vec{P}_{j_1}\cdot\vec{P}_{j_2})}. \tag{4.7}$$

We note that in Eq. (4.6), η_{j_1,j_2} is the difference in rapidity of the first and second leading jets. The ith jet is defined as

$$P^{\mu}_{\textit{ith-jet}} = (E_{j_1}, \vec{P}_{\textit{ith-jet}}) \tag{4.8}$$

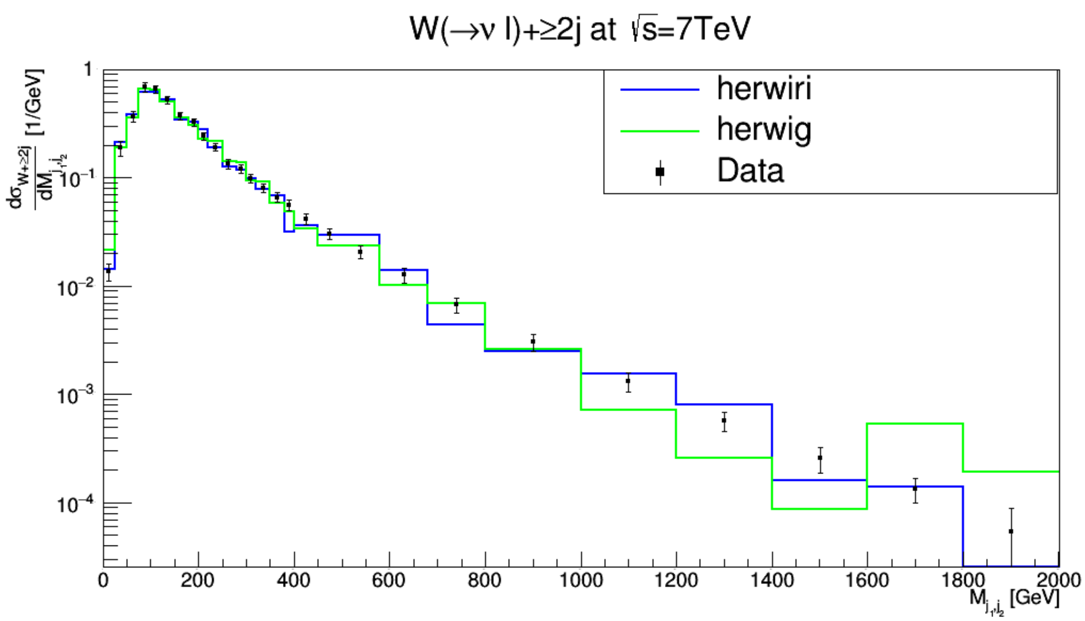

Figure 4.10: Cross section for the production of W + jets as a function of the di-jet invariant mass m_{j_1,j_2} between the two leading jets for $N_{jet} \geq 2$. The data are compared to predictions from MADGRAPH5_aMC@NLO/HERWIRI1.031 and MADGRAPH5_aMC@NLO/HERWIG6.521.

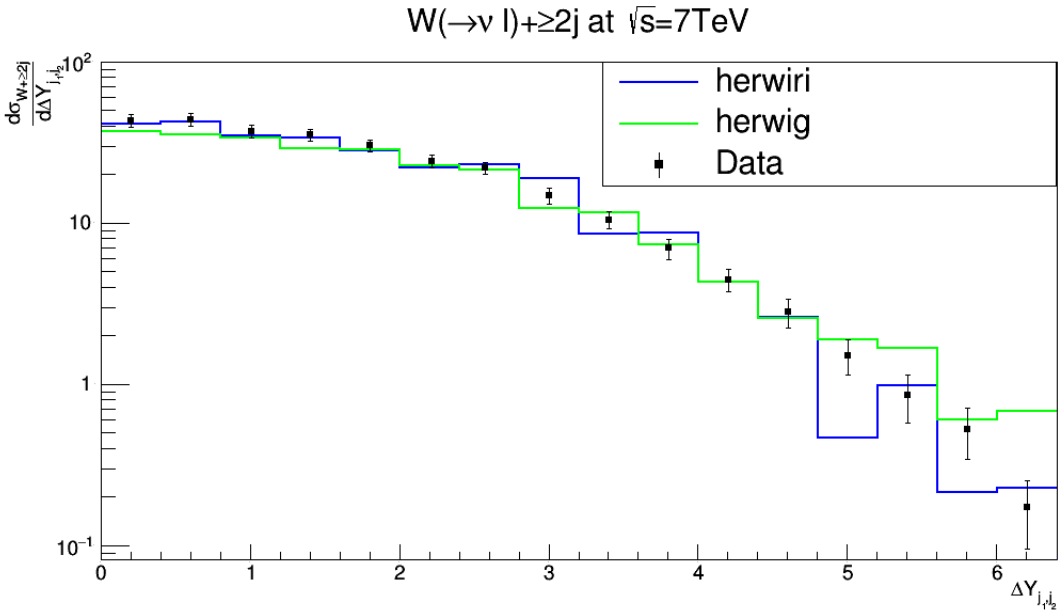

Figure 4.11: Cross section for the production of W + jets as a function of the difference in the rapidity between the two leading jets for $N_{jet} \geq 2$. The data are compared to predictions from MADGRAPH5_aMC@NLO/HERWIRI1.031 and MADGRAPH5_aMC@NLO/HERWIG6.521.

The differential cross sections for the production of W + ≥2 jets as a function of the dijet invariant mass between the two leading jets are shown in Figure 4.10. The cross sections are fairly well modeled by HERWIRI for $m_{j_1,j_2} < 400$ GeV. For $m_{j_1,j_2} > 400$ GeV there are cases in which HERWIRI gives a good fit to the data while HERWIG predictions either underestimate or overestimate the data. In comparison, predictions provided by HERWIRI describe the data better than HERWIG: $\left(\frac{\chi^2}{d.o.f}\right)_{\texttt{HERWIRI}} = 2.19$ and $\left(\frac{\chi^2}{d.o.f}\right)_{\texttt{HERWIG}} = 2.68$.

The differential cross sections for the production of W + ≥2 jets as a function of the difference in the rapidity between the two leading jets are shown in Figure 4.11. For $\Delta Y_{j_1 j_2} < 3$ the predictions provided by HERWIRI give a better fit to the data. For $3 < \Delta Y_{j_1 j_2} < 4$, HERWIG results provide a better description of the data: $\left(\frac{\chi^2}{d.o.f}\right)_{\texttt{HERWIRI}} = 2.08$ and $\left(\frac{\chi^2}{d.o.f}\right)_{\texttt{HERWIG}} = 4.77$.

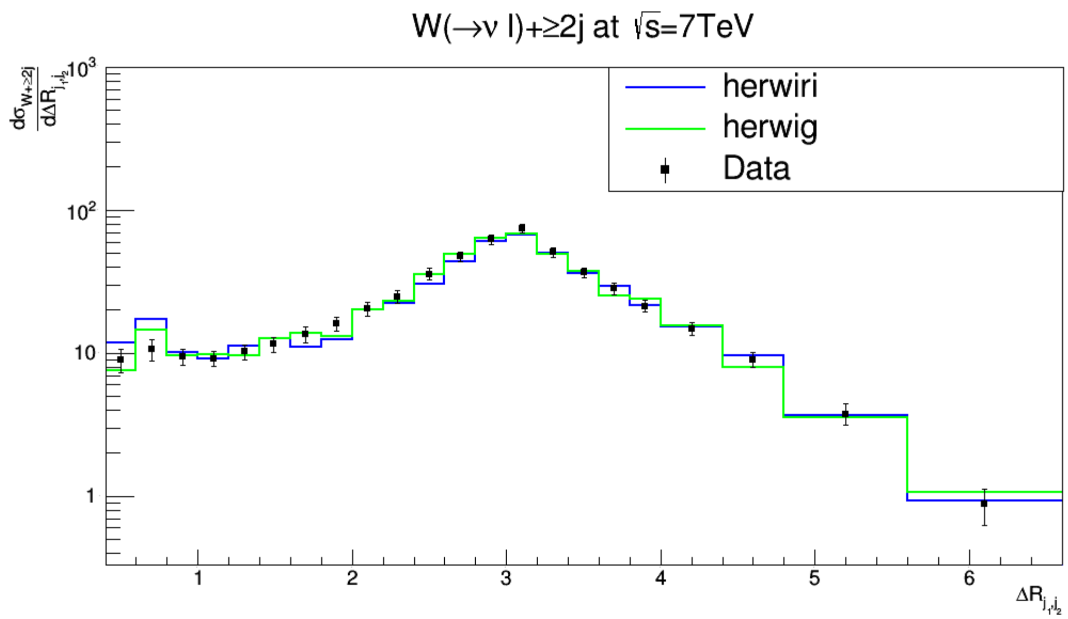

Figure 4.12: Cross section for the production of W + jets as a function of the angular separation between the two leading jets for $N_{jet} \geq 2$. The data are compared to predictions from MADGRAPH5_aMC@NLO/HERWIRI1.031 and MADGRAPH5_aMC@NLO/HERWIG6.521.

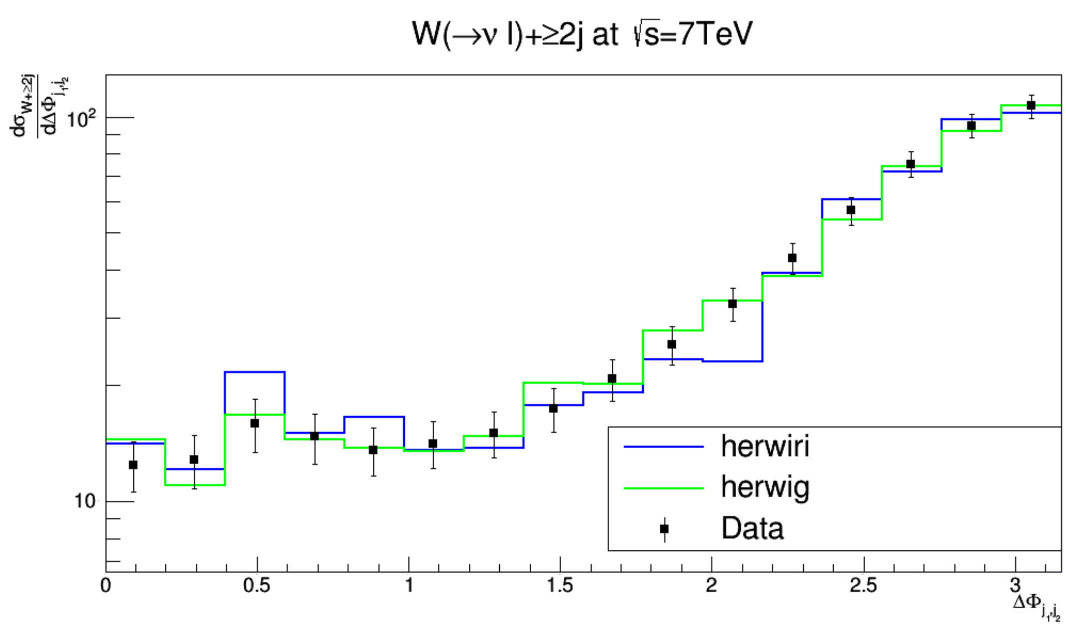

Figure 4.13: Cross section for the production of W + jets as a function of the difference in the azimuthal angle between the two leading jets for $N_{jet} \geq 2$. The data are compared to predictions from MADGRAPH5_aMC@NLO/HERWIRI1.031 and MADGRAPH5_aMC@NLO/HERWIG6.521.

The differential cross sections for the production of W + ≥2 jets as a function of the angular separation between the two leading jets are shown in Figure 4.12. For $\Delta R_{j_1,j_2} > 3$, the cross sections are fairly well modeled by the predictions of HERWIRI and HERWIG. For $\Delta R_{j_1,j_2} < 3$, in two cases the prediction provided by either of them fail to describe the data; in most cases they both give a satisfactory fit to the data: $\left(\frac{\chi^2}{d.o.f}\right)_{\texttt{HERWIRI}} = 1.59$ and $\left(\frac{\chi^2}{d.o.f}\right)_{\texttt{HERWIG}} = 0.78$.

The differential cross sections for the production of W + ≥2 jets as a function of the azimuthal angle between the two leading jets are shown in Figure 4.13. For $\Delta\phi_{j_1,j_2} > 2.2$ and $1 < \Delta\phi_{j_1,j_2} < 1.4$, the cross sections are well modeled by HERWIRI and HERWIG: $\left(\frac{\chi^2}{d.o.f}\right)_{\texttt{HERWIRI}} = 1.46$ and $\left(\frac{\chi^2}{d.o.f}\right)_{\texttt{HERWIG}} = 0.49$.

4.2.4 Scalar Sum H_T

In this subsection we will study the W + jets cross sections as a function of H_T, the summed scalar P_T of all identified object in the final state. For example, for a prototypical process

$$pp \to l + \nu_l + j_1 + j_2, \tag{4.9}$$

we define H_T as follows

$$H_T = P_T(l) + P_T(\nu_l) + P_T(j_1) + P_T(j_2), \tag{4.10}$$

where $l = e, \mu$.

The differential cross sections as a function of H_T are shown in Figure 4.14, Figure 4.15, Figure 4.16, Figure 4.17, Figure 4.18, and Figure 4.19 respectively. We will study the W + jets cross sections as a function of H_T for low H_T. We will see in some cases HERWIRI predictions are in agreement with the data and in some cases HERWIG predictions give a better fit to the data. In general, a better agreement is provided for the lower jet multiplicities, e.g. W + 1 jet and $W + \ \geq 1$ jet.

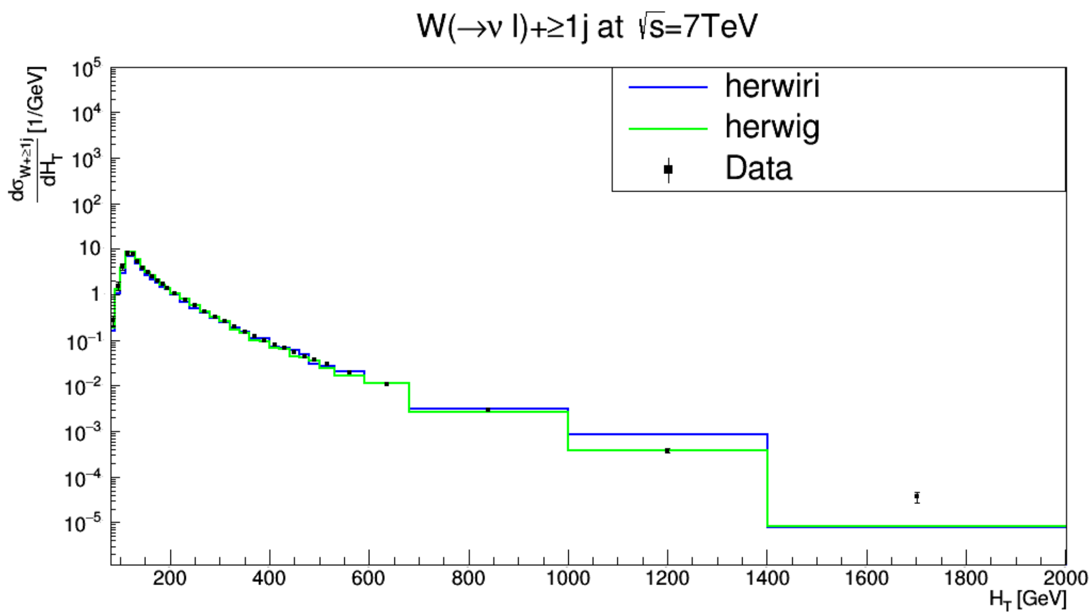

Figure 4.14: Cross section for the production of W + jets as a function of the scalar sum H_T for $N_{jet} \geq 1$. The data are compared to predictions from MADGRAPH5_aMC@NLO/HERWIRI1.031 and MADGRAPH5_aMC@NLO/HERWIG6.521.

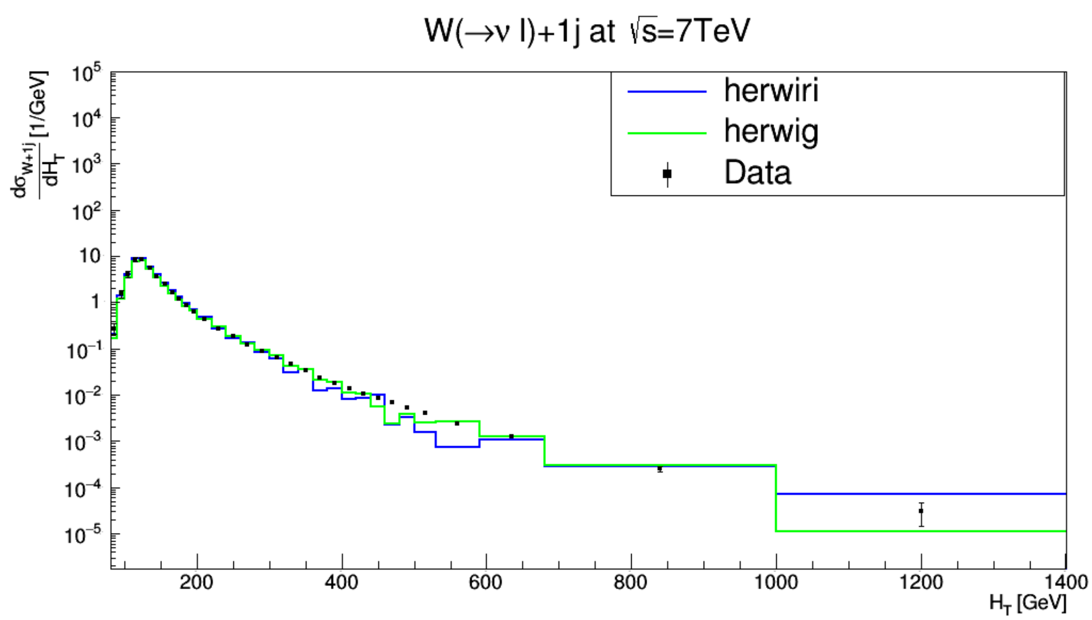

Figure 4.15: Cross section for the production of W + jets as a function of the scalar sum H_T for $N_{jet} = 1$. The data are compared to predictions from MADGRAPH5_aMC@NLO/HERWIRI1.031 and MADGRAPH5_aMC@NLO/HERWIG6.521.

The differential cross sections for the production of W + ≥1 jet as a function of the scalar sum H_T are shown in Figure 4.14. For $H_T < 100$ GeV, HERWIG predictions are in agreement with data while the predictions provided by HERWIRI underestimate the data: $\left(\frac{\chi^2}{d.o.f}\right)_{\texttt{HERWIRI}} = 2.41$ and $\left(\frac{\chi^2}{d.o.f}\right)_{\texttt{HERWIG}} = 1.41$. For $100 < H_T < 1000$ GeV, the differential cross sections are fairly well modeled by the HERWIRI and HERWIG predictions.

The differential cross sections for the production of W + 1 jet as a function of the scalar sum H_T are shown in Figure 4.15. For the case $H_T < 100$ GeV, HERWIG predictions are in agreement with the data while the predictions provided by HERWIRI overestimate the data: $\left(\frac{\chi^2}{d.o.f}\right)_{\texttt{HERWIRI}} = 2.07$ and $\left(\frac{\chi^2}{d.o.f}\right)_{\texttt{HERWIG}} = 0.74$. For $100 < H_T < 250$ GeV, the differential cross sections are fairly well modeled by the HERWIRI and HERWIG predictions. For $250 < H_T < 400$ GeV, the HERWIG predictions are in better agreement with the data. Finally, for higher energies, the predictions provided by HERWIRI and HERWIG tend to be either above or below the data.

The differential cross sections for the production of W + ≥2 jets as a function of the scalar sum H_T are shown in Figure 4.16. The predictions provided by HERWIRI and HERWIG underestimate the data at $H_T < 200$ GeV, with $\left(\frac{\chi^2}{d.o.f}\right)_{\texttt{HERWIRI}} = 3.10$ and $\left(\frac{\chi^2}{d.o.f}\right)_{\texttt{HERWIG}} = 1.32$. In the $200 < H_T < 250$ GeV range, HERWIG gives a better fit to the data; in the $250 < H_T < 350$ GeV range, HERWIRI predictions are in better agreement with the data. For large H_T, HERWIRI predictions either are in agreement with the data or have less discrepancy with the data than the results provided by HERWIG, as Figure 4.16 reveals.

The differential cross sections for the production of W + 2 jets as a function of the scalar sum H_T are shown in Figure 4.17. HERWIRI and HERWIG seem to be unable to provide a good fit for the data at $H_T < 200$ GeV where they underestimate the data: $\left(\frac{\chi^2}{d.o.f}\right)_{\texttt{HERWIRI}} = 4.85$ and $\left(\frac{\chi^2}{d.o.f}\right)_{\texttt{HERWIG}} = 3.16$.

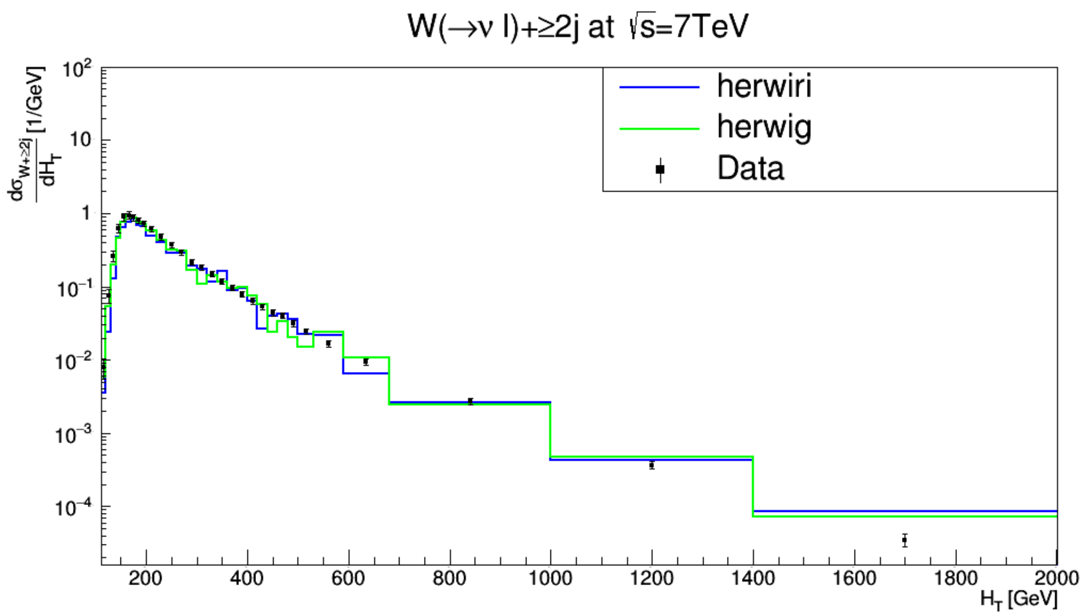

Figure 4.16: Cross section for the production of W + jets as a function of the scalar sum H_T for $N_{jet} \geq 2$. The data are compared to predictions from MADGRAPH5_aMC@NLO/HERWIRI1.031 and MADGRAPH5_aMC@NLO/HERWIG6.521.

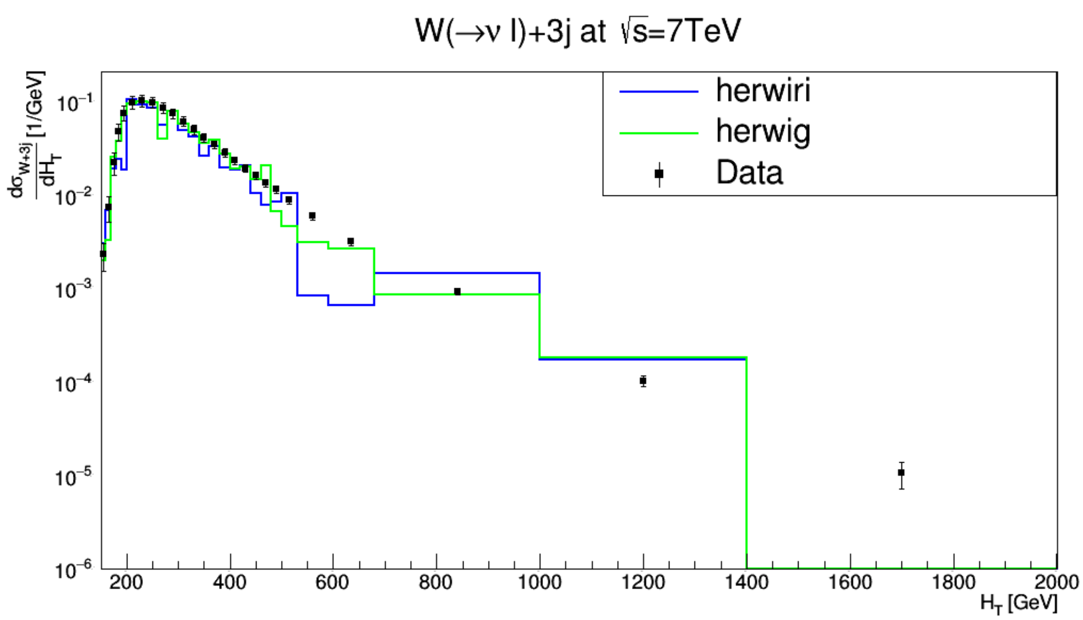

Figure 4.19: Cross section for the production of W + jets as a function of the scalar sum H_T for $N_{jet} = 3$. The data are compared to predictions from MADGRAPH5_aMC@NLO/HERWIRI1.031 and MADGRAPH5_aMC@NLO/HERWIG6.521.

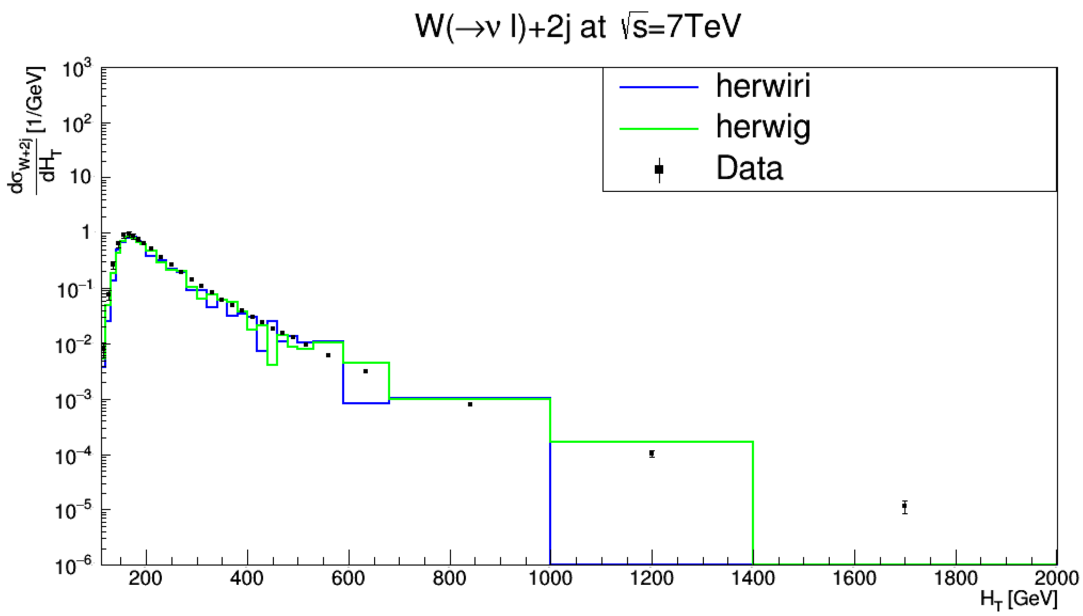

Figure 4.17: Cross section for the production of W + jets as a function of the scalar sum H_T for $N_{jet} = 2$. The data are compared to predictions from MADGRAPH5_aMC@NLO/HERWIRI1.031 and MADGRAPH5_aMC@NLO/HERWIG6.521.

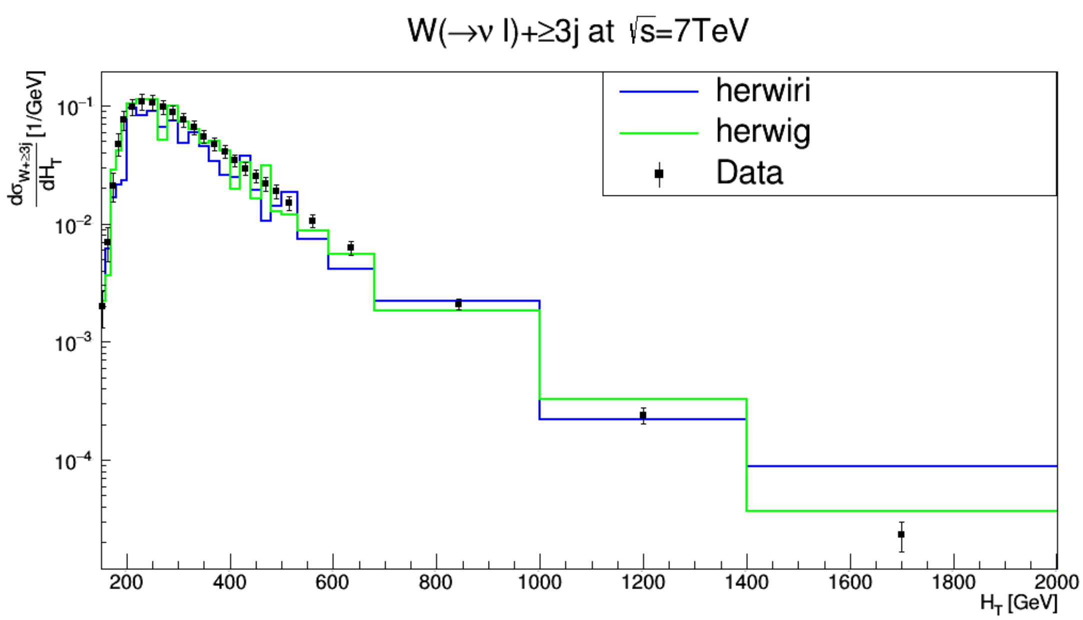

Figure 4.18: Cross section for the production of W + jets as a function of the scalar sum H_T for $N_{jet} \geq 3$. The data are compared to predictions from MADGRAPH5_aMC@NLO/HERWIRI1.031 and MADGRAPH5_aMC@NLO/HERWIG6.521.

At energies around $200 < H_T < 250$ GeV, HERWIRI and HERWIG predictions overlap fairly well with the data. In general, we conclude that the discrepancy of the predictions provided by HERWIRI is less than that of HERWIG.

The differential cross sections for the production of W + ≥3 jets as a function of the scalar sum H_T are shown in Figure 4.18. A good fit is provided by the HERWIG predictions for $H_T < 200$ GeV, where $\left(\frac{\chi^2}{d.o.f}\right)_{\texttt{HERWIRI}} = 4.01$ and $\left(\frac{\chi^2}{d.o.f}\right)_{\texttt{HERWIG}} = 1.84$. The HERWIG predictions overlap fairly well with the data for $200 < H_T < 400$ GeV. For the higher range $650 < H_T < 1000$ GeV, the HERWIRI predictions are in agreement with the data while HERWIG either underestimates or overestimates the data.

The differential cross sections for the production of W + 3 jets as a function of the scalar sum H_T are shown in Figure 4.19. HERWIG gives a better fit to the data for $H_T < 200$, with $\left(\frac{\chi^2}{d.o.f}\right)_{\texttt{HERWIRI}} = 3.75$ and $\left(\frac{\chi^2}{d.o.f}\right)_{\texttt{HERWIG}} = 2.34$. In general, the predictions provided by HERWIG give a better fit to the data.

4.2.5 Scalar Sum S_T

In this subsection, we study the behavior of W + jets cross sections as a function of the scalar sum S_T, where S_T is defined as the summed scalar P_T of all the jets in the event:

$$S_T = \sum_{i=1}^{Njet} |P_T(i)|, \tag{4.11}$$

where $|P_T(i)|$ is the transverse momentum of the ith jet and $Njet$ is the maximum number of jets in each event. The differential cross sections as a function of H_T are shown in Figure 4.20, Figure 4.21, Figure 4.22, Figure 4.23, and Figure 4.24 respectively. We will study the W + jets cross sections as a function of S_T for low S_T. We will see in some cases HERWIRI predictions are in agreement with the data and in some cases HERWIG predictions give a better fit to the data. In general, a better agreement is provided for the lower jet multiplicities, e.g. W + 1 jet and $W+\ \geq 1$ jet.

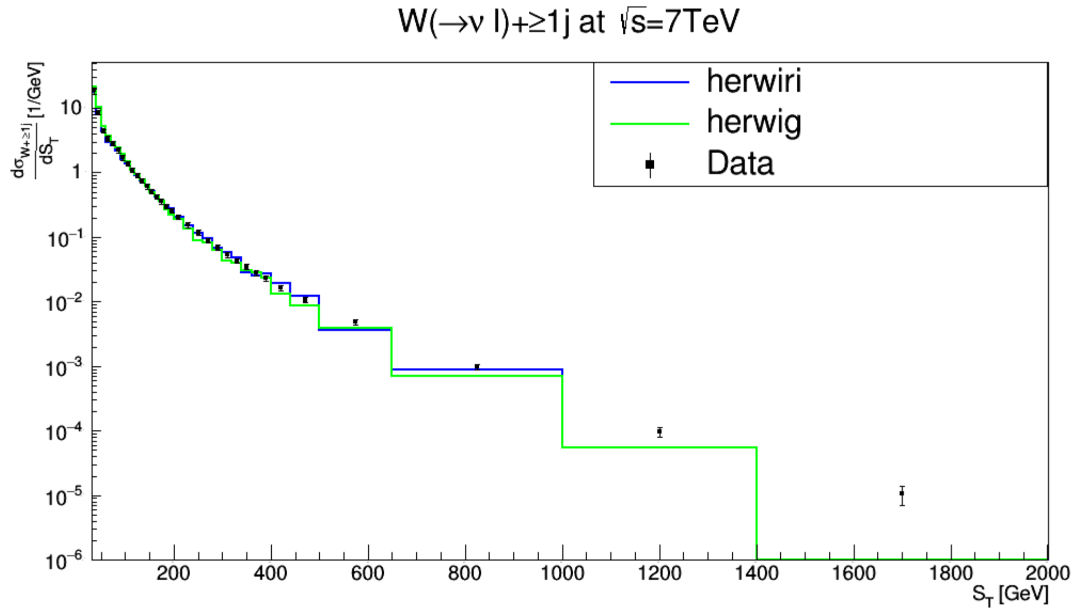

Figure 4.20: Cross section for the production of W + jets as a function of the scalar sum S_T for $N_{jet} \geq 1$. The data are compared to predictions from MADGRAPH5_aMC@NLO/HERWIRI1.031 and MADGRAPH5_aMC@NLO/HERWIG6.521.

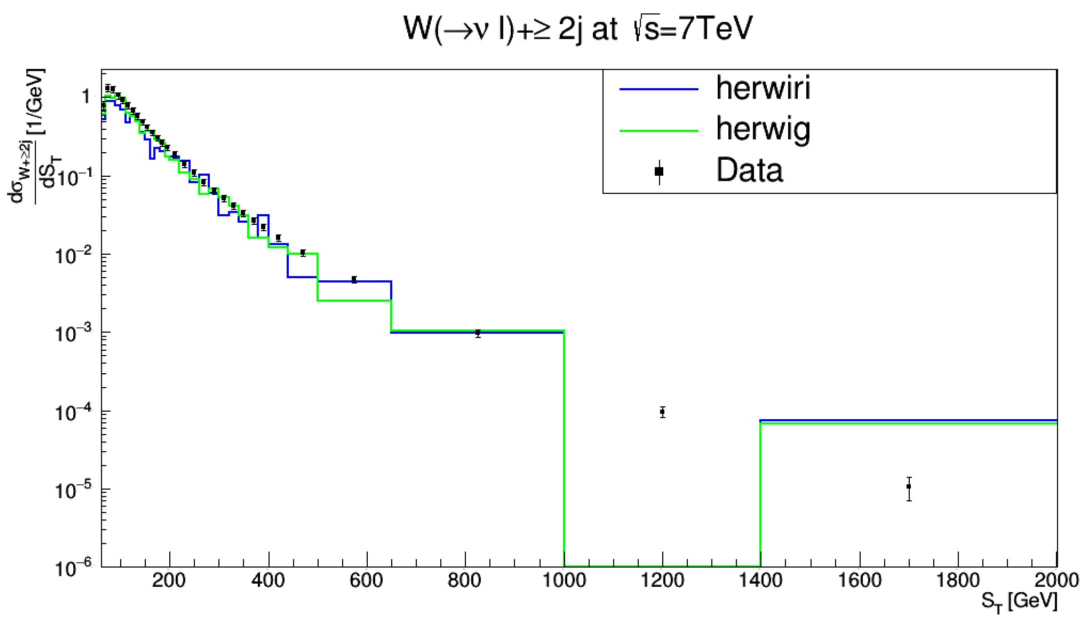

Figure 4.21: Cross section for the production of W + jets as a function of the scalar sum S_T for $N_{jet} \geq 2$. The data are compared to predictions from MADGRAPH5_aMC@NLO/HERWIRI1.031 and MADGRAPH5_aMC@NLO/HERWIG6.521.

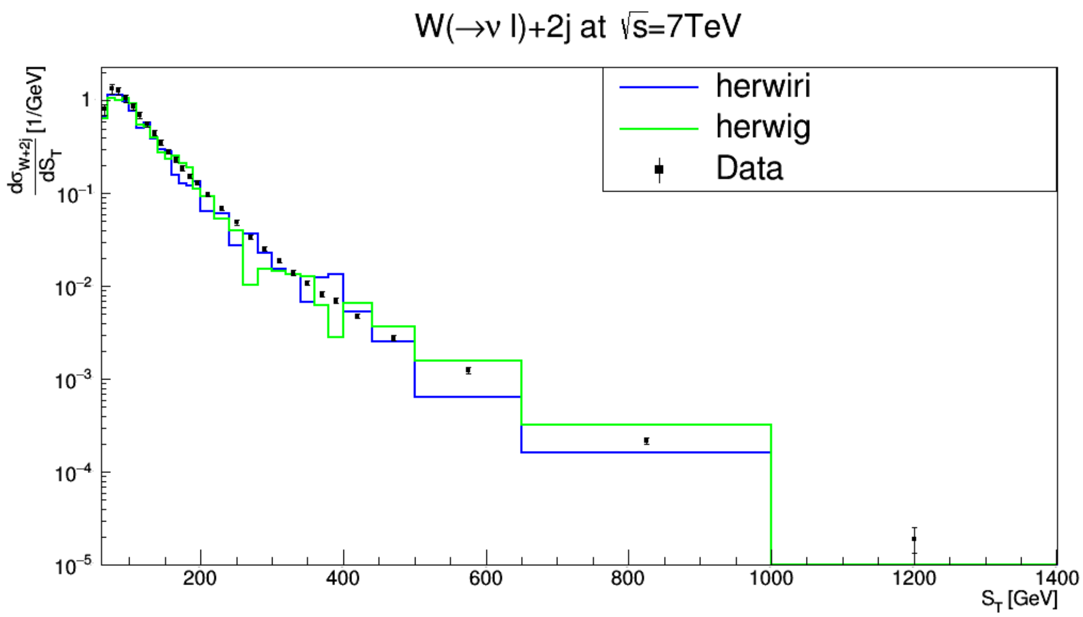

Figure 4.22: Cross section for the production of W + jets as a function of the scalar sum S_T for $N_{jet} = 2$. The data are compared to predictions from MADGRAPH5_aMC@NLO/HERWIRI1.031 and MADGRAPH5_aMC@NLO/HERWIG6.521.

The differential cross sections for the production of W + ≥1 jet as a function of the scalar sum S_T are shown in Figure 4.20. A good fit to the data is provided by HERWIRI at $S_T < 100$ GeV while HERWIG predictions lie above the data: $\left(\frac{\chi^2}{d.o.f}\right)_{\texttt{HERWIRI}} = 0.35$ and $\left(\frac{\chi^2}{d.o.f}\right)_{\texttt{HERWIG}} = 0.81$. For $100 < S_T < 400$ GeV, the HERWIRI and HERWIG predictions are in very good agreement with the data. For higher values of S_T, HERWIRI and HERWIG predictions lie below the data.

The differential cross sections for the production of W + ≥2 jets as a function of the scalar sum S_T are shown in Figure 4.21. For $S_T < 100$ GeV, The predictions provided by HERWIRI and HERWIG lie above the data: $\left(\frac{\chi^2}{d.o.f}\right)_{\texttt{HERWIRI}} = 12.07$ and $\left(\frac{\chi^2}{d.o.f}\right)_{\texttt{HERWIG}} = 3.50$. For medium energies, the HERWIG prediction gives a fair fit to the data. For large energies, HERWIG gives a good fit to the data.

The differential cross sections for the production of W + 2 jets as a function of the scalar sum S_T are shown in Figure 4.22. Good agreement is provided by the predictions of HERWIG at $S_T < 150$ GeV, where $\left(\frac{\chi^2}{d.o.f}\right)_{\texttt{HERWIRI}} = 5.47$ and $\left(\frac{\chi^2}{d.o.f}\right)_{\texttt{HERWIG}} = 4.19$. HERWIG in general gives either a better fit to the data or less discrepancy in comparison with HERWIRI.

In Figure 4.23, $\left(\frac{\chi^2}{d.o.f}\right)_{\texttt{HERWIRI}} = 4.31$ and $\left(\frac{\chi^2}{d.o.f}\right)_{\texttt{HERWIG}} = 0.70$. Figure 4.24 shows the cross sections for the production of W + jet as a function of the exclusive jet multiplicity. The predictions provided by HERWIG give a better fit to the data, with $\left(\frac{\chi^2}{d.o.f}\right)_{\texttt{HERWIRI}} = 7.31$ and $\left(\frac{\chi^2}{d.o.f}\right)_{\texttt{HERWIG}} = 1.08$.

It is clear in some cases HERWIRI predictions are in agreement with the data and in some cases HERWIG predictions give a better fit to the data. In general, a better agreement is provided for the lower jet multiplicities, e.g. W + 1 jet and $W + \geq 1$ jet.

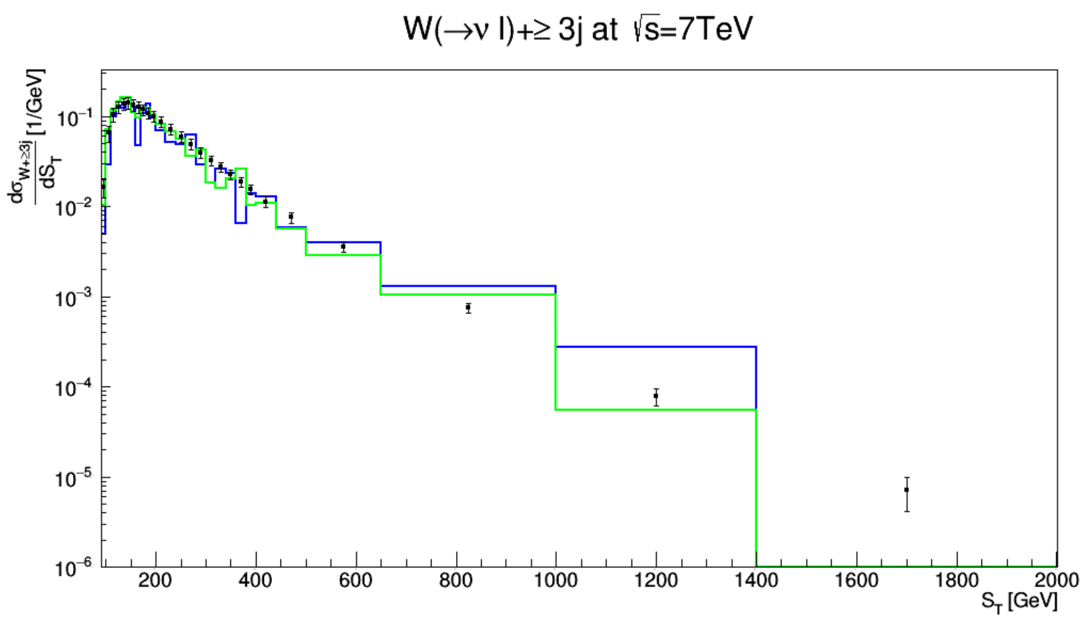

Figure 4.23: Cross section for the production of W + jets as a function of the scalar sum S_T for $N_{jet} \geq 3$. The data are compared to predictions from MADGRAPH5_aMC@NLO/HERWIRI1.031 and MADGRAPH5_aMC@NLO/HERWIG6.521.

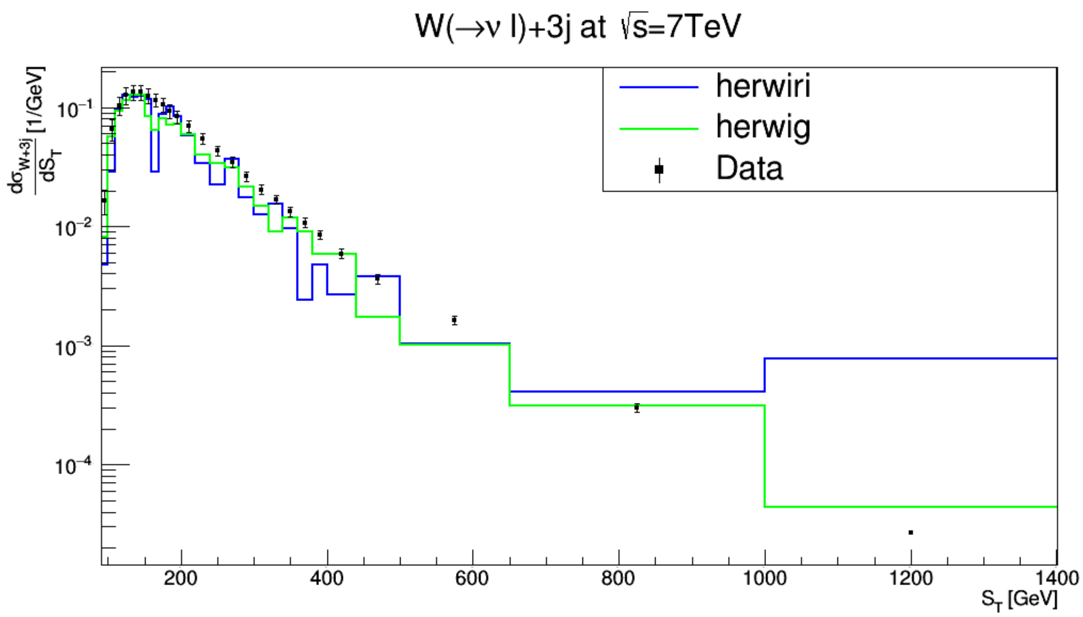

Figure 4.24: Cross section for the production of W + jets as a function of the scalar sum S_T for $N_{jet} = 3$. The data are compared to predictions from MADGRAPH5_aMC@NLO/HERWIRI1.031 and MADGRAPH5_aMC@NLO/HERWIG6.521.

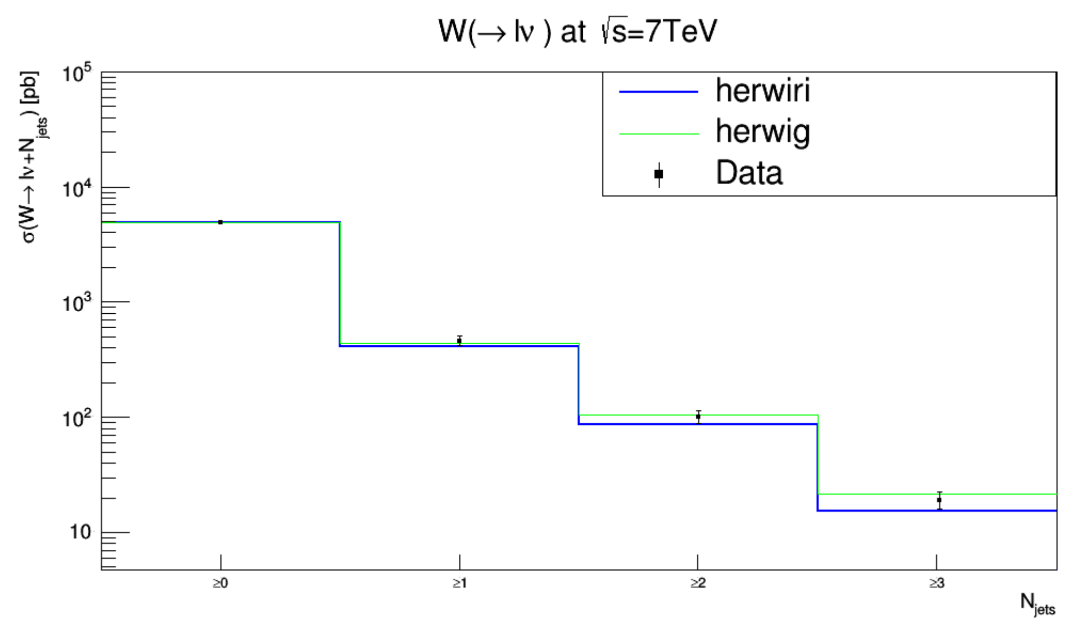

Figure 4.25: Cross section for the production of W + jets as a function of the inclusive jet multiplicity. The data are compared to predictions from MADGRAPH5_aMC@NLO/HERWIRI1.031 and MADGRAPH5_aMC@NLO/HERWIG6.521.

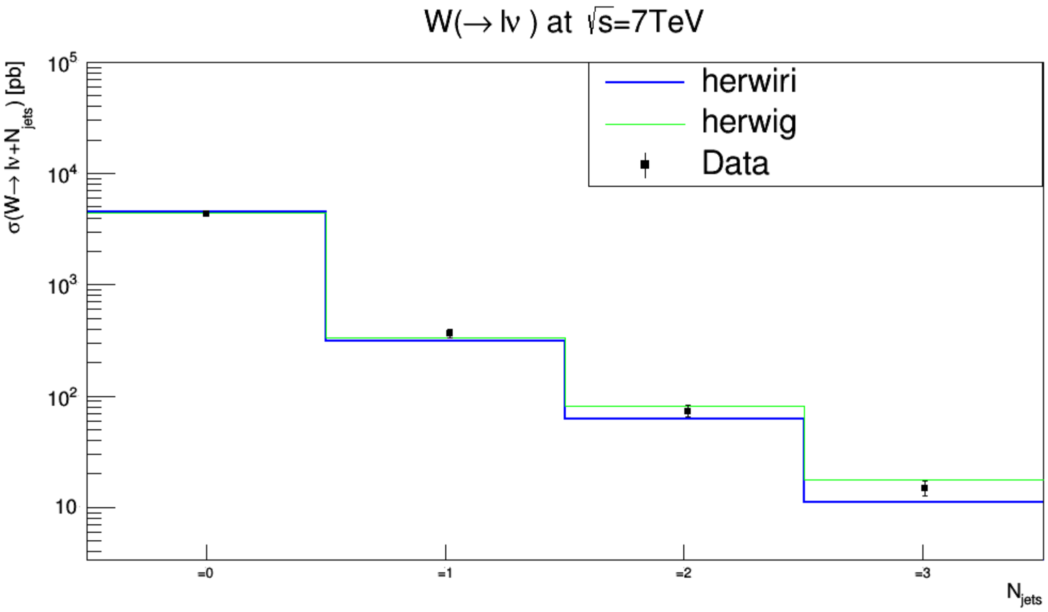

Figure 4.26: Cross section for the production of W + jets as a function of the exclusive jet multiplicity. The data are compared to predictions from MADGRAPH5_aMC@NLO/HERWIRI1.031 and MADGRAPH5_aMC@NLO/HERWIG6.521.

4.2.6 Cross Sections

The cross sections for $W \to l + \nu_l$ production as functions of the inclusive and exclusive jet multiplicity are shown in Figure 4.25 and Figure 4.26. Figure 4.25 shows the cross sections for the production of W + jet as a function of the inclusive jet multiplicity. A good fit is provided by HERWIRI and HERWIG for $N_{jet} \geq 1$ and $N_{jet} \geq 2$ while for $N_{jet} \geq 3$ and 4, HERWIRI predictions underestimate the data.

4.3 Summary

The realization of the IR-improved DGLAP-CS theory, when used in the MADGRAPH5_aMC@NLO/HERWIRI1.031 $\mathcal{O}(\alpha)$ ME-matched parton shower framework, provides us with the opportunity to explain the differential cross sections for a W boson produced in association with jets in pp collisions in the recent LHC data from ATLAS, without the need of an unexpectedly hard intrinsic Gaussian distribution with an rms value of PTRMS = 2.2 GeV in parton's wave function. In our view, this can be interpreted as providing a rigorous basis for the phenomenological correctness of such unexpectedly hard distributions insofar as describing these data using the usual unimproved DGLAP-CS showers is concerned.

4.4 Event Generation, Analysis and Cuts (CMS Collaboration)

The generators for W + jet events are MADGRAPH5_aMC@NLO [79] interfaced with HERWIG6.521 and HERWIRI1.031, which use next-to-leading-order (NLO) matrix element calculations. The number of events generated for the W, W + 1 jet, W + 2 jets, and W + 3 jets processes are 10^7, 10^6, 10^5, and 10^5, respectively. These events are showered by MADGRAPH5_aMC@NLO/HERWIRI1.031 (PTRMS = 0) and MADGRAPH5_aMC@NLO/HERWIG6.521 (PTRMS = 2.2 GeV).[2] During the analysis, jets were reconstructed using the anti-k_t algorithm with $R = 0.5$ with FastJet [80] and the cuts in Table 4.2 were imposed.

Table 4.2: Kinematic criteria defining the fiducial phase space for the $W \to \mu + \nu_\mu$ channel.

Muon channel	$(W \to \mu + \nu_\mu)$
Lepton P_T^μ	$P_T^\mu > 25$ GeV
Lepton rapidity η_μ	$\lvert\eta_\mu\rvert < 2.1$
Missing transverse energy	$E_T^{miss} > 25$ GeV
Transverse mass	$m_T > 50$ GeV
Jet algorithm	Anti-k_T
Radius parameter R	$R = 0.5$
Jet P_T^{jet}	$P_T^{jet} > 30$ GeV
Jet rapidity Y_{jet}	$\lvert Y_{jet}\rvert < 2.4$
Jet isolation	$\Delta R(\mu, \text{jet}) > 0.5$ (jet is removed)

The transverse mass, m_T, is defined as $m_T = \sqrt{2P_T^\mu P_T^{\nu_\mu}(1-\cos\Delta\phi)}$ where $\Delta\phi$ is the difference in the azimuthal angle between the direction of the muon momentum

[2]We will see later that HERWIRI gives either a better fit to the data or an acceptable fit without this extra Gaussian kick.

and the associated muon neutrino, ν_μ, which can be written as

$$\Delta\phi = \phi^{\mu} - \phi^{\nu_\mu}. \tag{4.12}$$

Rapidity is defined as $\frac{1}{2}\ln\left[\frac{E+p_z}{E-p_z}\right]$, where E denotes the energy of the particle and p_z is the longitudinal component of the momentum. Finally, the jet isolation, ΔR, which is a Lorentz invariant quantity, is defined as

$$\Delta R(\mu, \mathrm{jet}) = \sqrt{\Delta\phi^2(\mu, \mathrm{jet}) + \Delta\eta^2(\mu, \mathrm{jet})} \tag{4.13}$$

where

$$\begin{cases} \Delta\phi(\mu, \mathrm{jet}) = \phi_\mu - \phi_{\mathrm{jet}}, \\ \Delta\eta(\mu, \mathrm{jet}) = \eta_\mu - \eta_{\mathrm{jet}}, \\ \eta = -\ln\tan(\frac{\theta}{2}). \end{cases} \tag{4.14}$$

4.5 Results (CMS Collaboration)

The measured W($\rightarrow$ $\mu + \nu_\mu$) + jets fiducial cross sections [82] are shown and compared to the predictions of MADGRAPH5_aMC@NLO/HERWIRI1.031 and MADGRAPH5_aMC@NLO/HERWIG6.521. Each distribution is combined separately by minimizing a χ^2 function. The factors applied to the theory predictions are summarized in Appendix G.

4.5.1 Transverse Momentum Distributions P_T

The differential cross sections in jet P_T for inclusive jet multiplicities from 1 to 3 are shown in Figure 4.27, Figure 4.28 and Figure 4.29, and compared with predictions provided by HERWIRI1.031 and HERWIG6.521.

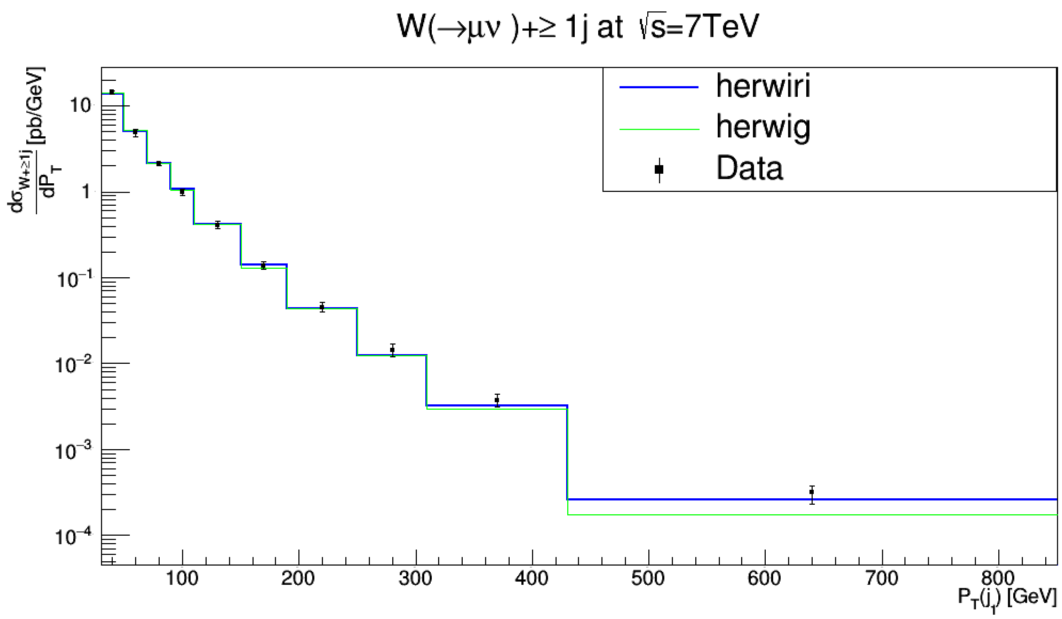

Figure 4.27: Cross section for the production of W + jets as a function of the leading jet P_T for $N_{jet} \geq 1$. The data are compared to predictions from MADGRAPH5_aMC@NLO/HERWIRI1.031 and MADGRAPH5_aMC@NLO/HERWIG6.521.

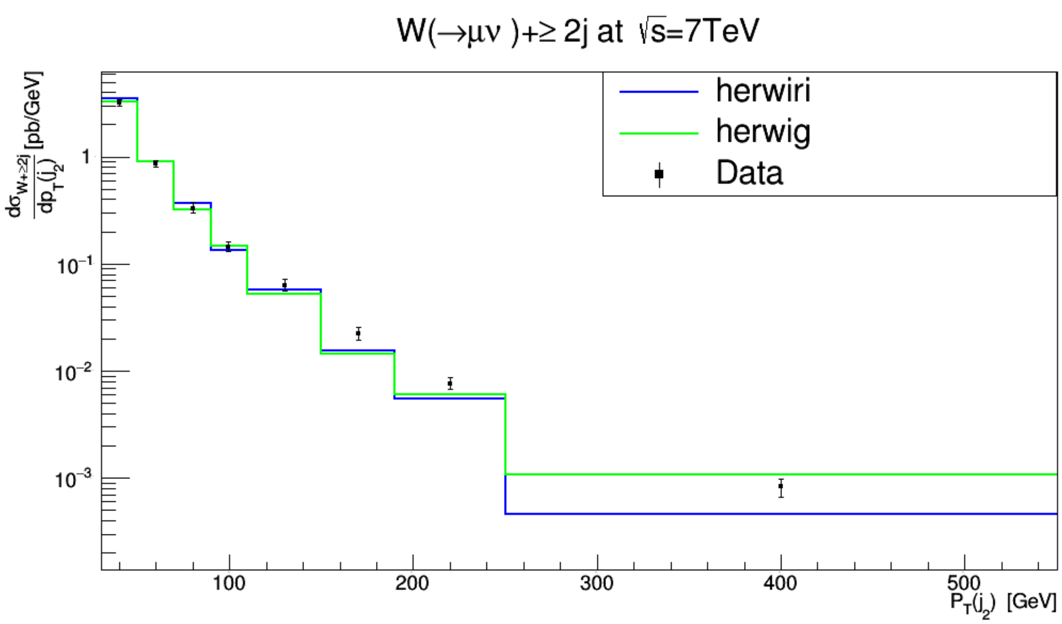

Figure 4.28: Cross section for the production of W + jets as a function of the second leading jet P_T for $N_{jet} \geq 2$. The data are compared to predictions from MADGRAPH5_aMC@NLO/HERWIRI1.031 and MADGRAPH5_aMC@NLO/HERWIG6.521.

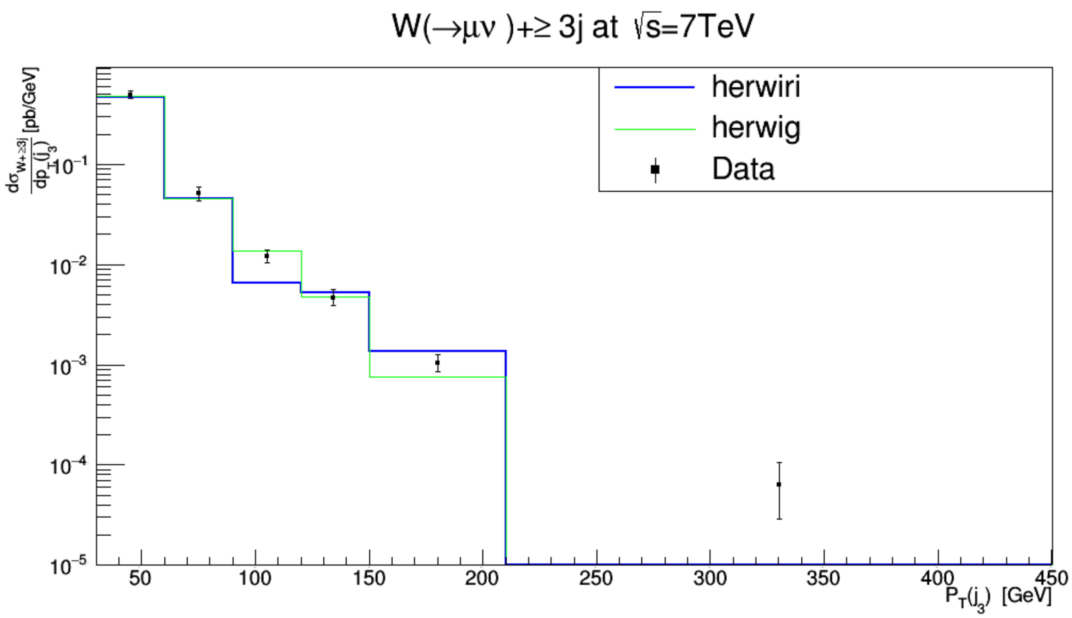

Figure 4.29: Cross section for the production of W + jets as a function of the third leading jet P_T for $N_{jet} \geq 3$. The data are compared to predictions from MADGRAPH5_aMC@NLO/HERWIRI1.031 and MADGRAPH5_aMC@NLO/HERWIG6.521.

The differential cross sections as functions of the first three leading jets are shown in Figure 4.27, Figure 4.28, and Figure 4.29. In Figure 4.27, the predictions provided by HERWIRI and HERWIG give a very good fit to the data, with $\left(\frac{\chi^2}{d.o.f}\right)_{\texttt{HERWIRI}} = 1.72$ and $\left(\frac{\chi^2}{d.o.f}\right)_{\texttt{HERWIG}} = 1.33$.

In Figure 4.28, for $P_T \leq 150$ GeV, a better fit is provided by HERWIG to the data points, where $\left(\frac{\chi^2}{d.o.f}\right)_{\texttt{HERWIRI}} = 6.53$ and $\left(\frac{\chi^2}{d.o.f}\right)_{\texttt{HERWIG}} = 3.60$. For higher values of P_T, the predictions provided by HERWIRI lie below the data while the HERWIG results either underestimate or overestimate the data.

In Figure 4.29, the HERWIG predictions, in general, give a better fit to the data: $\left(\frac{\chi^2}{d.o.f}\right)_{\texttt{HERWIRI}} = 5.21$ and $\left(\frac{\chi^2}{d.o.f}\right)_{\texttt{HERWIG}} = 3.18$.

4.5.2 The Scalar Sum of Jet Transverse Momenta H_T

In this subsection, the differential cross sections are shown as function of H_T for inclusive jet multiplicities 1–3. The scalar sum H_T is defined as

$$H_T = \sum_{i=1}^{N_{jet}} P_T(j_i), \tag{4.15}$$

for each event.

The differential cross sections as a function of H_T for inclusive jet multiplicities 1–3 are shown in Figure 4.30, Figure 4.31, and Figure 4.32. In Figure 4.30, the predictions provided by HERWIG give a better fit to the data with $\left(\frac{\chi^2}{d.o.f}\right)_{\texttt{HERWIRI}} = 5.19$ and $\left(\frac{\chi^2}{d.o.f}\right)_{\texttt{HERWIG}} = 2.58$. In Figure 4.31, for $H_T > 200$ GeV, HERWIRI gives a better fit to the data while in Figure 4.32 the predictions provided by HERWIG give a better fit to the data. In Figure 4.31, $\left(\frac{\chi^2}{d.o.f}\right)_{\texttt{HERWIRI}} = 48.55$ and $\left(\frac{\chi^2}{d.o.f}\right)_{\texttt{HERWIG}} = 57.57$. In Figure 4.32, $\left(\frac{\chi^2}{d.o.f}\right)_{\texttt{HERWIRI}} = 29.56$ and $\left(\frac{\chi^2}{d.o.f}\right)_{\texttt{HERWIG}} = 14.73$.

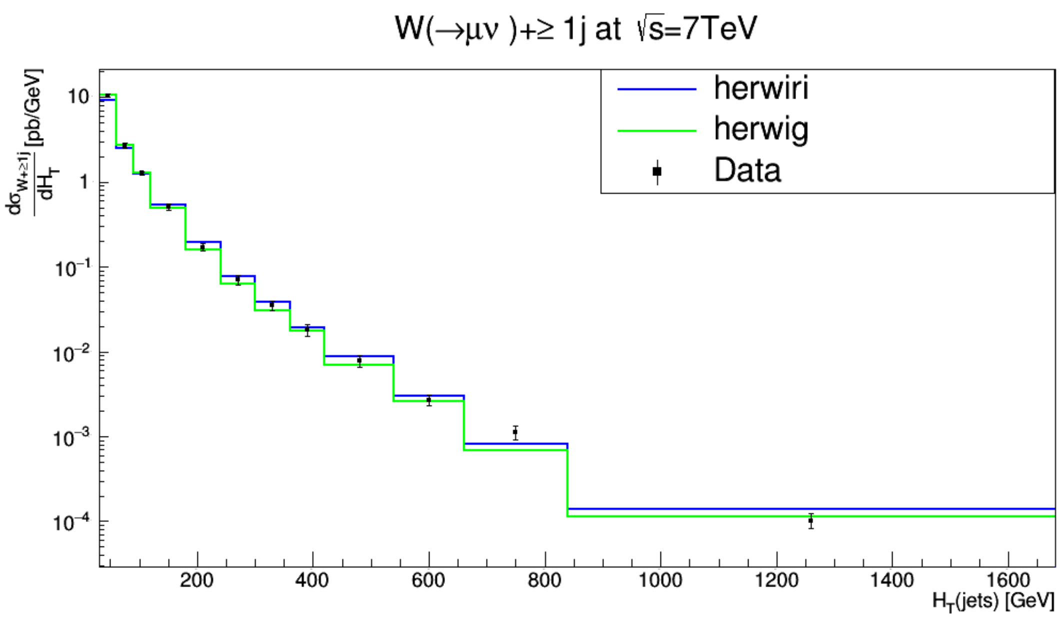

Figure 4.30: Cross section for the production of W + jets as a function of H_T for $N_{jet} \geq 1$. The data are compared to predictions from MADGRAPH5_aMC@NLO/HERWIRI1.031 and MADGRAPH5_aMC@NLO/HERWIG6.521.

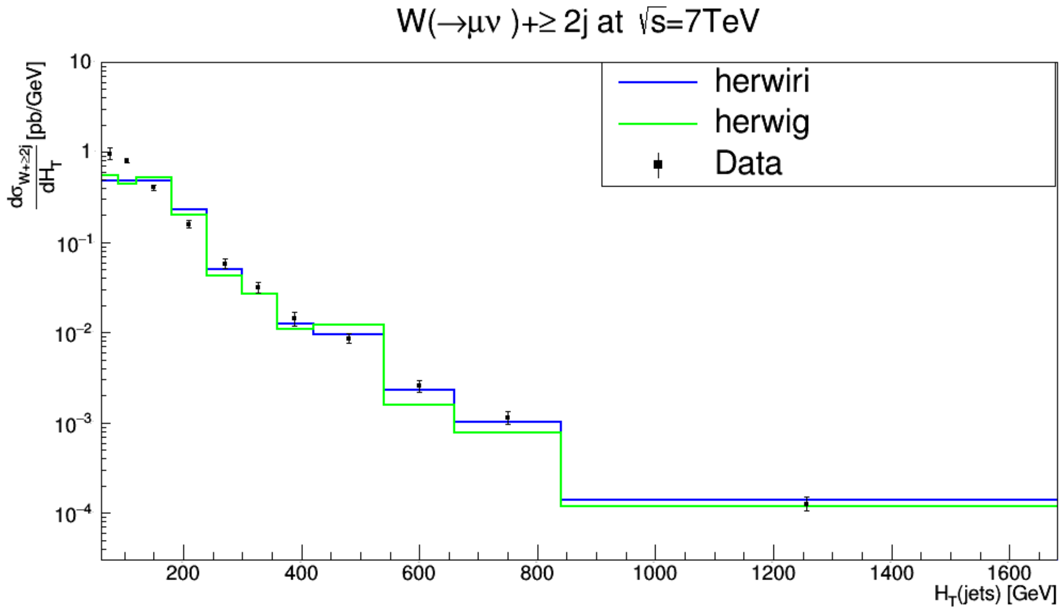

Figure 4.31: Cross section for the production of W + jets as a function of H_T for $N_{jet} \geq 2$. The data are compared to predictions from MADGRAPH5_aMC@NLO/HERWIRI1.031 and MADGRAPH5_aMC@NLO/HERWIG6.521.

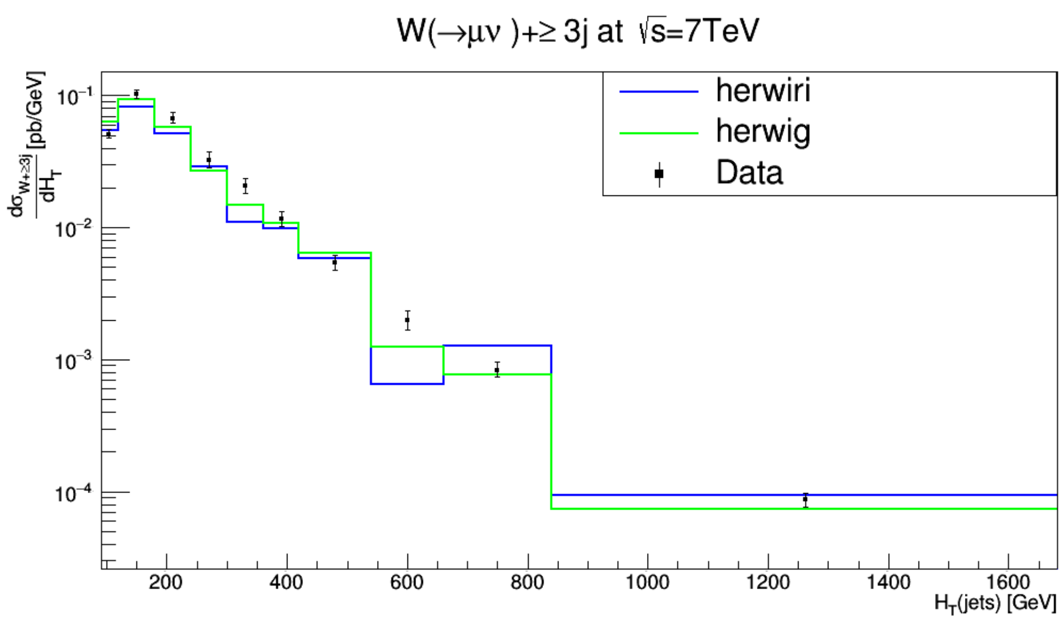

Figure 4.32: Cross section for the production of W + jets as a function of H_T for $N_{jet} \geq 3$. The data are compared to predictions from MADGRAPH5_aMC@NLO/HERWIRI1.031 and MADGRAPH5_aMC@NLO/HERWIG6.521.

4.5.3 *Pseudorapidity Distributions $|\eta(j)|$*

In this section, the differential cross sections are shown as functions of pseudorapidities of the three leading jets. The pseudorapidity is defined as

$$\eta \equiv -\ln\left(\tan\frac{\theta}{2}\right), \tag{4.16}$$

where θ is the angle between the particle three-momentum $\vec{P}$ and the positive direction of the beam axis. One can prove that Eq. (4.16) is written in the form

$$\eta = \frac{1}{2}\ln\left(\frac{|\vec{P}| + P_L}{|\vec{P}| - P_L}\right) = \operatorname{arctanh}\left(\frac{P_L}{|\vec{P}|}\right), \tag{4.17}$$

where P_L where is the component of the momentum along the beam axis.

The problem with rapidity is that it can be hard to measure for highly relativistic particles. We need the total momentum vector of a particle, especially at high values of the rapidity where the z component of the momentum is large, and the beam pipe can be in the way of measuring it precisely.

However, there is a way of defining a quantity that is almost the same thing as the rapidity which is much easier to measure than y for highly energetic particles. This leads to the concept of pseudorapidity η.

Hadron colliders measure physical momenta in terms of transverse momentum, P_T, polar angle in the transverse plane, ϕ, and pseudorapidity. To obtain Cartesian momenta (P_x, P_y, P_z), (with the z-axis defined as the beam axis), the following conversions are used:

$$\begin{cases} P_x = P_T\cos\phi, \\ P_y = P_T\sin\phi, \\ P_z = P_T\sinh\eta. \end{cases} \tag{4.18}$$

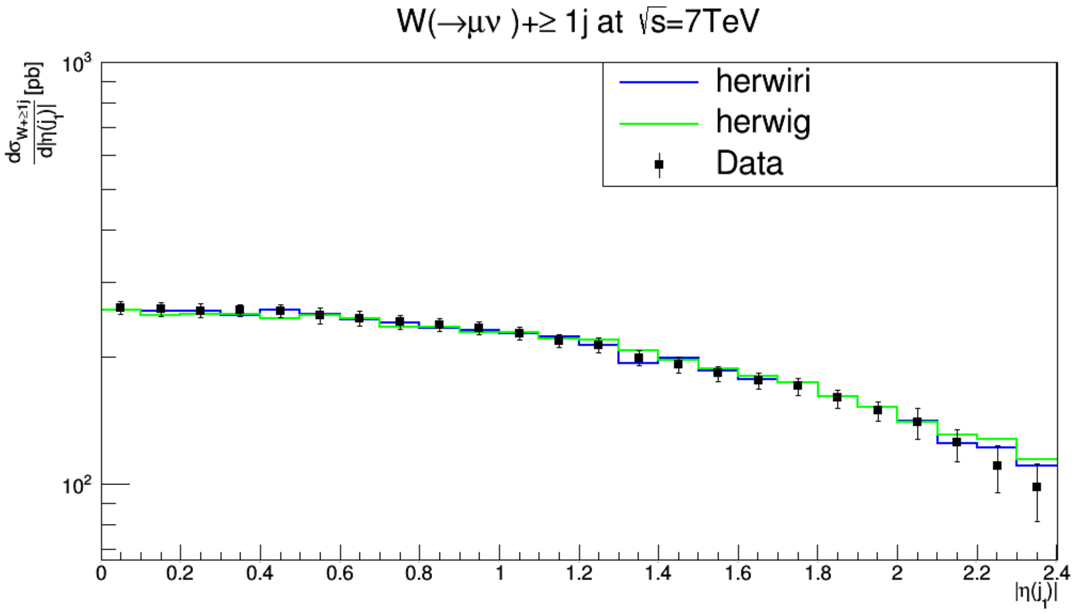

Figure 4.33: Cross section for the production of W + jets as a function of $|\eta(j_1)|$ for $N_{jet} \geq 1$. The data are compared to predictions from MADGRAPH5_aMC@NLO/HERWIRI1.031 and MADGRAPH5_aMC@NLO/HERWIG6.521.

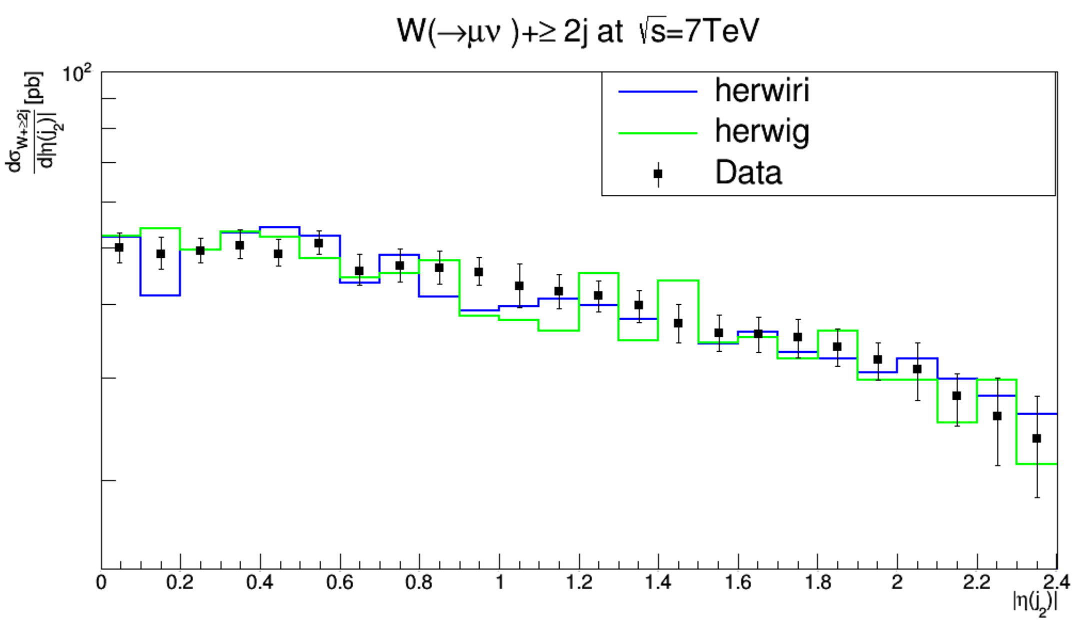

Figure 4.34: Cross section for the production of W + jets as a function of $|\eta(j_2)|$ for $N_{jet} \geq 2$. The data are compared to predictions from MADGRAPH5_aMC@NLO/HERWIRI1.031 and MADGRAPH5_aMC@NLO/HERWIG6.521.

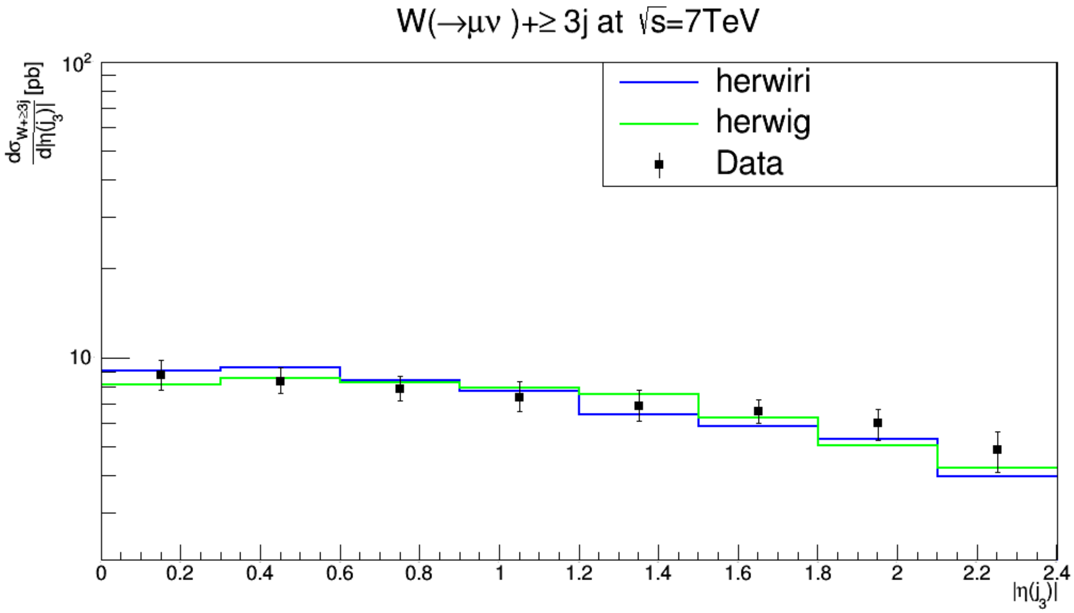

Figure 4.35: Cross section for the production of W + jets as a function of $|\eta(j_1)|$ for $N_{jet} \geq 3$. The data are compared to predictions from MADGRAPH5_aMC@NLO/HERWIRI1.031 and MADGRAPH5_aMC@NLO/HERWIG6.521.

In Figure 4.33 the cross section is shown as a function of $|\eta(j_1)|$, the leading jet pseudorapidity. The predictions provided by HERWIRI are in better agreement with the data, with $\left(\frac{\chi^2}{d.o.f}\right)_{\texttt{HERWIRI}} = 0.78$ and $\left(\frac{\chi^2}{d.o.f}\right)_{\texttt{HERWIG}} = 1.58$. In Figure 4.34, in general, HERWIG gives a better fit to the data, with $\left(\frac{\chi^2}{d.o.f}\right)_{\texttt{HERWIRI}} = 7.61$ and $\left(\frac{\chi^2}{d.o.f}\right)_{\texttt{HERWIG}} = 6.85$. Figure 4.35 shows that the HERWIG predictions are in better agreement with the data, with $\left(\frac{\chi^2}{d.o.f}\right)_{\texttt{HERWIRI}} = 3.27$ and $\left(\frac{\chi^2}{d.o.f}\right)_{\texttt{HERWIG}} = 2.43$.

4.5.4 Azimuthal Angular Distribution Between the Muon and the Leading Jet

The differential cross sections are shown as functions of the azimuthal angle between the muon and the first three leading jets for inclusive jet multiplicities 1–3. The azimuthal angle between the muon and the leading jet is defined as

$$\cos(\Delta\Phi(\mu, j_1)) = \frac{P_x(\mu)P_x(j_1) + P_y(\mu)P_y(j_1)}{\sqrt{P_x^2(\mu) + P_y^2(\mu)}\sqrt{P_x^2(j_1) + P_y^2(j_1)}}, \tag{4.19}$$

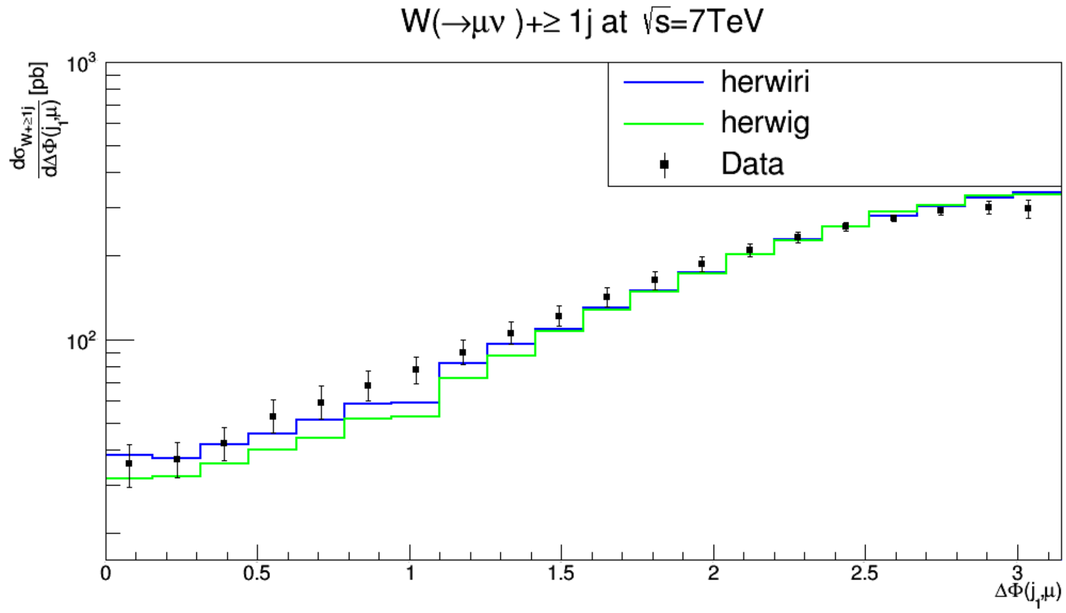

Figure 4.36: Cross section for the production of W + jets as a function of the azimuthal angle between the muon and the leading jet $\Delta\Phi(\mu, j_1)$ for $N_{jet} \geq 1$. The data are compared to predictions from MADGRAPH5_aMC@NLO/HERWIRI1.031 and MADGRAPH5_aMC@NLO/HERWIG6.521.

with

$$\begin{cases} \mu^\mu = (E_\mu, P_x(\mu), P_y(\mu), P_L(\mu)), \\ j_1^\mu = (E_{j_1}, P_x(j_1), P_y(j_1), P_L(j_1)), \end{cases} \tag{4.20}$$

The differential cross sections as functions of the azimuthal angle between the muon and the first three leading jets are shown in Figure 4.36, Figure 4.37, and Figure 4.38 for inclusive jet multiplicities 1–3, respectively.

In Figure 4.36 and Figure 4.38, the data are better modeled by the predictions provided by HERWIRI as expected as well as Figure 4.37 shows that the HERWIG predictions give a better fit to the data. In Figure 4.36, $\left(\frac{\chi^2}{d.o.f}\right)_{\texttt{HERWIRI}} = 5.07$ and $\left(\frac{\chi^2}{d.o.f}\right)_{\texttt{HERWIG}} = 10.68$. In Figure 4.37, $\left(\frac{\chi^2}{d.o.f}\right)_{\texttt{HERWIRI}} = 10.94$ and $\left(\frac{\chi^2}{d.o.f}\right)_{\texttt{HERWIG}} = 5.95$. In Figure 4.38, $\left(\frac{\chi^2}{d.o.f}\right)_{\texttt{HERWIRI}} = 3.54$ and $\left(\frac{\chi^2}{d.o.f}\right)_{\texttt{HERWIG}} = 2.457$.

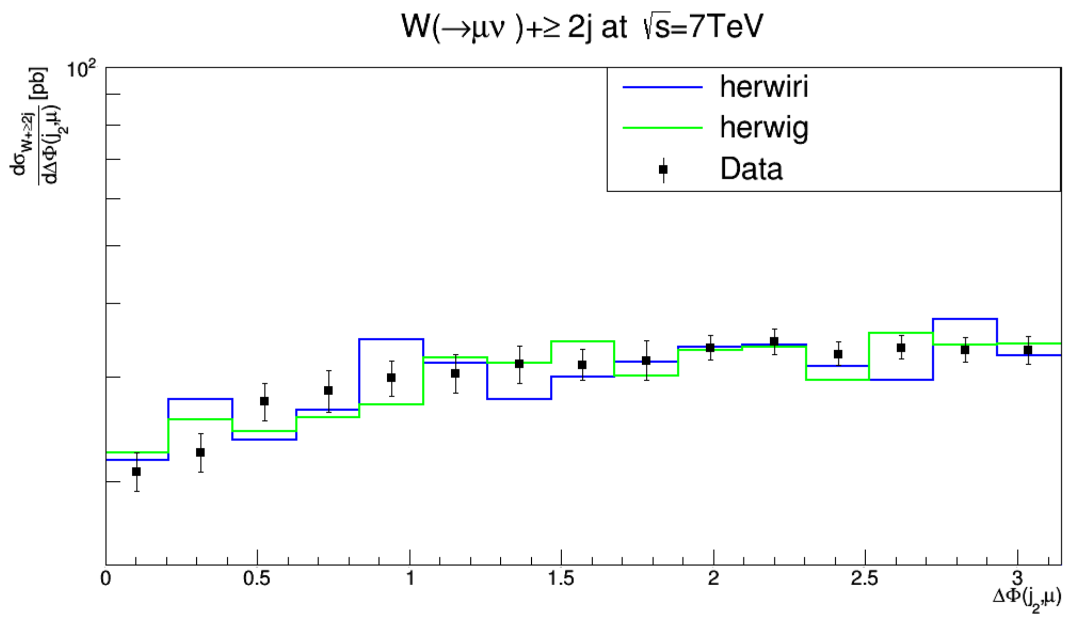

Figure 4.37: Cross section for the production of W + jets as a function of the azimuthal angle between the muon and the second leading jet $\Delta\Phi(\mu, j_2)$ for $N_{jet} \geq 2$. The data are compared to predictions from MADGRAPH5_aMC@NLO/HERWIRI1.031 and MADGRAPH5_aMC@NLO/HERWIG6.521.

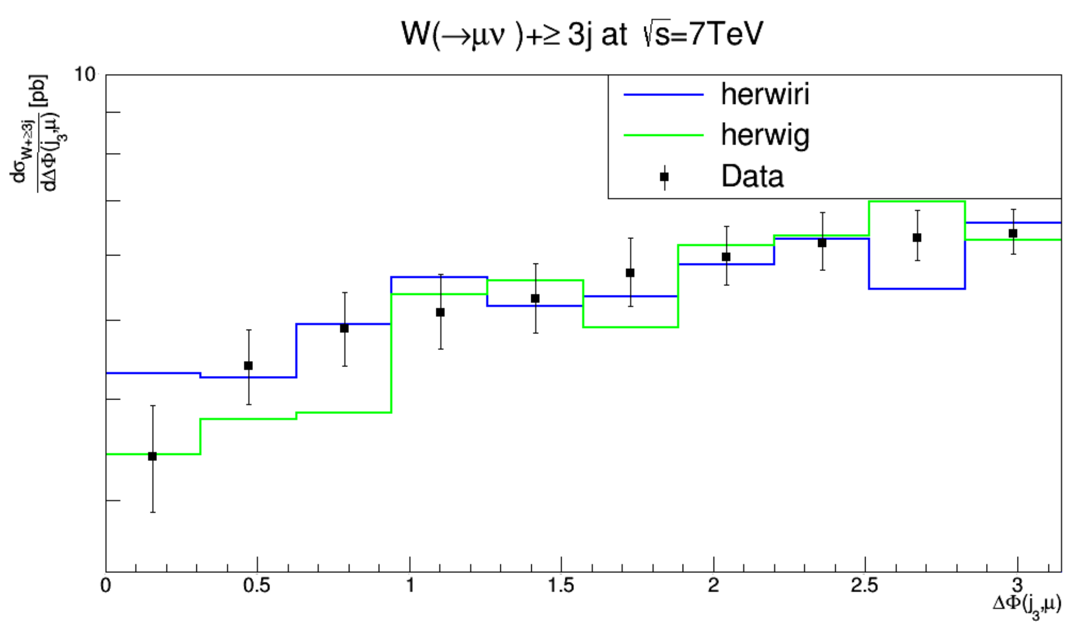

Figure 4.38: Cross section for the production of W + jets as a function of the azimuthal angle between the muon and the second leading jet $\Delta\Phi(\mu, j_3)$ for $N_{jet} \geq 3$. The data are compared to predictions from MADGRAPH5_aMC@NLO/HERWIRI1.031 and MADGRAPH5_aMC@NLO/HERWIG6.521.

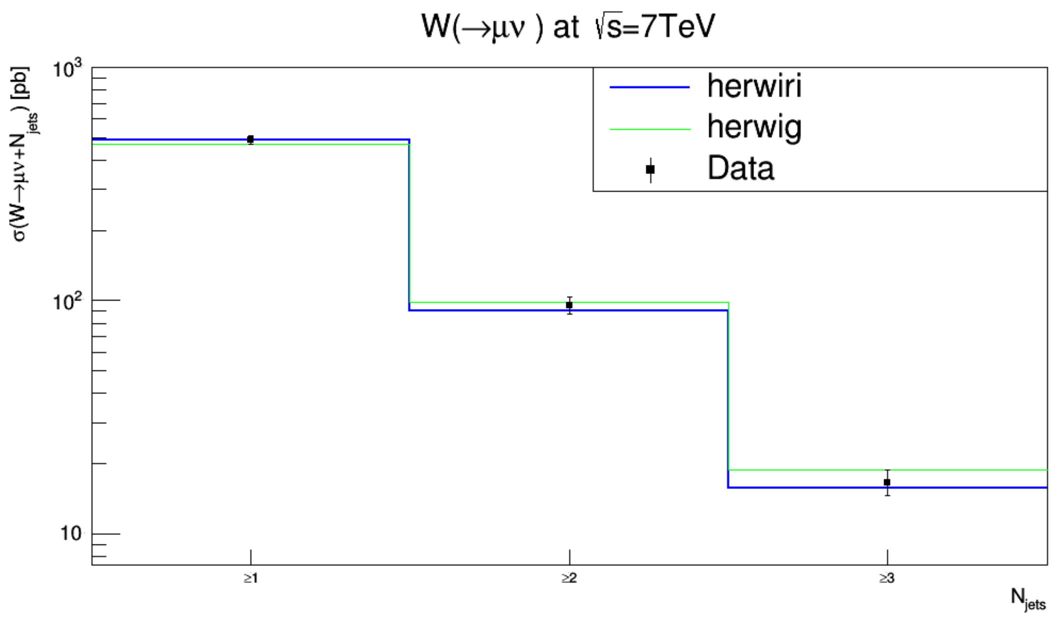

Figure 4.39: Measured cross section versus inclusive jet multiplicity. The data are compared to predictions from MADGRAPH5_aMC@NLO/HERWIRI1.031 and MADGRAPH5_aMC@NLO/HERWIG6.521.

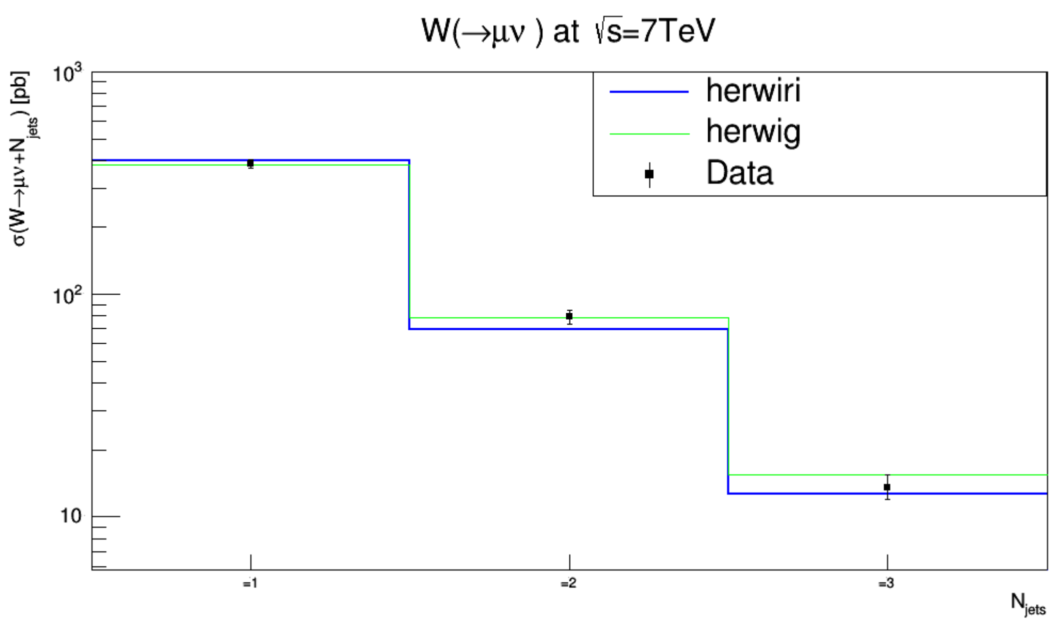

Figure 4.40: Measured cross section versus exclusive jet multiplicity. The data are compared to predictions from MADGRAPH5_aMC@NLO/HERWIRI1.031 and MADGRAPH5_aMC@NLO/HERWIG6.521.

4.5.5 Cross Sections

The measured $\mathrm{W}(\rightarrow \mu\nu_\mu)$ + jets fiducial cross sections are shown in Figure 4.39 and Figure 4.40 and compared to the predictions of MADGRAPH5_aMC@NLO/HERWIRI1.031 and MADGRAPH5_aMC@NLO/HERWIG6.521. The measured inclusive jet multiplicity distributions are in agreement with the predictions of HERWIRI, while the measured exclusive jet multiplicity distributions are in agreement with the predictions of HERWIG. Figure 4.39 shows the differential cross sections for the inclusive jet multiplicities 1–3. HERWIRI gives a better fit to the data. Figure 4.40 shows the differential cross sections for the exclusive jet multiplicities 1-3. The cross sections provide by HERWIG give a better fit to the data. In Figure 4.39, $\left(\frac{\chi^2}{d.o.f}\right)_{\texttt{HERWIRI}} = 0.92$ and $\left(\frac{\chi^2}{d.o.f}\right)_{\texttt{HERWIG}} = 2.30$ while in Figure 4.40, $\left(\frac{\chi^2}{d.o.f}\right)_{\texttt{HERWIRI}} = 4.66$ and $\left(\frac{\chi^2}{d.o.f}\right)_{\texttt{HERWIG}} = 1.65$.

4.6 Summary

The realization of the IR-improved DGLAP-CS theory, when used in the MADGRAPH5_aMC@NLO/HERWIRI1.031 $\mathcal{O}(\alpha)$ ME-matched parton shower framework, provides us with the opportunity to explain the differential cross sections for a W boson produced in association with jets in pp collisions in the recent LHC data from CMS, without the need of an unexpectedly hard intrinsic Gaussian distribution with an rms value of PTRMS = 2.2 GeV in parton's wave function. In our view, this can be interpreted as providing a rigorous basis for the phenomenological correctness of such unexpectedly hard distributions insofar as describing these data using the usual unimproved DGLAP-CS showers is concerned.

CHAPTER FIVE

IR-improved DGLAP-CS Parton Shower Effects for Associated Production of a W Boson and Jets in pp Collisions at $\sqrt{s} = 8$ TeV

5.1 *Event Generation, Analysis and Cuts (CMS Collaboration)*

The generators for W + jet events are MADGRAPH5_aMC@NLO [79] interfaced with HERWIG6.521 and HERWIRI1.031, which use next-to-leading-order (NLO) matrix element calculations. The number of events generated for the W, W + 1 jet, W + 2 jets, and W + 3 jets processes are 10^7, 10^6, 10^5, and 10^5, respectively. These events are showered by MADGRAPH5_aMC@NLO/HERWIRI1.031 (PTRMS = 0) and MADGRAPH5_aMC@NLO/HERWIG6.521 (PTRMS = 2.2 GeV).[1] During the analysis, jets were reconstructed using the anti-k_t algorithm with $R = 0.5$ with FastJet [80] and the cuts in Table 5.1 were imposed.

Table 5.1: Kinematic criteria defining the fiducial phase space for the $W \to \mu + \nu_\mu$ channel.

Muon channel	$(W \to \mu + \nu_\mu)$
Lepton P_T^μ	$P_T^\mu > 25$ GeV
Lepton rapidity η_μ	$\lvert\eta_\mu\rvert < 2.1$
Missing transverse energy	$E_T^{miss} > 25$ GeV
Transverse mass	$m_T > 50$ GeV
Jet algorithm	Anti-k_T
Radius parameter R	$R = 0.5$
Jet P_T^{jet}	$P_T^{jet} > 30$ GeV
Jet rapidity η_{jet}	$\lvert\eta_{jet}\rvert < 2.4$
Jet isolation	$\Delta R(\mu, \text{jet}) > 0.5$ (jet is removed)

[1]We will see later that HERWIRI gives either a better fit to the data or an acceptable fit without this extra Gaussian kick.

The transverse mass, m_T, is defined as $m_T = \sqrt{2P_T^{\mu}P_T^{\nu_\mu}(1-\cos\Delta\phi)}$ where $\Delta\phi$ is the difference in the azimuthal angle between the direction of the muon momentum and the associated muon neutrino, ν_μ, which can be written as

$$\Delta\phi = \phi^{\mu} - \phi^{\nu_\mu}. \tag{5.1}$$

Rapidity is defined as $\frac{1}{2}\ln\left[\frac{E+p_z}{E-p_z}\right]$, where E denotes the energy of the particle and p_z is the longitudinal component of the momentum. Finally, the jet isolation, ΔR, which is a Lorentz invariant quantity, is defined as

$$\Delta R(\mu,\text{jet}) = \sqrt{\Delta\phi^2(\mu,\text{jet}) + \Delta\eta^2(\mu,\text{jet})} \tag{5.2}$$

where

$$\begin{cases} \Delta\phi(\mu,\text{jet}) = \phi_\mu - \phi_{\text{jet}}, \\ \Delta\eta(\mu,\text{jet}) = \eta_\mu - \eta_{\text{jet}}, \\ \eta = -\ln\tan(\frac{\theta}{2}). \end{cases} \tag{5.3}$$

5.2 Results (CMS Collaboration)

The measured W($\rightarrow \mu+\nu_\mu$) + jets cross sections [83] are shown and compared to the predictions of MADGRAPH5_aMC@NLO/HERWIRI1.031 (PTRMS = 0) and MADGRAPH5_aMC@NLO/HERWIG6.521 (PTRMS = 2.2 GeV). The 8 TeV data sample allows us to determine the cross sections for jet multiplicities up to 3 and to study the fiducial cross sections as functions of most kinematic observables for up to three jets. Each distribution is combined separately by minimizing a χ^2 function. The factors applied to the theory predictions are summarized in Appendix H.

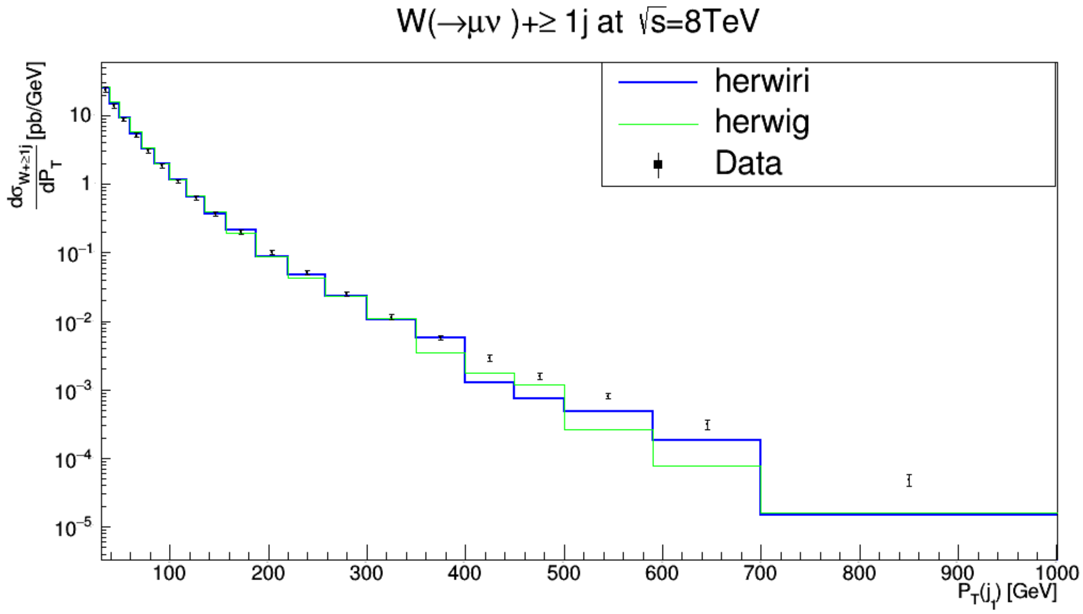

Figure 5.1: Cross section for the production of W + jets as a function of the leading-jet P_T in $N_{jet} \geq 1$. The data are compared to predictions from MADGRAPH5_aMC@NLO/HERWIRI1.031 and MADGRAPH5_aMC@NLO/HERWIG6.521.

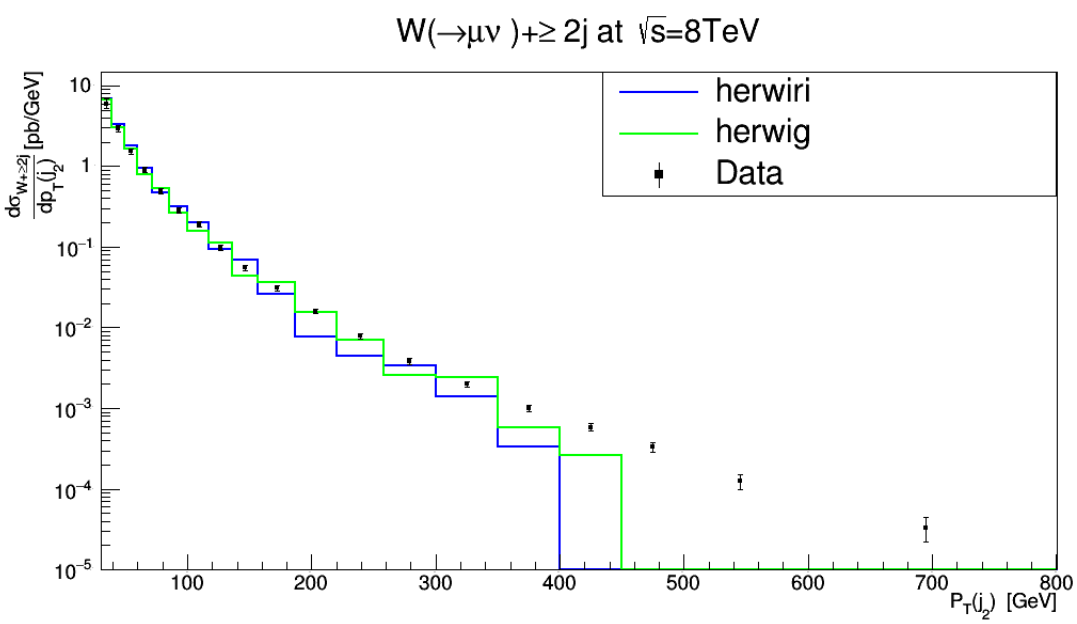

Figure 5.2: Cross section for the production of W + jets as a function of the second leading-jet P_T in $N_{jet} \geq 2$. The data are compared to predictions from MADGRAPH5_aMC@NLO/HERWIRI1.031 and MADGRAPH5_aMC@NLO/HERWIG6.521.

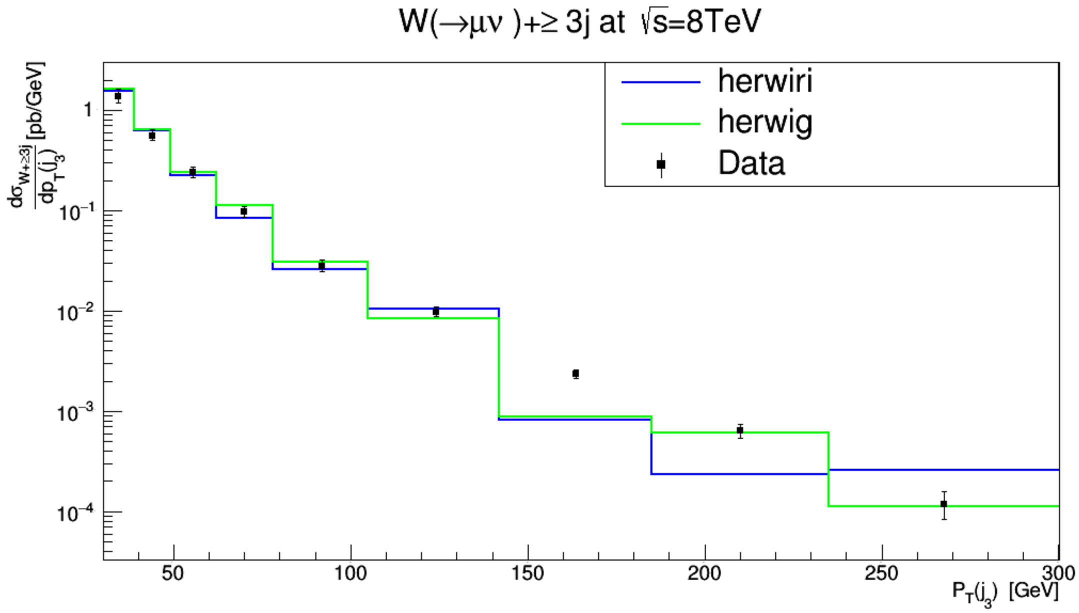

Figure 5.3: Cross section for the production of W + jets as a function of the third leading-jet P_T in $N_{jet} \geq 3$. The data are compared to predictions from MADGRAPH5_aMC@NLO/HERWIRI1.031 and MADGRAPH5_aMC@NLO/HERWIG6.521.

5.2.1 Transverse Momentum Distributions P_T

The differential cross sections in jet P_T for inclusive jet multiplicities from 1 to 3 are shown and compared with predictions provided by HERWIRI1.031 and HERWIG6.521. The differential cross sections as functions of the first three leading jets are shown in Figure 5.1, Figure 5.2, and Figure 5.3. In Figure 5.1, a good fit is provided by both HERWIRI and HERWIG for $P_T \leq 350$ GeV while for $P_T > 400$ GeV the predictions provided by HERWIRI and HERWIG lie below the data. However, the HERWIRI predictions are closer to the data. In Figure 5.2 both HERWIRI and HERWIG provide a fairly good fit to the data for $P_T \leq 100$ GeV. In $100 < P_T < 300$ GeV, there are cases in which the theoretical predictions provided by either HERWIRI or HERWIG overlap with the data. For higher values of P_T, $P_T > 350$ GeV, both HERWIRI and HERWIG underestimate the data although the HERWIG results are closer to the data in some cases. In Figure 5.1, for $P_T \leq 140$ GeV, $\left(\frac{\chi^2}{d.o.f}\right)_{\texttt{HERWIRI}} =$

1.36 and $\left(\frac{\chi^2}{d.o.f}\right)_{\texttt{HERWIG}} = 2.26$. In Figure 5.2 for $P_T < 140$ GeV, $\left(\frac{\chi^2}{d.o.f}\right)_{\texttt{HERWIRI}} = 8.50$ and $\left(\frac{\chi^2}{d.o.f}\right)_{\texttt{HERWIG}} = 8.57$.In Figure 5.3, a very good fit is provided by HERWIRI to the data for $P_T \leq 150$ GeV. For higher values of P_T, HERWIG predictions overlap with the data while HERWIRI predictions either underestimates or overestimates the data. In Figure 5.3, $\left(\frac{\chi^2}{d.o.f}\right)_{\texttt{HERWIRI}} = 3.21$ and $\left(\frac{\chi^2}{d.o.f}\right)_{\texttt{HERWIG}} = 2.24$.

5.2.2 The Scalar Sum of Jet Transverse Momenta H_T

In this section, the differential cross sections are shown as functions of H_T for inclusive jet multiplicities 1–3. The scalar sum H_T is defined as

$$H_T = \sum_{i=1}^{N_{\text{jet}}} P_T(j_i), \tag{5.4}$$

for each event. In this notation, H_T represents the scalar sum of the jets' transverse momenta.

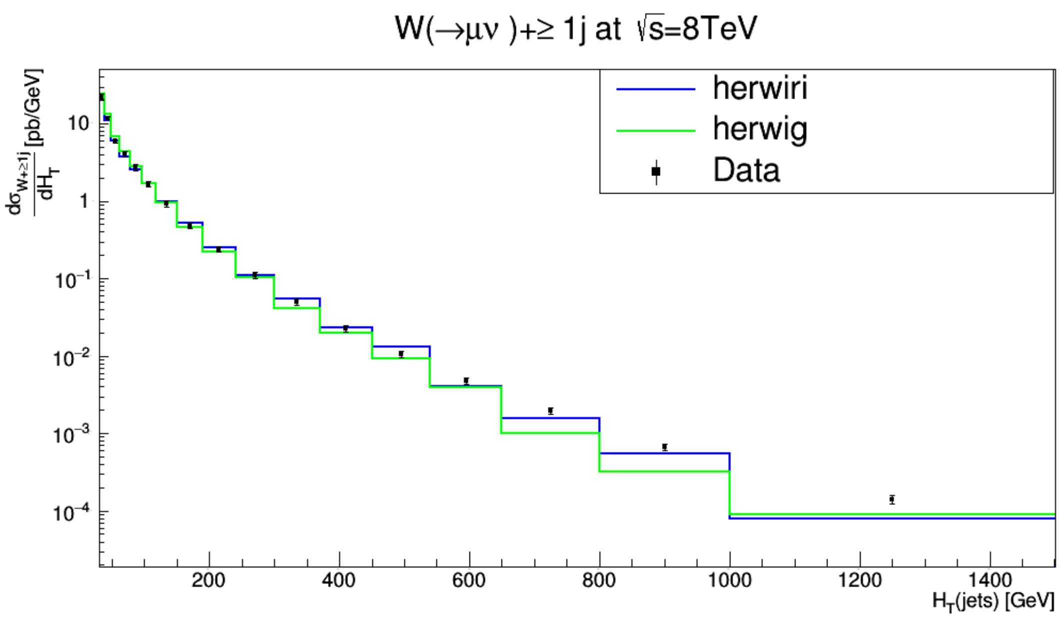

Figure 5.4: Cross section for the production of W + jets as a function of H_T in $N_{jet} \geq 1$. The data are compared to predictions from MADGRAPH5_aMC@NLO/HERWIRI1.031 and MADGRAPH5_aMC@NLO/HERWIG6.521.

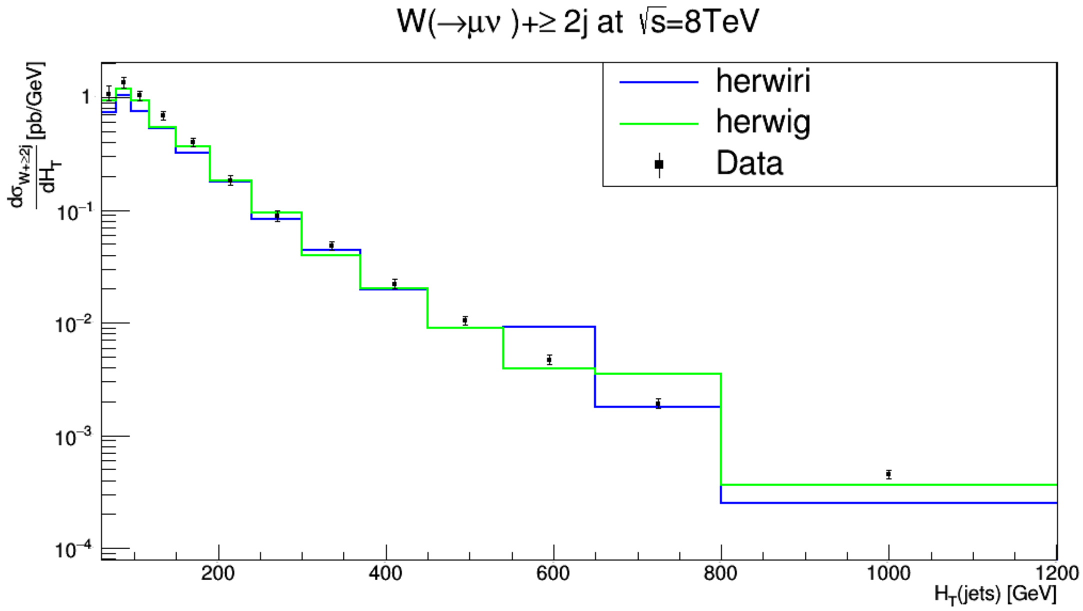

Figure 5.5: Cross section for the production of W + jets as a function of H_T in $N_{jet} \geq 2$. The data are compared to predictions from MADGRAPH5_aMC@NLO/HERWIRI1.031 and MADGRAPH5_aMC@NLO/HERWIG6.521.

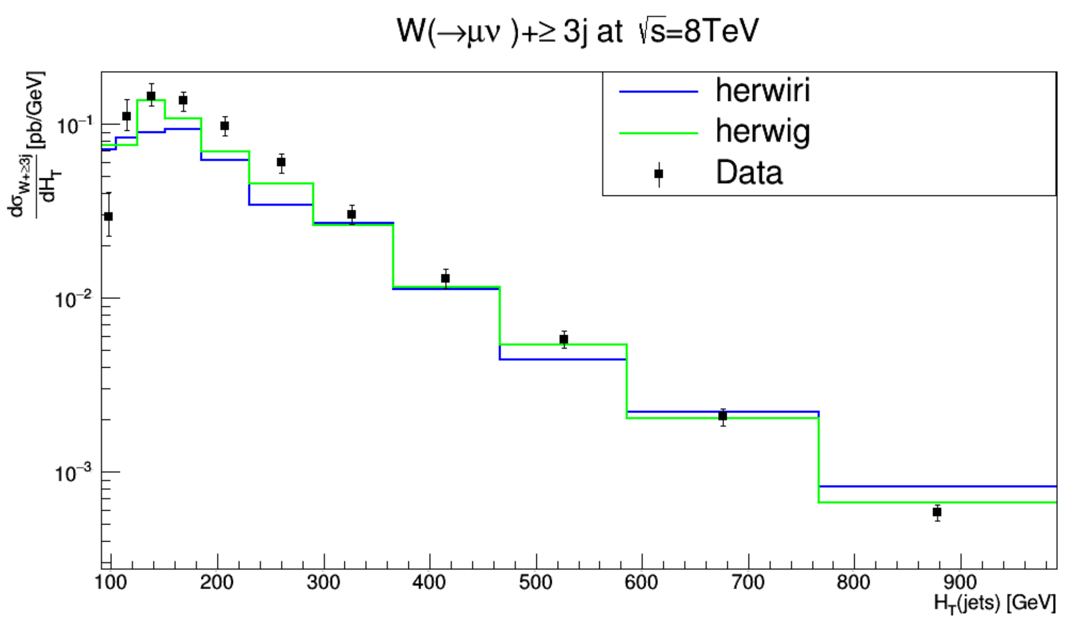

Figure 5.6: Cross section for the production of W + jets as a function of H_T in $N_{jet} \geq 3$. The data are compared to predictions from MADGRAPH5_aMC@NLO/HERWIRI1.031 and MADGRAPH5_aMC@NLO/HERWIG6.521.

The differential cross sections as functions of H_T for inclusive jet multiplicities 1–3 are shown in Figure 5.4, Figure 5.5, and Figure 5.6. In Figure 5.5, a good fit is provided by HERWIRI predictions for $H_T \leq 400$ GeV. For higher values of H_T, HERWIRI predictions are closer to the data. In Figure 5.5, in $H_T \leq 200$ GeV, HERWIG gives a better fit to the data. For $200 < H_T < 450$ GeV, both HERWIRI and HERWIG predictions overlap with the data. For higher values of H_T, in one case HERWIG overlaps and in one case HERWIRI overlaps with the data while for $800 < H_T < 1200$ GeV both HERWIRI and HERWIG underestimate the data. In Figure 5.4, $\left(\frac{\chi^2}{d.o.f}\right)_{\texttt{HERWIRI}} = 2.07$ and $\left(\frac{\chi^2}{d.o.f}\right)_{\texttt{HERWIG}} = 4.11$. In Figure 5.5, $\left(\frac{\chi^2}{d.o.f}\right)_{\texttt{HERWIRI}} = 13.10$ and $\left(\frac{\chi^2}{d.o.f}\right)_{\texttt{HERWIG}} = 7.96$. In Figure 5.6, $\left(\frac{\chi^2}{d.o.f}\right)_{\texttt{HERWIRI}} = 8.53$ and $\left(\frac{\chi^2}{d.o.f}\right)_{\texttt{HERWIG}} = 5.48$.

5.2.3 The Pseudorapidity Distributions $|\eta(j)|$

In this section, the differential cross sections are shown as functions of pseudorapidities of the three leading jets.

In Figure 5.7, the cross sections are shown as a function of $|\eta(j_1)|$, the leading jet pseudorapidity. The predictions provided by both HERWIRI and HERWIG give a very good fit to the data. In Figure 5.8, the cross sections are shown as a function of $|\eta(j_2)|$, the second leading jet pseudorapidity. The distribution is well modeled by both HERWIRI and HERWIG in $|\eta(j_2)| < 2.2$. For larger values of $|\eta(j_2)|$, HERWIG clearly gives a better fit to the data. In Figure 5.7, $\left(\frac{\chi^2}{d.o.f}\right)_{\texttt{HERWIRI}} = 0.30$ and $\left(\frac{\chi^2}{d.o.f}\right)_{\texttt{HERWIG}} = 0.38$. In Figure 5.8, $\left(\frac{\chi^2}{d.o.f}\right)_{\texttt{HERWIRI}} = 0.84$ and $\left(\frac{\chi^2}{d.o.f}\right)_{\texttt{HERWIG}} = 0.66$. In Figure 5.9, the cross sections are shown as a function of $|\eta(j_3)|$, the third leading jet pseudorapidity. A very good fit is provided by HERWIRI for $|\eta(j_3)| < 2$. For higher values of $|\eta(j_3)|$, both HERWIRI and HERWIG underestimate the data. However, the data is closer to HERWIG's predictions. In Figure 5.9, $\left(\frac{\chi^2}{d.o.f}\right)_{\texttt{HERWIRI}} = 0.62$ and $\left(\frac{\chi^2}{d.o.f}\right)_{\texttt{HERWIG}} = 1.02$.

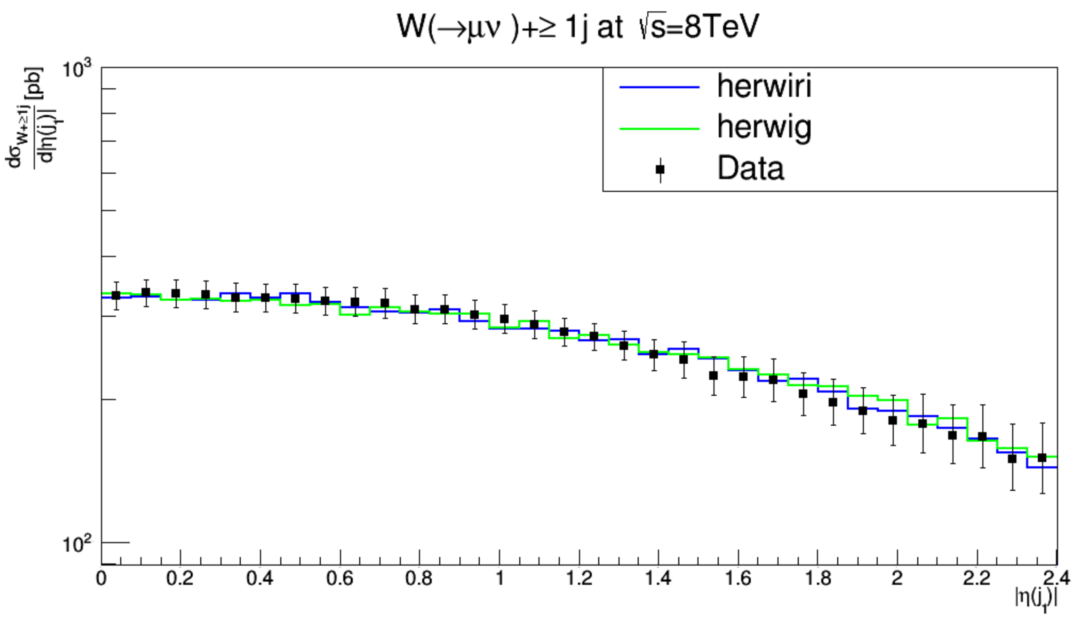

Figure 5.7: Cross section for the production of W + jets as a function of $|\eta(j_1)|$ in $N_{jet} \geq 1$. The data are compared to predictions from MADGRAPH5_aMC@NLO/HERWIRI1.031 and MADGRAPH5_aMC@NLO/HERWIG6.521.

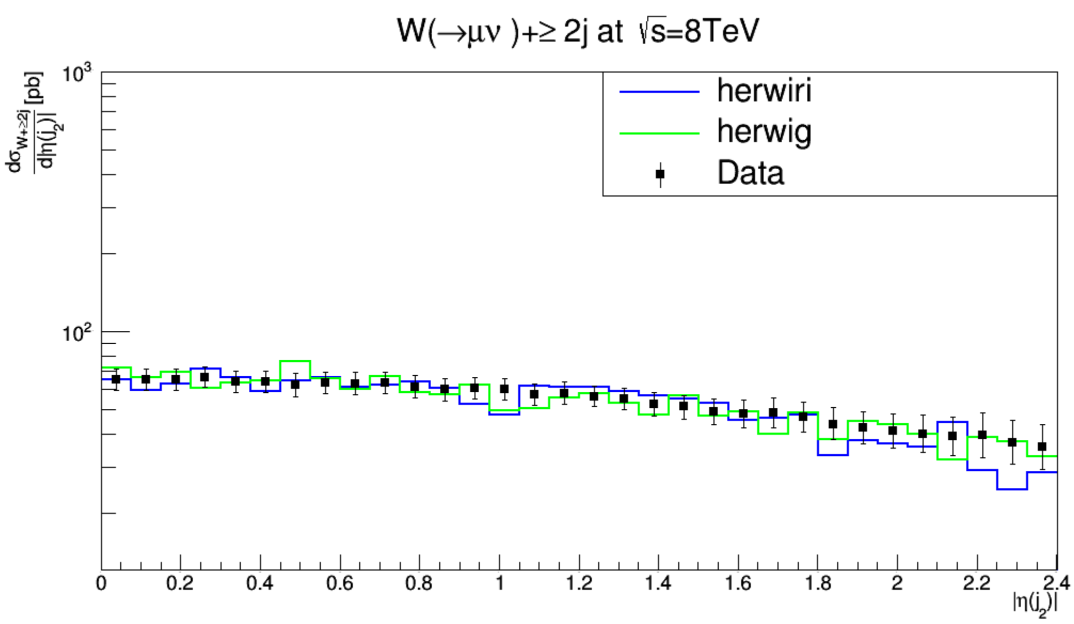

Figure 5.8: Cross section for the production of W + jets as a function of $|\eta(j_2)|$ in $N_{jet} \geq 2$. The data are compared to predictions from MADGRAPH5_aMC@NLO/HERWIRI1.031 and MADGRAPH5_aMC@NLO/HERWIG6.521.

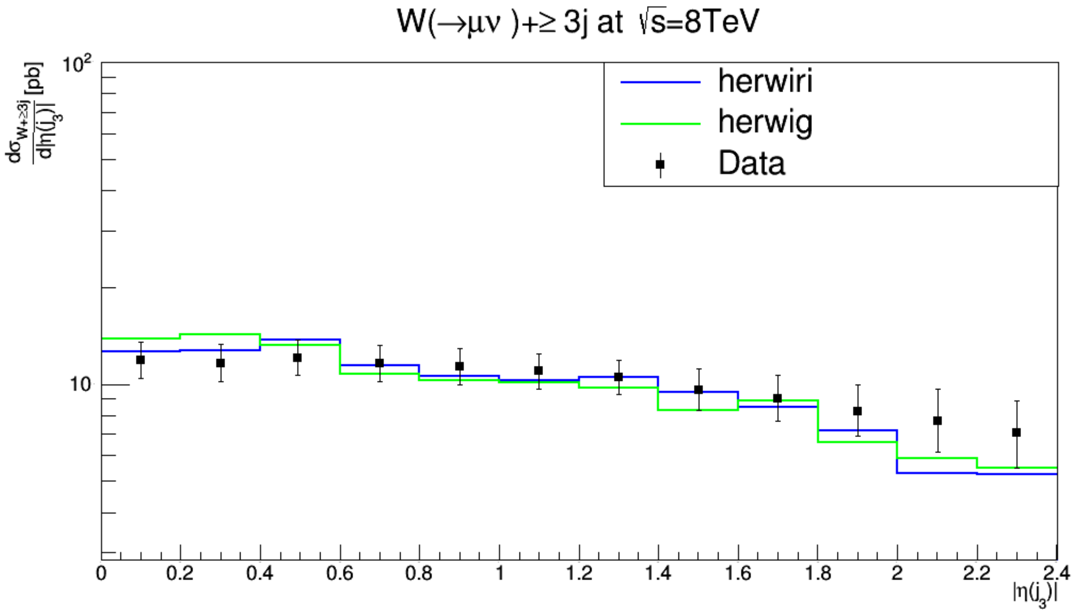

Figure 5.9: Cross section for the production of W + jets as a function of $|\eta(j_1)|$ in $N_{jet} \geq 3$. The data are compared to predictions from MADGRAPH5_aMC@NLO/HERWIRI1.031 and MADGRAPH5_aMC@NLO/HERWIG6.521.

5.2.4 *Dijet P_T Distributions*

In this section, the differential cross sections are shown as a functions of the dijet P_T (calculated from the two leading jets) for inclusive jet multiplicities 2–3. The dijet P_T is defined as

$$\text{dijet } P_T = \sqrt{(P_x(j_1) + P_x(j_2))^2 + ((P_y(j_1) + P_y(j_2))^2}, \tag{5.5}$$

with

$$\begin{cases} j_1^\mu = (E_{j_1}, P_x(j_1), P_y(j_1), P_L(j_1)), \\ j_2^\mu = (E_{j_2}, P_x(j_2), P_y(j_2), P_L(j_2)), \end{cases} \tag{5.6}$$

where

$$P_T = \sqrt{P_x^2 + P_y^2}. \tag{5.7}$$

In Figure 5.10, the cross section is shown as function of the dijet P_T for $N_{jet} \geq 3$. A better fit is provided for the data by the HERWIRI predictions in $P_T \leq 150$ GeV. For higher values of P_T, the predictions provided by both HERWIRI and HERWIG lie below the data points although HERWIRI is closer to the data. In Figure 5.10, $\left(\frac{\chi^2}{d.o.f}\right)_{\texttt{HERWIRI}} = 1.17$ and $\left(\frac{\chi^2}{d.o.f}\right)_{\texttt{HERWIG}} = 1.43$. In Figure 5.11, the cross section is shown as function of the dijet P_T for $N_{jet} \geq 2$. In this case again a better fit is provided by HERWIRI in $P_T \leq 350$ GeV. For $350 < P_T < 450$ GeV, HERWIG gives a better fit to the data. For $P_T \geq 450$ GeV, the predictions provided by both HERWIRI and HERWIG underestimate the data, although HERWIRI results are closer to the data. In Figure 5.11, $\left(\frac{\chi^2}{d.o.f}\right)_{\texttt{HERWIRI}} = 7.54$ and $\left(\frac{\chi^2}{d.o.f}\right)_{\texttt{HERWIG}} = 9.07$.

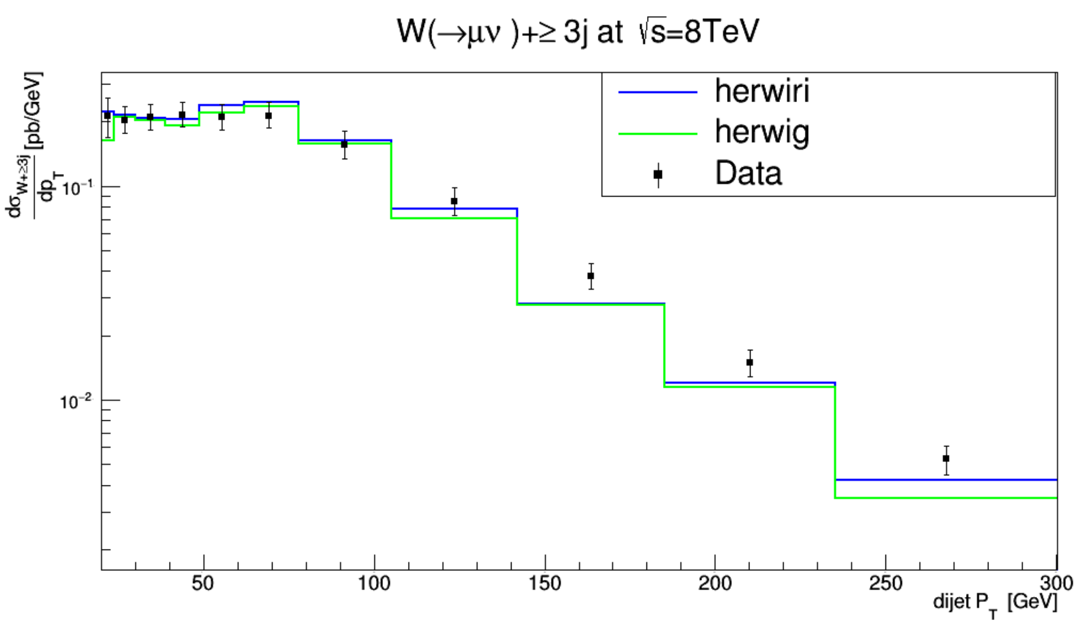

Figure 5.10: Cross section for the production of W + jets as a function of dijet P_T in $N_{jet} \geq 3$. The data are compared to predictions from MADGRAPH5_aMC@NLO/HERWIRI1.031 and MADGRAPH5_aMC@NLO/HERWIG6.521.

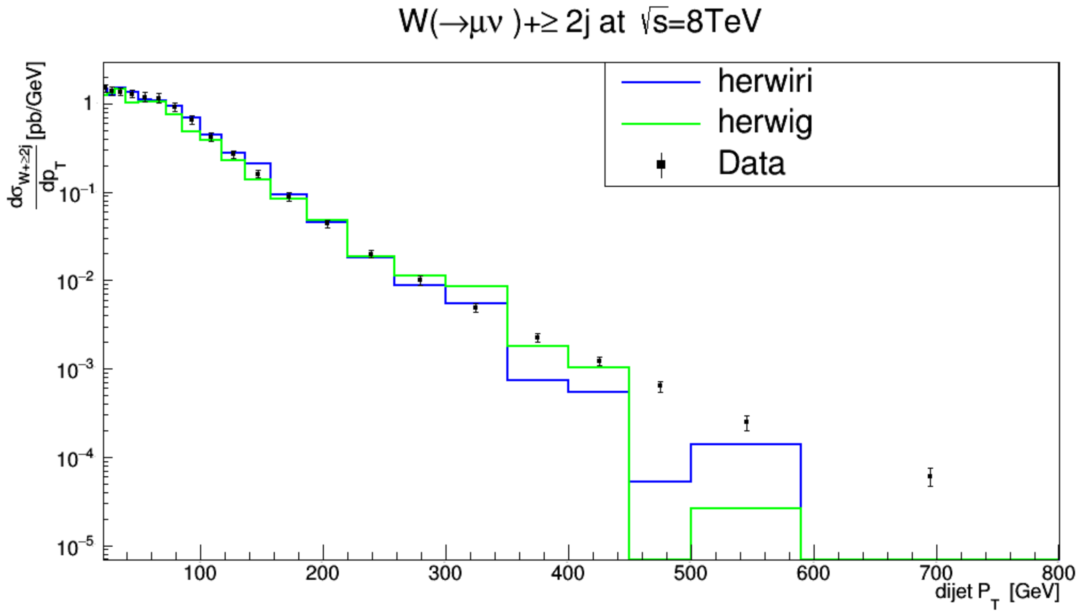

Figure 5.11: Cross section for the production of W + jets as function of dijet P_T in $N_{jet} \geq 2$. The data are compared to predictions from MADGRAPH5_aMC@NLOHERWIRI1.031 and MADGRAPH5_aMC@NLO/HERWIG6.521.

5.2.5 The Rapidity Difference Distributions

In this subsection, differential cross sections are presented as functions of the difference in rapidity. The difference in rapidity between the first and second leading jets is defined as

$$|\Delta Y(j_1, j_2)| = |Y(j_1) - Y(j_2)|, \tag{5.8}$$

with

$$\begin{cases} Y(j_1) = \dfrac{1}{2} \ln \left[\dfrac{E_{j_1} + P_L(j_1)}{E_{j_1} - P_L(j_1)} \right], \\ Y(j_2) = \dfrac{1}{2} \ln \left[\dfrac{E_{j_2} + P_L(j_2)}{E_{j_2} - P_L(j_2)} \right], \end{cases} \tag{5.9}$$

where E_{j_1} and E_{j_1} are energies for the first and the second leading jet, respectively. $P_L(j_1)$ and $P_L(j_2)$ represent the longitudinal momenta for the first and second leading jet.

In Figure 5.12 and Figure 5.13, cross sections are presented as functions of difference in rapidity for inclusive jet multiplicities 2–3. Figure 5.12 shows that for cases $|\Delta Y(j_1, j_2)| \leq 0.5$ and $1 < |\Delta Y(j_1, j_2)| \leq 3.5$, both HERWIRI and HERWIG give good fits to the data. In $0.5 < |\Delta Y(j_1, j_2)| < 1$, a better fit is given to the data by the predictions provided by HERWIG. In Figure 5.12, $\left(\frac{\chi^2}{d.o.f}\right)_{\texttt{HERWIRI}} = 2.00$ and $\left(\frac{\chi^2}{d.o.f}\right)_{\texttt{HERWIG}} = 1.98$. In Figure 5.13, $\left(\frac{\chi^2}{d.o.f}\right)_{\texttt{HERWIRI}} = 0.48$ and $\left(\frac{\chi^2}{d.o.f}\right)_{\texttt{HERWIG}} = 1.04$. In Figure 5.13, the data is well modeled by the predictions provided by both HERWIRI and HERWIG although the theoretical predictions provided by HERWIRI are closer to the data in many cases. In Figure 5.13, $\left(\frac{\chi^2}{d.o.f}\right)_{\texttt{HERWIRI}} = 0.48$ and $\left(\frac{\chi^2}{d.o.f}\right)_{\texttt{HERWIG}} = 1.04$.

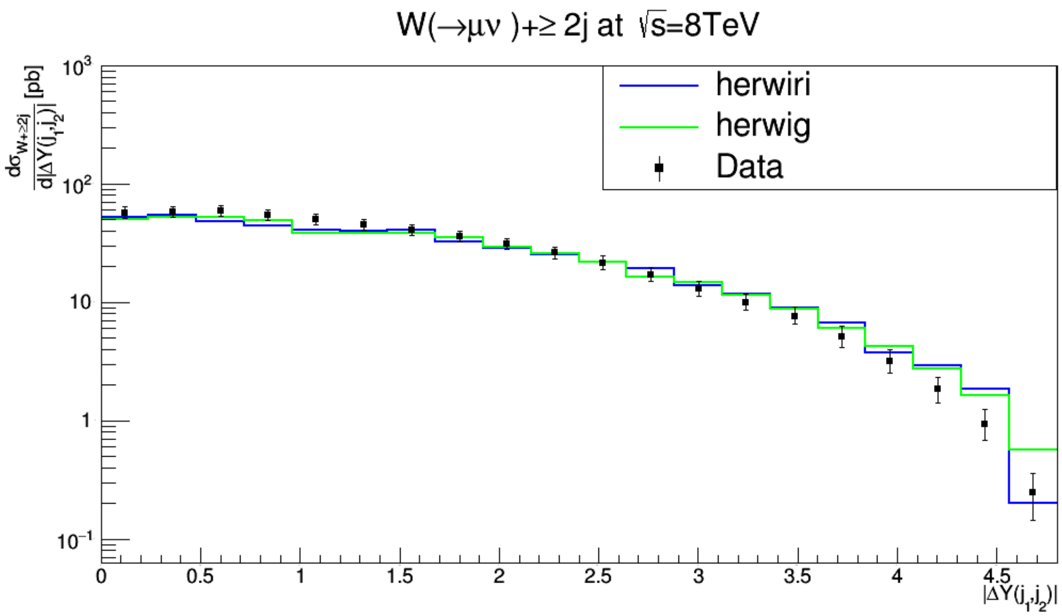

Figure 5.12: Cross section for the production of W + jets as a function of difference is rapidity $|\Delta Y(j_1, j_2)|$ in $N_{jet} \geq 2$. The data are compared to predictions from MADGRAPH5_aMC@NLO/HERWIRI1.031 and MADGRAPH5_aMC@NLO/HERWIG6.521.

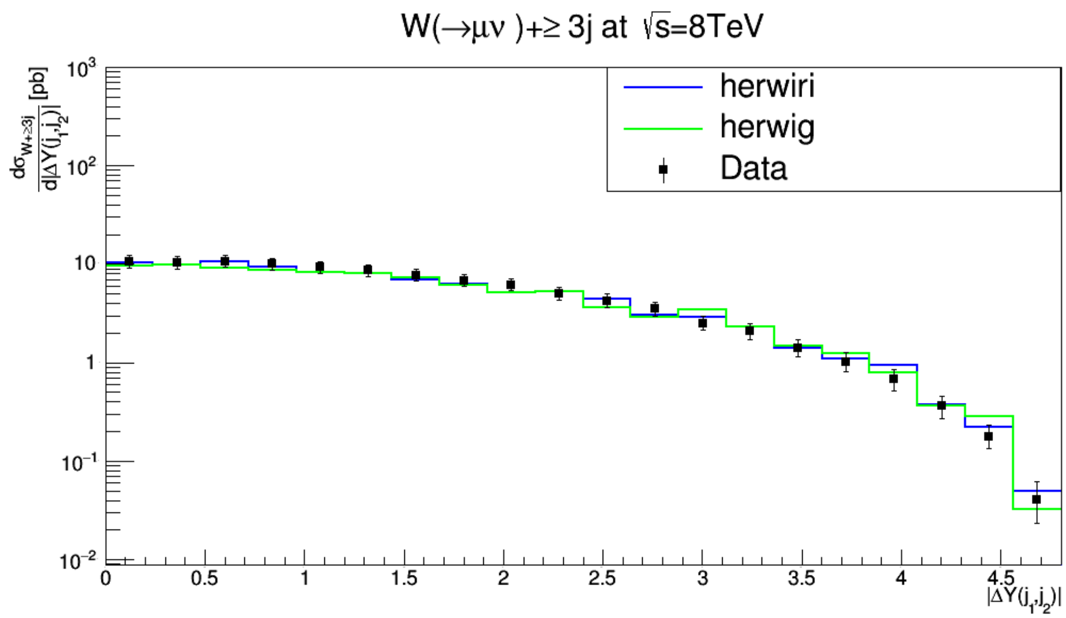

Figure 5.13: Cross section for the production of W + jets as a function of difference is rapidity $|\Delta Y(j_1, j_2)|$ in $N_{jet} \geq 3$. The data are compared to predictions from MADGRAPH5_aMC@NLO/HERWIRI1.031 and MADGRAPH5_aMC@NLO/HERWIG6.521.

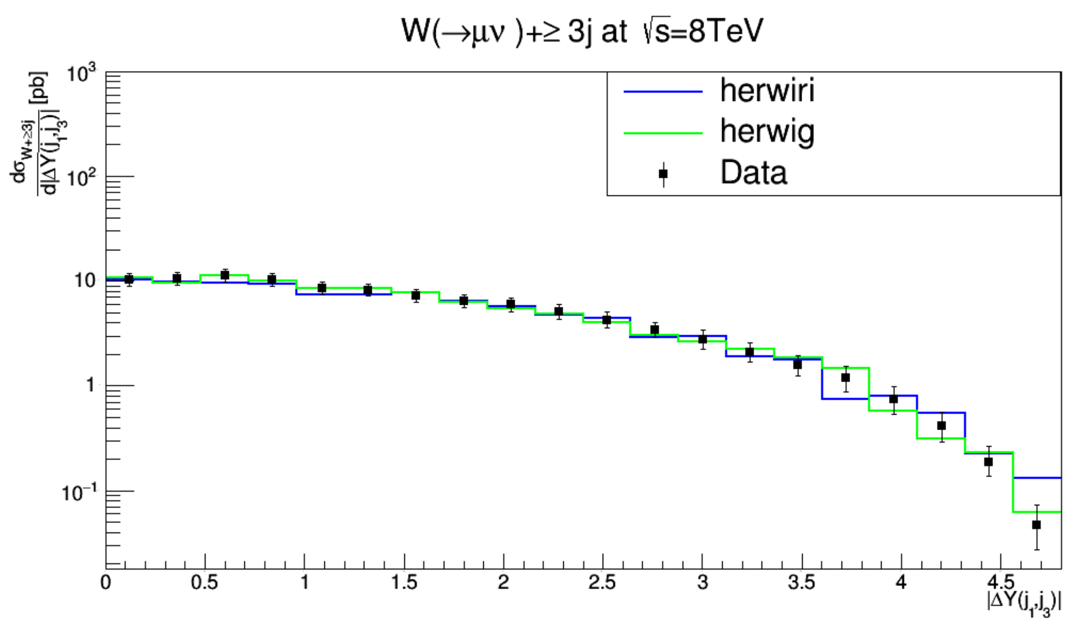

Figure 5.14: Cross section for the production of W + jets as a function of difference is rapidity $|\Delta Y(j_1, j_2)|$ in $N_{jet} \geq 2$. The data are compared to predictions from MADGRAPH5_aMC@NLO/HERWIRI1.031 and MADGRAPH5_aMC@NLO/HERWIG6.521.

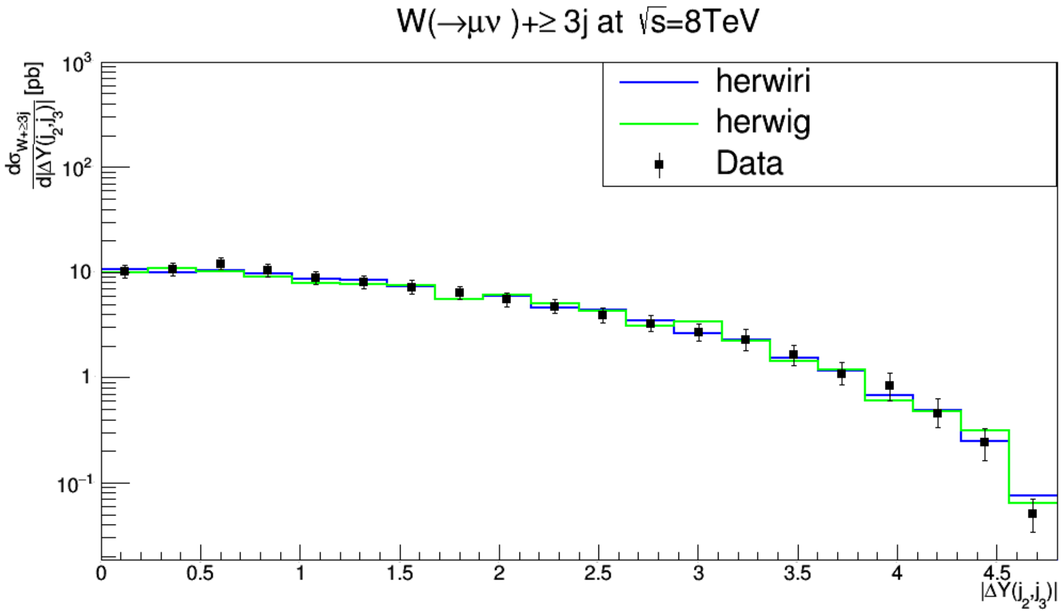

Figure 5.15: Cross section for the production of W + jets as a function of difference is rapidity $|\Delta Y(j_2, j_3)|$ in $N_{jet} \geq 3$. The data are compared to predictions from MADGRAPH5_aMC@NLO/HERWIRI1.031 and MADGRAPH5_aMC@NLO/HERWIG6.521.

In Figure 5.14 and Figure 5.15, cross sections are presented as functions of difference in rapidity for inclusive jet multiplicity 3. In both cases, the data is well modeled by the predictions provided by both HERWIRI and HERWIG. In many cases HERWIRI predictions are closer to the data. In Figure 5.14, $\left(\frac{\chi^2}{d.o.f}\right)_{\texttt{HERWIRI}} = 1.20$ and $\left(\frac{\chi^2}{d.o.f}\right)_{\texttt{HERWIG}} = 0.56$. In Figure 5.15, $\left(\frac{\chi^2}{d.o.f}\right)_{\texttt{HERWIRI}} = 0.33$ and $\left(\frac{\chi^2}{d.o.f}\right)_{\texttt{HERWIG}} = 0.52$.

5.2.6 Dijet Invariant Mass Distributions

The cross sections are shown as functions of the dijet invariant mass calculated from the two leading jets for inclusive jet multiplicities 2–3. The dijet invariant mass is defined as

$$m(j_1, j_2) = \sqrt{(E_{j_1} + E_{j_2})^2 - (\vec{P}_{j_1} + \vec{P}_{j_2})^2} = \sqrt{m_{j_1}^2 + m_{j_2}^2 + 2(E_{j_1}E_{j_2} - \vec{P}_{j_1} \cdot \vec{P}_{j_2})}, \tag{5.10}$$

where the leading jet is defined as $j_1^\mu = (E_{j_1}, \vec{P}_{j_1})$.

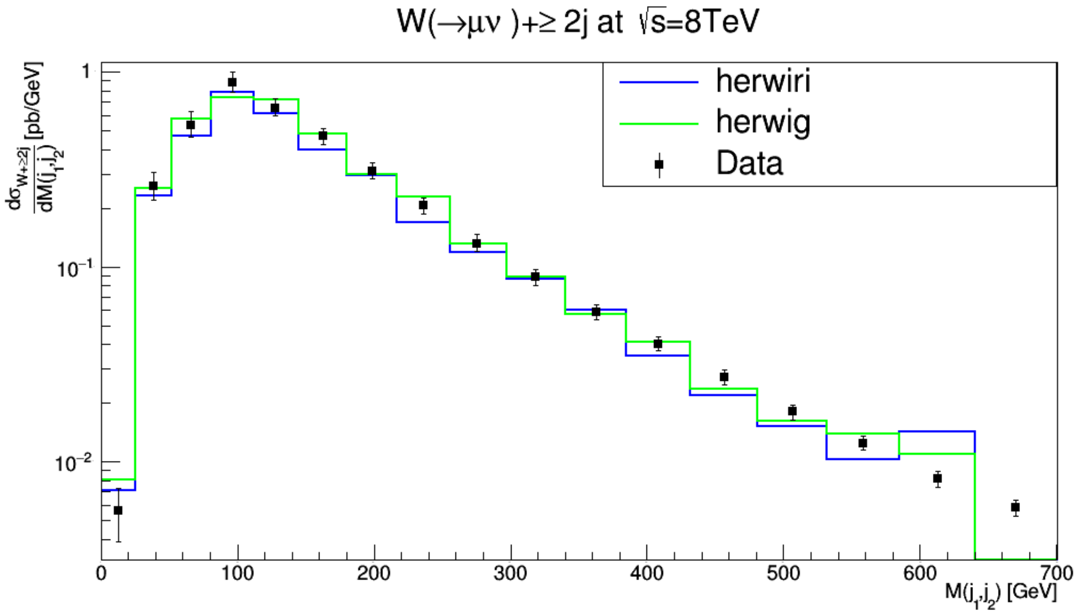

Figure 5.16: Cross section for the production of W + jets as a function of dijet invariant mass $|M(j_1, j_2)|$ in $N_{jet} \geq 2$. The data are compared to predictions from MADGRAPH5_aMC@NLO/HERWIRI1.031 and MADGRAPH5_aMC@NLO/HERWIG6.521.

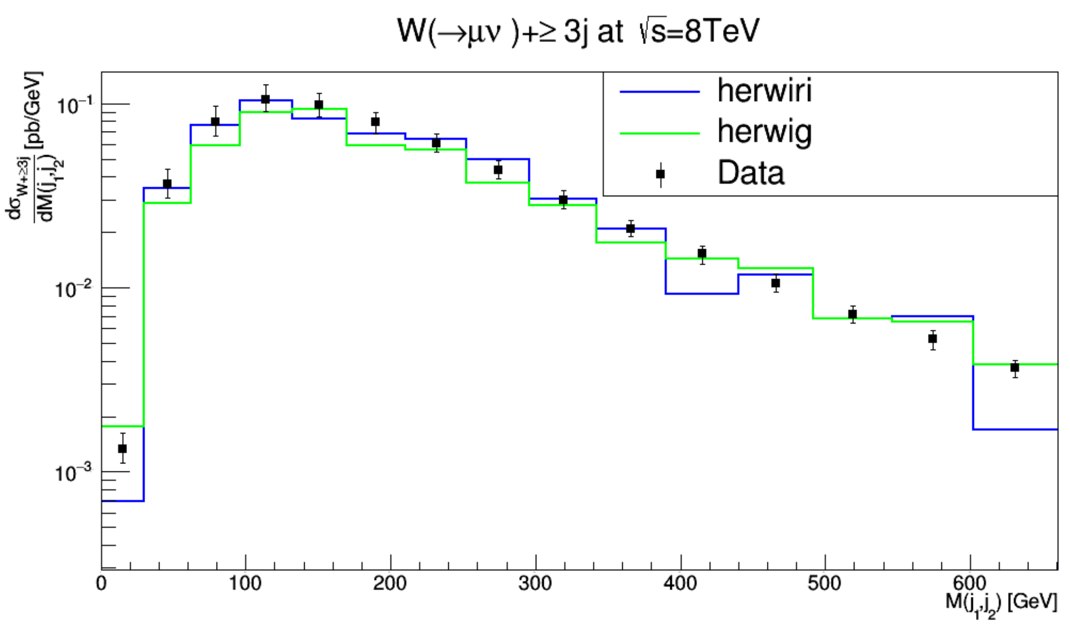

Figure 5.17: Cross section for the production of W + jets as a function of dijet invariant mass $|M(j_1, j_2)|$ in $N_{jet} \geq 3$. The data are compared to predictions from MADGRAPH5_aMC@NLO/HERWIRI1.031 and MADGRAPH5_aMC@NLO/HERWIG6.521.

In Figure 5.16 and Figure 5.17, the cross sections are shown as functions of the dijet invariant mass for inclusive jet multiplicities 2–3. In Figure 5.16, a good fit is provided by HERWIRI predictions to the data for $\Delta M(j_1, j_2) \leq 200$ GeV while for $200 < \Delta M(j_1, j_2) < 300$ GeV, HERWIG gives a better fit to the data. For higher values of ΔM, the predictions provided by HERWIG are in better agreement with the data. In Figure 5.17, a better fit is provided by HERWIRI to the data for $50 < \Delta M(j_1, j_2) < 400$ GeV. For higher values of ΔM, HERWIG predictions either overlap with the data or are closer to the data. In Figure 5.16, $\left(\frac{\chi^2}{d.o.f}\right)_{\texttt{HERWIRI}} = 1.85$ and $\left(\frac{\chi^2}{d.o.f}\right)_{\texttt{HERWIG}} = 0.73$. In Figure 5.17, $\left(\frac{\chi^2}{d.o.f}\right)_{\texttt{HERWIRI}} = 4.19$ and $\left(\frac{\chi^2}{d.o.f}\right)_{\texttt{HERWIG}} = 1.95$.

5.2.7 Dijet Angular Separation Distribution

The cross section is shown as a function of the angular separation between the two leading jets for jet inclusive multiplicity 2. The angular separation between the two leading jets is defined as

$$\Delta R(j_1, j_2) = \sqrt{(\Delta\phi(j_1, j_2)^2 + \Delta Y(j_1, j_2)^2}, \tag{5.11}$$

where $\Delta Y(j_1, j_2) = Y_{j_1} - Y_{j_2}$ and $\Delta\phi(j_1, j_2) = \phi(j_1) - \phi(j_1)$.

Figure 5.18 shows the cross section as a function of angular separation between the first two leading jets for inclusive jet multiplicity 2. For $2 < \Delta R(j_1, j_2) < 4.5$, HERWIRI predictions are in better agreement with the data. A better fit is provided to the data by HERWIG predictions for $\Delta R(j_1, j_2) < 2$. In Figure 5.18, $\left(\frac{\chi^2}{d.o.f}\right)_{\texttt{HERWIRI}} = 3.06$ and $\left(\frac{\chi^2}{d.o.f}\right)_{\texttt{HERWIG}} = 2.16$.

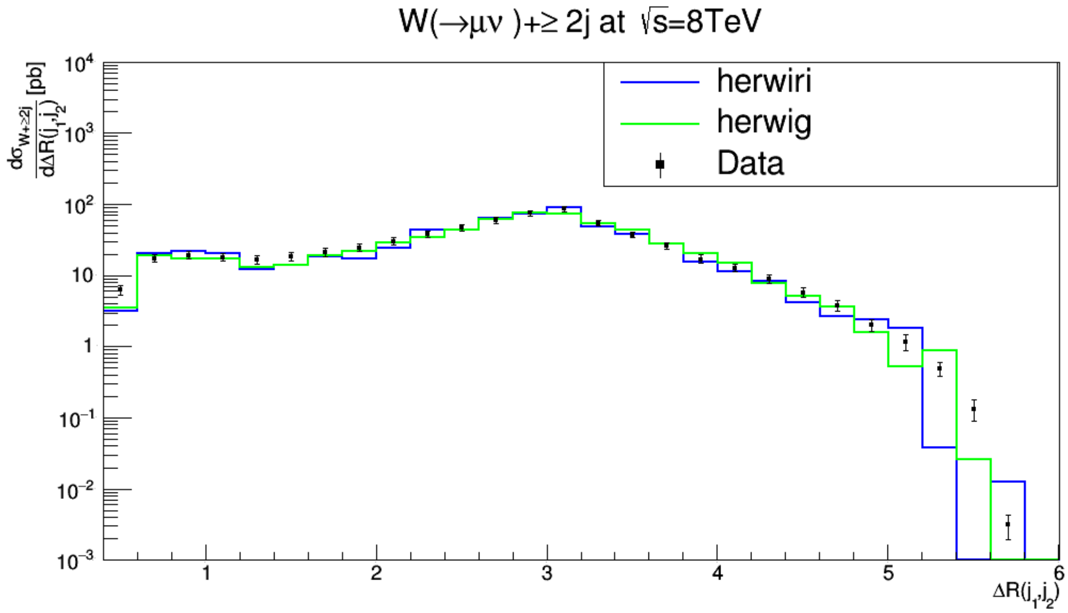

Figure 5.18: Cross section for the production of W + jets as a function of the angular separation between the two leading jets $\Delta R(j_1, j_2)$ in $N_{jet} \geq 2$. The data are compared to predictions from MADGRAPH5_aMC@NLO/HERWIRI1.031 and MADGRAPH5_aMC@NLO/HERWIG6.521.

5.2.8 Azimuthal Angular Distribution

The differential cross section is given as a function of the difference in azimuthal angle $\Delta\Phi(j_1, j_2)$ for an inclusive jet multiplicity 2. In Figure 5.19, the data is well modeled by the predictions provided by HERWIRI. In Figure 5.19, $\left(\frac{\chi^2}{d.o.f}\right)_{\texttt{HERWIRI}} = 0.81$ and $\left(\frac{\chi^2}{d.o.f}\right)_{\texttt{HERWIG}} = 0.97$.

The azimuthal angular distribution between the first and second leading jet is defined as

$$\cos(\Delta\Phi(j_1, j_2)) = \frac{P_x(j_1)P_x(j_2) + P_y(j_1)P_y(j_2)}{\sqrt{P_x^2(j_1) + P_y^2(j_1)}\sqrt{P_x^2(j_2) + P_y^2(j_2)}} \qquad (5.12)$$

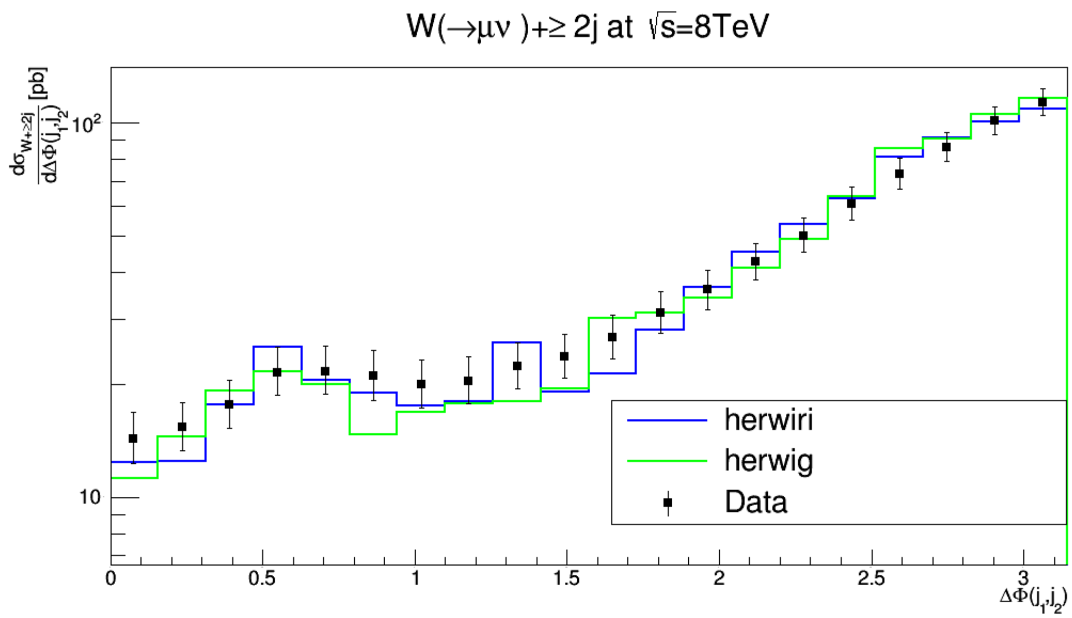

Figure 5.19: Cross section for the production of W + jets as a function of the difference in azimuthal angle between the two leading jets $\Delta\Phi(j_1, j_2)$ in $N_{jet} \geq 2$. The data are compared to predictions from MADGRAPH5_aMC@NLO/HERWIRI1.031 and MADGRAPH5_aMC@NLO/HERWIG6.521.

5.2.9 The Azimuthal Angular Distribution Between the Muon and the Leading Jet

The differential cross sections are shown as functions of the azimuthal angle between the muon and the first three leading jets for inclusive jet multiplicities 1–3. The azimuthal angle between the muon and the leading jet is defined as

$$\cos(\Delta\Phi(\mu, j_1)) = \frac{P_x(\mu)P_x(j_1) + P_y(\mu)P_y(j_1)}{\sqrt{P_x^2(\mu) + P_y^2(\mu)}\sqrt{P_x^2(j_1) + P_y^2(j_1)}}, \tag{5.13}$$

with

$$\begin{cases} \mu^\mu = (E_\mu, P_x(\mu), P_y(\mu), P_L(\mu)), \\ j_1^\mu = (E_{j_1}, P_x(j_1), P_y(j_1), P_L(j_1)), \end{cases} \tag{5.14}$$

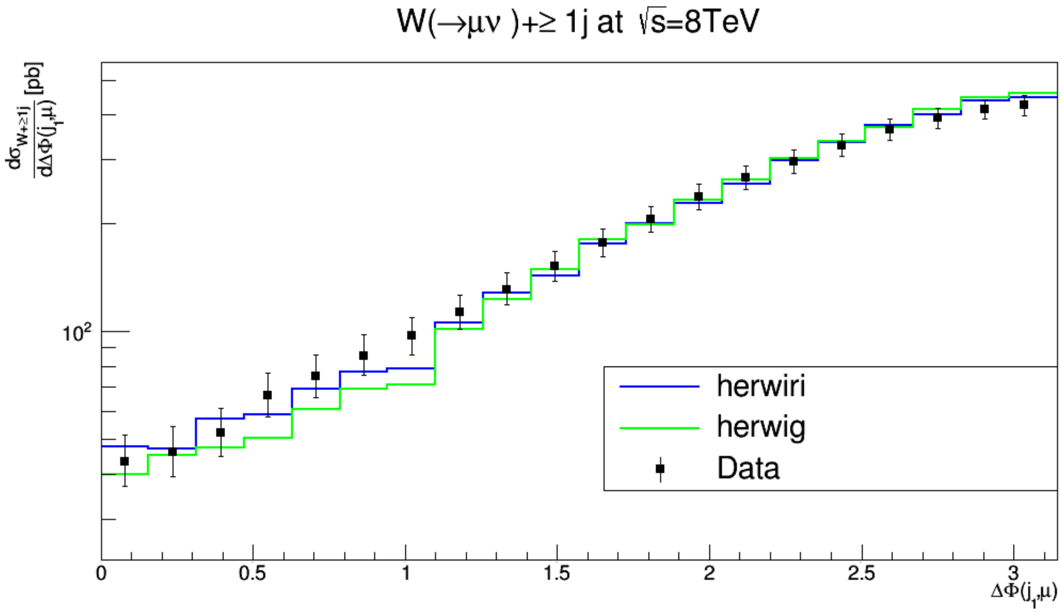

Figure 5.20: Cross section for the production of W + jets as a function of the azimuthal angle between the muon and the leading jet $\Delta\Phi(\mu, j_1)$ in $N_{jet} \geq 1$. The data are compared to predictions from MADGRAPH5_aMC@NLO/HERWIRI1.031 and MADGRAPH5_aMC@NLO/HERWIG6.521.

In Figure 5.20, Figure 5.21, and Figure 5.22 the data are better modeled by the predictions provided by HERWIRI as expected. In Figure 5.20, $\left(\frac{\chi^2}{d.o.f}\right)_{\texttt{HERWIRI}} = 0.42$ and $\left(\frac{\chi^2}{d.o.f}\right)_{\texttt{HERWIG}} = 0.98$. In Figure 5.21, $\left(\frac{\chi^2}{d.o.f}\right)_{\texttt{HERWIRI}} = 0.80$ and $\left(\frac{\chi^2}{d.o.f}\right)_{\texttt{HERWIG}} = 1.30$. In Figure 5.22, $\left(\frac{\chi^2}{d.o.f}\right)_{\texttt{HERWIRI}} = 0.92$ and $\left(\frac{\chi^2}{d.o.f}\right)_{\texttt{HERWIG}} = 0.95$.

5.2.10 Cross Sections

The measured $W(\rightarrow \mu\nu_\mu)$ + jets fiducial cross sections for inclusive and exclusive jet multiplicity distributions are shown in Figure 5.23 and Figure 5.24, respectively. For inclusive jet multiplicity a good fit is given to the data by the theoretical predictions provided by HERWIRI and HERWIG. On the other hand, in Figure 5.24, HERWIG gives a better fit to the measured cross sections for exclusive jet multiplicity 0–4. In Figure 5.23, $\left(\frac{\chi^2}{d.o.f}\right)_{\texttt{HERWIRI}} = 3.05$ and $\left(\frac{\chi^2}{d.o.f}\right)_{\texttt{HERWIG}} = 2.98$. In Figure 5.24, $\left(\frac{\chi^2}{d.o.f}\right)_{\texttt{HERWIRI}} = 5.37$ and $\left(\frac{\chi^2}{d.o.f}\right)_{\texttt{HERWIG}} = 2.19$.

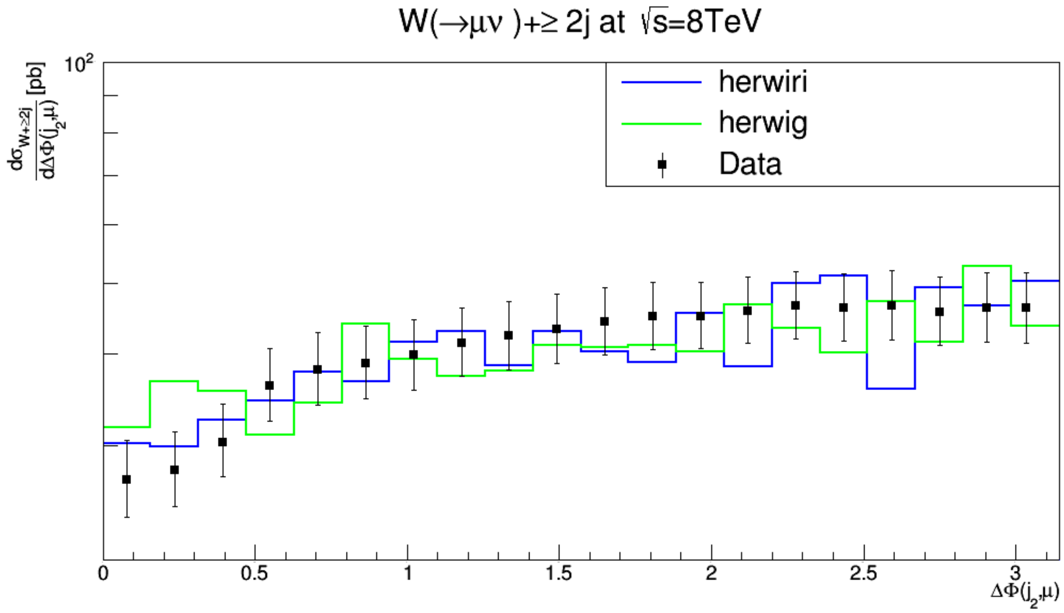

Figure 5.21: Cross section for the production of W + jets as a function of the azimuthal angle between the muon and the second leading jet $\Delta\Phi(\mu, j_2)$ in $N_{jet} \geq 2$. The data are compared to predictions from MADGRAPH5_aMC@NLO/HERWIRI1.031 and MADGRAPH5_aMC@NLO/HERWIG6.521.

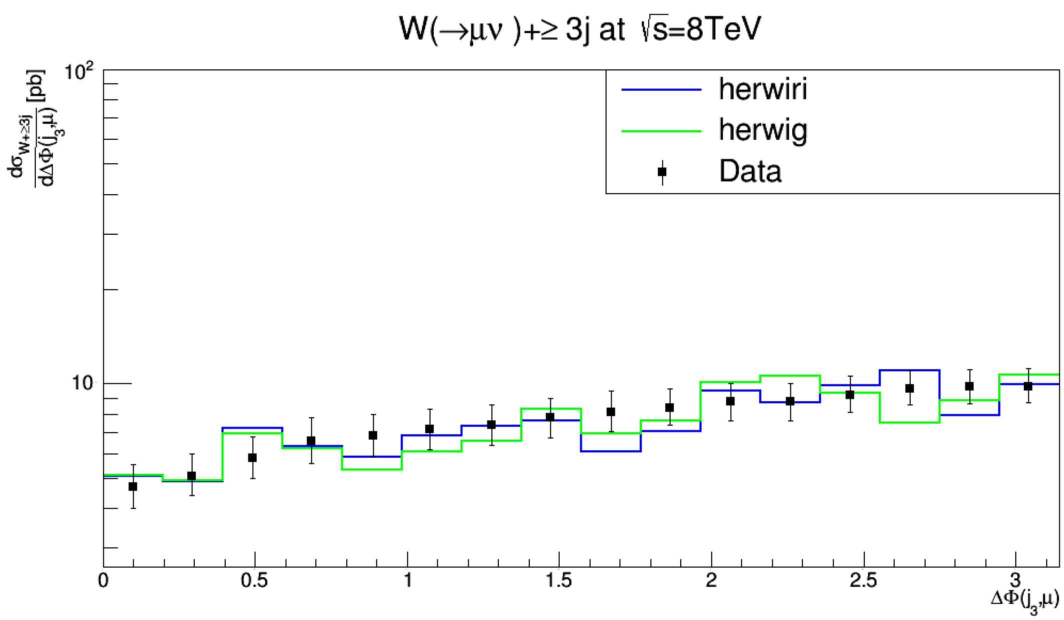

Figure 5.22: Cross section for the production of W + jets as a function of the azimuthal angle between the muon and the second leading jet $\Delta\Phi(\mu, j_2)$ in $N_{jet} \geq 3$. The data are compared to predictions from MADGRAPH5_aMC@NLO/HERWIRI1.031 and MADGRAPH5_aMC@NLO/HERWIG6.521.

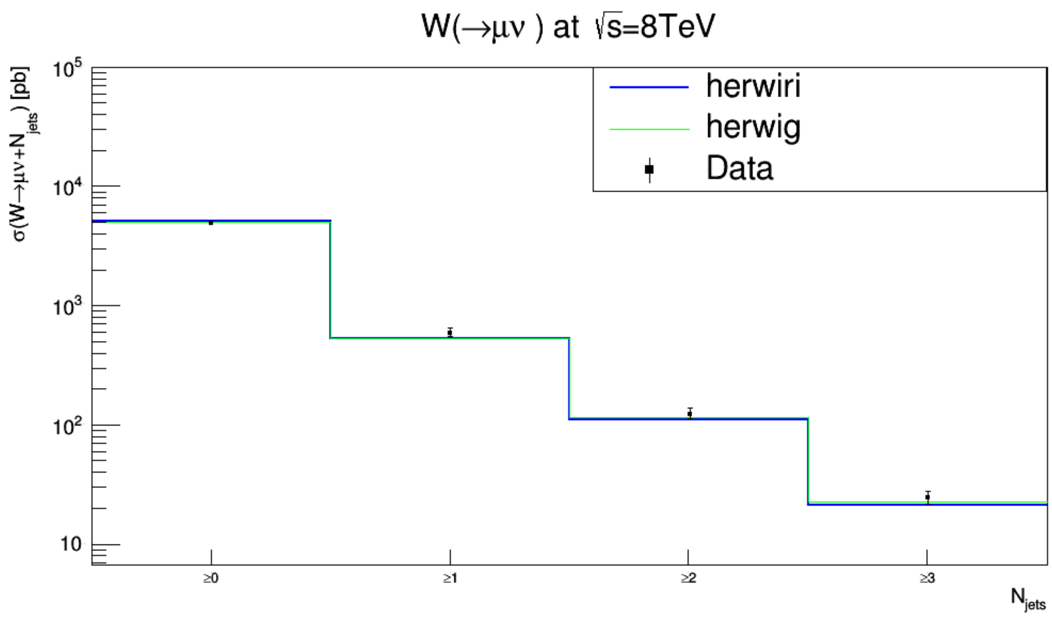

Figure 5.23: Measured cross section versus inclusive jet multiplicity. The data are compared to predictions from MADGRAPH5_aMC@NLO/HERWIRI1.031 and MADGRAPH5_aMC@NLO/HERWIG6.521.

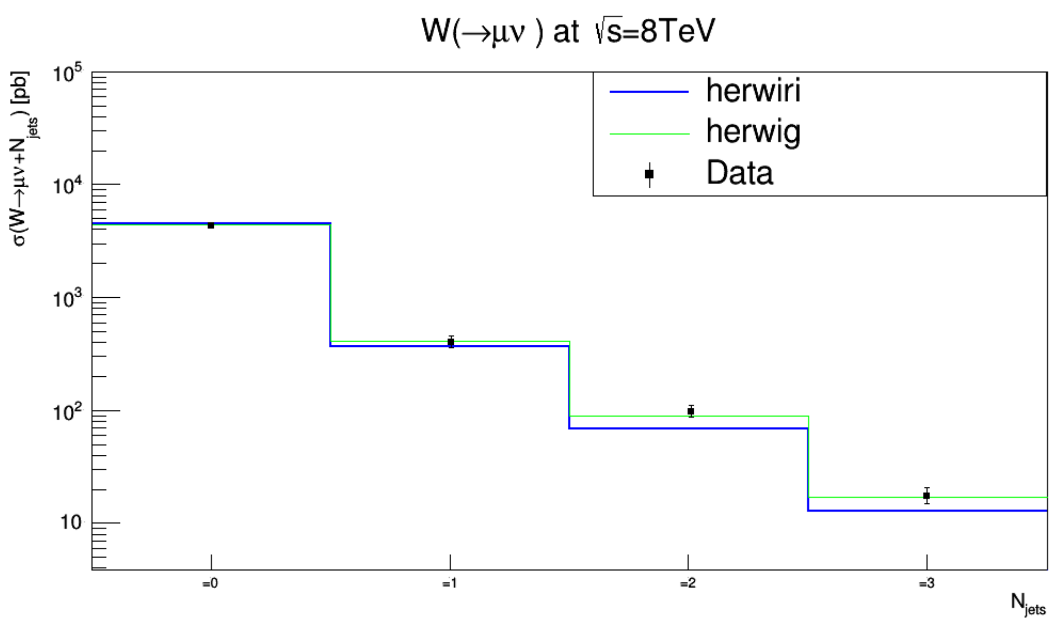

Figure 5.24: Measured cross section versus exclusive jet multiplicity. The data are compared to predictions from MADGRAPH5_aMC@NLO/HERWIRI1.031 and MADGRAPH5_aMC@NLO/HERWIG6.521.

5.3 *Summary*

The realization of the IR-improved DGLAP-CS theory, when used in the MADGRAPH5_aMC@NLO/HERWIRI1.031 $\mathcal{O}(\alpha)$ ME-matched parton shower framework, provides us with the opportunity to explain the differential cross sections for a W boson produced in association with jets in pp collisions in the recent LHC data from CMS, without the need of an unexpectedly hard intrinsic Gaussian distribution with an rms value of PTRMS = 2.2 GeV in parton's wave function. In our view, this can be interpreted as providing a rigorous basis for the phenomenological correctness of such unexpectedly hard distributions insofar as describing these data using the usual unimproved DGLAP-CS showers is concerned.

CHAPTER SIX

IR-improved DGLAP-CS Parton Shower Effects for Associated Production of a W Boson and Jets in pp Collisions at $\sqrt{s} = 13$ TeV

6.1 *Event Generation, Analysis and Cuts (CMS Collaboration)*

The generators for W + jet events are MADGRAPH5_aMC@NLO [79] interfaced with HERWIG6.521 and HERWIRI1.031, which use next-to-leading-order (NLO) matrix element calculations. The number of events generated for the W, W + 1 jet, W + 2 jets, and W + 3 jets processes are 10^7, 10^6, 10^5, and 10^5, respectively. These events are showered by MADGRAPH5_aMC@NLO/HERWIRI1.031 (PTRMS = 0) and MADGRAPH5_aMC@NLO/HERWIG6.521 (PTRMS = 2.2 GeV). During the analysis, jets were reconstructed using the anti-k_t algorithm with $R = 0.5$ with FastJet [80] and the cuts in Table 6.1 were imposed.

Table 6.1: Kinematic criteria defining the fiducial phase space for the $W \to \mu + \nu_\mu$ channel

Muon channel	$(W \to \mu + \nu_\mu)$
Lepton P_T^μ	$P_T^\mu > 25$ GeV
Lepton rapidity η_μ	$\lvert\eta_\mu\rvert < 2.1$
Missing transverse energy	$E_T^{miss} > 25$ GeV
Transverse mass	$m_T > 50$ GeV
Jet algorithm	Anti-k_T
Radius parameter R	$R = 0.5$
Jet P_T^{jet}	$P_T^{jet} > 30$ GeV
Jet rapidity Y_{jet}	$\lvert Y_{jet}\rvert < 2.4$
Jet isolation	$\Delta R(\mu, \text{jet}) > 0.5$ (jet is removed)

The transverse mass, m_T, is defined as $m_T = \sqrt{2P_T^\mu P_T^{\nu_\mu}(1 - \cos\Delta\phi)}$ where $\Delta\phi$ is the difference in the azimuthal angle between the direction of the muon momentum and the associated muon neutrino, ν_μ, which can be written as

$$\Delta\phi = \phi^{\mu} - \phi^{\nu_\mu}. \tag{6.1}$$

Rapidity is defined as $\frac{1}{2}\ln\left[\frac{E+p_z}{E-p_z}\right]$, where E denotes the energy of the particle and p_z is the longitudinal component of the momentum. Finally, the jet isolation, ΔR, which is a Lorentz invariant quantity, is defined as

$$\Delta R(\mu, \text{jet}) = \sqrt{\Delta\phi^2(\mu, \text{jet}) + \Delta\eta^2(\mu, \text{jet})} \tag{6.2}$$

where

$$\begin{cases} \Delta\phi(\mu, \text{jet}) = \phi_\mu - \phi_{\text{jet}}, \\ \Delta\eta(\mu, \text{jet}) = \eta_\mu - \eta_{\text{jet}}, \\ \eta = -\ln\tan(\frac{\theta}{2}). \end{cases} \tag{6.3}$$

6.1.1 *Transverse Momentum Distributions P_T*

The cross sections differential in jet P_T for inclusive jet multiplicities from 1 to 3 are shown in Figure 6.1, Figure 6.2, and Figure 6.3.

6.1.2 *Cross Sections*

The measured W($\rightarrow \mu\nu_\mu$) + jets fiducial cross sections are shown in Figure 6.4 and Figure 6.5.

6.2 *The Future Work*

The data for the 13 TeV cms energy should be available soon, so we have recorded several expectations in anticipation of their release [84].

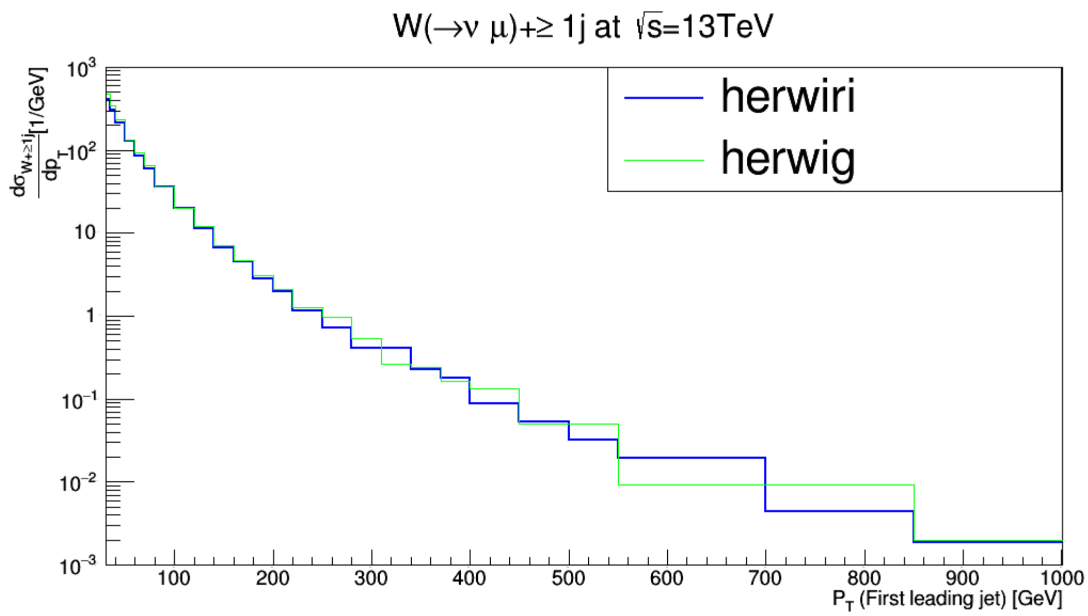

Figure 6.1: Cross section for the production of W + jets as a function of the leading jet P_T in $N_{jet} \geq 1$.

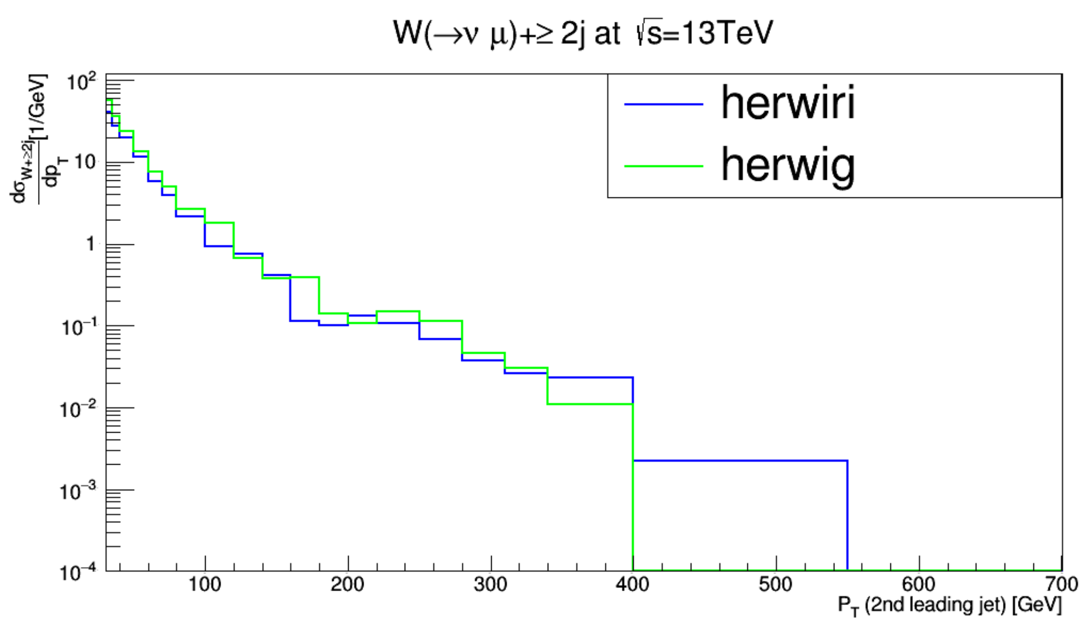

Figure 6.2: Cross section for the production of W + jets as a function of the second leading jet P_T in $N_{jet} \geq 2$.

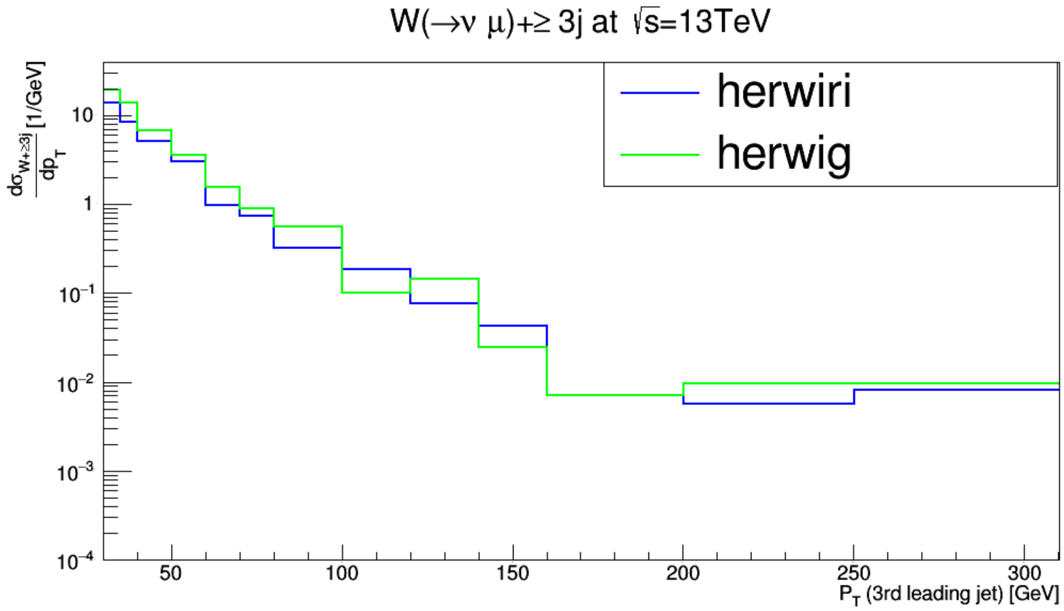

Figure 6.3: Cross section for the production of W + jets as a function of the third leading jet P_T in $N_{jet} \geq 3$.

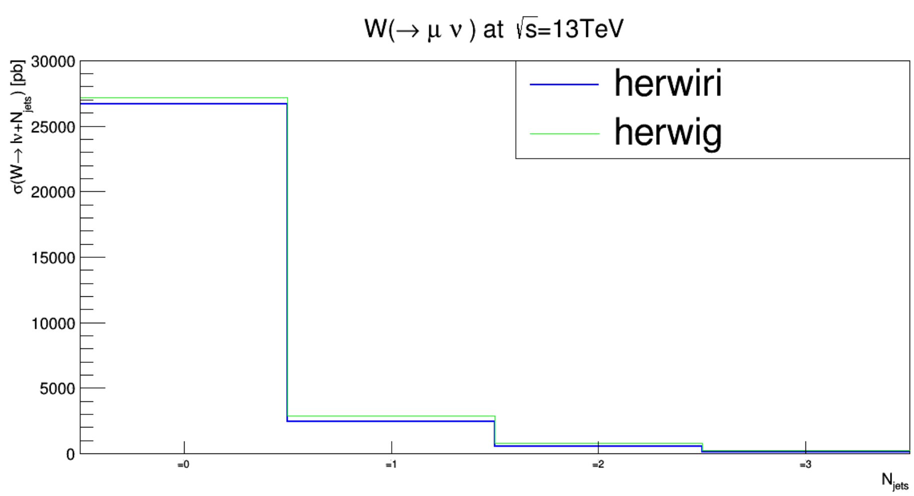

Figure 6.4: Cross sections versus exclusive jet multiplicity.

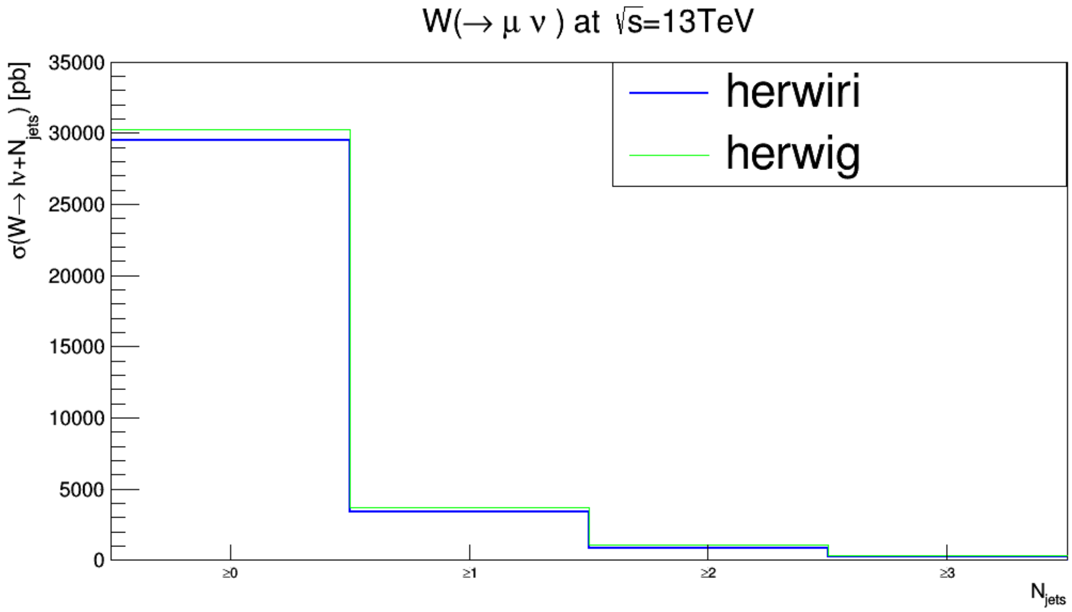

Figure 6.5: Cross sections versus inclusive jet multiplicity.

CHAPTER SEVEN

Overall Summary

In this study, we have made an extensive treatment of the role and interplay of IR-improved DGLAP-CS theory and precision theory for the important processes $pp \to$ W + n jets + X (n = 1, 2, 3) at the LHC cms energies of 7, 8, and 13 TeV. In the cases of 7 and 8 TeV cms energies, we have compared predictions with ATLAS and CMS data. We have found that, as we expected, in general, the IR-improvement of the exact NLO matrix-element matched parton shower predictions in the MADGRAPH5_aMC@NLO framework, with the parton shower realization via HERWIRI1.031 for the IR-improved results and via HERWIG6.5 for the comparison of unimproved results, are closer to the data in the soft regime of spectra such as those for various jet P_T's, H_T, and S_T, as well as for spectra that feature soft correlations such as $\Delta R(j_1, j_2)$. This study therefore shows that the improvement in the description of the soft regime of the single Z/γ^* production process at LHC and FNAL by the IR-improved exact NLO ME matched parton shower predictions, achieved by HERWIRI1.031 in the MC@NLO framework, in the observables such as the Z/γ^* P_T extends to the various observables in the processes $pp \to$ W + n jets + X at the LHC at 7 and 8 TeV (n = 1, 2, 3). The data for the 13 TeV cms energy should be available soon, so we have recorded several expectations in anticipation of their release [84].

We conclude by emphasizing that this study is the first study of IR-improvement effects in which the observables of jets are analyzed. Previous studies in Refs. [3,78,85] used lepton observables to probe the role of IR-improvement in precision physics studies at high energy colliding beam devices. What we see is that the IR-improvement effects are not washed out, in general, by soft strong interactions inherent in the hadronization processes that are involved in the transition from partons to hadrons in jets. This is consistent with the overall space-time view of the hard hadron-hadron collision, wherein the IR-improvement implemented on the partons in the hard subprocess occurs before these partons are hadronized to make the observable hadrons in jets. The jet observables should therefore be good probes of IR-improvement. Given the importance of the $pp \to \mathrm{W} + n$ jets + X processes for new physics searches, for example, our results argue strongly for the use of IR-improved results in analyzing their soft regimes. A complete precision study has to correctly predict both the hard and the soft regimes of the various observables.

APPENDICES

APPENDIX A

Group Theory

A.1 SU(3)

A.1.1 SU(3) Generators

$$\lambda_1 = \begin{pmatrix} 0 & 1 & 0 \\ 1 & 0 & 0 \\ 0 & 0 & 0 \end{pmatrix}, \quad \lambda_2 = \begin{pmatrix} 0 & -i & 0 \\ i & 0 & 0 \\ 0 & 0 & 0 \end{pmatrix}, \quad \lambda_3 = \begin{pmatrix} 1 & 0 & 0 \\ 0 & -1 & 0 \\ 0 & 0 & 0 \end{pmatrix}$$
$$\lambda_4 = \begin{pmatrix} 0 & 0 & 1 \\ 0 & 0 & 0 \\ 1 & 0 & 0 \end{pmatrix}, \quad \lambda_5 = \begin{pmatrix} 0 & 0 & -i \\ 0 & 0 & 0 \\ i & 0 & 0 \end{pmatrix}, \quad \lambda_6 = \begin{pmatrix} 0 & 0 & 0 \\ 0 & 0 & 1 \\ 0 & 1 & 0 \end{pmatrix} \tag{A.1}$$
$$\lambda_7 = \begin{pmatrix} 0 & 0 & 0 \\ 0 & 0 & -i \\ 0 & i & 0 \end{pmatrix}, \quad \lambda_8 = \frac{1}{\sqrt{3}} \begin{pmatrix} 1 & 0 & 0 \\ 0 & 1 & 0 \\ 0 & 0 & -2 \end{pmatrix}$$

A.1.2 Gell-Mann Matrices and Their Properties

$$T_a = \frac{1}{2}\lambda_a \tag{A.2}$$

$$\big[T_a, T_b\big] = i f_{abc} T_c \tag{A.3}$$

$$\big\{T_a, T_b\big\} = \frac{1}{3}\delta_{ab} + d_{abc} T_c \tag{A.4}$$

$$T_a T_b = \frac{1}{2}\Big[\frac{1}{3}\delta_{ab} + (d_{abc} + i f_{abc}) T_c\Big] \tag{A.5}$$

$$T^a_{ij} T^a_{kl} = \frac{1}{2}\big[\delta_{il}\delta_{jk} - \delta_{ij}\delta_{lk}\big] \tag{A.6}$$

$$\mathrm{Tr}(T_a) = 0 \tag{A.7}$$

$$\mathrm{Tr}(T_a T_b) = \frac{1}{2}\delta_{ab} \tag{A.8}$$

$$\mathrm{Tr}(T_a T_b T_c) = \frac{1}{4}(d_{abc} + i f_{abc}) \tag{A.9}$$

$$\mathrm{Tr}(T_a T_b T_a T_c) = -\frac{1}{12}\delta_{bc} \tag{A.10}$$

A.1.3 The Structure Constants

The structure constants satisfy the following Jacobi identities:

$$f_{abe} f_{ecd} + f_{cbe} f_{aed} + f_{dbe} f_{ace} = 0, \tag{A.11}$$

$$f_{abe} d_{ecd} + f_{cbe} d_{aed} + f_{dbe} d_{ace} = 0. \tag{A.12}$$

Where f_{abc} are antisymmetric $SU(3)$ structure constants with non-zero values given by

$$\begin{gathered} f_{123} = 1, \quad f_{147} = \frac{1}{2}, \quad f_{156} = -\frac{1}{2}, \quad f_{246} = \frac{1}{2}, \quad f_{257} = \frac{1}{2} \\ f_{345} = \frac{1}{2}, \quad f_{367} = -\frac{1}{2}, \quad f_{458} = \frac{\sqrt{3}}{2}, \quad f_{678} = \frac{\sqrt{3}}{2}. \end{gathered} \tag{A.13}$$

A.1.4 Some Definition and Terminology

Let T_a and T_b be the n-dimensional representation matrix and we define $T_n(R)$ and $C_2(n)$ by

$$\mathrm{Tr}(T_n^a T_n^b) = T_R(n)\delta^{ab} \tag{A.14}$$

$$T \cdot T = C_2(n)\ I \tag{A.15}$$

By convention, the normalization of the $SU(N)$ matrix is chosen to be $T_F \equiv T_R(n = N) = \frac{1}{2}$. With this choice, the $SU(N)$ matrices satisfy the following relations

$$T_F \equiv T_R(N_F) = \frac{1}{2} \tag{A.16}$$

$$T_R(N_A) = N \tag{A.17}$$

$$C_F \equiv C_2(N_F) = \frac{N^2 - 1}{N} \tag{A.18}$$

$$C_A = C_2(N_A) = N, \tag{A.19}$$

where subscript F denotes fundamental $n = N_F = N$ and A denotes adjoint ($n = N_A = N^2 - 1$).

APPENDIX B

The Plus Functions

B.1 Definition

The plus functions are well behaved if and only if convoluted with a smooth function that vanishes rapidly as $x \to 1$.

B.2 Property

They have the property that

$$\int_0^1 \big[F(x)\big]_+ = 0 \tag{B.1}$$

and are defined as follows

$$\big[F(x)\big]_+ \equiv \lim_{\beta\to 0}\left\{F(x)\theta(1-x-\beta) - \delta(1-x-\beta)\int_0^{1-\beta} F(y)\,dy\right\} \tag{B.2}$$

where

$$\theta(y) = 0 \quad \text{for} \quad y \leq 0, \tag{B.3}$$

$$\theta(y) = 1 \quad \text{for} \quad y \geq 0. \tag{B.4}$$

B.3 Famous Plus Functions

$$\frac{1}{(1-x)_+} \equiv \lim_{\beta\to 0}\left\{\frac{1}{(1-x)}\theta(1-x-\beta) + \delta(1-x-\beta)\log\beta\right\} \tag{B.5}$$

$$\left(\frac{\log(1-x)}{1-x}\right)_+ \equiv \lim_{\beta\to 0}\left\{\frac{\log(1-x)}{(1-x)}\theta(1-x-\beta) + \delta(1-x-\beta)\frac{1}{2}\log^2\beta\right\}. \tag{B.6}$$

B.4 Useful Identity

$$(1-z)^{a-1} = \frac{1}{a}\delta(1-z) + \frac{1}{(1-z)_+} + \sum_{j=1}^{\infty}\frac{a^j}{j!}\left[\frac{\log^j(1-z)}{1-z}\right] \tag{B.7}$$

APPENDIX C

Decomposition of Momentum

In this appendix we find the the decomposition of momentum in the p_∞ frame for massless particles.

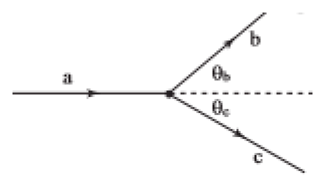

Figure C.1: Diagram for a process that emits an extra parton (denoted as c) in the final state. Parton b carries fraction z of the momentum of parton a [4].

We define variables in the infinite momentum frame as follows

$$P_a^\mu = (E_a, \vec{0}, P_{za}) \tag{C.1}$$

$$P_b^\mu = (E_b, \vec{P_T}, P_{zb}) \tag{C.2}$$

$$P_c^\mu = (E_c, -\vec{P_T}, P_{zc}), \tag{C.3}$$

where $P_a^2 = P_b^2 = P_c^2 = 0$ and $E_a = p$. We find

$$P_{zb} = zp = zP_{za} \ \rightarrow \ \frac{P_{zb}}{P_{za}} = z \tag{C.4}$$

$$P_{zc} = (1-z)p = (1-z)P_{za} \ \rightarrow \ \frac{P_{zc}}{P_{za}} = (1-z) \tag{C.5}$$

$$\theta = \theta_b + \theta_c. \tag{C.6}$$

We can rewrite eqs. (C.1), (C.2), and (C.3)

$$P_a^\mu = (E_a, \vec{0}, p) \tag{C.7}$$

$$P_b^\mu = (E_b, \vec{P_T}, pz) \tag{C.8}$$

$$P_c^\mu = (E_c, -\vec{P_T}, p(1-z)). \tag{C.9}$$

If we use the fact that we neglected the mass of partons, it can be shown that

$$P_a^2 = 0 \;\rightarrow\; E_a^2 - p^2 = 0 \tag{C.10}$$

$$P_b^2 = 0 \;\rightarrow\; E_b^2 - |P_T|^2 - p^2 z^2 = 0 \tag{C.11}$$

$$P_c^2 = 0 \;\rightarrow\; E_c^2 - |P_T|^2 - (1-z)^2 p^2 = 0. \tag{C.12}$$

We solve eqs. (C.10), (C.11), and (C.12) to find the energy of each particle. We obtain

$$E_a = p \tag{C.13}$$

$$E_b = zp\left(1 + \frac{P_T^2}{z^2 p^2}\right)^{\frac{1}{2}} \simeq zp + \frac{P_T^2}{2zp} \tag{C.14}$$

$$E_c = (1-z)p\left(1 + \frac{P_T^2}{(1-z)^2 p^2}\right)^{\frac{1}{2}} \simeq (1-z)p + \frac{P_T^2}{2(1-z)p}. \tag{C.15}$$

We decompose the momentum of each particle into transverse and longitudinal components in the p_∞ frame as follows:

$$P_a^\mu = (p, \vec{0}, p) \tag{C.16}$$

$$P_b^\mu = \left(zp + \frac{P_T^2}{2zp}, \vec{P}_T, zp\right) \tag{C.17}$$

$$P_c^\mu = \left((1-z)p + \frac{P_T^2}{2(1-z)p}, -\vec{P}_T, (1-z)p\right). \tag{C.18}$$

The following equations are very useful for future calculations:

$$\frac{E_B}{E_A} = \frac{zp\left(1 + \frac{P_T^2}{z^2 p^2}\right)}{p} \simeq z + O(P_T^2) \tag{C.19}$$

$$\frac{dP_T^2}{P_T^2} = d(\ln P_T^2). \tag{C.20}$$

We find θ_b and θ_b in Figure C.1.

$$|P_T| = P_{zb} \sin\theta_b \simeq zp\ \theta_b \tag{C.21}$$

$$|P_T| = P_{zc} \sin\theta_c \simeq (1-z)p\ \theta_c \tag{C.22}$$

$$\rightarrow \frac{\theta_b}{1-z} = \frac{\theta_c}{z} \tag{C.23}$$

$$\theta = \theta_b + \theta_c = \frac{\theta_b}{1-z} = \frac{\theta_c}{z}. \tag{C.24}$$

One can easily prove that

$$t = -Q^2 = (P_a - P_c)^2 = \frac{|P_T|^2}{1-z}. \tag{C.25}$$

APPENDIX D

Analysis

```
c
c Example analysis for "p p > e+ ve [QCD]" process.
c Example analysis for "p p > e- ve~ [QCD]" process.
c Example analysis for "p p > mu+ vm [QCD]" process.
c Example analysis for "p p > mu- vm~ [QCD]" process.
c Example analysis for "p p > ta+ vt [QCD]" process.
c Example analysis for "p p > ta- vt~ [QCD]" process.
c
C----------------------------------------------------------------------
      SUBROUTINE RCLOS()
C     DUMMY IF HBOOK IS USED
C----------------------------------------------------------------------
      END


C----------------------------------------------------------------------
      SUBROUTINE HWABEG
C     USER''S ROUTINE FOR INITIALIZATION
C----------------------------------------------------------------------
      INCLUDE 'HERWIG65.INC'
      include 'reweight0.inc'
      integer j,kk,l,i
      character*5 cc(2)
      data cc/'     ','Born '/
      integer nwgt,max_weight,nwgt_analysis
      common/cnwgt/nwgt
      common/c_analysis/nwgt_analysis
      parameter (max_weight=maxscales*maxscales+maxpdfs+1)
      character*15 weights_info(max_weight)
      common/cwgtsinfo/weights_info
c
      call inihist
      nwgt_analysis=nwgt
      do i=1,1
      do kk=1,nwgt_analysis
        l=(kk-1)*16+(i-1)*8
        call mbook(l+1,'total rate '//cc(i)//weights_info(kk),
     &       1.0d0,0.5d0,5.5d0)
        call mbook(l+2,'lep rapidity '//cc(i)//weights_info(kk),
```

```
     &       0.5d0,-5d0,5d0)
          call mbook(l+3,'lep pt '//cc(i)//weights_info(kk),
     &       10d0,0d0,200d0)
          call mbook(l+4,'et miss '//cc(i)//weights_info(kk),
     &       10d0,0d0,200d0)
          call mbook(l+5,'trans. mass '//cc(i)//weights_info(kk),
     &       5d0,0d0,200d0)
          call mbook(l+6,'w rapidity '//cc(i)//weights_info(kk),
     &       0.5d0,-5d0,5d0)
          call mbook(l+7,'w pt '//cc(i)//weights_info(kk),
     &       10d00,0d0,200d0)
          call mbook(l+8,'cphi[l,vl] '//cc(i)//weights_info(kk),
     &       0.05d0,-1d0,1d0)
          call mbook(l+9,'j1 pt5       '//cc(j)//weights_info(kk),
     &       5d0,30d0,40d0)
          call mbook(l+10,'j1 pt10       '//cc(j)//weights_info(kk),
     &       10d0,40d0,80d0)
          call mbook(l+11,'j1 pt20       '//cc(j)//weights_info(kk),
     &       20d0,80d0,160d0)
          call mbook(l+12,'j1 pt40       '//cc(j)//weights_info(kk),
     &       40d0,160d0,200d0)
          call mbook(l+13,'j1 pt50       '//cc(j)//weights_info(kk),
     &       50d0,200d0,250d0)
          call mbook(l+14,'j1 pt60       '//cc(j)//weights_info(kk),
     &       60d0,250d0,310d0)


      enddo
      enddo
 999  END

C----------------------------------------------------------------------
      SUBROUTINE HWAEND
C     USER''S ROUTINE FOR TERMINAL CALCULATIONS, HISTOGRAM OUTPUT, ETC
C----------------------------------------------------------------------
      INCLUDE 'HERWIG65.INC'
      REAL*8 XNORM
      INTEGER I,J,KK,l,nwgt_analysis
      integer NPL
      parameter(NPL=15000)
      common/c_analysis/nwgt_analysis
      OPEN(UNIT=99,FILE='HERLL.TOP',STATUS='UNKNOWN')
      OPEN(UNIT=98,FILE='wptATLAS-ptmp5pti0wrd.DAT',STATUS='NEW')
C XNORM IS SUCH THAT THE CROSS SECTION PER BIN IS IN PB, SINCE THE HERWIG
C WEIGHT IS IN NB, AND CORRESPONDS TO THE AVERAGE CROSS SECTION
```

```
      XNORM=1.D3/DFLOAT(NEVHEP)
      DO I=1,NPL
        CALL MFINAL3(I)
        CALL MCOPY(I,I+NPL)
        CALL MOPERA(I+NPL,'F',I+NPL,I+NPL,(XNORM),0.D0)
        CALL MFINAL3(I+NPL)
      ENDDO
C
       CALL MPRINT(7)
      do i=1,1
      do kk=1,nwgt_analysis
         l=(kk-1)*16+(i-1)*8
         call multitop(NPL+l+1,NPL-1,3,2,'total rate   ',' ','LIN')
         call multitop(NPL+l+2,NPL-1,3,2,'lep rapidity ',' ','LIN')
         call multitop(NPL+l+3,NPL-1,3,2,'lep pt       ',' ','LOG')
         call multitop(NPL+l+4,NPL-1,3,2,'et miss      ',' ','LOG')
         call multitop(NPL+l+5,NPL-1,3,2,'trans. mass  ',' ','LOG')
         call multitop(NPL+l+6,NPL-1,3,2,'w rapidity   ',' ','LIN')
         call multitop(NPL+l+7,NPL-1,3,2,'w pt         ',' ','LOG')
         call multitop(NPL+l+8,NPL-1,3,2,'cphi[l,vl]   ',' ','LOG')
         call multitop(NPL+l+9,NPL-1,2,3,'j1 pt5        ',' ','LOG')
         call multitop(NPL+l+10,NPL-1,2,3,'j1 pt10        ',' ','LOG')
         call multitop(NPL+l+11,NPL-1,2,3,'j1 pt20        ',' ','LOG')
         call multitop(NPL+l+12,NPL-1,2,3,'j1 pt40        ',' ','LOG')
         call multitop(NPL+l+13,NPL-1,2,3,'j1 pt50        ',' ','LOG')
         call multitop(NPL+l+14,NPL-1,2,3,'j1 pt60        ',' ','LOG')




      enddo
      enddo
      CLOSE(99)
      CLOSE(98)
      END

C-----------------------------------------------------------------------
      SUBROUTINE HWANAL
C     USER''S ROUTINE TO ANALYSE DATA FROM EVENT
C-----------------------------------------------------------------------
      INCLUDE 'HERWIG65.INC'
      include 'reweight0.inc'
      DOUBLE PRECISION HWVDOT,PSUM(4),PPV(5),PTW,YW,YE,PPL(5),PPLB(5),
     & PTE,PLL,PTLB,PLLB,var,mtr,etmiss,cphi
      INTEGER ICHSUM,ICHINI,IHEP,IV,IFV,IST,ID,IJ,ID1,JPR,IDENT,
```

```
     #  ILL,ILLB,IHRD,jbfw,IDBSH,ISTBSH
      INTEGER njet,count_j,jpart,MU,NT
      integer maxtrack,maxjet,bahram
      parameter (maxtrack=2048,maxjet=2048)
      integer ntracks,jetvec(maxtrack)
      double precision ptj1,jet_ktradius,jet_ktptmin,palg,getpt,
     &pjet(4,maxtrack),ptrack(4,maxtrack)
      LOGICAL DIDSOF,FOUNDL,FOUNDN,ISL,ISN
      REAL*8 PI,getrapidity
      PARAMETER (PI=3.14159265358979312D0)
      REAL*8 WWW0,TINY,SIGNL,SIGNN
      INTEGER KK,I,L,IL,IN,J
      DATA TINY/.1D-5/
      integer nwgt_analysis,max_weight
      common/c_analysis/nwgt_analysis
      parameter (max_weight=maxscales*maxscales+maxpdfs+1)
      double precision ww(max_weight),www(max_weight)
      common/cww/ww
      data bahram/0/
c
      IF (IERROR.NE.0) RETURN
      IF (WW(1).EQ.0D0) THEN
         WRITE(*,*)'WW(1) = 0. Stopping'
         STOP
      ENDIF
C CHOOSE IDENT = 11 FOR E - NU_E
C        IDENT = 13 FOR MU - NU_MU
C        IDENT = 15 FOR TAU - NU_TAU
      IDENT=11
C INCOMING PARTONS MAY TRAVEL IN THE SAME DIRECTION: IT''S A POWER-SUPPRESSED
C EFFECT, SO THROW THE EVENT AWAY
      IF(SIGN(1.D0,PHEP(3,4)).EQ.SIGN(1.D0,PHEP(3,5)))THEN
        CALL HWWARN('HWANAL',111)
        GOTO 999
      ENDIF
      DO I=1,nwgt_analysis
         WWW(I)=EVWGT*ww(i)/ww(1)
      ENDDO
      CALL HWVSUM(4,PHEP(1,1),PHEP(1,2),PSUM)
      CALL HWVSCA(4,-1D0,PSUM,PSUM)
      ICHSUM=0
      ICHINI=ICHRG(IDHW(1))+ICHRG(IDHW(2))
      DIDSOF=.FALSE.
      FOUNDL=.FALSE.
      FOUNDN=.FALSE.
```

```
      DO 100 IHEP=1,NHEP
        IF (IDHW(IHEP).EQ.16) DIDSOF=.TRUE.
        IF (ISTHEP(IHEP).EQ.1) THEN
          CALL HWVSUM(4,PHEP(1,IHEP),PSUM,PSUM)
          ICHSUM=ICHSUM+ICHRG(IDHW(IHEP))
        ENDIF
        IST=ISTHEP(IHEP)
        ID=IDHW(IHEP)
        ID1=IDHEP(IHEP)
Cbflw=======================================================
        DO jbfw = 1,3
        ISL=ABS(ID1).EQ.IDENT
        ISN=ABS(ID1).EQ.IDENT+1
        IF(((IST.GE.120.AND.IST.LE.125).OR.IST.EQ.1.OR.IST.EQ.198)
     &      .AND.ISL.AND..NOT.FOUNDL)THEN
            IL=IHEP
            FOUNDL=.TRUE.
            SIGNL=SIGN(1D0,DBLE(ID1))
         ENDIF
         IF(((IST.GE.120.AND.IST.LE.125).OR.IST.EQ.1)
     &       .AND.ISN.AND..NOT.FOUNDN)THEN
            IN=IHEP
            FOUNDN=.TRUE.
            SIGNN=SIGN(1D0,DBLE(ID1))
         ENDIF
         IF(.NOT.FOUNDL.OR..NOT.FOUNDN)THEN
         IDENT=IDENT+2
         ENDIF
         ENDDO
         IDENT = 11
Cbflw=========================================================
  100 CONTINUE
      IF(.NOT.FOUNDL.OR..NOT.FOUNDN)THEN
         WRITE(*,*)'NO LEPTONS FOUND.'
         WRITE(*,*)'CURRENTLY THIS ANALYSIS LOOKS FOR'
         IF(IDENT.EQ.11)WRITE(*,*)'E - NU_E'
         IF(IDENT.EQ.13)WRITE(*,*)'MU - NU_MU'
         IF(IDENT.EQ.15)WRITE(*,*)'TAU - NU_TAU'
         WRITE(*,*)'IF THIS IS NOT MEANT,'
         WRITE(*,*)'PLEASE CHANGE THE VALUE OF IDENT IN THIS FILE.'
         STOP
      ENDIF
      IF(SIGNN.EQ.SIGNL)THEN
         WRITE(*,*)'TWO SAME SIGN LEPTONS!'
         WRITE(*,*)IL,IN,SIGNL,SIGNN
```

```
         STOP
      ENDIF
C CHECK MOMENTUM AND CHARGE CONSERVATION
      IF (HWVDOT(3,PSUM,PSUM).GT.1.E-4*PHEP(4,1)**2) THEN
         CALL HWUEPR
         CALL HWWARN('HWANAL',112)
         GOTO 999
      ENDIF
      IF (ICHSUM.NE.ICHINI) THEN
         CALL HWUEPR
         CALL HWWARN('HWANAL',113)
         GOTO 999
      ENDIF
      DO IJ=1,5
        PPL(IJ)=PHEP(IJ,IN)
        PPLB(IJ)=PHEP(IJ,IL)
        PPV(IJ)=PPL(IJ)+PPLB(IJ)
      ENDDO
      ye     = getrapidity(pplb(4), pplb(3))
      yw     = getrapidity(ppv(4), ppv(3))
      pte    = dsqrt(pplb(1)**2 + pplb(2)**2)
      ptw    = dsqrt(ppv(1)**2+ppv(2)**2)
      etmiss = dsqrt(ppl(1)**2 + ppl(2)**2)
      mtr    = dsqrt(2d0*pte*etmiss-2d0*ppl(1)*pplb(1)-2d0*ppl(2)*pplb(2))
      cphi   = (ppl(1)*pplb(1)+ppl(2)*pplb(2))/pte/etmiss
      var    = 1.d0
C INITIALIZE JETS
      NT=0
      NTRACKS=0
      NJET=0
      DO IHEP=1,NHEP
         IF (ISTHEP(IHEP).EQ.1) THEN
            CALL HWVSUM(4,PHEP(1,IHEP),PSUM,PSUM)
            ICHSUM=ICHSUM+ICHRG(IDHW(IHEP))
         ENDIF
         ISTBSH=ISTHEP(IHEP)
         IDBSH=IDHEP(IHEP)
c Define particles that go into jet.
        IF (ISTBSH.EQ.1.AND.ABS(IDBSH).GE.100)THEN
           NTRACKS=NTRACKS+1
           DO MU=1,4
              PTRACK(MU,NTRACKS)=PHEP(MU,IHEP)
           ENDDO
           IF(NTRACKS.EQ.MAXTRACK) THEN
              WRITE(*,*)'HWANAL: TOO MANY PARTICLES, INCREASE MAXTRACK'
```

```
                STOP
             ENDIF
          ENDIF
        ENDDO
         IF (NTRACKS.EQ.0) THEN
            WRITE(*,*) 'NO TRACKS FOUND, DROP ANALYSIS OF THIS EVENT'
            GOTO 999
         ENDIF
CCCCCCCCCCCCCCCCCCCCCCCCCCCCCCCCCCCCCC
C KT ALGORITHM, FASTJET IMPLEMENTATION
CCCCCCCCCCCCCCCCCCCCCCCCCCCCCCCCCCCCCC
      NJET=0
      JET_KTRADIUS = 0.4D0
      JET_KTPTMIN  = 30D0
      PALG=-1D0
      CALL fastjetppgenkt(PTRACK,NTRACKS,JET_KTRADIUS,JET_KTPTMIN,PALG,
     $     PJET,NJET,JETVEC)
c Check that jets are ordered in pt
      do i=1,njet-1
         if (getpt(pjet(1,i)).lt.getpt(pjet(1,i+1)) ) then
            write (*,*) 'ERROR jets not ordered'
            stop
         endif
      enddo
c Choosing The Leading Jet's Pt for njet=3
      if (njet.ge.3) then
      ptj1 = getpt(pjet(1,3))
      endif
c Filling The Histograms

      do i=1,1
         do kk=1,nwgt_analysis
            l=(kk-1)*16+(i-1)*8
            call mfill(l+1,var,www(kk))
            call mfill(l+2,ye,www(kk))
            call mfill(l+3,pte,www(kk))
            call mfill(l+4,etmiss,www(kk))
            call mfill(l+5,mtr,www(kk))
            call mfill(l+6,yw,www(kk))
            call mfill(l+7,ptw,www(kk))
            call mfill(l+8,cphi,www(kk))
c Imposing Rapidity Cut For the Leading Jet, where |y|< 4.4

            if (dabs(getrapidity(pjet(4,1),pjet(3,1))).lt.4.4d0.and.
     &      pte.gt.25d0.and.(dabs(ye).lt.2.5d0).and.etmiss.gt.25d0.and.mtr.gt.40d0) then
```

```
            call mfill(l+9,ptj1,www(kk))
            call mfill(l+10,ptj1,www(kk))
            call mfill(l+11,ptj1,www(kk))
            call mfill(l+12,ptj1,www(kk))
            call mfill(l+13,ptj1,www(kk))
            call mfill(l+14,ptj1,www(kk))

            endif
         enddo
      enddo
 999  END

      function getrapidity(en,pl)
      implicit none
      real*8 getrapidity,en,pl,tiny,xplus,xminus,y
      parameter (tiny=1.d-8)
      xplus=en+pl
      xminus=en-pl
      if(xplus.gt.tiny.and.xminus.gt.tiny)then
         if( (xplus/xminus).gt.tiny.and.(xminus/xplus).gt.tiny)then
            y=0.5d0*log( xplus/xminus  )
         else
            y=sign(1.d0,pl)*1.d8
         endif
      else
         y=sign(1.d0,pl)*1.d8
      endif
      getrapidity=y
      return
      end

      function getpt(p)
      implicit none
      real*8 getpt,p(4)
      getpt=dsqrt(p(1)**2+p(2)**2)
      return
      end
```

APPENDIX E

Fortran Functions

E.1 P_T Distributions

First leading jet P_T

```
getpt(pjet(1,1))
```

Second leading jet P_T

```
getpt(pjet(1,2))
```

Third leading jet P_T

```
getpt(pjet(1,3))
```

where

```
function getpt(p)
implicit none
real*8 getpt,p(4)
getpt=dsqrt(p(1)**2+p(2)**2)
return
```

E.2 Rapidity Distributions

Leading jet rapidity

```
getrapidity(pjet(4,1),pjet(3,1))
```

Second leading jet rapidity

```
getrapidity(pjet(4,2),pjet(3,2))
```

Third leading jet rapidity

```
getrapidity(pjet(4,3),pjet(3,3))
```

where

```
function getrapidity(en,pl)
implicit none
real*8 getrapidity,en,pl,tiny,xplus,xminus,y
parameter (tiny=1.d-8)
xplus=en+pl
xminus=en-pl
```

```
      if(xplus.gt.tiny.and.xminus.gt.tiny)then
         if( (xplus/xminus).gt.tiny.and.(xminus/xplus).gt.tiny)then
            y=0.5d0*log( xplus/xminus  )
         else
            y=sign(1.d0,pl)*1.d8
         endif
      else
         y=sign(1.d0,pl)*1.d8
      endif
      getrapidity=y
      return
      end
```

E.3 Pseudorapidity Distributions

Leading jet $|\eta|$

```
      dabs(getpseudorap(pjet(1,1)))
```

Second leading jet $|\eta|$

```
      dabs(getpseudorap(pjet(1,2)))
```

Third leading jet $|\eta|$

```
      dabs(getpseudorap(pjet(1,3)))
```

where

```
      function getpseudorap(p)
      implicit none
      real*8 getpseudorap,en,ptx,pty,pl,tiny,pt,eta,th,p(4)
      parameter (tiny=1.d-5)
c
      en=p(4)
      ptx=p(1)
      pty=p(2)
      pl=p(3)
      pt=sqrt(ptx**2+pty**2)
      if(pt.lt.tiny.and.abs(pl).lt.tiny)then
```

```
    eta=sign(1.d0,pl)*1.d8
  else
    th=atan2(pt,pl)
    eta=-log(tan(th/2.d0))
  endif
  getpseudorap=eta
  return
  end
```

E.4 $\Delta\Phi(\mu, j)$ Distributions

Leading jet and the muon

```
acos((pjet(1,1)*pplb(1)+pjet(2,1)*pplb(2))/(getpt(pjet(1,1))*pte))
```

Second leading jet and the muon

```
acos((pjet(1,2)*pplb(1)+pjet(2,2)*pplb(2))/(getpt(pjet(1,2))*pte))
```

Third leading jet and the muon

```
acos((pjet(1,3)*pplb(1)+pjet(2,3)*pplb(2))/(getpt(pjet(1,3))*pte))
```

where

```
pte = dsqrt(pplb(1)**2 + pplb(2)**2).
```

APPENDIX F

Scale Factors for ATLAS at $\sqrt{s} = 7$ TeV

Table F.1: Summary of the scale factors applied to the theoretical predictions for ATLAS at $\sqrt{s} = 7$ TeV

Figure number	$\alpha_{\texttt{HERWIRI}}$	$\alpha_{\texttt{HERWIG}}$	$\left(\frac{\chi^2}{d.o.f}\right)_{\texttt{HERWIRI}}$	$\left(\frac{\chi^2}{d.o.f}\right)_{\texttt{HERWIG}}$
Figure 4.1	0.02335	0.02513	9.98474	16.9469
Figure 4.2	0.01863	0.01717	23.1067	11.1928
Figure 4.3	0.03113	0.03241	6.51761	8.87521
Figure 4.4	0.03501	0.03221	24.0232	16.5196
Figure 4.5	0.01460	0.01481	0.941833	0.163036
Figure 4.6	0.01562	0.01141	4.85216	13.4582
Figure 4.7	0.03978	0.04038	0.353112	0.709754
Figure 4.8	0.05890	0.06062	1.01752	0.637338
Figure 4.9	0.02850	0.03601	1.05569	0.434552
Figure 4.10	0.01298	0.01297	2.1948	2.68611
Figure 4.11	0.08608	0.08051	2.0814	4.77456
Figure 4.12	0.01311	0.01324	1.59142	0.78912
Figure 4.13	0.01322	0.01328	1.4619	0.49994
Figure 4.14	0.10004	0.10673	1.88696	1.562
Figure 4.15	0.13106	0.09607	23.3802	8.52
Figure 4.16	0.3112	0.2617	7.1233	6.109
Figure 4.17	0.3304	0.2424	28.5654	21.648
Figure 4.18	0.3124	0.2593	8.19456	2.98847
Figure 4.19	0.3543	0.2311	14.1328	7.50
Figure 4.20	0.1076	0.1128	1.43	2.71
Figure 4.21	0.2720	0.2436	21.5295	14.342
Figure 4.22	0.3429	0.2521	22.763	19.7175
Figure 4.23	0.3514	0.2625	22.195	18.234
Figure 4.24	0.3421	0.2075	30.821	18.2947
Figure 4.25	0.5547	0.5309	4.31	0.70
Figure 4.26	0.5420	0.5172	7.31	1.08

APPENDIX G

Scale Factors for CMS at $\sqrt{s} = 7$ TeV

Table G.1: Summary of the scale factors applied to the theoretical predictions for CMS at $\sqrt{s} = 7$ TeV

Figure number	$\alpha_{\mathtt{HERWIRI}}$	$\alpha_{\mathtt{HERWIG}}$	$\left(\frac{\chi^2}{d.o.f}\right)_{\mathtt{HERWIRI}}$	$\left(\frac{\chi^2}{d.o.f}\right)_{\mathtt{HERWIG}}$
Figure 4.27	0.04373	0.04521	1.16335	1.9151
Figure 4.28	0.06442	0.06216	5.591	3.82266
Figure 4.29	0.52852	0.4025	6.103	2.4118
Figure 4.30	0.18762	0.1915	2.5960	1.29178
Figure 4.31	0.3491	0.2943	21.777	28.785
Figure 4.32	0.4285	0.3658	14.784	7.369
Figure 4.33	0.04635	0.046702	0.7881	1.584
Figure 4.34	0.06175	0.062021	3.8088	3.4261
Figure 4.35	0.02552	0.025342	1.6397	1.2184
Figure 4.36	0.01701	0.01671	2.53745	5.34
Figure 4.37	0.022356	0.022522	5.47165	2.9765
Figure 4.38	0.009275	0.0092	1.7727	2.2856
Figure 4.39	0.6836	0.559	0.92899	1.1542
Figure 4.40	0.6251	0.5551	2.3304	0.825

APPENDIX H

Scale Factors for CMS at $\sqrt{s} = 8$ TeV.

Table H.1: Summary of the scale factors applied to the theoretical predictions for CMS at $\sqrt{s} = 8$ TeV

Figure number	$\alpha_{\texttt{HERWIRI}}$	$\alpha_{\texttt{HERWIG}}$	$\left(\frac{\chi^2}{d.o.f}\right)_{\texttt{HERWIRI}}$	$\left(\frac{\chi^2}{d.o.f}\right)_{\texttt{HERWIG}}$
Figure 5.1	0.05581	0.05855	6.0504	9.144
Figure 5.2	0.07883	0.07482	41.7595	21.4685
Figure 5.3	0.030104	0.03287	19.0735	10.0991
Figure 5.4	0.2119	0.2210	2.0716	4.1188
Figure 5.5	0.4781	0.4672	13.10445	7.96725
Figure 5.6	0.4071	0.3479	8.53955	5.4858
Figure 5.7	0.052016	0.052775	0.305495	0.387096
Figure 5.8	0.06923	0.07114	0.84021	0.66108
Figure 5.9	0.02769	0.028416	0.62492	1.02488
Figure 5.10	0.03445	0.03287	1.17762	1.431335
Figure 5.11	0.025012	0.022301	7.5463	9.0727
Figure 5.12	0.07566	0.07701	2.008275	1.982775
Figure 5.13	0.03193	0.03173	0.4878	1.0485
Figure 5.14	0.031543	0.033212	1.206995	0.561883
Figure 5.15	0.033432	0.034312	0.332517	0.521925
Figure 5.16	0.022063	0.024331	1.85015	0.730665
Figure 5.17	0.010332	0.009302	4.1995	1.95863
Figure 5.18	0.02432	0.02427	3.06359	2.168
Figure 5.19	0.025132	0.025212	0.817415	0.97
Figure 5.20	0.0189112	0.01888931	0.429538	0.98431
Figure 5.21	0.0249110	0.0245101	0.80973	1.30554
Figure 5.22	0.0103311	0.0104312	0.92223	0.95851

APPENDIX I

The Factorization Theorem

The Factorization Theorem [86–90] describes the separation of the physics associated with jet formation from that associated with the hard-scattering in high-energy particle collisions. For example, for the case of muon production, the process is written as follows

$$A(P_1) + B(P_2) \to \mu^+(k_1) + \mu^-(k_2) + \mathrm{X}, \tag{I.1}$$

where the incoming hadrons A and B have momenta P_1 and P_2, respectively, the outgoing muons have momenta K_1 and K_2, and X denotes any additional final-state particles. The four-momentum of the virtual photon that couples to the lepton pair is $q = k_1 + k_2$, with mass $Q^2 = q^2$. The partons are assumed to be spread randomly inside the hadrons, each parton carrying a momentum fraction x_1, x_2 where $x_1, x_2 \in [0, 1]$ so that their momenta are $p_1 = x_1 P_1$ and $p_2 = x_2 P_2$, respectively. The masses of the partons and the hadrons are neglected, since they are much smaller than Q^2. The hadronic cross section is written as a convolution of the hard (partonic) scattering cross section with the parton densities of the hadrons A and B as

$$d\sigma^H(S) = \sum_{i,j} \int_0^1 dx_1 dx_2 f_{iA}(x_1) f_{jB}(x_2) d\sigma_{ij}(s), \tag{I.2}$$

where S is the hadronic and $s = x_1 x_2 S$ is the partonic CM energy. The parton density functions (PDF) are f_{iA} and f_{jB}. More precisely, $f_{iA}(x_i)$ describes the probability of finding a parton i with momentum fraction x_i inside the hadron A. The PDFs are not calculable because of the large coupling constant at the energy scales of the proton; however, they are universal functions which can be measured in one process

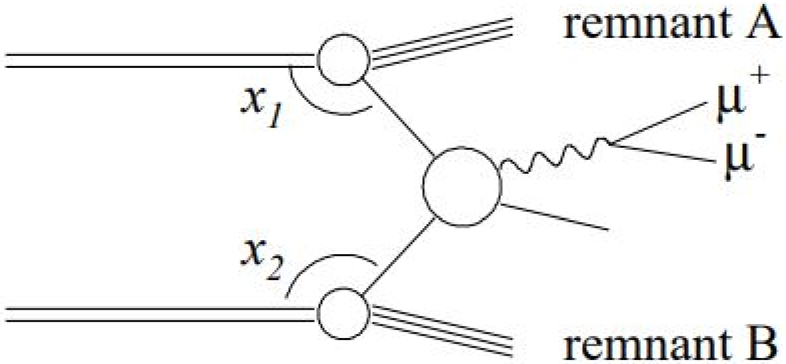

Figure I.1: Factorization of hard and soft processes in the Drell-Yang reaction[1].

and used to predict any other. The factorization may be pictured as in Figure.I.1. The small blobs represent the PDF's of the initial hadrons and the large blob in the center stands for the hard scattering.

[1]Picture taken from `http://www.physics.smu.edu/~olness/cteqpp/potter_dy.pdf`

APPENDIX J

Jet Clustering and Anti-k_t Algorithm

Jets are produced due to the hard partons that participate in the short-distance interaction at the early times of a hadron-hadron collision. The cross sections in QCD diverge when the angle of emission or the energy of the emitted gluon go to zero. In perturbative QCD, each emission corresponds to the real part of a higher-order correction and comes with a power of the strong coupling, α_s. From the previous arguments, it is clear that n emissions contribute to the $\mathcal{O}(\alpha_s^n)$ correction. However, the complete $\mathcal{O}(\alpha_s^n)$ correction requires diagrams up to n loops. It is shown that these come with divergences that match exactly those of the real emissions.

The above mechanism of cancellation of the singularities fails with a bad choice of a jet definition. This can be shown schematically in the following picture. In the top section of Figure J.1, the real and virtual corrections to dijet production are presented. The red cones represent a jet definition. Each correction is denoted by a $\frac{1}{\epsilon}$ pole of the dimensional regularization. These corrections can be written as

$$\frac{1}{\epsilon}J^{(2)}_{IRC-safe} - \frac{1}{\epsilon}J^{(2)}_{IRC-safe} \rightarrow \text{finite}. \tag{J.1}$$

The above equation shows that the divergences coming from the real correction are canceled by the divergences associated to the virtual correction. On the contrary, in the bottom picture where a different jet definition was applied to the very same real and virtual diagrams, the real diagram is classified as a 3-jet event while the virtual diagram is still a 2-jet event. This has serious consequences because the poles are now multiplied by different jet functions, respectively $J^{(3)}$ and $J^{(2)}$. Thus, the cancellation of singular terms does not occur, and the final result is infinite. This can be shown mathematically as

$$\frac{1}{\epsilon}J^{(3)}_{IRC-safe} - \frac{1}{\epsilon}J^{(2)}_{IRC-safe} \to \infty. \tag{J.2}$$

The above equation shows that the divergences coming from the real correction are not canceled by the divergences associated with the virtual correction. Hence, the fact that we obtain a nonsensical theoretical results in the above example comes from the bad choice of jet definition.

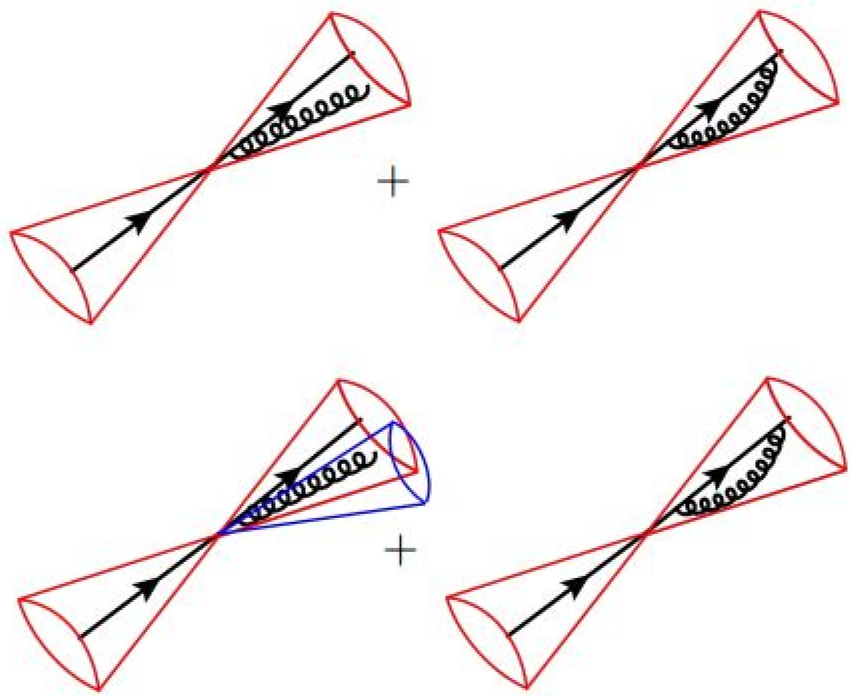

Figure J.1: The infrared and collinear safety of a jet algorithm[1].

It is clear from the above examples that the IRC-safety of a jet definition is a crucial requirement if we are not to waste the results for higher-order corrections to

[1]Taken from Ref. [91].

processes with jets. A complete jet definition consists of the following elements:

$$\text{Jet definition} = \text{jet algorithm} + \text{parameters} + \text{recombination scheme} \qquad \text{(J.3)}$$

Jet algorithms fall into two classes: the cone algorithms and the sequential recombination algorithms. The sequential recombination algorithms dominate almost exclusively in the jet measurements at the LHC. They represent a bottom-up approach by starting to combine the closest particles, according to a distance measure which can be generally written as

$$d_{ij} = \min(P_{Ti}^{2p}, P_{Tj}^{2p})\frac{\Delta R_{ij}^2}{R^2}, \qquad d_{iB} = P_{Ti}^{2p} \qquad \text{(J.4)}$$

where d_{ij} is the distance between the particles i and j and d_{iB} is a distance between the particle i and the beam. The parameter R is called the jet radius and $\Delta R_{ij}^2 = (y_i - y_j)^2 + (\phi_i - \phi_j)^2$ is the geometric distance between the particles i and j in the rapidity-azimuthal angle plane. The value of the parameter p defines specific algorithm from the sequential-recombination family: $p = 1$ for the k_t algorithm [92, 93], $p = 0$ for the Cambridge/Aachen (C/A) algorithm [94], and $p = -1$ for the anti-k_t algorithm [95]. Given a set of the final-state particles, each procedure of finding jets with the sequential-recombination algorithm consists of the following steps:

- Compute distances between all pairs of final-state particles, d_{ij}, as well as the particle-beam distances d_{iB}.
- If d_{ij} and d_{iB} recombine the two particles, remove them from the list of final-state particles, and add the particle ij to that list.
- if $d_{iB} < d_{ij}$, call the particle i a jet and remove it from the list of particles.
- Repeat the above procedure until there are no particles left.

In spite of the fact that the distance measure of the three algorithms can be written as a single formula, because of the different values of the power p, each of them exhibits a different behaviour. The k_t algorithm starts from clustering together the low-p_T objects and it successively accumulates particles around them. The C/A algorithm is insensitive to the transverse momenta of particles and it builds up jets by merging particles closest in the $y - \phi$ plane. The anti-k_t algorithm starts from accumulating particles around high-p_T objects, just opposite to the behaviour of the k_t algorithm. In the anti-k_t algorithm, the clustering stops when there is nothing within radius R around the hard center. For that reason, anti-k_t leads to jets that take circular shapes in the $y - \phi$ plane. This last feature makes the anti-k_t algorithm particularly attractive from the experimental point of view [91].

BIBLIOGRAPHY

[1] Matthew D. Schwartz. *Quantum Field Theory and the Standard Model*. Cambridge University Press, 2014.

[2] B. F. L. Ward. IR-Improved DGLAP Theory: Kernels, Parton Distributions, Reduced Cross Sections. *Annals Phys.*, 323:2147–2171, 2008.

[3] S. Joseph, S. Majhi, B. F. L. Ward, and S. A. Yost. New Approach to Parton Shower MC's for Precision QCD Theory: HERWIRI 1.0(31). *Phys. Rev.*, D81:076008, 2010.

[4] Yorikiyo Nagashima. *Elementary particle physics. Vol. 1: Quantum field theory and particles*. 2010.

[5] S. L. Glashow. Partial Symmetries of Weak Interactions. *Nucl. Phys.*, 22:579–588, 1961.

[6] Abdus Salam. N. Svartholm (Ed.),Elementry Particle Theory. page 367, 1969.

[7] Steven Weinberg. A Model of Leptons. *Phys. Rev. Lett.*, 19:1264–1266, 1967.

[8] Peter W. Higgs. Broken Symmetries and the Masses of Gauge Bosons. *Phys. Rev. Lett.*, 13:508–509, 1964.

[9] Peter W. Higgs. Spontaneous Symmetry Breakdown without Massless Bosons. *Phys. Rev.*, 145:1156–1163, 1966.

[10] F. Englert and R. Brout. Broken Symmetry and the Mass of Gauge Vector Mesons. *Phys. Rev. Lett.*, 13:321–323, 1964.

[11] G. S. Guralnik, C. R. Hagen, and T. W. B. Kibble. Global Conservation Laws and Massless Particles. *Phys. Rev. Lett.*, 13:585–587, 1964.

[12] T. W. B. Kibble. Symmetry breaking in nonAbelian gauge theories. *Phys. Rev.*, 155:1554–1561, 1967.

[13] M. J. G. Veltman. Perturbation theory of massive Yang-Mills fields. *Nucl. Phys.*, B7:637–650, 1968.

[14] Gerard 't Hooft. Renormalization of Massless Yang-Mills Fields. *Nucl. Phys.*, B33:173–199, 1971.

[15] Gerard 't Hooft and M. J. G. Veltman. Regularization and Renormalization of Gauge Fields. *Nucl. Phys.*, B44:189–213, 1972.

[16] Gerard 't Hooft and M. J. G. Veltman. Combinatorics of gauge fields. *Nucl. Phys.*, B50:318–353, 1972.

[17] Gerard 't Hooft. Renormalizable Lagrangians for Massive Yang-Mills Fields. *Nucl. Phys.*, B35:167–188, 1971.

[18] Steven Weinberg. Effects of a neutral intermediate boson in semileptonic processes. *Phys. Rev.*, D5:1412–1417, 1972.

[19] S. L. Glashow, J. Iliopoulos, and L. Maiani. Weak Interactions with Lepton-Hadron Symmetry. *Phys. Rev.*, D2:1285–1292, 1970.

[20] Peter W. Higgs. Broken symmetries, massless particles and gauge fields. *Phys. Lett.*, 12:132–133, 1964.

[21] H. David Politzer. Asymptotic Freedom: An Approach to Strong Interactions. *Phys. Rept.*, 14:129–180, 1974.

[22] D. J. Gross and Frank Wilczek. Asymptotically Free Gauge Theories. 1. *Phys. Rev.*, D8:3633–3652, 1973.

[23] D. J. Gross and Frank Wilczek. Asymptotically Free Gauge Theories. 2. *Phys. Rev.*, D9:980–993, 1974.

[24] Chen-Ning Yang and Robert L. Mills. Conservation of Isotopic Spin and Isotopic Gauge Invariance. *Phys. Rev.*, 96:191–195, 1954.

[25] Elliott D. Bloom et al. High-Energy Inelastic e p Scattering at 6-Degrees and 10-Degrees. *Phys. Rev. Lett.*, 23:930–934, 1969.

[26] F. J. Hasert et al. Observation of Neutrino Like Interactions Without Muon Or Electron in the Gargamelle Neutrino Experiment. *Phys. Lett.*, 46B:138–140, 1973.

[27] F. J. Hasert et al. Observation of Neutrino Like Interactions without Muon or Electron in the Gargamelle Neutrino Experiment. *Nucl. Phys.*, B73:1–22, 1974.

[28] F. J. Hasert et al. Search for Elastic ν_μ Electron Scattering. *Phys. Lett.*, 46B:121–124, 1973.

[29] Jihn E. Kim, Paul Langacker, M. Levine, and H. H. Williams. A Theoretical and Experimental Review of the Weak Neutral Current: A Determination of Its Structure and Limits on Deviations from the Minimal SU(2)-L x U(1) Electroweak Theory. *Rev. Mod. Phys.*, 53:211, 1981.

[30] C. Y. Prescott et al. Parity Nonconservation in Inelastic Electron Scattering. *Phys. Lett.*, 77B:347–352, 1978.

[31] C. Y. Prescott et al. Further Measurements of Parity Nonconservation in Inelastic electron Scattering. *Phys. Lett.*, 84B:524–528, 1979.

[32] L. M. Barkov and M. S. Zolotorev. PARITY VIOLATION IN ATOMIC BISMUTH. *Phys. Lett.*, B85:308–313, 1979.

[33] L. M. Barkov and M. S. Zolotorev. Observation of Nonconservation of Parity in Atomic Transitions. *JETP Lett.*, 27:357, 1978. [Pisma Zh. Eksp. Teor. Fiz.27,379(1978)].

[34] J. G. Branson. The 1981 international symposium on lepton and photon interactions at high energies. In W. Pfei, editor, *Proceedings of The 1981 International Symposium on Lepton and Photon Interactions at High Energies*, pages 279–301. Universitat Bonn, August 1981.

[35] Jrgen Beck Hansen. *A Combination of Preliminary Electroweak Measurements and Constraints on the Standard Model: Prepared for the 2000 summer conferences.* CERN-LHCC-2008-014, CERN-ALICE-TDR-014, 2001.

[36] Georges Aad et al. Observation of a new particle in the search for the Standard Model Higgs boson with the ATLAS detector at the LHC. *Phys. Lett.*, B716:1–29, 2012.

[37] F. Bloch and A. Nordsieck. Note on the Radiation Field of the electron. *Phys. Rev.*, 52:54–59, 1937.

[38] D. R. Yennie, Steven C. Frautschi, and H. Suura. The infrared divergence phenomena and high-energy processes. *Annals Phys.*, 13:379–452, 1961.

[39] G. Grammer, Jr. and D. R. Yennie. Improved treatment for the infrared divergence problem in quantum electrodynamics. *Phys. Rev.*, D8:4332–4344, 1973.

[40] B. F. L. Ward. IR-Improved Operator Product Expansions in non-Abelian Gauge Theory. *Mod. Phys. Lett.*, A28:1350069, 2013. [Mod. Phys. Lett.A28,0069(2013)].

[41] B. F. L. Ward and S. A. Yost. QED x QCD Resummation and Shower/ME Matching for LHC Physics. *Acta Phys. Polon.*, B38:2395–2403, 2007.

[42] B. F. L. Ward. Ir-improved DGLAP theory. *Adv. High Energy Phys.*, 2008:682312, 2008.

[43] D. DeLaney, S. Jadach, S. M. Kim, C. Shio, G. Siopsis, and B. F. L. Ward. Multiple gluon effects in $q + \bar{q} \to t + \bar{t} + X$ at FNAL energies: Semianalytical results. *Mod. Phys. Lett.*, A12:2425–2434, 1997.

[44] D. B. DeLaney, S. Jadach, C. Shio, G. Siopsis, and B. F. L. Ward. Multiple gluon effects in fermionanti-fermion scattering at SSC / CERN LHC energies. *Phys. Rev.*, D52:108–115, 1995. [Erratum: Phys. Rev.D66,019903(2002)].

[45] D. B. DeLaney, S. Jadach, C. Shio, G. Siopsis, and B. F. L. Ward. Renormalization group improved exponentiation of soft gluons in QCD. *Phys. Lett.*, B342:239–244, 1995.

[46] Stanislaw Jadach and B. F. L. Ward. Exponentiation of Soft Photons in the Monte Carlo: The Case of Bonneau and Martin. *Phys. Rev.*, D38:2897, 1988. [Erratum: Phys. Rev.D39,1471(1989)].

[47] Stanislaw Jadach and B. F. L. Ward. Yfs2: The Second Order Monte Carlo for Fermion Pair Production at LEP / SLC With the Initial State Radiation of Two Hard and Multiple Soft Photons. *Comput. Phys. Commun.*, 56:351–384, 1990.

[48] S. Jadach, W. Placzek, E. Richter-Was, B. F. L. Ward, and Z. Was. Upgrade of the Monte Carlo program BHLUMI for Bhabha scattering at low angles to version 4.04. *Comput. Phys. Commun.*, 102:229–251, 1997.

[49] Richard P. Feynman. Very high-energy collisions of hadrons. *Phys. Rev. Lett.*, 23:1415–1417, 1969.

[50] R. D. Field and R. P. Feynman. A Parametrization of the Properties of Quark Jets. *Nucl. Phys.*, B136:1, 1978.

[51] Guido Altarelli. Partons in Quantum Chromodynamics. *Phys. Rept.*, 81:1, 1982.

[52] Guido Altarelli and G. Parisi. Asymptotic Freedom in Parton Language. *Nucl. Phys.*, B126:298–318, 1977.

[53] Howard Georgi and H. David Politzer. Electroproduction scaling in an asymptotically free theory of strong interactions. *Phys. Rev.*, D9:416–420, 1974.

[54] E. J. Williams. Nature of the high-energy particles of penetrating radiation and status of ionization and radiation formulae. *Phys. Rev.*, 45:729–730, 1934.

[55] M. A. Ahmed and Graham G. Ross. Polarized Lepton - Hadron Scattering in Asymptotically Free Gauge Theories. *Nucl. Phys.*, B111:441–460, 1976.

[56] M. A. Ahmed and Graham G. Ross. Spin-Dependent Deep Inelastic electron Scattering in an Asymptotically Free Gauge Theory. *Phys. Lett.*, 56B:385–390, 1975.

[57] Andrzej J. Buras. Asymptotic Freedom in Deep Inelastic Processes in the Leading Order and Beyond. *Rev. Mod. Phys.*, 52:199, 1980.

[58] G. Corcella, I. G. Knowles, G. Marchesini, S. Moretti, K. Odagiri, P. Richardson, M. H. Seymour, and B. R. Webber. HERWIG 6: An Event generator for hadron emission reactions with interfering gluons (including supersymmetric processes). *JHEP*, 01:010, 2001.

[59] G. Marchesini and B. R. Webber. Monte Carlo Simulation of General Hard Processes with Coherent QCD Radiation. *Nucl. Phys.*, B310:461–526, 1988.

[60] I. G. Knowles. Spin Correlations in Parton - Parton Scattering. *Nucl. Phys.*, B310:571–588, 1988.

[61] I. G. Knowles. A Linear Algorithm for Calculating Spin Correlations in Hadronic Collisions. *Comput. Phys. Commun.*, 58:271–284, 1990.

[62] B. F. L. Ward and S. Jadach. YFS MC approach to QCD soft gluon exponentiation. *Acta Phys. Polon.*, B33:1543–1558, 2002.

[63] C. Glosser, S. Jadach, B. F. L. Ward, and S. A. Yost. QED x QCD threshold corrections at the LHC. *Mod. Phys. Lett.*, A19:2113–2120, 2004.

[64] B. F. L. Ward, C. Glosser, S. Jadach, and S. A. Yost. Threshold corrections in precision LHC physics: QED x QCD. *Int. J. Mod. Phys.*, A20:3735–3738, 2005.

[65] D. B. DeLaney, S. Jadach, Ch. Shio, G. Siopsis, and B. F. L. Ward. Multiple photon effects in p p scattering at SSC energies. *Phys. Lett.*, B292:413–416, 1992. [Erratum: Phys. Lett.B302,540(1993)].

[66] R. Keith Ellis, Howard Georgi, Marie Machacek, H. David Politzer, and Graham G. Ross. Factorization and the Parton Model in QCD. *Phys. Lett.*, 78B:281–284, 1978.

[67] R. Keith Ellis, Howard Georgi, Marie Machacek, H. David Politzer, and Graham G. Ross. Perturbation Theory and the Parton Model in QCD. *Nucl. Phys.*, B152:285–329, 1979.

[68] Stephen B. Libby and George F. Sterman. Jet and Lepton Pair Production in High-Energy Lepton-Hadron and Hadron-Hadron Scattering. *Phys. Rev.*, D18:3252, 1978.

[69] V. N. Gribov and L. N. Lipatov. Deep inelastic e p scattering in perturbation theory. *Sov. J. Nucl. Phys.*, 15:438–450, 1972. [Yad. Fiz.15,781(1972)].

[70] Stanislaw Jadach and B. F. L. Ward. Multi - Photon Monte Carlo for Bhabha Scattering at Low Angles. *Phys. Rev.*, D40:3582–3589, 1989.

[71] S. Jadach, M. Skrzypek, and B. F. L. Ward. Soft pairs corrections to low angle Bhabha scattering: YFS Monte Carlo approach. *Phys. Rev.*, D55:1206–1215, 1997.

[72] S. Jadach, B. F. L. Ward, and Z. Was. Coherent exclusive exponentiation for precision Monte Carlo calculations. *Phys. Rev.*, D63:113009, 2001.

[73] S. Jadach and B. F. L. Ward. Final state multiple photon effects in fermion pair production at SLC / LEP. *Phys. Lett.*, B274:470–472, 1992.

[74] S. Jadach, W. Placzek, and B. F. L. Ward. BHWIDE 1.00: O(alpha) YFS exponentiated Monte Carlo for Bhabha scattering at wide angles for LEP-1 / SLC and LEP-2. *Phys. Lett.*, B390:298–308, 1997.

[75] B. R. Webber. Monte Carlo Simulation of Hard Hadronic Processes. *Ann. Rev. Nucl. Part. Sci.*, 36:253–286, 1986.

[76] B. F. L. Ward. New Approach to Hard Corrections in Precision QCD for LHC and FCC Physics. *Mod. Phys. Lett.*, A31(22):1650126, 2016.

[77] Stefano Frixione and Bryan R. Webber. Matching NLO QCD computations and parton shower simulations. *JHEP*, 06:029, 2002.

[78] A. Mukhopadhyay, B. F. L. Ward, S. K. Majhi, and S. A. Yost. Phenomenological Study of the Interplay between IR-Improved DGLAP-CS Theory and the Precision of an NLO ME Matched Parton Shower MC. *Annals Phys.*, 350:485–500, 2014.

[79] J. Alwall, R. Frederix, S. Frixione, V. Hirschi, F. Maltoni, O. Mattelaer, H. S. Shao, T. Stelzer, P. Torrielli, and M. Zaro. The automated computation of tree-level and next-to-leading order differential cross sections, and their matching to parton shower simulations. *JHEP*, 07:079, 2014.

[80] Matteo Cacciari, Gavin P. Salam, and Gregory Soyez. FastJet User Manual. *Eur. Phys. J.*, C72:1896, 2012.

[81] Georges Aad et al. Measurements of the W production cross sections in association with jets with the ATLAS detector. *Eur. Phys. J.*, C75(2):82, 2015.

[82] Vardan Khachatryan et al. Differential cross section measurements for the production of a W boson in association with jets in protonproton collisions at $\sqrt{s} = 7$ TeV. *Phys. Lett.*, B741:12–37, 2015.

[83] Vardan Khachatryan et al. Measurements of differential cross sections for associated production of a W boson and jets in proton-proton collisions at $\sqrt{s} =$ 8 TeV. *Phys. Rev. D*, 2016. [Phys. Rev.D95,052002(2017)].

[84] Albert M Sirunyan et al. Measurement of the differential cross sections for the associated production of a W boson and jets in proton-proton collisions at sqrt(s) = 13 TeV. 2017.

[85] A. Mukhopadhyay and B. F. L. Ward. Interplay between IR-Improved DGLAP-CS Theory and the Precision of an NLO ME Matched Parton Shower MC in Relation to LHCb Data. *Mod. Phys. Lett.*, A31(11):1650063, 2016.

[86] John C. Collins, Davison E. Soper, and George F. Sterman. Factorization of Hard Processes in QCD. *Adv. Ser. Direct. High Energy Phys.*, 5:1–91, 1989.

[87] John C. Collins, Leonid Frankfurt, and Mark Strikman. Factorization for hard exclusive electroproduction of mesons in QCD. *Phys. Rev.*, D56:2982–3006, 1997.

[88] A. V. Efremov and A. V. Radyushkin. Factorization and Asymptotical Behavior of Pion Form-Factor in QCD. *Phys. Lett.*, 94B:245–250, 1980.

[89] S. Catani, M. Ciafaloni, and F. Hautmann. High-energy factorization in QCD and minimal subtraction scheme. *Phys. Lett.*, B307:147–153, 1993.

[90] George F. Sterman. Partons, factorization and resummation, TASI 95. In *QCD and beyond. Proceedings, Theoretical Advanced Study Institute in Elementary Particle Physics, TASI-95, Boulder, USA, June 4-30, 1995*, pages 327–408, 1995.

[91] Sebastian Sapeta. QCD and Jets at Hadron Colliders. *Prog. Part. Nucl. Phys.*, 89:1–55, 2016.

[92] S. Catani, Yuri L. Dokshitzer, M. H. Seymour, and B. R. Webber. Longitudinally invariant K_t clustering algorithms for hadron hadron collisions. *Nucl. Phys.*, B406:187–224, 1993.

[93] Stephen D. Ellis and Davison E. Soper. Successive combination jet algorithm for hadron collisions. *Phys. Rev.*, D48:3160–3166, 1993.

[94] Yuri L. Dokshitzer, G. D. Leder, S. Moretti, and B. R. Webber. Better jet clustering algorithms. *JHEP*, 08:001, 1997.

[95] Matteo Cacciari, Gavin P. Salam, and Gregory Soyez. The Anti-k(t) jet clustering algorithm. *JHEP*, 04:063, 2008.